5-1-2017

Automated Multiplexed Electrochemiluminescence based Immunoarrays for Prostate Cancer Biomarker Protein Detection & Genotoxic Screening Assays Using Electrochemiluminescence and LC-MS/MS

Karteek Kadimisetty
University of Connecticut, karteek.kadimisetty@gmail.com

Automated Multiplexed Electrochemiluminescence based Immunoarrays for Prostate Cancer Biomarker Protein Detection

&

Genotoxic Screening Assays Using Electrochemiluminescence and LC-MS/MS

Karteek Kadimisetty

University of Connecticut, 2017

Abstract

Cancer is the leading cause of death in U.S. next to deaths caused by heart diseases. Cancer causes extreme pain to the patient physical and mental health. Prostate cancer is one of the most common type of cancer in American men besides skin cancer. Even though extreme efforts are being placed in the field of science and technology to develop reliable cancer therapeutics, no cure was found to eradicate or alleviate the pain caused by cancer. Cancer biomarker proteins that are abnormally expressed and secreted into blood in a diseased state could provide early cancer diagnosis and provide better healthcare. This helps in addressing better therapeutic options in much early stages of cancer even before advanced tumors developed where the survival rates are extremely low. As of now for prostate cancer, serum levels of prostate specific antigen is widely used as a diagnostic tool. But over expression of PSA could be from many other prostate related issues leading to false positives. This further results in causing patients stress due to exaggerated diagnosis and treatment options. Detection of panel of prostate cancer biomarkers from serum

sample simultaneous with high sensitivity and selectivity could provide valuable information for early cancer diagnostics and better treatment options.

The primary goal of this thesis is to develop ECL based automated diagnostic platforms that can detect panel of prostate cancer biomarkers with high sensitivity and high throughput. The assay platforms being low cost, rapid and non-complex they can be easily translated into public health care much faster and provide conclusive results with no ambiguity for better treatment options. This thesis explores many new device fabrication, automation strategies and liquid handing systems for easier completion of sensitive immunoassays with ultralow detection limits. Nano structured detection platforms and RuBPY dye doped silica nanoparticles have been used as amplification strategies to detect the serum proteins at low femtogram levels. We successfully developed immunoassay platforms that can detect small protein panel (3 proteins) to large protein (8 proteins) panel. We demonstrated 3-D printing as rapid fabrication tool to make microfluidic immunoarrays that enabled low cost sensors with relatively low sample volume requirements. The developed ECL arrays holds great promise in accurate detection of early stages of cancer in physician’s clinic and point of care settings.

Automated Multiplexed Electrochemiluminescence based Immunoarrays for Prostate Cancer Biomarker Protein Detection

&

Genotoxic Screening Assays Using Electrochemiluminescence and LC-MS/MS

Karteek Kadimisetty

B. Pharmacy Andhra University, 2008

M.S. Chemistry Lamar University, 2011

A Dissertation

Submitted in Partial Fulfillment of the

Requirements for the Degree of

Doctor of Philosophy

At the

University of Connecticut

2017

2017

Approval Page

Doctor of Philosophy Dissertation

Automated Multiplexed Electrochemiluminescence based Immunoarrays for Prostate Cancer Biomarker Protein Detection

&

Genotoxic Screening Assays Using Electrochemiluminescence and LC-MS/MS

Presented by

Karteek Kadimisetty

Major advisor _____

James F. Rusling

Associate advisor _____

Mark W. Peczuh

Associate advisor _____

Jing Zhao

University of Connecticut

2017

Dedicated to

My Parents and Family

Kadimisetty Nageswara Rao
Kadimisetty Venakata Ratnam
Spundana Malla
Durga Revathi &
Durga Satish

& Educators

Dr. Shyam S. Shukla
Dr. James F. Rusling

Acknowledgement

I am extremely thankful to Jim (Dr.James F. Rusling) for all his support and suggestions throughout my career. He always inspired me and educated me to do better things and achieve great heights with our work. His words of wisdom and motivation are invaluable along with his years of experience, I learned a lot in my life. I follow his suggestion and always found success, whether it may be in regards to writing a paper or designing an experiment or presenting a work or personal issues. I respect him from bottom of my heart. Given an opportunity I would love to be associated with him in future as well both personally and professionally. Other great mentor and teacher in my life is Dr.Shyam S. Shukla who thought me about being simple, kind and always do good and good things will happen. He is my master's thesis advisor who still guides me both personally, professionally and spiritually to be a better human being.

My Co-Advisors Dr. Mark W. Peczuh and Dr. Jing Zhao have been extremely supportive and kind. Always opened their doors when I am in need for a suggestion or being on my committee or providing references in spite of their busy schedules. Special thanks to Dr. Jessica L. Rouge for agreeing to be on my thesis committee in the last minute. I appreciate all her help and support. I also thank Dr. Adamson for being on my general exam committee and helped with his suggestions. Dr. Dharamainder Choudhary my other advisor is one of my major collaborator and always helped me with his guidance both professionally and personally. He was always there when I needed him and provided excellent support throughout my PhD.

I want to thank my mentors Vigneshwaran Mani and Naimish P.Sardesai along with group members Snehasis, Itti Bist, Amit Joshi, Islam Mosa, Di, Chi Tang, Min Shen, Colleen, Brunah, Gayatri, Yun, Abby Jones, Mohammed, Boya, Bhaskara, Ketki, Kiran Bano, Greg bishop, Chandra dixit for their valuable suggestions and discussion throughout my Ph.D career. I would like to

extend my special thanks to all my collaborators for travelling with me and supporting me. I would like to specially mention Dr. Ronaldo C. Faria a dear friend who visited our laboratory from whom I learned many skills. Special thanks to Dr. Norman Lee from George Washington University for his support. I would like to thank Dr. Abhay for his valuable suggestions and discussions. I would also like to thank my dear friends Lavanya, Vasu, Santosh, Divya, Sravan, Spandana, Saketh Gudipati, Priyanka and Soumya for their support and fun times. I am very thankful to Dr. Roger Ristau for training session on TEM and SEM along with Daniel Daleb our machine shop personnel for his advice and extreme support during my initial years of microfluidics fabrication. Dan is extremely fun to work with and always had solutions to all my problems and made my job easy.

I am grateful to all chemistry department staff especially Emilie, Oskar, Ashley and Aneesa for assisting me with all administrative things and help my stay at UCONN go smooth. I thank Charlene Fuller for all the help with crazy number of orders she processes every day for all the students and very inspiring with her hard work.

Finally I would like to thank almighty and all my family members for this wonderful Ph.D. journey, I am honored to receive all their love and support.

Table of Contents

LIST OF SCHEMES

LIST OF FIGURES

LIST OF TABLES

Chapter 1

Introduction

1.1 Purpose of Study and Significance

Cancer is leading cause of death in United States, second only to heart disease. Prostate cancer is most common type of cancer in American men besides skin cancer.[1] As per American cancer society new prostate cancer cases are about 161,360 and about 26,730 deaths from prostate cancer. The average age of prostate cancer diagnosis is about 66 years and usually 6 in 10 men diagnosed with prostate cancer are above age of 65 years. 1 in 7 men will be diagnosed with prostate cancer during their lifetime.[2] Currently prostate specific antigen (PSA) detection in serum samples is being used as early detection tool. While doctors agree that just doing PSA test alone can't be prefect to find prostate cancer reliably, doctors rely upon getting biopsies using transrectal ultrasound lo locate cancerous tissues. Still there is chance of missing as it may not detect certain areas of the containing cancer. This causes extreme discomfort to the patient mentally and physically even before knowing the presence of cancer. Besides just identification of presence of cancer staging the cancer or knowing the extent of cancer also plays crucial role in determining better treatment options. Imaging tests are currently employes to understand the extent of tumor but several type of scanning procedures used currently like computed tomography scan (CT) or magnetic resonance imaging (MRI) can't detect small areas of cancerous tissues like lymph nodes. Looking at the magnitude of the cancer prevalence and issues dealing with diagnosing cancer and staging cancer with less false positives and less false negatives it is of absolute necessity. There is

need to develop a diagnostic tool that can detect the diseased state with relatively less complexity and more confidence can increase the chance of survival of cancer individual and provide better therapeutic choices.

Detecting elevated levels of proteins in blood serum have a great prospective as biomarkers of a diseased state can be used in early detection of cancer. [3,4] Detecting panel of these biomarkers from serum samples promise better futuristic personized health care.[5,6,7] detection of these multiple proteins from serum samples simultaneously could reduce the possibility of false positives and false negatives enormously as supposed to just single protein detection might have variations in expression from person to person.[8,9] There is a lesser chance of failed expression of all the biomarkers in a panel compared to a single marker. This increases the confidence in diagnosis of cancer and help in better judgment of cancer treatment options. Diagnostic platforms which can detect such panels of biomarkers needs universal acceptance to maximize their use for better patient health care. The protein measurements of such panels at clinical point of care requires to be rapid (short assay times), simple (no complex operations so that they can be adapted easily without need for new training procedures and can be adapted to current health care settings), sensitive (should be able to detect the selective markers in complex serum samples with precision and low detections), automated (for better and cohesive work flow reducing errors from human operations) finally need to be inexpensive so that it can replace current methodologies with benefit of cost reduction.[4,5]

Diagnostic platforms based on microfluidics promises all the above mentioned advantages while having a lot of complex operations integrated into a simple, portable, inexpensive, compact devices also having greater fluidic control of reagents required for the assay.[10,4] Current methodologies that are commercially used and considered as gold standard to detect proteins are

single protein enzyme linked immunosorbent assay (ELISA) and western blot assays.[11] While these assays are considered to most reliable and being widely used some critical issues like assay time, cost, complexity and labor intensive protocols hinder them to be acting a point of care diagnostic tools for better health care.[12] Besides the complexity issues use of higher sample volume of precious biological samples is also an important issue to address. Some new age commercial techniques like bead based optical detection and electrochemiluminescent (ECL) assays hold a great prospect in performing multiplex immunoassay.[13,14] But low cost, automation, better detection limits with wider dynamic ranges are some challenges still need to be addressed.

Goal of this research is to develop such new age diagnostic assay platforms that can detect multiple proteins in serum samples with extreme ease and automation. The thesis address several strategies employed to develop such automated platforms that performs immunoassays with fraction of costs compared to current commercial platforms while getting good sensitivities and broader dynamic ranges. So that the methods can be applied several biomarkers at a time for several diseased states. We developed ECL based automated biosensors for detection of several biomarkers like Prostate specific antigen (PSA), Prostate specific membrane antigen (PSMA), Platelet factor-4 (PF-4), Interlukin-6 (IL-6) etc., relevant to early diagnosis of prostate cancer. In this thesis we demonstrated that we developed several biosensors that are high throughput and easy to use diagnostic platforms. Our platforms were designed with vision of thier performance in doctor's office or clinic as simple point of care diagnostic tools that can help in better therapeutic outcomes and relieve patients for mental and physical stress. The first 5 chapters of this thesis deal with such prostate cancer biomarker detection platforms with significant improvement from our previous efforts. Our efforts here using ECL based platforms utilizes nanostructured detection platforms with light emitting ruthenium bipyridine substrate (RuBPY/$Ru(bpy)_3^{2+}$) in a silica

nanoparticle as detection label. When applied voltage/potential in presence of a co-reactant light emitted and captured by a simple CCD camera. Chapter 1 gives overall view of the principles and background relevant to the work.

Chapter 2 demonstrates development of automated multiplexed ECL immunoarrays for prostate cancer biomarkers from human serum samples. This platform here described is a simple, low cost, microprocessor controlled microfluidic immunoarray for detection of 4 proteins simultaneously. The device mainly includes a 30-microwell detection chip coupled with sample/reagent loading cassette connected by micropumps. The reagent/sample loading cassette has all the reagents required to complete the immunoassay and micropumps controlled by Arduino microprocessor delivers all the reagents on to single walled carbon nanotube forest with capture antibodies for selective proteins capture. RuBPY silica detection antibody conjugate completes the sandwich immunoassay that emits ECL when applied with potential in presence of a co-reactant tripropylamine which is measured by a CCD camera. Our assays were thoroughly validated with real cancer patient samples by comparison with gold standard ELISA and found good correlation.

In chapter 3 we demonstrated the use of 3-D printing for the first time in developing immunoassay based diagnostic platform. 3-D printing being an attractive alternative to traditional methods of microfluidic device fabrication. We used low cost desktop fused deposition modeling based 3-D printer to fabricate a low tech immunoarray. Here we demonstared pumpless gravity assisted microfluidic immunoarray to detect 3 prostate cancer biomarkers simultaneously from serm samples using ECL based sandwich immunoassay. Here we used detection antibody coated RuBPY silica nanoparticles as detection labels which emits ECL from the sandwich immunoassay in presence of co-reactant tripropylamine which is measured by a CCD camera. Here for the first time we also showed use of portable, miniaturized power source like supercapacitors to apply

potential for ECL generation for futuristic diagnostic platforms. The supercapacitors were rapidly photo charged via a solar panel to power ECL reaction, and we demonstrated high sensitivity detection of 3 biomarkers and validated with comparison by single protein ELISAs.

In chapter 4, we demonstrated use of stereolithographic 3-D printers to make clear plastic compact microfluidic devices for sensitive detection of 2 prostate cancer biomarkers from human serum samples. We showed here use of low volumes of serum samples compared to our previous platforms with shortened assay times resulting similar sensitive detection limits and dynamic ranges. Here we utilized advantages of microfluidics for automated liquid handling resulting in completion of immunoassays with minimal manual interference. In this project we also wanted to demonstrate diagnostic significance of PSMA as prostate cancer biomarker hence we analyzed relatively higher number of patient samples (38) than our previous array to see their concentrations in serum and further validated with gold standard single protein ELISA.

Chapter 5 briefly discusses about automated detection of big panel of prostate cancer biomarkers, 8 proteins at a time on a single array. We utilized all our experience from previous projects to develop this low cost, point of care ECL based immunosensor. One thing we haven't addressed in previous arrays was user friendly modules to have coherent work flow and show the steps of immunoassay while happening, so that the operator has better user experience while performing the assays. We showed the reproducibility of our 8 protein assay platform with spiked samples in human serum and analysis of real human serum samples.

Chapter 6 with introduction of genotoxicity & 7 we used 3-D printing to develop automated DNA based genotoxicity sensor that can perform multi-analyte analysis from environmental samples. The electrochemiluminescent (ECL) detection platform incorporates layer-by-layer (LbL) assembled films of microsomal enzymes, DNA and an ECL-emitting ruthenium metallopolymer in ~10 nm deep microwells. Liquid samples are introduced into the array, metabolized by the human enzymes,

products react with DNA if possible, and DNA damage is detected by ECL with a camera. Here we assessed genotoxic potential of E-cigarettes and polluted water samples. This array is addressed towards onsite monitoring application with rapid assessment.

Chapter 8, briefly discusses LC-MS/MS based genotoxic evaluation methods that can detect site specific DNA damage of carcinogens. Our goal was to develop analytical method that pin points the possible site of adduction that might result in mutation, which further can be correlated with an organ specific cancer.

1-2. Electrochemiluminescence and sandwich immunoassay

Electrochemiluminescence (ECL) is also called electro generated chemiluminescence where chemical species at a electrode surface undergo high energy electron transfer reactions to reach excited state that can emit light when they relax.[15,16,17] ECL has become a powerful tool in analytical field with its applications in many field like immunoassays. Environmental analysis, bio-imaging, toxicology studies etc.[17] The major advantage of ECL over chemiluminescence (CL) in analytical platforms is that ECL allows control over time and position of reaction happening. Controlling position of ECL reaction specific to detector improves sensitivity by decreasing the signal to noise to ratio. This also allowed multiple reactions monitoring in a same sample.[18] In our case multiple reactions can be monitored in a same array with different microwells. Compared to fluorescence ECL is much more sensitive as there is no background signal from a light source to generate signal.[19] Use of ECL as detection platform has been increased in the recent past for detection of serum proteins as biomarkers to diagnose a diseased state.

Protein detection based on ECL mainly depends of presence of ECL label such as $Ru(bpy)_3^{2+}$ as detection tag. Usually ECL tags are preferentially labelled to antibodies and these

antibodies as part of sandwich immunoassay give ECL signal. In a simple sandwich immunoassay the specific capture antibodies are attached to detection platform usually a solid support/solid electrode. The proteins of interest are captured from samples and followed ECL tagged detection/secondary antibodies are attached to form sandwich immunoassay. The concentration of analytes/proteins is proportional to ECL species tagged secondary antibody. ECL signals produced in presence of ECL co-reactant are usually measured by charge-coupled device (CCD) camera[20] or a much more sensitive photo-multiplier tube.[21] Thus ECL can be used as ultrasensitive detection technique for biomolecule identification and quantification. Besides the advantages of ECL being sensitive, ECL can be used in high throughput biosensor technologies that is capable of multiplexed detection with good selectivity and low detection limits.

1-3. ECL generation using $Ru(bpy)_3^{2+}$ and Tripropylamine (TPrA)

After the sandwich immunoassay was done ECL was generated from reduction of $[Ru(bpy)_3]^{2+}$ via direct oxidation of TPrA. TPrA was oxidized at electrode surface with 0.95 -1.0 V vs Ag/AgCl forming a TPrA cation radical ($TPrA^{*+}$) as shown in scheme 1.1, step1. $TPrA^{*+}$ was then deprotonated to form $TPrA^{*}$ when reacted with $[Ru(bpy)_3]^{2+}$ scheme 1.1, step2. $TPrA^{*}$ is necessary reduce $[Ru(bpy)_3]^{2+}$ to $[Ru(bpy)_3]^{+}$ scheme 1.1, step3. The $TPrA^{*+}$ in the system then oxidizes $[Ru(bpy)_3]^{+}$ to photo excited $[Ru(bpy)_3]^{2+*}$ the emits light at 610 nm scheme 1.1, step4&5. This RuBPY/TPrA system has been widely utilized for ECL generation as this provides extremely sensitive subpicomolar protein concentration detection.[22,23] RuBPY/TPrA has been successfully implemented in commercial protein detection platforms from Meso-Scale Discovery (MSD).[14]

STEP 1: $TPrA \rightarrow TPrA^{\bullet+} + e^-$

STEP 2: $TPrA^{\bullet+} \rightarrow TPrA^{\bullet} + H^+$

STEP 3:

$TPrA^{\bullet} + [Ru\text{-}(bpy)_3]^{2+} \rightarrow [Ru\text{-}(bpy)_3]^{+} + Products$

STEP 4:

$[Ru\text{-}(bpy)_3]^{+} + TPrA^{\bullet+} \rightarrow [Ru\text{-}(bpy)_3]^{2+*} + Products$

STEP 5:

$[Ru\text{-}(bpy)_3]^{2+*} \rightarrow [Ru\text{-}(bpy)_3]^{2+} + h\upsilon\ (610\ nm)$

Scheme 1.1 Proposed mechanism for ECL generation at electrode surface from $Ru(bpy)_3^{2+}$ via TrPA.

1-4. Dye ($[Ru(bpy)_3]^{2+}$) Doped Silica nanoparticles for Amplified ECL detection

Nanoparticles have been excellent choice in the recent past for many researchers due to their versatile characteristics like variable compositions, surface modifications, encapsulations and executional simplicities. The use of nanoparticles have been extended to many fields like therapeutic monitoring biomedical imaging,[24,25] sensing,[26,27] sensor amplification,[28] drug load and delivery.[29] From the time since Stöber *et al.*,[30] showed that availability of colloid silica nanoparticles with defined structure and porosity, silica nanoparticles have been used in many fields of Biomedical research where the mesoporous nature, hybrid construction capabilities and load carrying capacity have been exploited.[31] Dye doped silica nanoparticles with combination of various surface modifications could provide great edge in selective recognition for bio-sensing and imaging.[32] Dye doped silica nanoparticles as they can enclose large number of dye molecules in confined silica matrix can enhance their signal enormously compared to that of organic fluorophores.[33] These advantages make our dye doped mesoporous silica nanoparticles suitable for using them as both amplification and detection probe

in our immunoassays without need for introducing another signal amplification strategies. In this work we synthesized dye doped ($[Ru(bpy)_3]^{2+}$) silica nanoparticles where positively charged $[Ru(bpy)_3]^{2+}$ were electrostatically enclosed and bound to negatively charged silica particles. Nanoparticles have been prepared using in water in oil emulsion methods where controlled hydrolysis of tetraethyl orthosilicate (TEOS) resulted in monodisperse $[Ru(bpy)_3]^{2+}$ doped silica nanoparticles.[34] As the $[Ru(bpy)_3]^{2+}$ is doped inside the silica network core of the nanoparticle the outer surface has been use to conjugate the bio-recognition molecules such as antibodies via a stable amide bond, to use them as detection probes in the immunoassays.[35] These $[Ru(bpy)_3]^{2+}$ silica nanoparticles can provide amplified detection ECL signal and minimized dye photo degradation as they are present inside the nanoparticles. In this study we demonstrated the use of $[Ru(bpy)_3]^{2+}$ silica particles for detection of multiple proteins on a single platform by decorating them with detection antibodies as required.

1-5. Single Wall Carbon Nanotube (SWCNT) forests

Carbon nanotubes have been previously reported in 1991 by Iijima using simple carbon arc synthesis as finite graphite structures that are needle like tubes called carbon nanotubes.[36] Carbon nanotubes have been recognized to have wide range of interesting properties like high thermal stability, chemical stability, flexibility, great conductivity and excellent mechanical strength.[37] Previously carbon nanotubes have been exploited for their advantages and been sued in many applications like electrochemical sensing and ECL platforms.[38,39] High surface areas estimated as high as 1600 m^2g^{-1} [40]and excellent conductivity along with presence of functionalized surface groups relates to achieving high biomolecule densities such as antibodies and proteins for sensing applications.[41] This in turn facilitated device miniaturization while not sacrificing the

sensitivity. Previously a team from UCONN led by Dr. Fotios Papadimitrakopoulos demonstrated self-assembly of 20-30 nm single walled carbon nanotubes (SWCNT) in solid supports into dense carboxylate functionalized SWCNT forest.[42] These forests developed as SWCNTs as standing upright bundles on a nafion - iron oxide decorated conductive surfaces with coverage >98%. Efficient electrical communication was also established between electrode surface via carbon nanotubes to the biomolecules like HRP attached to the ends.[43] Our group has previously shown using carbon nanotubes as amplification strategy for highly sensitive detection of cancer biomarkers.[44] These single walled carbon nanotube forests have been successfully used to detect single and multiple proteins from complex serum matrix of prostate and oral cancer patients.[45-47] These amplification strategies with capture antibodies enabled high capture protein efficiency resulting in sensitive ultralow detection limits.

Briefly single walled carbon nanotube forest is prepared by firstly shortening the long SWCNTs to short 20-30 nm size SWCNTs. The carboxylated ends of the SWCNTs was formed by oxidation via acid treatment with HNO_2 and H_2SO_4 as shown in scheme 1 described in detail in reference.[42] These SWCNTs stand in upright bundles on thin nafion iron oxide films prepared on a pyrolytic graphite chip. The carboxylated ends exposed will enable conjugation of capture antibodies efficiently via a amide bond by EDC-NHSS amidization. Firstly thin layer of negatively charged polyelectrolyte nafion and $Fe(OH)_x$ was prepared on the surface of the pyrolytic graphite chip. Then DMF dispersions of shortened SWCNTs was allowed to self-assembled on previously prepared metal functionalized substrate Scheme 1. The elevated pH of DMF wash and DMF in SWCNTs solution causes surface immobilized Fe^{3+} layer to transform into its basic hydroxide form that provides initial driving force for acid base neutralization of carboxylated SWCNTs and $Fe(OH)_x$ layer resulting in self-assembly to occur. This allowed the upright position of SWCNTs

bundles as carboxyl groups were only present at the ends. In my research these SWCNTs forest that provides high capture antibody density along with signal amplification from RuBPY doped silica nanoparticles provided sensitive detection of multiple cancer biomarker proteins from serum samples at ultralow detection limits.

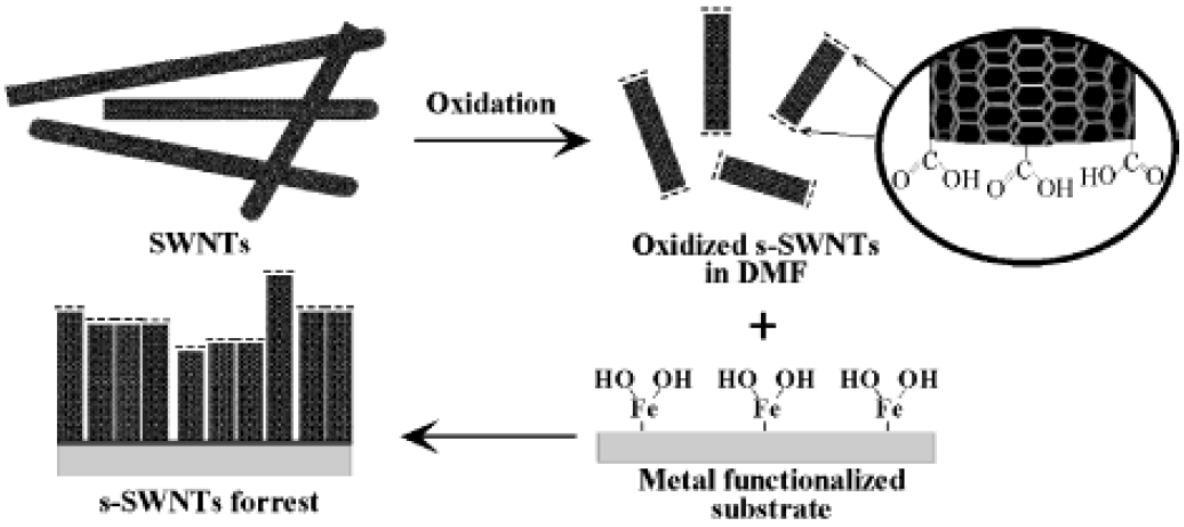

Scheme 1-2. Schematic representation of preparation of single walled carbon nanotube forest.[42] (Reprinted from reference 42, Copyright 2001, with permission from American Chemical Society).

1-6. Microfluidics and automation

Microfluidics refers to phenomenon with set of technologies involved in efficient manipulation of fluids in small volumes within an artificially fabricated system.[48] Microfluidics offer portability of conventional immunoassay platforms with better fluidic handing. Microfluidics enable to reduce risk of operator errors, increase reaction efficiencies and lower assay times.[49] Microfluidics enables to miniaturize, integrate complex procedures and automate diagnostic assay platforms. Microfluidics allows small sample volume as it has enhanced surface area to volume ratio in a confined space such as micro channels. In case on sandwich immunoassay this allows

high analyte capture efficiency in a given small volume of sample provided availability of capture agents on the surface. Fluidic arrays provide short diffusion distance inside the channels, providing reduced use of sample volumes for similar or enhanced chemical or biological reactions compared to conventional methods.[50] In addition to the development of platforms, overall time, sample volume, and automation are other important factors to be addressed for POC applications. In accordance with the CLIA regulations, integration of microfluidics with the analytical system is crucial for reducing the overall immunoassay times and sample volumes, and for introducing pump-less reagent delivery.[51] Microfluidic designing is a well-researched area,[52] but lithography-based prototyping is a costly and time consuming process due to the requirement of mask designing and master-mold development. Therefore, new tools for enabling such rapid microfluidic prototyping are highly sought that are also easy to use even for new entrants. Using microfluidics as path our group's goal to develop diagnostic platforms that can be easily translated to physician's clinics for onsite pint of care diagnostics. We have developed many microfluidic assay platforms for detection of cancer biomarkers in serum samples efficiently with ultralow detection limits.[53-57] Besides conventional methods of fabricating the microfluidic arrays we have been pioneers since past two years in utilizing 3-D printing for rapid fabrication of our bio-analytical microfluidic arrays.

1-7. 3-D printing

3D printing involves the production of an object from a computer-aided design (CAD) file by depositing a material or multiple materials in successive layers using precisely controlled positioning and delivery systems. In general, 3D printing requires few steps: preparation of a design file using CAD software, generation of instructions for the printing process using a slicer

program, printing the designed object by delivering or hardening a material onto a platform according to the instructions defined by the slicer program, removal of the object from the printer platform, and post-processing to remove printed supports or other extraneous material.[58] This simple approach enables relatively rapid production of a wide variety of prototypes and offers an advantage over other fabrication methods, which usually require multiple production steps and greater capital investment in infrastructure. 3D printing, also called additive manufacturing, can be accomplished by several strategies that vary in basic operating principles, complexity, and cost. Such techniques include deposition of thin threads of heated thermoplastic (fused deposition modeling (FDM)) or viscoelastic materials (syringe deposition or direct ink writing), sintering of powders, or by exposure of photocurable resins (stereolithography (SLA)) or inks (MultiJet, PolyJet) using a laser, digital light processing (DLP) projector, or other light source.[59,60] In my research we mainly used FDM based printers and SLA based printers for device fabrication.

In FDM, a thermoplastic filament, typically 1.75 or 3.00 mm in diameter, is forced through a heated nozzle about 0.2–0.5 mm in diameter onto a moving platform. Common thermoplastic filament materials include poly(lactic acid), poly(carbonate), and acrylonitrile butadiene styrene (ABS). SLA was the first form of 3D printing that was invented and commercialized. This method employs a light source, such as a laser, to fabricate objects in a layer-by-layer fashion from photocurable resin. Bioanalytical measurements often require systems capable of handling small volumes (μl or less). We used 3-D printing to fabricate the diagnostic assay platforms to detect the biomarker proteins for serum. The new age printers have good printing resolutions enabled us to produce the microfluidic structures as low as 500 µM resulting in use of low sample volume which are often scarce in biological samples. The use of 3D printing as a quick and easy alternative to traditional methods for preparing fluidic devices in case of diagnostics will enable their faster

translation into public healthcare. We used 3-D printing in both cancer diagnostics and genotoxic evaluation of environmental pollutants at relatively to low cost and low sample volumes. Our initiate in using 3-D printing has opened up huge bio-analytical space where our methods can be adapted to many more applications. In the coming chapters of this thesis we will discuss elaborately all the strategies mentioned in this chapter to develop and enhance our immunoassay platforms for sensitive detection cancer biomarker proteins for serum.

1.8 References

1. Smith, R. A.; Brooks, D.; Cokkinides, V.; Saslow, D.; Brawley, O. W. Cancer screening in the United States, 2013. *CA: a cancer journal for clinicians* **2013**, *63*, 87-105.

2. https://www.cancer.org/cancer/prostate-cancer/about.html, Accessed April 11, 2017.

3. Kingsmore, S. F. Multiplexed protein measurement: technologies and applications of protein and antibody arrays. *Nature reviews Drug discovery* **2006**, *5*, 310-321.

4. Rusling, J. F. Multiplexed electrochemical protein detection and translation to personalized cancer diagnostics. *Anal. Chem.* **2013**, *85*, 5304-5310.

5. Rusling, J. F.; Kumar, C. V.; Gutkind, J. S.; Patel, V. Measurement of biomarker proteins for point-of-care early detection and monitoring of cancer. *Analyst* **2010**, *135*, 2496-2511.

6. Wulfkuhle, J. D.; Liotta, L. A.; Petricoin, E. F. Proteomic applications for the early detection of cancer. *Nature reviews cancer* **2003**, *3*, 267-275.

7. Hawkridge, A. M.; Muddiman, D. C. Mass spectrometry–based biomarker discovery: toward a global proteome index of individuality. *Annual Review of Analytical Chemistry* **2009**, *2*, 265-277.

8. Giljohann, D. A.; Mirkin, C. A. Drivers of biodiagnostic development. *Nature* **2009**, *462*, 461-464.

9. Ludwig, J. A.; Weinstein, J. N. Biomarkers in cancer staging, prognosis and treatment selection. *Nature Reviews Cancer* **2005**, *5*, 845-856.

10. Yager, P.; Edwards, T.; Fu, E.; Helton, K.; Nelson, K.; Tam, M. R.; Weigl, B. H. Microfluidic diagnostic technologies for global public health. *Nature* **2006**, *442*, 412-418.

11. Wang, J. Electrochemical biosensors: towards point-of-care cancer diagnostics. *Biosensors and Bioelectronics* **2006**, *21*, 1887-1892.

12. Cox, K. L.; Devanarayan, V.; Kriauciunas, A.; Manetta, J.; Montrose, C.; Sittampalam, S. In *Immunoassay Methods;* Sittampalam, G. S., Coussens, N. P., Brimacombe, K., Grossman, A., Arkin, M., Auld, D., Austin, C., Baell, J., Bejcek, B., Chung, T. D. Y., Dahlin, J. L., Devanaryan, V., Foley, T. L., Glicksman, M., Hall, M. D., Hass, J. V., Inglese, J., Iversen, P. W., Lal-Nag, M., Li, Z., McGee, J., McManus, O., Riss, T., Trask OJ, J., Weidner, J. R., Xia, M. and Xu, X., Eds.; Assay Guidance Manual; Bethesda (MD), 2004; .

13. http://www.roche.com/about/business/diagnostics.htm Accessed April, 2017

14. https://www.mesoscale.com/ Accessed April, 2017

15. Miao, W. Electrogenerated chemiluminescence and its biorelated applications. *Chem. Rev.* **2008**, *108*, 2506-2553.

16. Tokel, N. E.; Bard, A. J. Electrogenerated chemiluminescence. IX. Electrochemistry and emission from systems containing tris (2, 2′-bipyridine) ruthenium (II) dichloride. *J. Am. Chem. Soc.* **1972**, *94*, 2862-2863.

17. Bard, A. J. *Electrogenerated chemiluminescence;* CRC Press: 2004.

18. Wilson, R.; Clavering, C.; Hutchinson, A. Electrochemiluminescence enzyme immunoassays for TNT and pentaerythritol tetranitrate. *Anal. Chem.* **2003**, *75*, 4244-4249.

19. Bard, A. J.; Debad, J. D.; Leland, J. K.; Sigal, G. B.; Wilbur, J. L.; Wohlsatdter, J. N. In Encyclopedia of Analytical Chemistry: Applications, Theory and Instrumentation; Meyers, R. A., Ed.; Wiley: New York, 2000; Vol. 11, p 9842.

20. Marquette, C. A.; Degiuli, A. Electrochemiluminescent biosensors array for the concomitant detection of choline, glucose, glutamate, lactate, lysine and urate. *Biosensors and Bioelectronics* **2003**, *19*, 433-439.

21. Blackburn, G. F.; Shah, H. P.; Kenten, J. H.; Leland, J.; Kamin, R. A.; Link, J.; Peterman, J.; Powell, M. J.; Shah, A.; Talley, D. B. Electrochemiluminescence detection for development of immunoassays and DNA probe assays for clinical diagnostics. *Clin. Chem.* **1991**, *37*, 1534-1539.

22. Miao, W.; Bard, A. J. Electrogenerated chemiluminescence. 77. DNA hybridization detection at high amplification with [Ru (bpy) 3] 2 -containing microspheres. *Anal. Chem.* **2004**, *76*, 5379-5386.

23. Forster, R. J.; Bertoncello, P.; Keyes, T. E. Electrogenerated chemiluminescence. *Annual Review of Analytical Chemistry* **2009**, *2*, 359-385.

24. Erathodiyil, N.; Ying, J. Y. Functionalization of inorganic nanoparticles for bioimaging applications. *Acc. Chem. Res.* **2011**, *44*, 925-935.

25. Sounderya, N.; Zhang, Y. Use of core/shell structured nanoparticles for biomedical applications. *Recent Patents on Biomedical Engineering* **2008**, *1*, 34-42.

26. Jain, P. K.; Huang, X.; El-Sayed, I. H.; El-Sayed, M. A. Noble metals on the nanoscale: optical and photothermal properties and some applications in imaging, sensing, biology, and medicine. *Acc. Chem. Res.* **2008**, *41*, 1578-1586.

27. Lee, Y. K.; Kopelman, R. Optical nanoparticle sensors for quantitative intracellular imaging. *Wiley Interdisciplinary Reviews: Nanomedicine and Nanobiotechnology* **2009**, *1*, 98-110.

28. Mani, V.; Chikkaveeraiah, B. V.; Patel, V.; Gutkind, J. S.; Rusling, J. F. Ultrasensitive immunosensor for cancer biomarker proteins using gold nanoparticle film electrodes and multienzyme-particle amplification. *ACS Nano* **2009**, *3*, 585-594.

29. Namiki, Y.; Fuchigami, T.; Tada, N.; Kawamura, R.; Matsunuma, S.; Kitamoto, Y.; Nakagawa, M. Nanomedicine for cancer: lipid-based nanostructures for drug delivery and monitoring. *Acc. Chem. Res.* **2011**, *44*, 1080-1093.

30. Stöber, W.; Fink, A.; Bohn, E. Controlled growth of monodisperse silica spheres in the micron size range. *J. Colloid Interface Sci.* **1968**, *26*, 62-69.

31. Wang, L.; Wang, K.; Santra, S.; Zhao, X.; Hilliard, L. R.; Smith, J. E.; Wu, Y.; Tan, W. *Watching silica nanoparticles glow in the biological world* **2006**.

32. Bae, S. W.; Tan, W.; Hong, J. Fluorescent dye-doped silica nanoparticles: new tools for bioapplications. *Chemical Communications* **2012**, *48*, 2270-2282.

33. Zhao, X.; Bagwe, R. P.; Tan, W. Development of Organic-Dye-Doped Silica Nanoparticles in a Reverse Microemulsion. *Adv Mater* **2004**, *16*, 173-176.

34. Santra, S.; Zhang, P.; Wang, K.; Tapec, R.; Tan, W. Conjugation of biomolecules with luminophore-doped silica nanoparticles for photostable biomarkers. *Anal. Chem.* **2001**, *73*, 4988-4993.

35. Sardesai, N.; Pan, S.; Rusling, J. Electrochemiluminescent immunosensor for detection of protein cancer biomarkers using carbon nanotube forests and [Ru-(bpy) 3] 2 -doped silica nanoparticles. *Chemical Communications* **2009**, 4968-4970.

36. Iijima, S. Helical microtubules of graphitic carbon. *Nature* **1991**, *354*, 56.

37. Iijima, S.; Ichihashi, T. Single-shell carbon nanotubes of 1-nm diameter. *Nature* **1993**, *363*, 603-605.

38. Wei, H.; Wang, E. Electrochemiluminescence of tris (2, 2′-bipyridyl) ruthenium and its applications in bioanalysis: a review. *Luminescence* **2011**, *26*, 77-85.

39. Choi, Y.; Kwak, J.; Park, J. W. Nanotechnology for early cancer detection. *Sensors* **2010**, *10*, 428-455.

40. Cinke, M.; Li, J.; Chen, B.; Cassell, A.; Delzeit, L.; Han, J.; Meyyappan, M. Pore structure of raw and purified HiPco single-walled carbon nanotubes. *Chemical Physics Letters* **2002**, *365*, 69-74.

41. Kim, S. N.; Rusling, J. F.; Papadimitrakopoulos, F. Carbon nanotubes for electronic and electrochemical detection of biomolecules. *Adv Mater* **2007**, *19*, 3214-3228.

42. Chattopadhyay, D.; Galeska, I.; Papadimitrakopoulos, F. Metal-assisted organization of shortened carbon nanotubes in monolayer and multilayer forest assemblies. *J. Am. Chem. Soc.* **2001**, *123*, 9451-9452.

43. Yu, X.; Chattopadhyay, D.; Galeska, I.; Papadimitrakopoulos, F.; Rusling, J. F. Peroxidase activity of enzymes bound to the ends of single-wall carbon nanotube forest electrodes. *Electrochemistry Communications* **2003**, *5*, 408-411.

44. Yu, X.; Munge, B.; Patel, V.; Jensen, G.; Bhirde, A.; Gong, J. D.; Kim, S. N.; Gillespie, J.; Gutkind, J. S.; Papadimitrakopoulos, F.; Rusling, J. F. Carbon nanotube amplification strategies for highly sensitive immunodetection of cancer biomarkers. *J. Am. Chem. Soc.* **2006**, *128*, 11199-11205.

45. Malhotra, R.; Patel, V.; Vaque, J. P.; Gutkind, J. S.; Rusling, J. F. Ultrasensitive electrochemical immunosensor for oral cancer biomarker IL-6 using carbon nanotube forest electrodes and multilabel amplification. *Anal. Chem.* **2010**, *82*, 3118-3123.

46. Sardesai, N. P.; Kadimisetty, K.; Faria, R.; Rusling, J. F. A microfluidic electrochemiluminescent device for detecting cancer biomarker proteins. *Analytical and bioanalytical chemistry* **2013**, *405*, 3831-3838.

47. Munge, B. S.; Dowd, R. S.; Krause, C. E.; Millord, L. N. Ultrasensitive Hydrogen Peroxide Biosensor Based on Enzyme Bound to Layered Nonoriented Multiwall Carbon Nanotubes/Polyelectrolyte Electrodes. *Electroanalysis* **2009**, *21*, 2241-2248.

48. Whitesides, G. M. The origins and the future of microfluidics. *Nature* **2006**, *442*, 368-373.

49. Halldorsson, S.; Lucumi, E.; Gómez-Sjöberg, R.; Fleming, R. M. Advantages and challenges of microfluidic cell culture in polydimethylsiloxane devices. *Biosensors and Bioelectronics* **2015**, *63*, 218-231.

50. Kai, J.; Puntambekar, A.; Santiago, N.; Lee, S. H.; Sehy, D. W.; Moore, V.; Han, J.; Ahn, C. H. A novel microfluidic microplate as the next generation assay platform for enzyme linked immunoassays (ELISA). *Lab on a Chip* **2012**, *12*, 4257-4262.

51. Dixit, C. K.; Kadimisetty, K.; Otieno, B. A.; Tang, C.; Malla, S.; Krause, C. E.; Rusling, J. F. Electrochemistry-based approaches to low cost, high sensitivity, automated, multiplexed protein immunoassays for cancer diagnostics. *Analyst* **2016**, *141*, 536-547.

52. J. C. McDonald and G. M. Whitesides, *Acc Chem Res*, 2002, **35(7)**, 491-499.

53. Otieno, B. A.; Krause, C. E.; Latus, A.; Chikkaveeraiah, B. V.; Faria, R. C.; Rusling, J. F. On-line protein capture on magnetic beads for ultrasensitive microfluidic immunoassays of cancer biomarkers. *Biosensors and Bioelectronics* **2014**, *53*, 268-274.

54. Malhotra, R.; Patel, V.; Chikkaveeraiah, B. V.; Munge, B. S.; Cheong, S. C.; Zain, R. B.; Abraham, M. T.; Dey, D. K.; Gutkind, J. S.; Rusling, J. F. Ultrasensitive detection of cancer

biomarkers in the clinic by use of a nanostructured microfluidic array. *Anal. Chem.* **2012**, *84*, 6249-6255.

55. Rusling, J. F. Multiplexed electrochemical protein detection and translation to personalized cancer diagnostics. *Anal. Chem.* **2013**, *85*, 5304-5310.

56. Kadimisetty, K.; Malla, S.; Sardesai, N. P.; Joshi, A. A.; Faria, R. C.; Lee, N. H.; Rusling, J. F. Automated multiplexed ECL Immunoarrays for cancer biomarker proteins. *Anal. Chem.* **2015**, *87*, 4472-4478.

57. Tang, C. K.; Vaze, A.; Rusling, J. F. Fabrication of immunosensor microwell arrays from gold compact discs for detection of cancer biomarker proteins. *Lab on a Chip* **2012**, *12*, 281-286.

58. Bishop, G. W.; Satterwhite-Warden, J. E.; Kadimisetty, K.; Rusling, J. F. 3D-printed bioanalytical devices. *Nanotechnology* **2016**, *27*, 284002.

59. Gross, B. C.; Erkal, J. L.; Lockwood, S. Y.; Chen, C.; Spence, D. M. *Evaluation of 3D printing and its potential impact on biotechnology and the chemical sciences* **2014**.

60. O'Neill, P.; Ben Azouz, A.; Vázquez, M.; Liu, J.; Marczak, S.; Slouka, Z.; Chang, H. C.; Diamond, D.; Brabazon, D. Advances in three-dimensional rapid prototyping of microfluidic devices for biological applications. *Biomicrofluidics* **2014**, *8*, 052112.

CHAPTER 2

Automated Multiplexed ECL Immunoarrays for Cancer Biomarker Proteins

2-1 ABSTRACT

Point-of-care diagnostics based on multiplexed protein measurements face challenges of simple, automated, low cost, high throughput operation with high sensitivity. Herein we describe an automated, microprocessor-controlled microfluidic immunoarray for simultaneous multiplexed detection of small protein panels in complex samples. A microfluidic sample/reagent delivery cassette was coupled to a 30 microwell detection array to achieve sensitive detection of 4 prostate cancer biomarker proteins in serum. The proteins are prostate specific antigen (PSA), prostate specific membrane antigen (PSMA), platelet factor-4 (PF-4) and interlukin-6 (IL-6). The six channel system is driven by integrated micropumps controlled by an inexpensive programmable microprocessor. The reagent delivery cassette and detection array feature channels made by precision-cut 0.8 mm silicone gaskets. Single-wall carbon nanotube forests were grown in printed microwells on a pyrolytic graphite detection chip and decorated with capture antibodies. The detection chip is housed in a machined microfluidic chamber with a steel metal shim counter electrode and Ag/AgCl reference electrode for electrochemiluminescent (ECL) measurements. The preloaded sample/reagent cassette automatically delivers antigen proteins, wash buffers and

ECL RuBPY-silica-antibody detection nanoparticles sequentially. An on-board microcontroller controls micropumps and reagent flow to the detection chamber according to a preset program. Detection employs tripropylamine, a sacrificial reductant, while applying 0.95 V vs Ag/AgCl. Resulting ECL light was measured by a CCD camera. Ultralow detection limits of 10-100 fg mL^{-1} were achieved in simultaneous detection of the four protein in 36 min. assays. Results for the 4 proteins in prostate cancer patient serum gave excellent correlation with single protein ELISA.

2-2. Introduction

Biomarker protein panels hold great promise for future personalized cancer diagnostics.[1-5] Widespread use of diagnostic protein measurements at clinical point-of-care will require simple, cheap, fast, sensitive, automated assay devices.[4-6] Microfluidic devices integrated with sensitive nanomaterials-based measurement technologies have potential for future devices that fit these requirements.[7-11] Microfluidic immunoarrays have evolved to feature glass substrates with silicon patterns,[12] fabricated microchannels[13] and valves[14] made with soft lithography. A major practical challenge involves integrating components into low cost, fully automated devices for clinical use.[15]

Many current methods of specific biomarker protein detection are based on enzyme linked immunosorbent assays (ELISA), including commercial magnetic bead-based devices.[10,16] Critical issues in these systems are cost, method complexity, and the need for technically trained operators and frequent maintenance. Immunoassays in general suffer from multiple operations to load samples and add reagents to block non-specific binding, remove interferences, and detect target proteins. Significantly improved automation is needed to translate immunoassays to point-of-care use.[6,15] While semi-automated microfluidic reagent addition was reported previously for single and 2-antigen immunoassays, those systems do not achieve ultrasensitive detection and employ passive fluid delivery by a downstream syringe that requires operator attention.[17]

We previously developed modular microfluidic immunoarrays for multiplexed protein detection on 8-unit gold nanoparticle AuNP film sensor arrays using magnetic beads heavily loaded with enzyme labels and antibodies for detection.[18-20] In the latest version of this device, target proteins are captured on-line on the magnetic beads and delivered to an amperometric detection chamber. We have determined up to 4 biomarker proteins in serum at levels as low as 5

fg mL^{-1} with this system. We also developed microfluidic immunoarrays for electrochemiluminescence (ECL) detection[21] using a slightly different approach. Here, a thin pyrolytic graphite (PG) wafer was equipped with printed microwells, single-wall carbon nanotube (SWCNT) forests were grown in the microwells and decorated with antibodies, and $Ru(bpy)_3^{2+}$ (RuBPY) labels embedded in 100 nm silica nanoparticles coated with antibodies were used for protein detection at 10-100 fg mL^{-1} levels.[22] ECL detection obviates the need for individually addressable sensors, and the microwells need only be separated in space on the chip for light detection with a camera. While these systems afford some degree of automation, a skilled operator

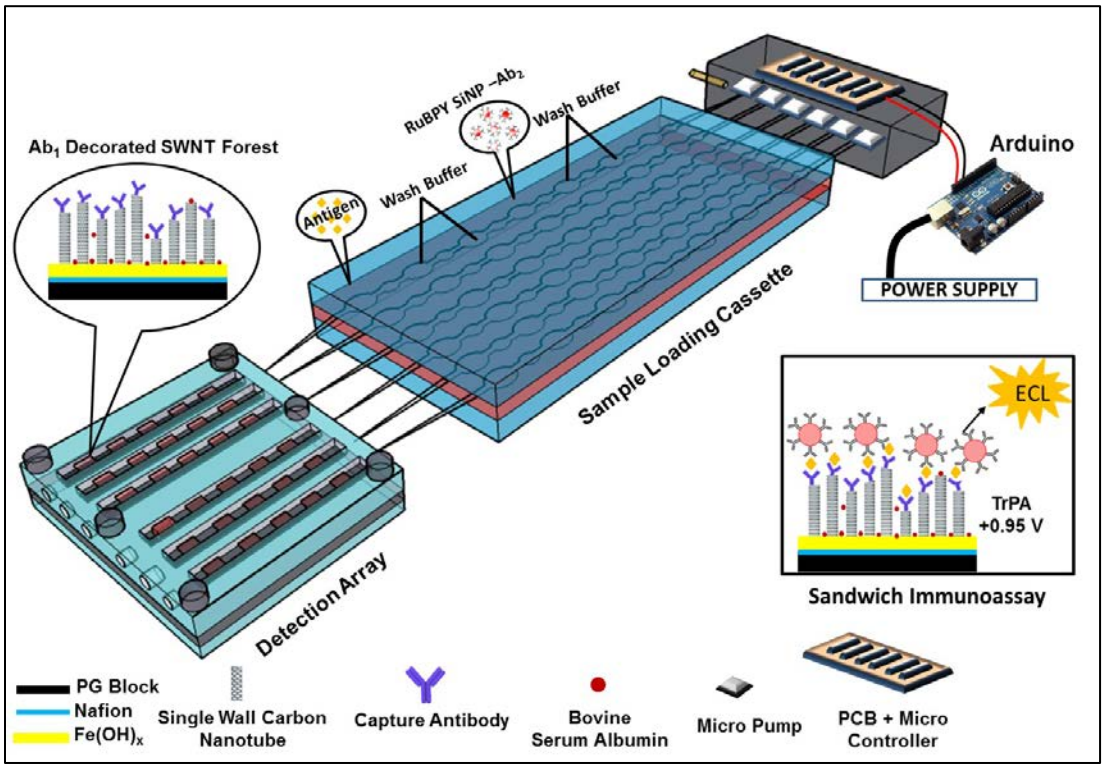

is needed to add samples and reagents and co-ordinate assay timing.

Scheme 2-1. Schematic representation of automated PCB integrated electrochemiluminescent microfluidic array. Detection array is connected to the sample loading cassette and micro pumps.

Preprogrammed Arduino microcontroller controls the micropump on-off cycles according to an optimized program. Insert depicts sandwich immunoassay and ECL detection.

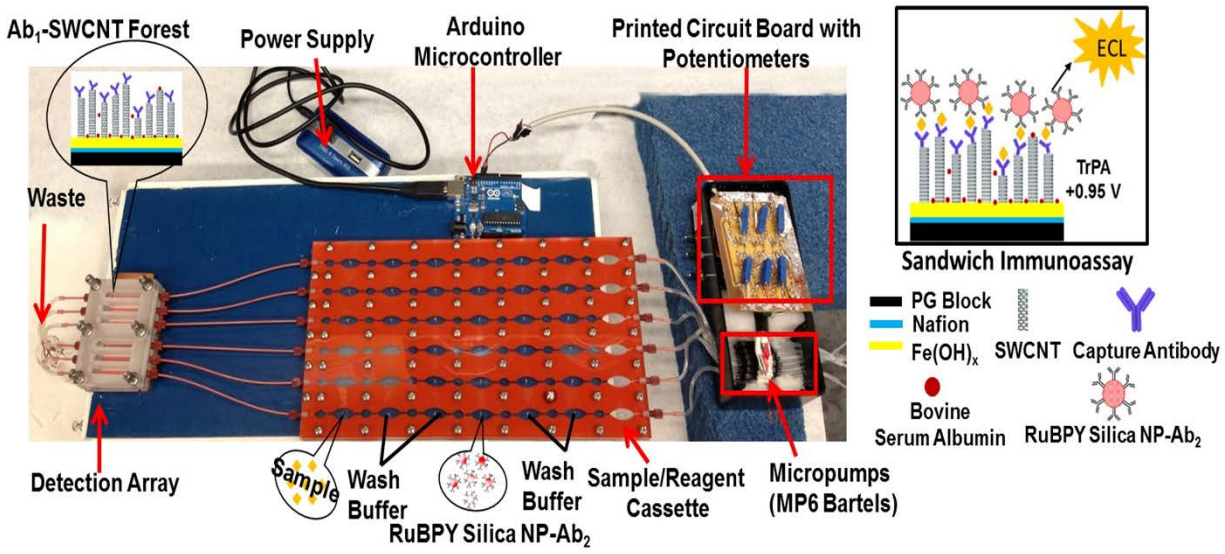

Figure 2-1. Automated microfluidic system featuring 30-microwell detection array connected to sample/reagent cassette and PCB-controlled micropumps. An onboard programmed Arduino microcontroller runs a micropump program to achieve the assay.

In this paper, we describe an inexpensive automated multiplexed protein immunoarray featuring an onboard microprocessor to control micropumps,[23] and a microfluidic sample/reagent cassette upstream of a microwell ECL immunoarray (Figure 2-1, and Scheme 2-1). The microfluidic channels are precision cut from silicone gaskets. The system automatically delivers all necessary samples and reagents, and controls timing of sample-sensor and detection particle incubations. The detection module features six 60 µL microfluidic channels on a single PG chip with 30 computer printed microwells containing dense, upright SWCNT forests decorated with capture antibodies. We demonstrate the properties of the device by simultaneous detection of four proteins employing 120 nm RuBPY-silica (RuBPY-Si) nanoparticles coated with secondary antibodies (Ab_2), with detection by CCD camera. We targeted a general panel of prostate cancer

biomarkers including prostate specific antigen (PSA),[24,25] interleukin-6 (IL-6), platelet factor-4 (PF-4), and prostate specific membrane antigen (PSMA).[26] Simultaneous detection of the four proteins in undiluted calf serum was achieved with high specificity and selectivity in 36 min assays, with detection limits of 10-100 fg mL^{-1}. Assays on human serum samples from prostate cancer patients confirmed very good correlations with single protein ELISAs.

2-3. Experimental Section

2-3.1 Chemicals. Pooled human serum was from Capital Biosciences and individual patient serum samples were provided by George Washington University Hospital. RuBPY-Si nanoparticles with average diameter 121±9 nm (Figure 2-2) were prepared and coated with layers of polydiallyldimethylammonium chloride (PDDA) and polyacrylic acid (PAA), then covalently linked to secondary antibodies (Ab_2) as described previously.[27] Two RuBPY-Si detection nanoparticles were made, one with antibodies for PSA (PSA-Ab_2) and IL-6 (IL-6-Ab_2), and a second featuring PSMA-Ab_2 and PF-4-Ab_2. We measured averages of 4.6 x 10^5 RuBPY and 44 Ab_2 per Si nanoparticle (Figure 2-2). Immunoreagents were dissolved in pH 7.2 phosphate buffer saline (PBS). Co-reactant solution to develop ECL was 200 mM tripropylamine (TPrA) with 0.05% Tween-20 (T_{20}) and 0.05% Triton-X in 0.2 M Phosphate buffer. Calf serum as a surrogate for human serum was used to dissolve standard proteins.[28]

2-3.2 Synthesis of $[Ru(bpy)_3]^{2+}$ -doped silica (RuBPY-Silica) nanoparticles

$[Ru(bpy)_3]^{2+}$ -doped silica (RuBPY-Silica) nanoparticles were synthesized by water in oil (W/O) microemulsion.[29] 0.04 M $[Ru(bpy)_3]^{2+}$ stock solution was prepared by dissolving $[Ru(bpy)_3]^{2+}$ in pure water. 340 µL of stock was mixed with 1.8 g of Triton X 100, 1.8 mL of n-hexanol and 7.5

mL of cyclohexane and stirred for 30 minutes. 60 µL of fresh ammonium hydroxide (28-30 % weight) and 100 µL of tetraethylorthosilicate (TEOS) were added to the above mixture and stirred for 24 hours in dark. This mixture was precipitated using acetone. The precipitate was separated using a centrifuge followed by washing with ethanol and water for three times each. This precipitate was vacuum dried at room temperature overnight. The final product was weighed and stored in dark at 4ºC. These particles were further characterized using transmission electron microscopy (TEM).

2-3.3 Characterization of RuBPY silica nanoparticles by TEM

2.0 mg of RuBPY particles were dispersed in 1 mL of pure water and further diluted five times to prepare the sample for TEM. A drop of this dispersion was added on to carbon coated copper TEM grid and dried under vacuum. The average diameter of these particles was 121 ± 9 nm. These RuBPY particles were modified to prepare ECL label. (Figure 2-2A & B)

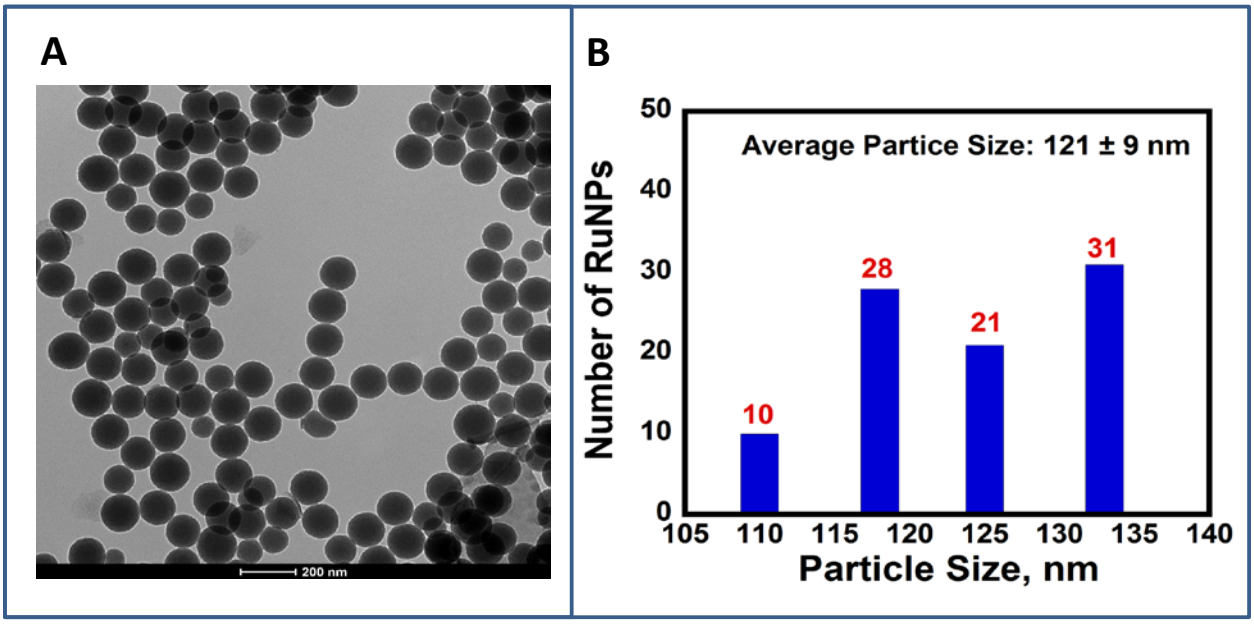

Figure 2-2. (A) TEM image of RuBPY-silica nano particles on a 200 nm scale bar. (B) Size distribution of RuBPY silica nanoparticles with an average diameter of 121 ± 9 nm.

2-3.4 RuBPY-Silica nanoparticles bioconjugate preparation

2 mg mL^{-1} RuBPY silica particles are used in making the bioconjugate. The solid particles are firstly sonicated for a minute to remove any loosely bound or leaked $[Ru\text{-}(bpy)_3]^{2+}$ from the particles and separated using centrifugation at 10,000 rpm for 10 min. Layer of polydiallyldimethylammonium chloride (PDDA) was formed by adding 0.33mg mL^{-1} of aqueous PDDA solution. The mixture was allowed to stand for 15min to form a thin layer. This was further centrifuged at 9,000 rpm to remove excess and subsequently washed 3X with water. Later these particles were suspended in 0.33mg mL^{-1} of polyacrylic acid (PAA) for 15 min to form a carboxylic acid groups on the surface of the nanoparticle. Excess PAA was removed by centrifugation and washing 3X with water. Carboxylic acid groups present on the surface was used to bind the desired protein using (400mM-100mM) EDC-NHSS amidization. After leaving the nanoparticles with EDC-NHSS mixture for 10 min the excess was removed and washed with water as explained earlier at 9,000 rpm. Multiplexed label was prepared by adding mixture of PSA Ab_2 (8µg mL^{-1}) and IL-6 Ab_2 (3µg mL^{-1}) on one set of prepared particles and PSMA Ab_2 (4.5µg mL^{-1}) and PF-4 Ab_2 (4.5µg mL^{-1}) on other set of particles. The prepared mixture with proteins and modified RuBYP silica nanoparticles are incubated overnight on a rotor. The resultant mixture with excess proteins were removed by centrifugation at 8,000rpm in a refrigerated centrifuge and washed 3X with PBS buffer at 7.4 pH. The resultant bioconjugate is finally dispersed in 1 mL of 2% BSA in 0.05% Tween-20/PBS buffer (7.4 pH) to block any nonspecific binding during the immunoassay also helping in forming a uniform dispersion. These prepared bioconjugates (one set with PSA, IL-6 and other with PSMA, PF-4 secondary antibodies) were mixed in equal ratios prior to a multiplexed detection.

2-3.5 Estimating the number of RuBPY in Si particles

Relation between viscosity of a dilute solution of spherical nanoparticles and the volume fraction of suspended nanoparticles (Φ) as shown in equation1, where h is the viscosity of the nanoparticle suspension and h_0 is the viscosity of the solution without nanoparticles. Viscosity of the nanoparticle suspension was estimated to be 1.0078 and the viscosity of pure solvent is 1.00. Substituting the values in equation 1, we get the value of volume fraction (Φ), to be 0.0031.

$$h/h_0 = 1 + 2.5\Phi \qquad (1)$$

The number of nanoparticles (N) per volume was obtained by using equation 2, where r is the radius of the particles in cm. The diameter of the nanoparticles was estimated using transmission electron microscopy to be 120 ± 9 nm. Substituting these values in equation 2 we calculated number of particles to be 3.4 X 10^{12} per mL of solution.

$$N = \Phi /(4/3\pi r^3) \qquad (2)$$

2-3.6 Ratio of Ab_2/RuBPY Silica particles in ECL bio-conjugate label

Fluorescence emission spectroscopy was used to calculate the number of antibodies attached to the RuBPY Silica particles. Antibodies contain tryptophan, which excites specifically at 280nm. Calibration curve was developed for known concentration of Ab_2 as shown in figure 2-3A. The unknown concentration of Ab_2 on the bio-conjugate label (PSA-Ab_2, IL-6-Ab_2, PSMA-Ab_2, PF4-Ab_2 in 2 % BSA, PBS Tween-20; at pH7.2) and a control (2 % BSA, PBS Tween-20; at pH7.2) was estimated from the linear calibration curves. After exciting at 280 nm, the fluorescence intensity obtained for control was 180 and for the bio-conjugate label was 310. The difference was calculated to be 130 and the corresponding concentration for Ab_2 from calibration curve obtained

was 39.9 µgmL^{-1}. The number of Ab_2 in the ECL bio-conjugate label was calculated to be 1.5 X 10^{14}. Therefore the ratio of Ab2/RuBPY Silica nanoparticles was estimated to be 44:1.

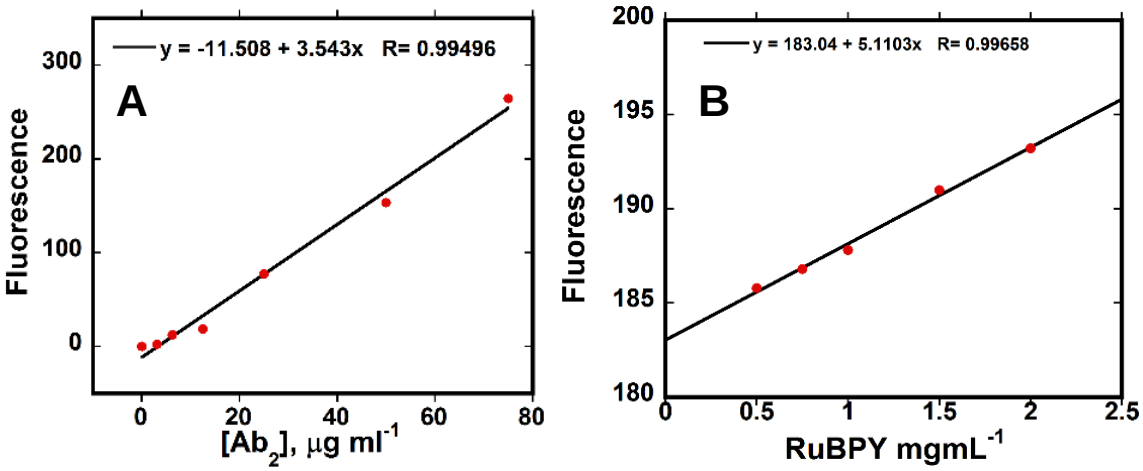

Figure 2-3. Influence of concentration of secondary antibody and [[Ru-(bpy)$_3$]$^{2+}$] on fluorescence intensity (a) at 280nm wavelength with [secondary antibody] range: 3.125 - 75 µg mL^{-1}. (b) at 457 nm wavelength with [[Ru-(bpy)$_3$]$^{2+}$] range: 0.5 - 2 mg mL^{-1}

[[Ru-(bpy)$_3$]$^{2+}$] per RuBPY-Si nanoparticle. A calibration curve for different RuBPY was prepared using fluorescence spectroscopy by exciting at 457 nm. The unknown concentration of RuBPY in the bio-conjugate label was determined by extrapolating from the linear calibration curve (Figure 2-3B). The number of moles were obtained using the molecular weight of Tris(2,2'-bipyridine)dichlororuthenium(II) hexahydrate, 748.62. The number of Ru-(bpy)$_3$]$^{2+}$ ions were estimated using Avogadro's number. Rel. fluorescence intensity 192 was obtained for ECL- bio-conjugate label when excited at 457 nm. The amount of Ru-(bpy)$_3$]$^{2+}$ ions was estimated to be 1.9 mg/mL and the number of Ru-(bpy)$_3$]$^{2+}$ ions were calculated to be 1.55 x10^{18}. The number of Ru-

$(bpy)_3]^{2+}$] ions per particle were estimated by dividing with the total number of RuBPY silica nano particles in 1 mL of bio-conjugate label dispersion, which is 4.6 X 10^5.

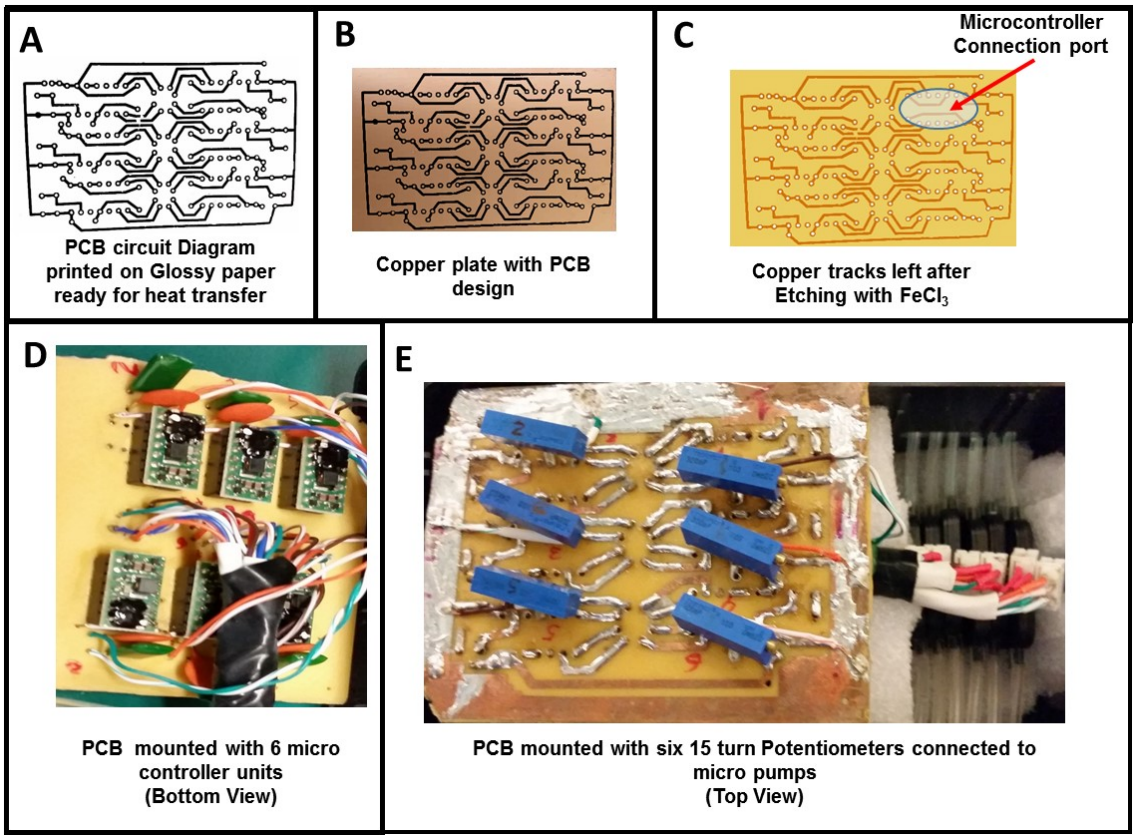

Figure 2-4. Fabrication of printed circuit board integrated with potentiometer and micro controller units connected to micro pumps. A) PCB circuit design prepared on autocad for integrating 6 micro controller units printed on glossy paper. B) PCB design heat transferred on copper plate. C) Etched copper plate with conductive tracks for assembly of various electronics. D) Micro controller units mounted on the bottom side of PCB. E) 15 turn Potentiometers mounted on the top side of PCB.

2-3.7 Microfluidic device. Figure 1 shows the automated microfluidic immunoarray featuring (i) printed-circuit board (PCB)-linked, microprocessor-controlled micropumps, (ii) 6-channel

sample/reagent delivery cassette, and (iii) 6-channel microfluidic detection array. A PCB circuit design was constructed to serve 6 micropumps. Micropumps (Mp6, Bartels) featuring piezo-actuated membranes were optimized to 155 ± 1.5 µL min^{-1} by tuning potentiometers for each pump

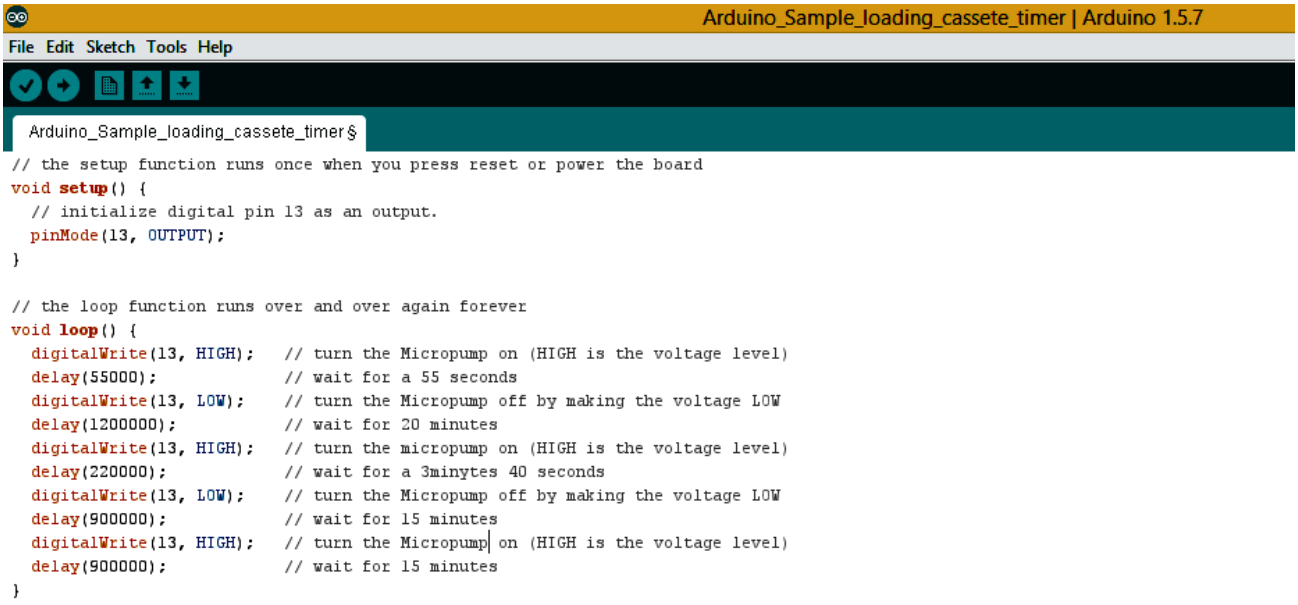

(Figure 2-4). An Arduino microcontroller was used to switch on and off micropumps according to a preset program to deliver sample and immunoreagents, and to stop flow for incubations (Figure 2-5).

Figure 2-5. Arduino program for automated stepwise delivery of sample/reagent into the ECL immunoarray from sample/reagent loading cassette.

Microfluidic channels were made by precision cutting 0.80 mm silicone gaskets (MSC industrial Supply) with the desired patterns using an inexpensive, programmable Accugraphic Klic-N-Kut (KNK) groove cutting machine. The cut gaskets (Figure 2-6A) were placed, between two machined hard PMMA plates (Figure 2-6B&C) to assemble the final sample/reagent delivery cassette (Figure 2-6D. The final assembled sample/reagent delivery cassette was 11 in x 5.5 inches

with six channels, each having 7 loading chambers separated individually by smaller air-filled channels to ensure delivery of reagents without mixing (Figure 2-6D). The top PMMA plate was machined with 1 mm dia. holes to fill the chambers, and the bottom plate has screw holes to tighten and seal the assembly. Each chamber holds 80 µL volume. Chambers were prefilled by syringe, and openings sealed with tape

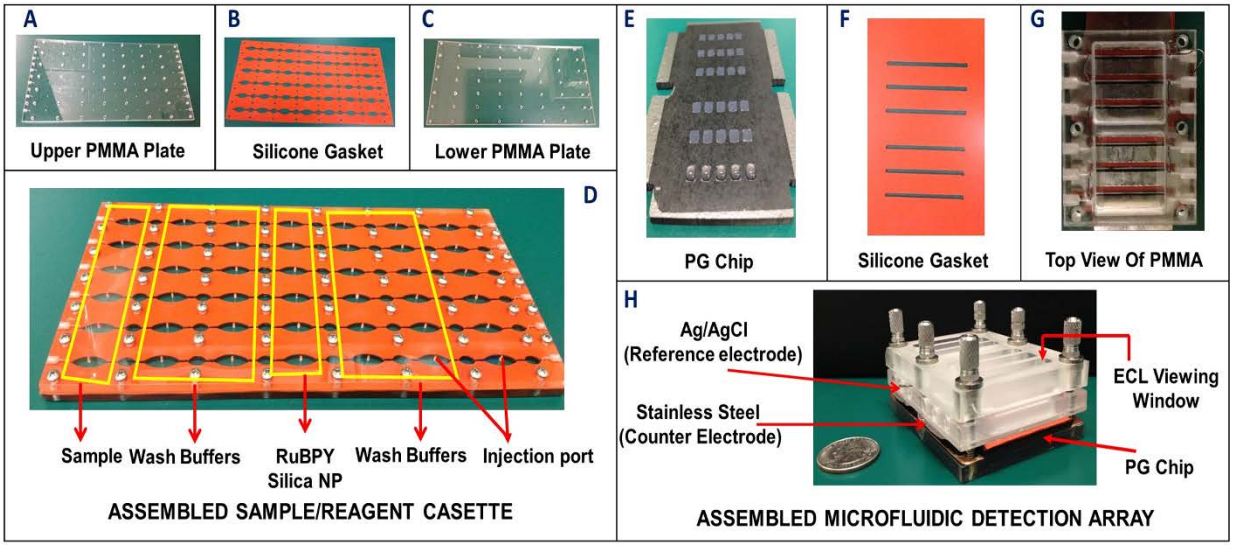

Figure 2-6. Immunoarray components: On left, sample/reagent delivery cassette consisting of (A) 0.8 mm silicon gasket cut to scale using a KNK cutter, (B) Upper hard PMMA plate machined with injection ports, (C) lower PMMA plate and (D) Assembled sample/reagent cassette shown with chambers for solutions, assembled with screws. Right panels show detection array consisting of (E) PG wafer with computer-printed microwells, (F) silicone gasket cut with 6 precision channels, (G) top PMMA plate showing attached stainless steel counter electrode on top with clear windows for ECL detection and Ag/AgCl reference electrode and (H) fully assembled microfluidic detection array with clear windows in top PMMA plate positioned above microwells in each channel.

The detection chamber also features 6 microfluidic channels (60 ± 2 µL) cut from a silicone gasket that is then placed on a thin 2 x 3 in PG wafer with computer-printed microwells[22,30] (Figure 2-6E). This gasket (Figure 2-6F) is placed on the PG slab and sealed by bolting between two flat machined PMMA plates. The top PMMA plate (Figure 2-6G) houses symmetrically placed Ag/AgCl reference and stainless steel metal shim (MSC Industrial Supply) counter electrodes that are aligned into each of six channels completing a symmetric electrochemical cell with the entire PG chip as working electrode (Figure 2-6H). The top PMMA plate is fitted with optically clear acrylic[22] windows above each microwell channel to pass ECL light to a CCD camera.

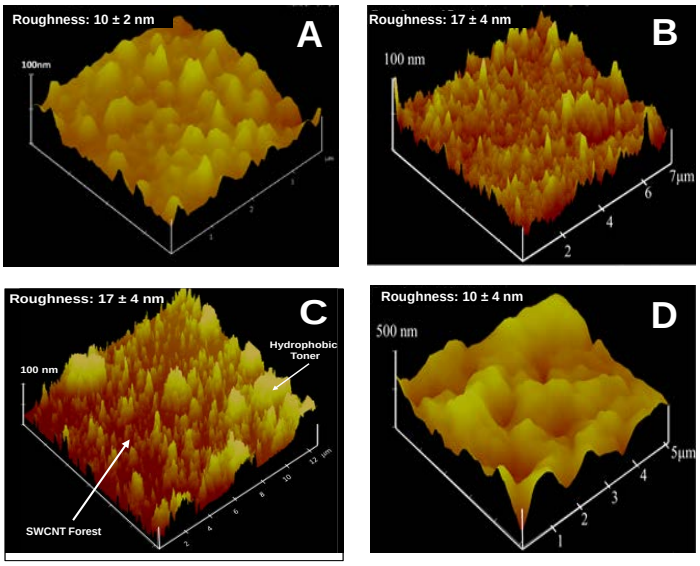

Figure 2-7. Tapping mode AFM images (A) Nafion/FeO(OH)-FeOCl bilayer on freshly cleaved mica surface; (B) SWCNT forests on Nafion/FeO(OH)-FeOCl bilayer; (C) SWCNT forests on Nafion/FeO(OH)-FeOCl bilayer at the edge of microwell formed by hydrophobic toner boundaries; (D) Covalently linked Ab_1 on SWCNT forest in the bottom of a microwell.

Dense SWCNT forests were grown in each microwell (volume 2 ± 0.5 □L).[22,31] Tapping-mode atomic force microscopy and Raman spectrum confirmed vertical aligned SWCNT forests

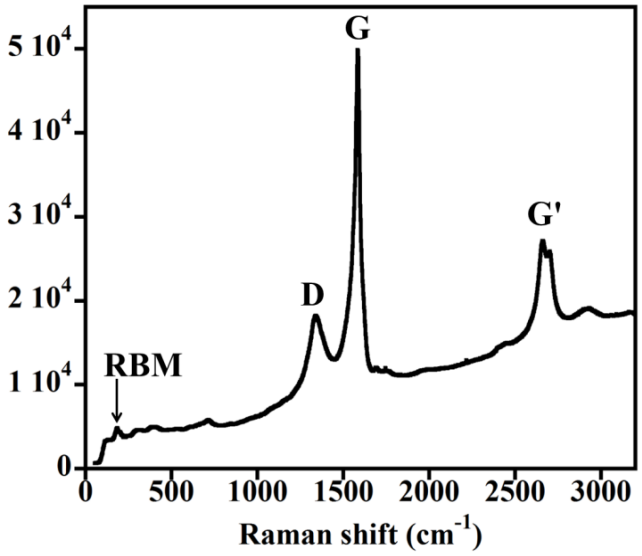

in the microwells with surface roughness 17 ± 4 nm surrounded by the hydrophobic printed wall (Figure 2-7 & 2-8). Terminal carboxylic groups on SWCNTs were activated by freshly prepared 400 mM EDC + 100 mM NHSS to attach cognate primary antibodies (Ab_1) by amidization.[22,28]

Figure 2-8. Raman spectrum of SWCNT forest on a silicon wafers over frequency range using E_{laser} = 514 nm showing the radial breathing mode (RBM), the graphite-like in-plane mode G-band, the disorder-induced D-band and its second-order harmonic G'-band.

2-3.8 Immunoassay Protocol, The Ab_1-decorated PG chip microwells containing SWCNT-Ab_1 were spotted with 2% BSA in PBS containing 0.05% Tween 20 to minimize non-specific binding (NSB). The PG chip was assembled into the detection chamber, which was then connected to a prefilled sample/reagent cassette. The Arduino microcontroller precisely times sample and reagent delivery by micropumps to the detection chamber according to a pre-optimized program.

The immunoassay protocol was developed by optimizing micropump flow rates (Figure 2-9), using a 15 turn 10kOhms. Flow rates were optimized at 155 μL^{-1} by carefully changing the

amplitude of all the micro pumps while turning the screw of the potentiometer. Incubation times were also optimized for protein binding steps to ensure high sensitivity and reproducibility with spot to spot variability <10%. The capture antibody-decorated immunoarray sensor chamber was

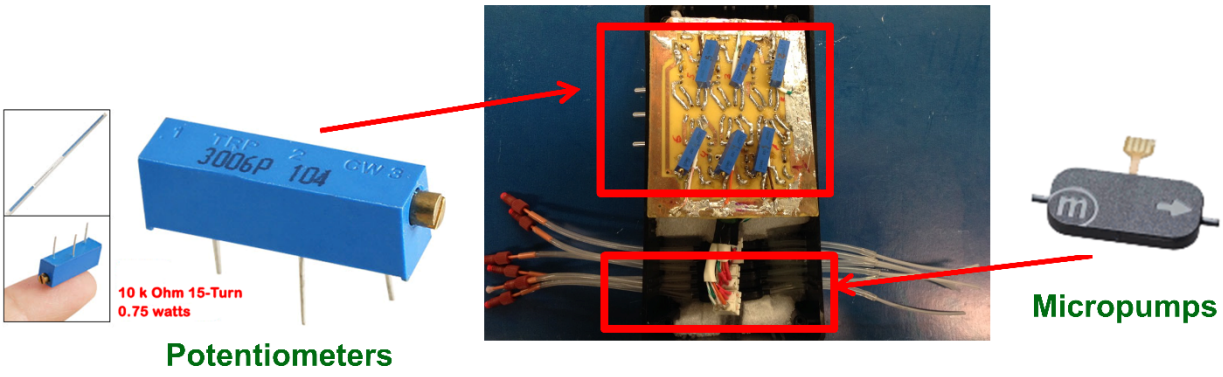

Pump #	Pump 1	Pump 2	Pump 3	Pump 4	Pump 5	Pump 6
Average Flow Rate, μL min^{-1}	155.0	152.2	155.4	156.2	154.4	156.2
STDEV (5 trials)	0.71	1.48	2.51	2.86	2.30	2.49
Average Flow Rate = 154.9 μL min^{-1}						
Standard Deviation in Flow Rates Between Pumps = ± 1.5 μL min^{-1}						
Relative Standard Deviation in Flow Rates Between Pumps = 1 %						

incubated with 2% BSA in PBS T20 prior to the assay to block the non-specific binding (NSB) for 50 min, then washed with PBS T20 and PBS. Patient serum samples of 5-10 µL were diluting 30-500 fold in calf serum prior to assay.

Figure 2-9. Optimization of flow rates using 15 turn 10kOhm potentiometers mounted on PCB, Figure showing six potentiometers used for setting the amplitude of all the 6 micropumps. Table in the figure shows average flow rate of all the micropumps along with their individual flow rates and standard deviation.

Once the sample/reagent cassette is loaded, micropumps turn on initially for 55 s to deliver sample to the detector. Second, flow is stopped for 20 min to allow analyte proteins in the sample

to bind onto Ab_1's in microwells. Next, micropumps activate again for 220 s to deliver wash buffer to move sample solution and unbound target proteins out of the detection channels. Then, pumps deliver RuBPY-Si-Ab_2 nanoparticles to the detector, and a 900 s stopped-flow incubation follows. Flow then turns on to wash away unbound RuBPY-silica nanoparticles. Finally, with the detection

STEP 1: $TPrA \rightarrow TPrA^{\bullet+} + e^-$

STEP 2: $TPrA^{\bullet+} \rightarrow TPrA^{\bullet} + H^+$

STEP 3:

$TPrA^{\bullet} + [Ru\text{-}(bpy)_3]^{2+} \rightarrow [Ru\text{-}(bpy)_3]^{+} + Products$

STEP 4:

$[Ru\text{-}(bpy)_3]^{+} + TPrA^{\bullet+} \rightarrow [Ru\text{-}(bpy)_3]^{2+*} + Products$

STEP 5:

$[Ru\text{-}(bpy)_3]^{2+*} \rightarrow [Ru\text{-}(bpy)_3]^{2+} + h\upsilon\ (610\ nm)$

chamber in a dark box, micropumps deliver TPrA co-reactant to the detection channels (Scheme 2-2), and a potential of 0.95 V vs. Ag/AgCl is applied for 400 s to generate ECL from RuBPY-Si particles, while a CCD camera captures the ECL light.

Scheme 2-2. ECL generation mechanism at 0.95 V vs Ag/AgCl when reacted with tripropylamine that in turn reacts with RuBPY. Direct oxidation of Tripropylamine (TPrA) on the electrode surface to TPrA cation radical which in return forms TPrA radical and H^+. TPrA radical reacts with $[[Ru\text{-}(bpy)_3]^{2+}]$ to generate $[[Ru\text{-}(bpy)_3]^{+}]$. This $[[Ru\text{-}(bpy)_3]^{+}]$ reacts with TPrA cation radical to generative photo excited $[[Ru\text{-}(bpy)_3]^{2+}]^*$ that readily generates ECL light at 610nm

2-4. Results

2-4.1 Reproducibility Relative ECL intensities for the immunoarray with controls (undiluted calf serum) showed spot to spot variability of <9 % for n=5 per channel (Figure 2-10). First and the

last channels were used for controls and the inner 4 channels were used for detection of the four target proteins. Array to array reproducibility of background signals was measured by injecting

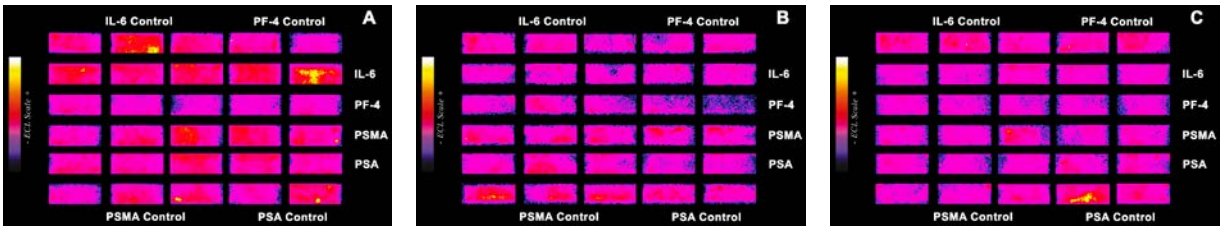

undiluted calf serum into all six channels (Figure 2-10) giving array to array variability ~11 %. Calibrations were then done for each of the four individual proteins in calf serum giving relative standard deviations <10% (see Figure 2-11 and 2-12).

Figure 2-10. Reproducibility of immunoarray (n=3) to undiluted calf serum (control 0 pg mL^{-1} test protein)

Figure 2-11. Recolorized ECL CCD images (A-D) for different concentrations showing reproducibility of individual biomarkers. A) IL-6 from 0.1 $pgmL^{-1}$ to 125 $pgmL^{-1}$ B) PF-4 from 0.1 $pgmL^{-1}$ to 250 $pgmL^{-1}$ C) PSA from 0.1 $pgmL^{-1}$ to 100 $pgmL^{-1}$ D) PSMA from 0.1 $pgmL^{-1}$ to

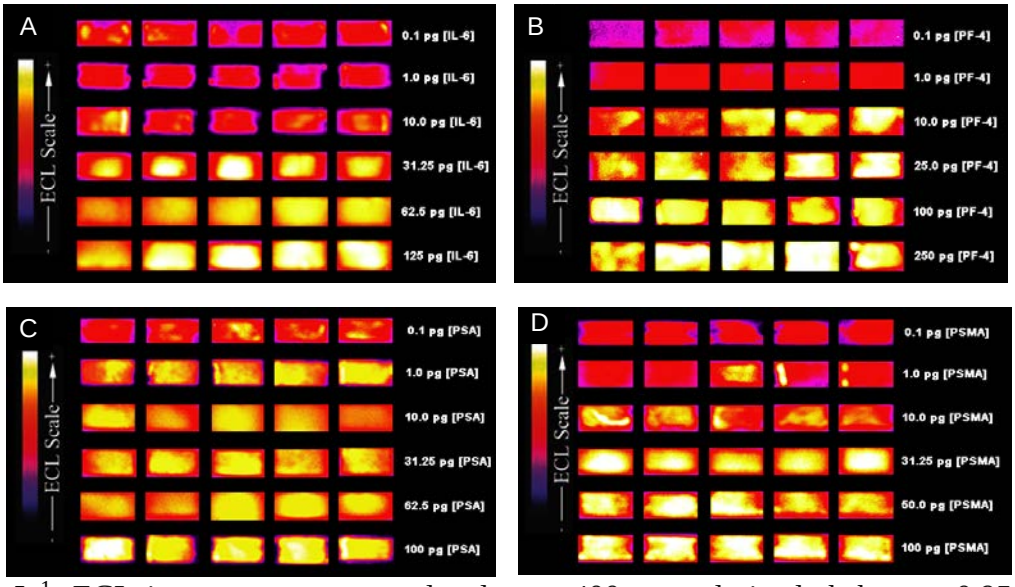

100 $pgmL^{-1}$. ECL images were accumulated over 400 seconds in dark box at 0.95 V versus

Ag/AgCl in the presence of 0.05 % Tween-20+0.05 % Triton-X 100 and 200 mM TPrA in 0.2 M phosphate buffer, pH 7.4

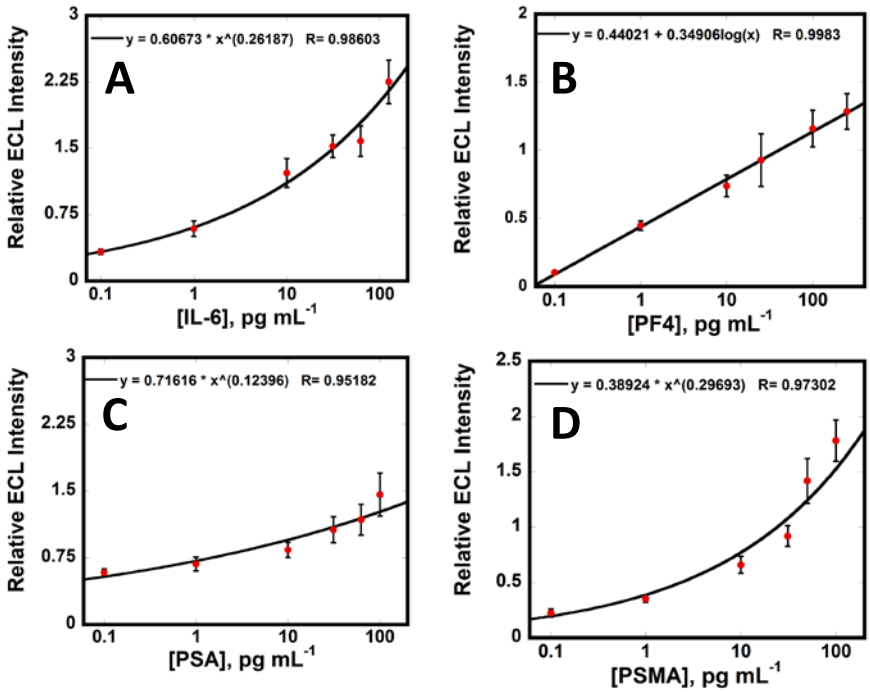

Figure 2-12. Calibration curves for single biomarker detection A) IL-6 from 0.1 pgmL^{-1} to 125 pgmL^{-1} B) PF-4 from 0.1 pgmL^{-1} to 250 pgmL^{-1} C) PSA from 0.1 pgmL^{-1} to 100 pgmL^{-1} D) PSMA from 0.1 pgmL^{-1} to 100 pgmL^{-1}. Error bars show standard deviation, n=5.

2-4.2 Multiplexed detection. . Calibration studies were done by dissolving the four target protein standards in calf serum, which serves as a human serum surrogate without human proteins.[31] Thus, the four proteins were detected selectively and simultaneously from samples containing thousands of proteins. Channels 1 and 6 in the detection array were used as controls, and only undiluted calf serum was introduced into these channels. Channels 2 to 5 were assigned for detection of IL-6, PF4, PSMA and PSA, respectively. Simultaneous detection was achieved by using a mixture of the 2 RuBPY-Si-Ab$_2$ detection nanoparticles that were each decorated with antibodies for 2 of the

4 proteins. RuBPY-Si-Ab_2 were prepared with 4.5 x 10^5 [$[Ru\text{-}(bpy)_3]^{2+}$] ions and 44 Ab_2 per particle.

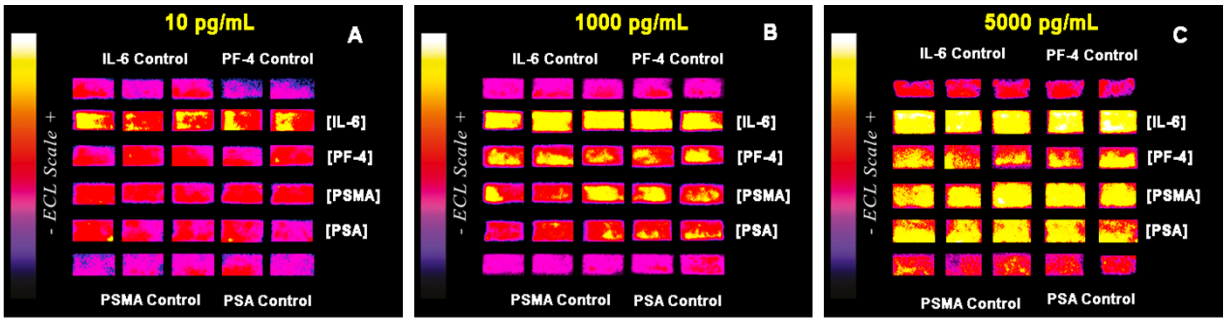

Figure 2-13. Recolourized CCD images of 3 microfluidic immunoarray experiments showing reproducibility in simultaneous detection of IL-6, PF-4, PSMA and PSA in calf with respective controls at protein concentrations: (A) 10 pg mL^{-1} (B) 1000 pg mL^{-1} (C) 5000 pg mL^{-1}.

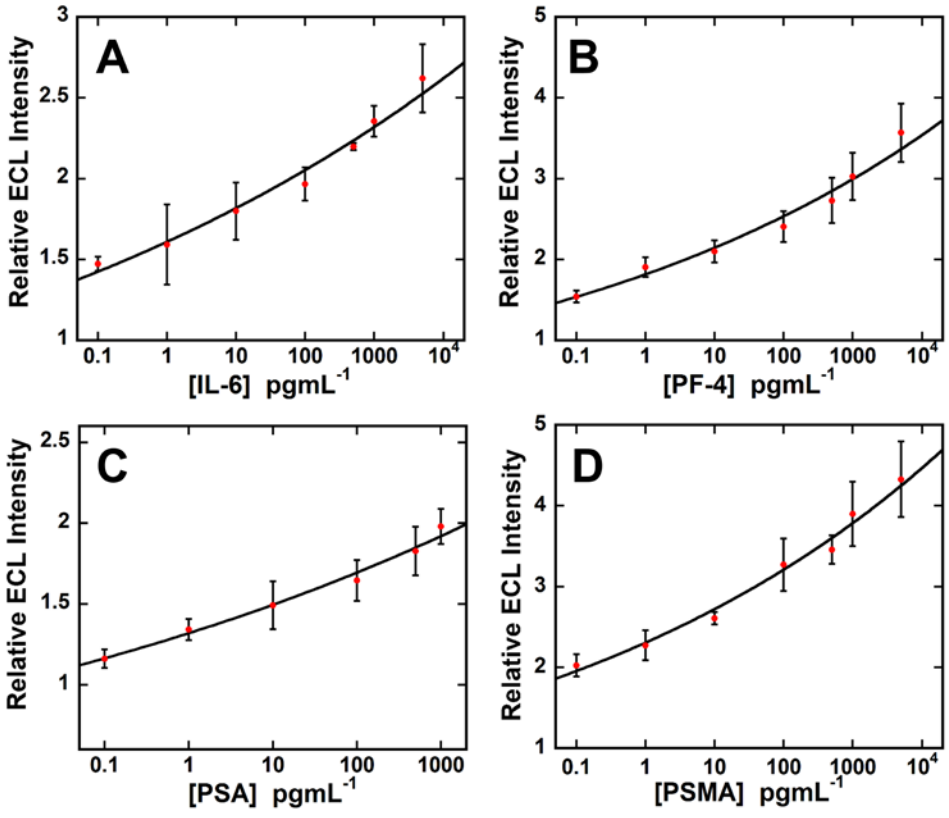

Figure 2-14. Calibration curves in undiluted calf serum, with ECL responses integrated over 400 s, for A) IL-6 B) PF-4 concentration on ECL signal, C) influence of PSA concentration on ECL

signal, D) influence of PSMA concentration on ECL signal. Error bars show standard deviation, n=5.

CCD camera images of the ECL response for multiple protien detection (Figure 2-13) illustrate increased ECL light with increased concentrations of proteins in the mixture. Using the average ECL signal divided by the average blank on each chip, we achieved dynamic ranges for of 100 fg mL^{-1} to 1 ng mL^{-1} for PSA ,100 fg mL^{-1} to 10 ng mL^{-1} for PSMA, and 100 fg mL^{-1} to 5 ng mL^{-1} for IL-6 and PF-4 (Figure 2-14). There is a small amount of nonlinearity in these curves so powerfit was used as curve fitting with corelation coefficient (R) value ≥ 0.99, but they are perfectly suitable for use in protein determinations. Limits of detection (LD) were measured 3 standard deviations of the zero protien control signal at 50 fg mL^{-1} for PSA , 100 fg mL^{-1} for PSMA and IL-6, and 10 fg mL^{-1} for PF4.

2-4.3 Assay validation. Nine serum samples from prostate cancer patients and two samples from cancer free patients were analyzed and compared with single protein ELISA. ELISA was performed on the samples using commercially available kits, PSA (RAB0331- Human PSA total ELISA kit), IL-6 (RAB0306- Human IL-6 total ELISA kit), and PF-4 (RAB0402- Human PF-4 total ELISA kit) were obtained from Sigma Aldrich. PSMA (EL008782HU-96 – Human PSMA/FOLH1 ELISA Kit) was obtained from Lifeome Biolabs/Cusabio. Samples were diluted 30-500 fold in calf serum prior to assay to bring ECL responses in acceptable range of the calibration curves. Concentrations of PF-4, PSMA and PSA fall within the detection limits of ELISA but IL-6 concentrations in the serum samples were well below the detection limit of ELISA. For purposes of the validation study, we spiked the samples with known concentrations of IL-6 from 100 pg mL^{-1} to 500 pg mL^{-1} and then analyzed them by both methods. The immunoarray values gave good correspondence with ELISA values (Figure 2-15). Variability of the assay in

terms of standard deviations might have resulted in small variation in the spiked human serum sample of IL-6 results for ECL and ELISA. Unspiked samples gave IL-6 values from <1 to ~17 pg mL^{-1} (Figure 2-16)

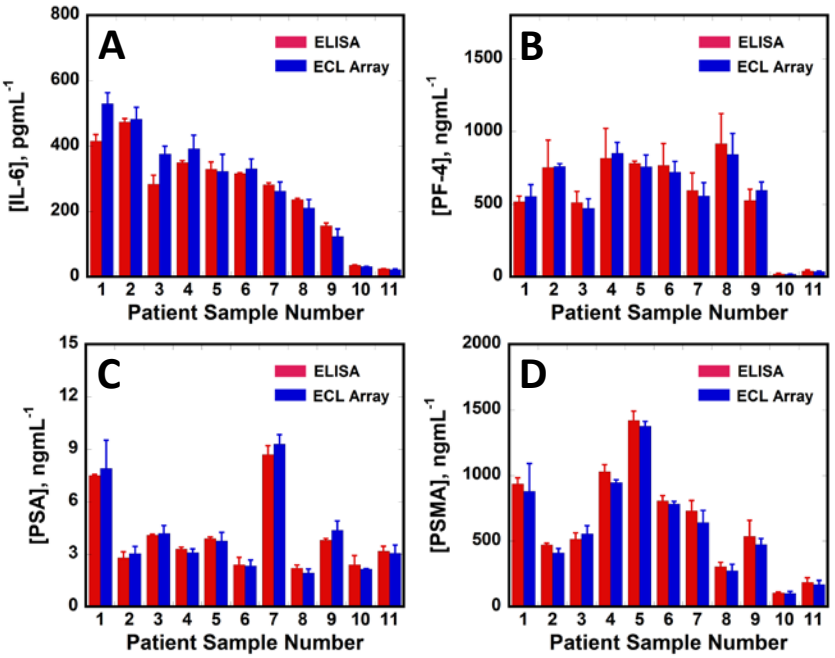

Figure 2-15. Assays of human serum samples comparing immunoarray single protein ELISA Results. Samples 1 - 9 from prostate cancer patients and 10-11 from cancer-free patients. A) IL-6 was spiked into samples as follows: **1** (500 pg mL^{-1}), **2** (450 pg mL^{-1}), **3** (400 pg mL^{-1}), **4** (350pg mL^{-1}), **5** (300 pg mL^{-1}), **6** (250 pg mL^{-1}), **7** (200pg mL^{-1}), **8** (150 pg mL^{-1}), **9** (100 pg mL^{-1}), **10** (30 pg mL^{-1}), **11** (20 pg mL^{-1}). (B) PF-4 (C) PSA, and (D) PSMA. Error bars are standard deviations for ECL (n=5) and ELISA (n=3).

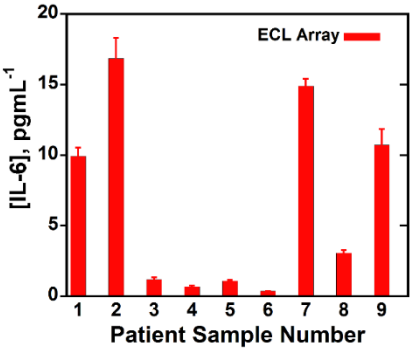

Figure 2-16. IL-6 results from unspiked human serum samples from ECL array.

Linear correlation plots of the ELISA vs. immunoarray data (Figure 2-17, Table 2-1) gave slopes that were all close to 1.0, i.e. 1.14 ± 0.1 for IL-6, 0.97 ± 0.046 for PF-4, 1.11 ± 0.035 for PSA and 0.96 ± 0.029 for PSMA. Intercepts of these plots were within one standard deviation of zero, i.e. 0.022 ± 0.029 for IL-6, 0.011 ± 0.029 for PF-4, -0.0367 ± 0.158 for PSA and -0.013 ± 0.021 for PSMA. Excellent correlation of the automated immunoassay results with ELISA on patient serum samples confirms the high selectivity and specificity of the assay for each of the four proteins in the presence of thousands of other proteins, many at higher concentrations, in the human serum[32].

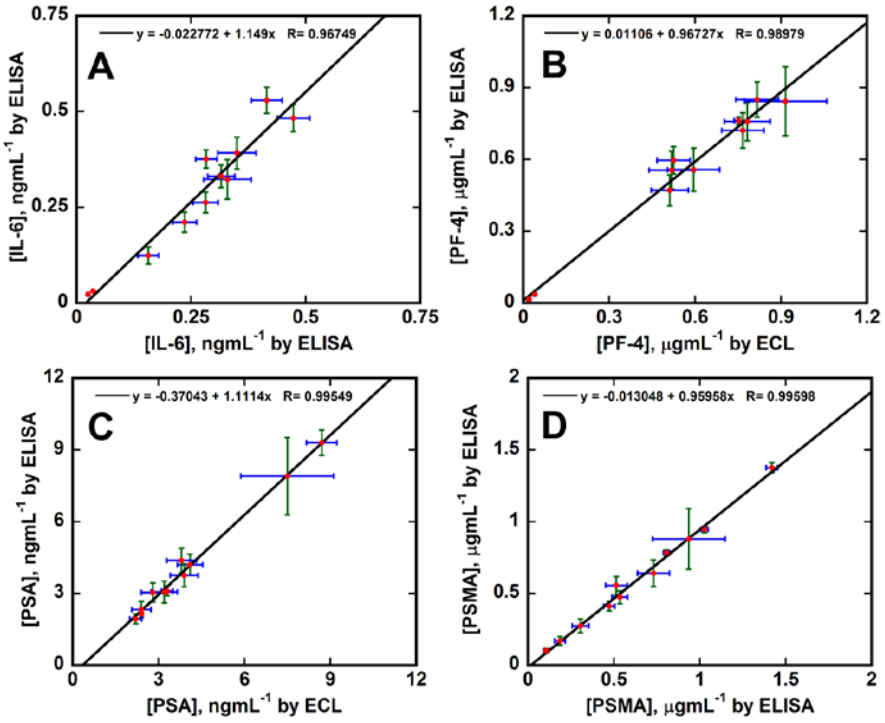

Figure 2-17. Correlation plots of ELISA vs. ECL immunoarray for human serum samples for (A) IL-6, (B) PF-4, (C) PSA, and (D) PSMA.

Table 2-1 Results from correlation plots of ECL array assays vs. ELISA for patient samples

Protein	Slope	Intercept	Correlation Coefficient
PSMA	0.96 ± 0.029	-0.013 ± 0.021	0.9959
PF-4	0.97 ± 0.046	0.011 ± 0.029	0.9898
PSA	1.11 ± 0.035	-0.367 ± 0.158	0.9955
IL-6	1.14 ± 0.100	-0.022 ± 0.029	0.9675

2-5. DISCUSSION

Results above demonstrate an automated immunoarray requiring minimal operator attention for sensitive, simultaneous quantitative measurements of up to 4 proteins. Once the sample/reagent cassette is filled, automated operation and detection takes less than 40 min. Including two control lanes in the detector enables dividing the average protein signals by the average blank signal for each individual assay to minimize chip-to-chip variability (Figure 2-12). Ultrasensitive detection in serum was achieved down to concentrations of 10 fg mL^{-1} over dynamic ranges of 5 orders of magnitude in concentration (Figure 2-14). We observed relative standard deviations ranging from 1-15%, these standard deviations do not effect the value of the assay since we were able to achieve comparable or better standard deviations than ELISA (Figure 2-15). Immunoarray assays showed very good correlations with standard ELISA for serum from prostate cancer patients using only 5-10 μL of sample (Figures 2-15 and 2-17). Selectivity and specificity of the assay was established by determining the four proteins of interest from a pool of thousands of proteins present in human serum samples.[32] In addition, the immunoarray successfully

determined levels of IL-6 below 3 pg mL^{-1} (Figure 2-16) that were below the detection limit of ELISA.

Automation of the methodology is under control of the Arduino microcontroller that turns micropumps on and off according to a preset program and controls the flow of reagents from the preloaded sample/reagent cassette to the detection chamber then to waste (Figure 2-1). This open source electronic platform is very cheap and utilizes free software. The program is easily changed to accommodate changes in the assay protocol, so that the system can be adapted to any reasonable set of assay conditions.

The microfluidic channels (Figure 2-6) in the sample/reagent cassette and the detection chamber were precision cut using an inexpensive, programmable KNK cutter from a 0.8 mm silicon gasket of the kind used in automobile engines. The cut gaskets are then press fitted between appropriately machined hard plastic plates to seal the channels and provide inlets and outlets. This approach is cheap and versatile, allows rapid design changes, and avoids lithography, molding and polymerization steps. The resulting system performs as well or better than a non-automated ECL microfluidic immunoarray we constructed using molded, polymerized polydimethylsiloxane (PDMS) channels.[22] Sample/reagent cassette and detection device made by this approach costs just 15$, whereas micropumps and other electronics cost 450$. All these components are reusable, making the cost per assay very economical.

We have adapted several features from our earlier non-automated immunoarrays to the automated system. Utilization of the SWCNT forests in detector chip microwells provides a high-area nanostructured surface to enhance antibody concentration in each microwell, contributing significantly to high sensitivity.[27,28] The multilabel RuBPY-Si-Ab_2 nanoparticle provides nearly ½ million RuBPY labels per bound target protein to provide the second important component for

ultrasensitive detection. The use of TPrA in Triton X-100 detergent solution as co-reactant allows a detection potential of 0.95 V vs. Ag/AgCl where only TPrA is oxidized electrochemically to enhance production and deprotonation of $TPrA^{*+}$ to drive the complex redox process that provides electronically excited $[RuBPY]^{2+}*$ for ECL.[22,27,33]

2-6. SUMMARY

In summary, a cheap, automated, microprocessor controlled microfluidic immunoarray has been developed for simultaneous detection of four prostate cancer biomarkers at high sensitivity. Inexpensive components and simple fabrication procedures facilitate a low cost device costing about $550 in materials. The device is versatile and in principle can be reprogrammed for the detection of virtually any small protein panel.

2-7. References

1. Hawkridge, A. M.; Muddiman, D. C. *Annu. Rev. Anal. Chem.* **2009**, *2*, 265-277.

2. Wulfkuhle, J. D.; Liotta, L. A.; Petricoin, E. F. *Nat. Rev. Cancer* **2003**, *3*, 267-275.

3. Kingsmore, S. F. *Nat. Rev. Drug Discovery* **2006**, *5*, 310-320.

4. Giljohann, D. A.; Mirkin, C. A. *Nature* **2009**, *462*, 461-464.

5. Rusling, J. F.; Kumar, C. V.; Gutkind, J. S.; Patel, V. *Analyst* **2010**, *135*, 2496-2511.

6. Rusling, J. F. *Anal. Chem.* **2013**, *85*, 5304-5310.

7. Janasek, D.; Franzke, J.; Manz, A. *Nature* **2006**, *442*, 374-380.

8. Zhang, C.; Xing, D. *Chem. Rev.* **2010**, *110*, 4910-4947.

9. Whitesides, G. M. *Nature* **2006**, *442*, 368-373.

10. Wang, J. *Biosens. Bioelectron.* **2006**, *21*, 1887-1892.

11. Rusling J.F.; Bishop, G. W.; Doan, N. M.; Papadimitrakopoulos, F. *J. Mater. Chem. B* **2014,** *2*, 12-30.

12. Gervais, L.; de Rooij, N.; Delamarche, E. *Adv. Mater.* **2011**, *23*, 151-176.

13. Hulme, S. E.; Shevkoplyas, S. S.; Whitesides, G. M. *Lab Chip* **2009**, *9*, 79–86.

14. Weibel, D. B.; Kruithof, M.; Potenta, S.; Sia, S. K.; Lee, A.; Whitesides, G. M. *Anal. Chem.* **2005**, *77*, 4726-4733.

15. Chin, C. D.; Linder, V.; Sia, S. K. *Lab Chip* **2012**, *12*, 2118-2134.

16. Beveridge, J. S.; Stephens, J. R.; Williams, M. E. *Annu. Rev. Anal. Chem.* **2011**, *4*, 251-273.

17. (a) Linder, V.; Sia, S. K.; Whitesides, G. M. *Anal. Chem.* **2005**, *77*, 64-71; (b) Chin, C. D.; Laksanasopin, T.; Cheung, Y. K. et al. *Nature Med.* **2011**, *17*, 1015-1020.

18. Chikkaveeraiah, B. V.; Mani, V.; Patel, V.; Gutkind, J. S.; Rusling, J. F. *Biosens. Bioelectron.* **2011**, *26*, 4477-4483.

19. Malhotra, R.; Patel, V.; Chikkaveeraiah, B. V.; Munge, B. S.; Cheong, S. C.; Zain, R. B.; Abraham, M. T.; Dey, D. K.; Gutkind, J. S.; Rusling, J. F. *Anal. Chem.* **2012**, *84*, 6249-6255.

20. Otieno, B. A.; Krause, C. E.; Latus, A.; Chikkaveeraiah, B. V.; Faria, R. C.; Rusling, J. F. *Biosens. Bioelectron.* **2014**, *53*, 268-274.

21. Forster, R. J.; Bertoncello, P.; Keyes, T. E. *Annu. Rev. Anal. Chem.* **2009**, *2*, 359-385.

22. Sardesai, N. P.; Kadimisetty, K.; Faria, R. C.; Rusling, J. F. *Anal. Bioanal. Chem.* **2013**, *405*, 3831-3838.

23. http://arduino.cc

24. Telesca, D.; Etzioni, R.; Gulati, R. *Biometrics* **2008**, *64*, 10-19.

25. Lilja, H.; Ulmert, D.; Vickers, A. J. *Nat. Rev. Cancer* **2008**, *8*, 268-278.

26. Chikkaveeraih, B. V.; Bhirde, A.; Malhotra, R.; Patel, V.; Gutkind, J. S.; Rusling, J. F. *Anal. Chem.* **2009**, *81*, 9129–9134.

27. Sardesai, N.; Pan, S.; Rusling, J. F. *Chem. Commun.* **2009**, 4968-4970.

28. Malhotra, R.; Papadimitrakopoulos, F.; Rusling, J. F. *Langmuir* **2010**, *26*, 15050-15056.

29. Sardesai, N.; Pan, S.; Rusling, J. F. *Chem. Comm.* **2009**, 4968-4970.

30. Tang, C. K.; Vaze, A.; Rusling, J. F. *Lab Chip* **2012**, *12*, 281-286.

31. Yu, X.; Munge, B.; Patel, V.; Jensen, G.; Bhirde, A.; Gong, J. D.; Kim, S. N.; Gillespie, J.; Gutkind, J. S.; Papadimitrakopoulos, F.; Rusling, J. F. *J. Am. Chem. Soc.* **2006**, *128*, 11199-11205.

32. Pieper, R.; Gatlin, C. L.; Makusky, A. J.; Russo, P. S.; Schatz, C. R.; Miller, S. S.; Su, Q.; McGrath, A. M.; Estock, M. A.; Parmar, P. P.; Zhao, M.; Huang, S.; Zhou, J.; Wang, F.; Esquer-Blasco, R.; Anderson, N. L.; Taylor, J.; Steiner, S. *Proteomics.* **2003**, *3*, 1345-1364

33. Miao, W.; Bard, A. J. *Anal. Chem.* **2004**, *76*, 5379–5386.

CHAPTER 3

3D-Printed Supercapacitor-Powered Electrochemiluminescent Protein Immunoarray

3-1. Abstract

Herein we report a low cost, sensitive, supercapacitor-powered electrochemiluminescent (ECL) protein immunoarray fabricated by an inexpensive 3-dimensional (3D) printer. The immunosensor detects three cancer biomarker proteins in serum in 35 min. The 3D-printed device employs hand screen printed carbon sensors with gravity flow for sample and reagent delivery and washing. Prostate cancer biomarker proteins prostate specific antigen (PSA), prostate specific membrane antigen (PSMA) and platelet factor-4 (PF-4) in serum were captured on the antibody-coated carbon sensors followed by delivery of detection-antibody-coated $Ru(bpy)_3^{2+}$ (RuBPY)-doped silica nanoparticles in a sandwich immunoassay. ECL light was initiated from RuBPY in the silica nanoparticles by electrochemical oxidation with tripropylamine (TPrA) co-reactant using supercapacitor power and ECL was captured with a CCD camera. The supercapacitor was rapidly photo-recharged between assays using an inexpensive solar cell. Detection limits were 300-500 fg mL^{-1} for the 3 proteins in undiluted calf serum. Assays of 6 prostate cancer patient serum samples gave good correlation with conventional single protein ELISAs. This technology could provide sensitive onsite cancer diagnostic tests in resource-limited settings with the need for only moderate-level training.

3-2. Introduction

The recent emergence of inexpensive 3D printers offers revolutionary low cost options for designing and constructing biosensor systems.[1] Fabrication of microfluidic devices by 3D-printing has been explored for rapid prototyping. Early applications include master for faster production of microfluidic channels from PDMS[2] and reaction ware for chemical synthesis and spectroscopic analysis.[3,4] Flow injection systems for monitoring metal ions[5] and add-on accessories for turning smartphones into sensors for food allergens and albumin have been printed.[6,7,8,9,10] Milli- and microfluidic devices have been printed for nanoparticle synthesis.11,[12] Other applications include calorimetry,[13] cell growth monitoring[14], blood evaluation[15] and pathogenic bacteria detection.[16] Electrochemical sensing integrated into a 3D-printed fluidic device was used to detect dopamine and nitric oxide.[17] We recently reported a 3D-printed microfluidic amperometric sensor for hydrogen peroxide.[18]

Microfluidic arrays integrating complex procedures into simple, portable, inexpensive diagnostic platforms will be valuable for future personalized healthcare. [19,20] Detection of biomarker panels holds great promise for early cancer detection and monitoring,[21,22,23,24,25] and promises to lead to improved therapeutic outcomes.[26] Ideally, widespread clinical applications will require low cost, low tech, multiplexed assay devices.[21,22,23,24,25,27] Sensitive, fast, accurate multiplexed protein detection has been achieved using conventionally fabricated microfluidic arrays integrated with nanoscale materials.[23,24,25,28]

Microfluidic array devices are often made using lithography,[29,30,31,32] but prototype development time and cost can be limiting factors. Injection molding can also be used, but both approaches require economies of scale to become cost effective.[33,34] We have developed microfluidic arrays for multiple biomarker detection using molded or precision cut microfluidic

channels. We coupled amperometric detection on gold nanostructured sensor arrays with magnetic particles massively loaded with enzyme labels and antibodies, and demonstrated simultaneous ultrasensitive detection of up to four cancer biomarker proteins.[35,36,37] We also developed electrochemiluminescent (ECL)[38] arrays with antibody-coated $Ru(bpy)_3^{2+}$ (RuBPY)-doped silica nanoparticles for detection on single wall carbon nanotube forests patterned on pyrolytic graphite chips.[39,40] Both approaches utilized non-lithographic fabrication to achieve ultrasensitive detection of multiple proteins in short assays (~35 min). Nonetheless, decreasing time and cost of prototyping and optimizing such devices may lead to benefits in faster translation to public health care.[41]

Electronically simple, miniature power sources are also important for clinical immunoarray development. Small supercapacitors, i.e. high performance electrochemical capacitors (EC) that store electrical energy,[42] have not been widely explored for powering sensors. They have unique advantages including high power density, multiple cycling capability[43]and fast charge-discharge rates.[44] There are few reports of integrating supercapacitors into analytical systems for signal amplification,[45,46] but no examples of powering biosensors.

Herein we report a 3D-printed, gravity flow microfluidic immunoarray for multiple protein detection. These arrays are powered by inexpensive light-rechargeable supercapacitor costing €10 that supplies voltage to screen-printed carbon electrodes for electrochemiluminescence (ECL) light generation that is detected by CCD camera. Simultaneous measurement of prostate cancer biomarkers, prostate specific antigen (PSA),[47,48] prostate specific membrane antigen (PSMA) and platelet factor-4 (PF-4)[49] was achieved at clinically relevant detection limits 0.3-0.5 pg mL^{-1}. To our knowledge, this is the first 3D-printed microfluidic immunosensor, and first application of supercapacitors to a voltage-driven biosensor. Assays of human serum from cancer patients and

cancer-free controls gave good correlations to single-protein enzyme-linked immunosorbent assays (ELISA).

3-3. Experimental Section

3-3.1 Chemicals and Materials

Polylactic acid (PLA) filaments, 1.75 mm diameter for 3D-printing were from MakerBot. Carbon graphite (C2050106D7) and silver/silver chloride inks (C2051014P10) were from Gwent Electronics. Poly(diallyldimethylammoniumchloride) (PDDA), poly(acrylic acid) (PAA), bovine serum albumin (BSA), 1-(3-(Dimethylamino)propyl)-3-ethylcarbodiimidehydrochloride (EDC) and N-hydroxysulfosuccinimide (NHSS) were from Sigma. Pooled human serum samples were from Capital Biosciences and individual patient serum samples were provided by George Washington University Hospital. Calf serum as a surrogate for human serum[50] was used for all calibrations with standard proteins.

3-3.2 Array Device Fabrication

A commercial desktop 3D Fused Deposition Modeling (FDM) printer, MakerBot Replicator 2X, was used. The microfluidic immunoarray was printed from polylactic acid (PLA).[51] Initially, a computer-aided design (CAD) was created with 123D Design (Autodesk), and converted to 3D printer format using splicing software. Optimized printer settings are crucial for good resolution and reproducibility. The heated platform was set to 60 ºC and extruder temperature was 230 ºC, with layer height 200 µm. Extruder speed while travelling was optimized at 80 mm s^{-1}, whereas speed while extruding was 40 mm s^{-1}. Figure 3-1A shows the main array printed with 40 mm length x 30 mm width of the base. It has three reagent chambers connected to a common

downstream microfluidic channel, Figure 3-2. The volume of the reagent chambers is 170 ± 5 µL and the volume required for the microfluidic channel to fill completely is 160 µL. Reservoir volumes were chosen to completely fill the detection channel in a horizontal position under hydrostatic pressure. The reservoirs are prefilled with sample or reagents through port holes located in custom fit 3D-printed inserts (Figure 3-1A) with rods that seal the outlets of the reservoirs. Flow of sample and reagents is controlled by placing the insert to seal the reservoir, or removing it to drain the reservoir into the detection channel in a horizontal position. All reagents are prefilled on the array, and the operator needs only to release reagents sequentially by removing the inserts.

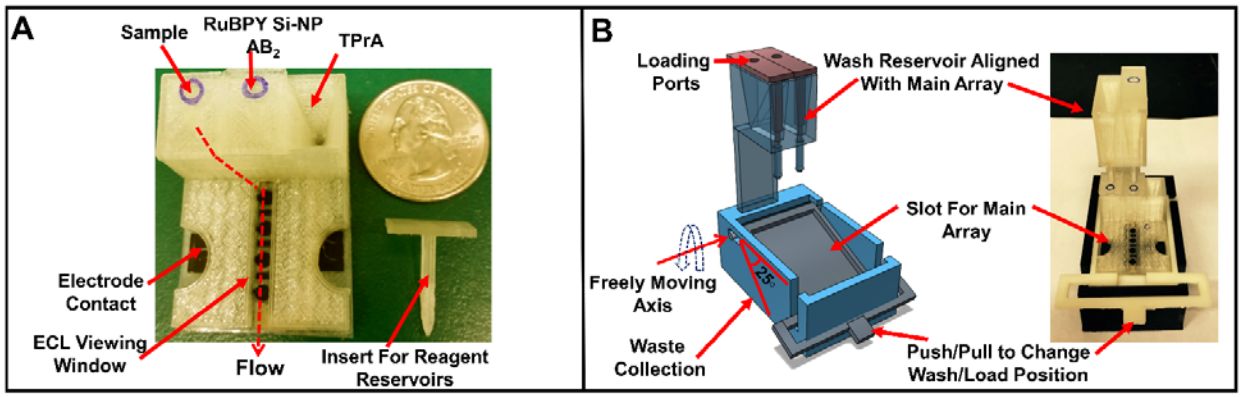

Figure 3-1. 3D-printed main array and wash reservoir module. (A) Basic array showing three reagent reservoirs equipped with inserts along with flow path for reagents to reach microfluidic channel. (B) Wash reservoir module (1B Left) 3D model showing freely moving lever to change between wash and load position along with wash reservoirs aligned with main array, (1B Right) assembled immunoarray setup with both main array and wash module.

Figure 3-1B shows the add-on wash reservoir designed to work with a lever-assisted moving platform device that accommodates the sensor array, wash reservoirs and a waste collector at the bottom. The wash reservoir was designed to align with reagent reservoirs of the main array and is 68 mm length x 44 mm width x 26 mm height with capacity of ~1.6 mL buffer. Wash buffer

in these reservoirs is used to wash off excess sample/reagent from the main array microfluidic channels after the immunoassay. Wash reservoirs employ custom fit inserts to turn flow on and off similar to the reagent chambers. Normal load position has the detection channel with the sensors horizontal. Changing the lever on the wash reservoir to wash position provides a 25º tilt angle to the sensor array (Figure 3-1B), which enables washing of the immunoreagents to a waste chamber at the bottom of the detection channel.

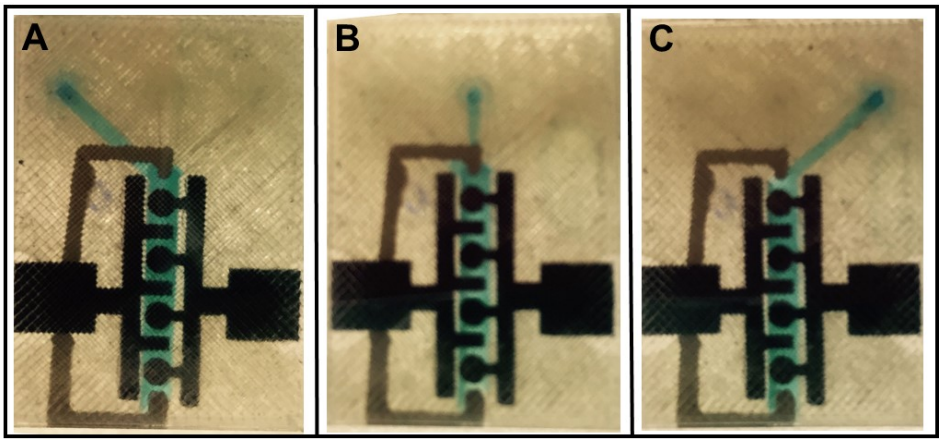

Figure. 3-2. Bottom view of main array showing reservoir's outlet leading to microfluidic channel. (A) Blue color food dye solution released from reservoir 1 reaching a common microfluidic channel (B) Blue color food dye solution released from reservoir 2 reaching a common microfluidic channel (C) Blue color food dye solution released from reservoir 3 reaching a common microfluidic channel.

The sensor electrodes were fabricated by hand screen printing carbon graphitic ink using a patterned adhesive-backed vinyl mask template.[52] First, a mask template was designed using AutoCAD and converted to compatible format for cutting, then a vinyl mask was cut using a portable precision desktop cutter (Cameo®, Silhouette America, Inc.). A vinyl sheet was patterned with a common working electrode and a counter electrode. Then, this vinyl mask was transferred

onto heat resistant transparency film (Highland ™ 707 clear film) and screen printing was done by spreading a thin layer of carbon graphitic ink evenly over the patterned surface, followed by heating at 90 ºC for 15 min. Subsequently, the adhesive vinyl mask was removed revealing the patterned screen printed electrodes (Figure. 3-3A). A patterned 100 µm thick lamination film with holes revealing the electrodes was also made by precision cutting. These lamination films were sealed onto the pattern of electrodes in a heat press at 110 ºC, creating hydrophobic microwells around the sensors that hold up to 5 µL of aqueous solution (Figure 3-3B). Lastly, a template was patterned from transparency film to print Ag/AgCl paste reference electrode (Figure 3-3B). The laminated, screen-printed sensor assembly was then attached to the 3D-printed immunoarray using silicone glue (Proseal clear RTV silicone adhesive sealant), which was dried for at least 2 hr (Figure 3-3C).

Supercapacitors (Cellergy, 2.1 V, 80 mF) used to power ECL arrays were low equivalent series resistance (ESR) aqueous state electrolyte, high output electrochemical double layer capacitors (EDLC's). A solar panel (Sparkfun, 0.45 W, 94 mA) was used to charge the supercapacitor to 1.5 V under ambient room, sun, or iPhone light. Voltage was checked with a digital multimeter prior to every experiment to ensure accuracy. ECL was generated by electrochemical oxidation of both tripropylamine (TPrA) and RuBPY on the sensors when 1.5 V was applied. This initiates a complex redox pathway involving RuBPY in the silica nanoparticle and results in electronically excited $[RuBPY]^{2+}*$ that emits light at 610 nm.[38,53] Generated ECL was captured from the sensor array using a CCD camera.[39]

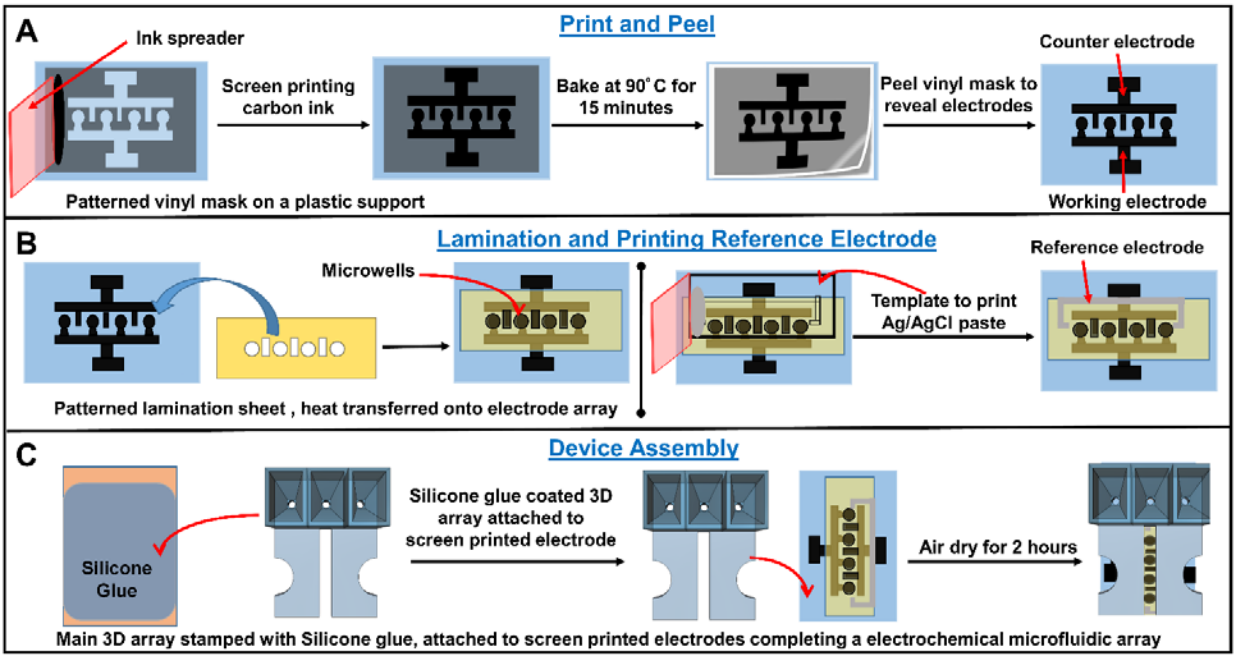

Figure 3-3. Schematic representation of steps for screen printing carbon electrodes and assembling the immunosensor chip. (A) Technique to screen print carbon graphitic ink over the vinyl electrode template using an ink spreader followed by heating to form solid screen printed electrodes. (B) Laminating the exposed electrodes to leave 4 microwells followed by screen printing Ag/AgCl reference electrode. (C) Printed electrodes glued to complete immunoarray device.

RuBPY-silica nanoparticles (RuBPY-SiNP) with average diameter of 117 ± 10 nm were synthesized and characterized as described previously and coated with successive layers of PDDA and PAA, followed by covalently linking secondary antibodies to –COOH groups of PAA.[39] Three different RuBPY-SiNP-Ab_2 were prepared featuring anti-PSA, anti-PSMA and anti-PF-4 as Ab_2. Optimized Ab_2 concentrations for attachment onto RuBPY-SiNPs were 8 µg mL^{-1} for PSA, and 7.5 µg mL^{-1} for PSMA and PF-4, Figure 3-4. For simultaneous detection of all 3 proteins, the three RuBPY-SiNPs were mixed in equal proportions. The Ab_2/RuBPY-SiNP ratio was measured at 38:1. Estimated yield and cost for preparation of silica nanoparticle-Ab_2 bio-conjugate per assay

is approximately 47 % and €0.20 respectively. Covalent linking of antibodies to RuBPY silica nanoparticles have been successfully used previously[39,40] and are stable up to 30 days when stored at 4ºC. TprA at 350 mM in 0.2 M phosphate buffer + 0.05% Tween-20 (T_{20}) and 0.05% Triton-X at pH 7.5 was used as ECL co-reactant.

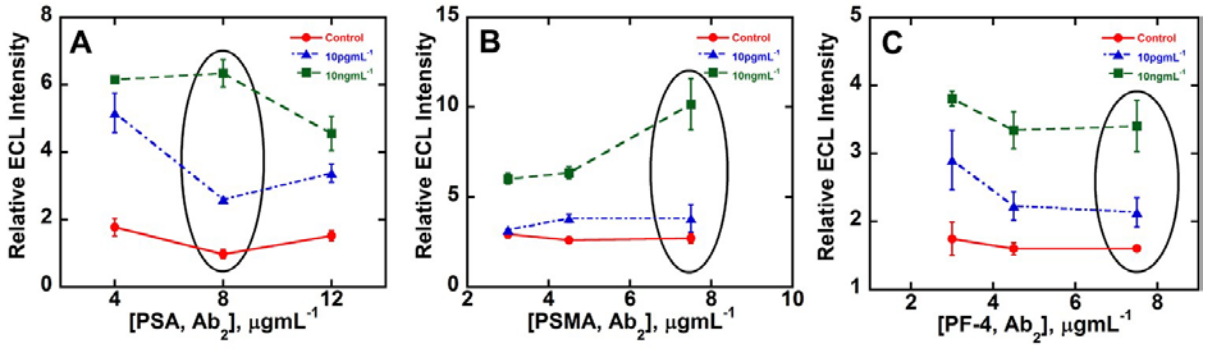

Figure 3-4. Optimization of detection antibody (Ab_2) concentrations used to derivatize RuBPY silica nanoparticles. Concentrations in the circle were found to give largest difference between control and protein signal: (A) PSA, optimized Ab_2 8 µg mL^{-1} (B) PSMA, optimized Ab_2 is 7.5 µg mL^{-1} (C) PF-4, Optimized Ab_2 7.5 µg mL^{-1}

3-3.3 Assay Procedure

Carbon sensors were modified by covalently attaching capture antibody (Ab_1) using EDC-NHSS. Complete details in supplementary information. Ab_1-coated sensors were incubated with 1 % casein in PBS for 1 hr to minimize non-specific binding (NSB). These capture antibody coated carbon sensors are stable up to 7 days when stored at 4ºC. Reagent chambers on the array were prefilled with serum samples, detection antibody (Ab_2)-coated RuBPY-SiNP dispersions, and TprA solution. Serum samples (2-5 µL) were first diluted 500-fold in calf serum prior to loading.

Delivery of sample/reagents from prefilled reservoirs of the main array is accomplished by removing the insert top. The reagents flow downstream to fill the detection channel. Prefilled wash

buffers from wash reservoirs flush the detection channel when the wash module lever is adjusted to 25° tilt angle.

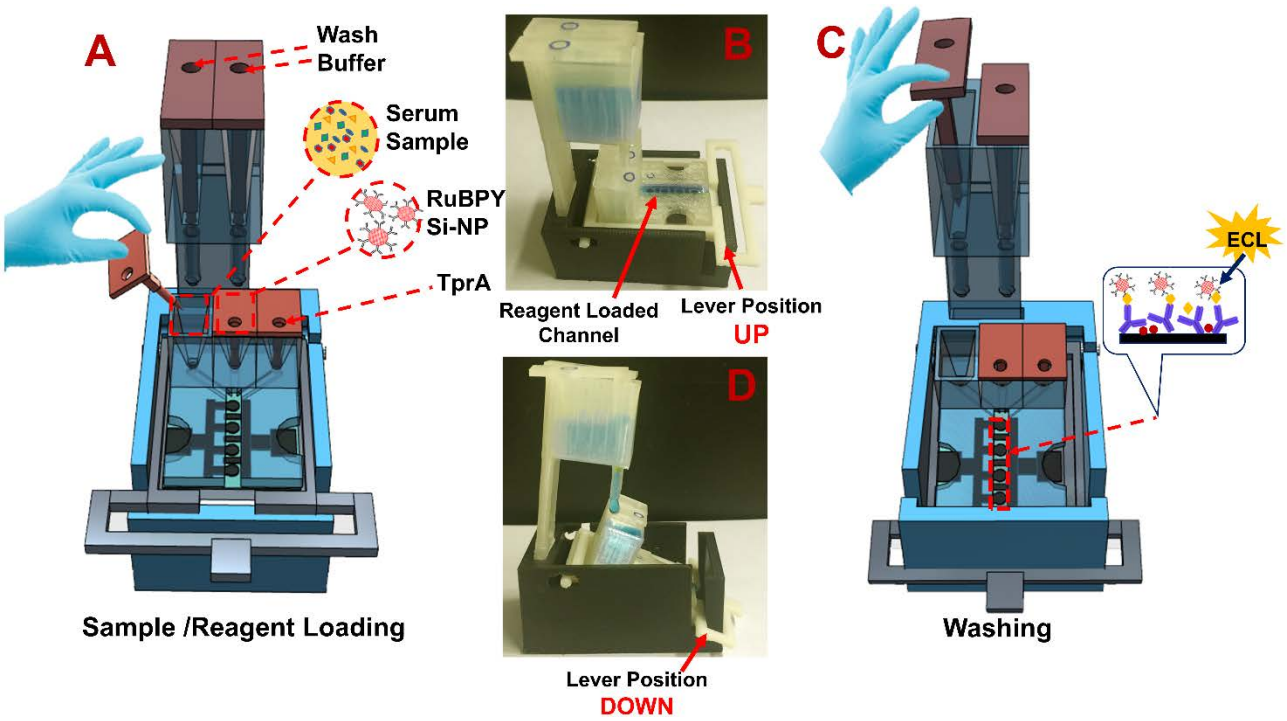

Figure 3-5. Details of the assay procedure: (A) Cartoon showing removal of insert for sample delivery from reservoir by gravity flow. (B) Load position shown with blue food color solution filling the horizontal detection channel with lever up. (C) Cartoon showing buffer delivery from wash reservoir to detection channel for washing away unbound proteins (inset shows sandwich immunoassay on sensors). (D) Wash position showing blue food color solution delivered from wash reservoir to main array when lever is down for 25° tilt of detection channel.

Individual assay steps are: (1) Release sample from its reservoir to fill the detection channel and incubate for 20 min (Figure 3-5A) in horizontal load position (Figure 3-5B). This allows analyte proteins to be captured on Ab_1-coated sensors. (2) Move platform to wash position (25° tilt) by pushing the lever down, then release wash buffer from its reservoir (Figure 3-5C). Buffer

from the larger wash reservoir passes through the sample reservoir into the detection channel and flushes unbound protein to waste (Figure 3-5D). (3) The platform lever is then returned to the load position, followed by release of Ab_2-RuBPY-SiNPs into the horizontal detection chamber, and incubation for 15 min is allowed to bind to previously captured proteins. (4) Wash unbound silica nanoparticles to waste by placing the lever in wash position. (5) TPrA solution is released from its reservoir into the horizontal detection channel, the array is placed under the CCD camera in a dark box and potential of 1.5 V vs. Ag/AgCl is applied with the supercapacitor to generate ECL for 60 s. Acquired ECL images are then processed by software to estimate light intensities from each microwell on the array.[39]

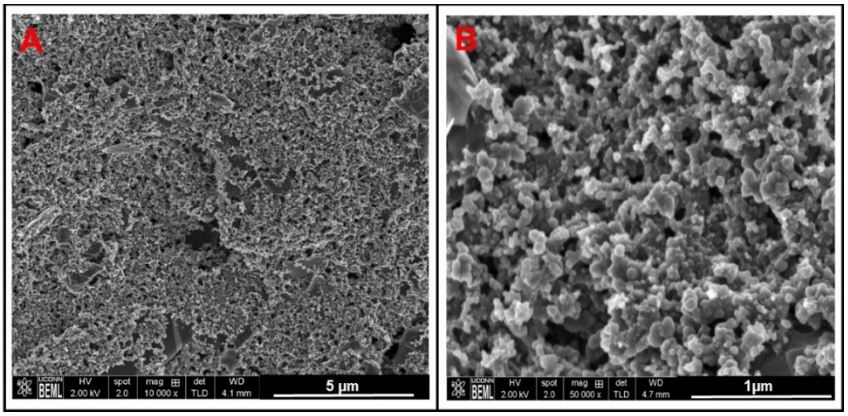

Figure 3-6. Scanning electron microscopy (A-B) PDDA/PAA modified SCE at (A) 5 µM scale revealed rough surface (B) 1 µM scale image for SCE.

3-4. Results

3-4.1 Array Characterization & Optimization

Surface areas of the screen printed electrode, Figure 3-6 were measured from cyclic voltammetry (CV) of 0.06 mM methanol (FcMeOH) in 1 M NaCl from 10 - 750 mV s^{-1} showing a diffusion-controlled, one electron reversible oxidation-reduction peak pair with separations 60-67 mV, Figure 3-7. From the slope of peak current (i_p) versus square root of scan rate ($\nu^{1/2}$) using the Randles-Sevcik equation,[54] and diffusion coefficient 2.5 x 10^{-7} cm^2 s^{-1}, Figure 3-8[55] estimated

surface area of the printed electrodes at 0.293 ± 0.015 cm^2, RSD ± 5% (n=12). Electrochemically measured area is higher compared to geometric area of 0.071 cm^2 due to the rough, porous nature of the screen printed electrodes as confirmed by scanning electron microscopy, Figure 3-6. Supercapacitor was characterized by cyclic voltammetry (CV), Figure 3-7B and by observing galvanostatic charge-discharge cycles (CC), Figure 3-7C. Results show rectangular CVs at scan rates up to 2 V s^{-1}, as well as triangular CC curves at current density 30 mA cm^{-2} suggesting nearly ideal capacitive behavior under fast charge-discharge conditions.

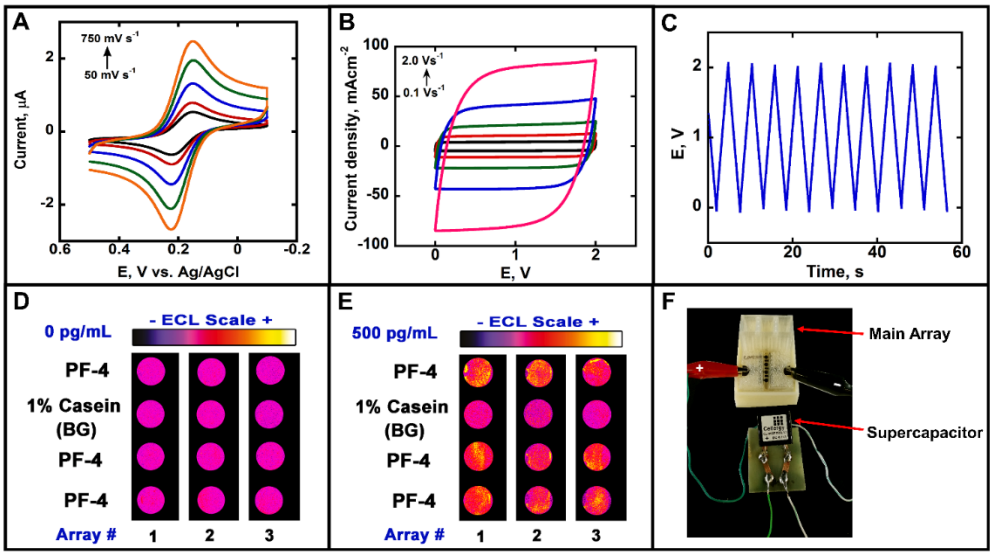

Figure 3-7. Electroanalytical characterization of sensors and supercapacitor: (A) Cyclic voltammograms of screen printed carbon electrodes with 0.06 mM FcMeOH in 1 M NaCl, showing oxidation-reduction reversible peak pair separated by ~60 mV at low scan rates. (B) CV's for supercapacitors up to 2 V s^{-1} showing nearly ideal electrical double layer capacitance behavior. (C) Galvanostatic charge-discharge cycles at current density 30 mA cm^{-2}. (D) Recolorized ECL images demonstrating reproducibility between 9 spots across 3 arrays at 0 pg mL^{-1} PF-4; (E) Recolorized ECL image demonstrating reproducibility between 9 spots across 3 arrays at 500 pg mL^{-1} PF-4. (F) Mounted supercapacitor connected to ECL array inside a dark box.

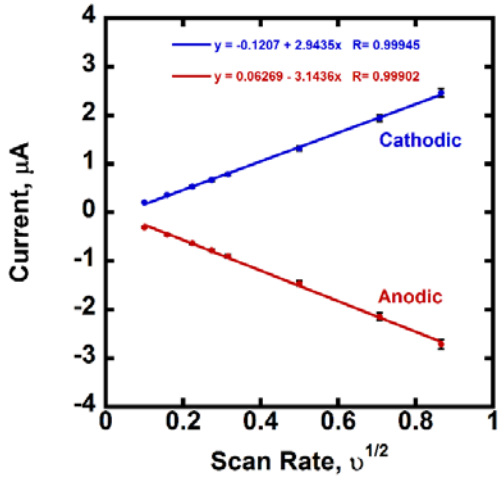

Figure 3-8. Cyclic voltammetry characterization of screen printed carbon electrode showing trumpet plot of peak current vs. square root of scan rate.

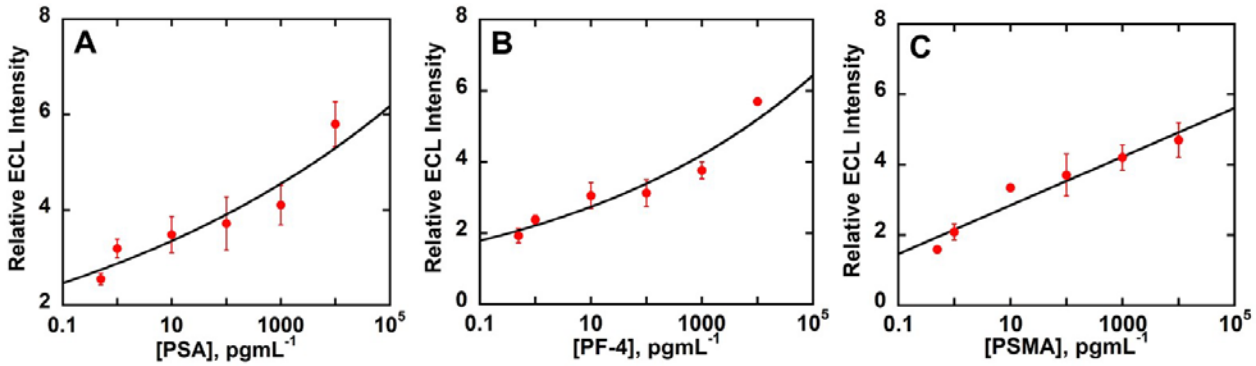

Figure 3-9. Calibration curves for single protein detection (A-C) demonstrating good reproducibility: A) PSA from 0.5 pg mL^{-1} to 10,000 pg mL^{-1} B) PSMA from 0.5 pg mL^{-1} to 10,000 pg mL^{-1} C) PF-4 from 0.5 pg mL^{-1} to 10,000 pg mL^{-1}.Error bars show standard deviation, n=3.

3-4.2 Reproducibility & Immunoarray Calibrations

Reproducibility of array sensors was evaluated at 0 and 500 pg mL^{-1} for the 3 protein analytes. Variation in relative ECL intensities was ≤ 7 % (n=3) array-to-array and ≤10 % spot-to-spot (n=9) (Figure 3-7D&E. Out of four sensors on the array, sensors 1, 3 and 4 were used for specific protein detection. Sensor 2 at the center was used to measure background for each array, and was coated with 1 % casein only. Calibrations were done for all 3 proteins individually in calf serum, with

relative standard deviations ≤ 13 % Figure 3-9. Figure 3-7F shows the supercapacitor mounted on a printed circuit board (PCB), connected to the array inside a dark box to generate ECL.

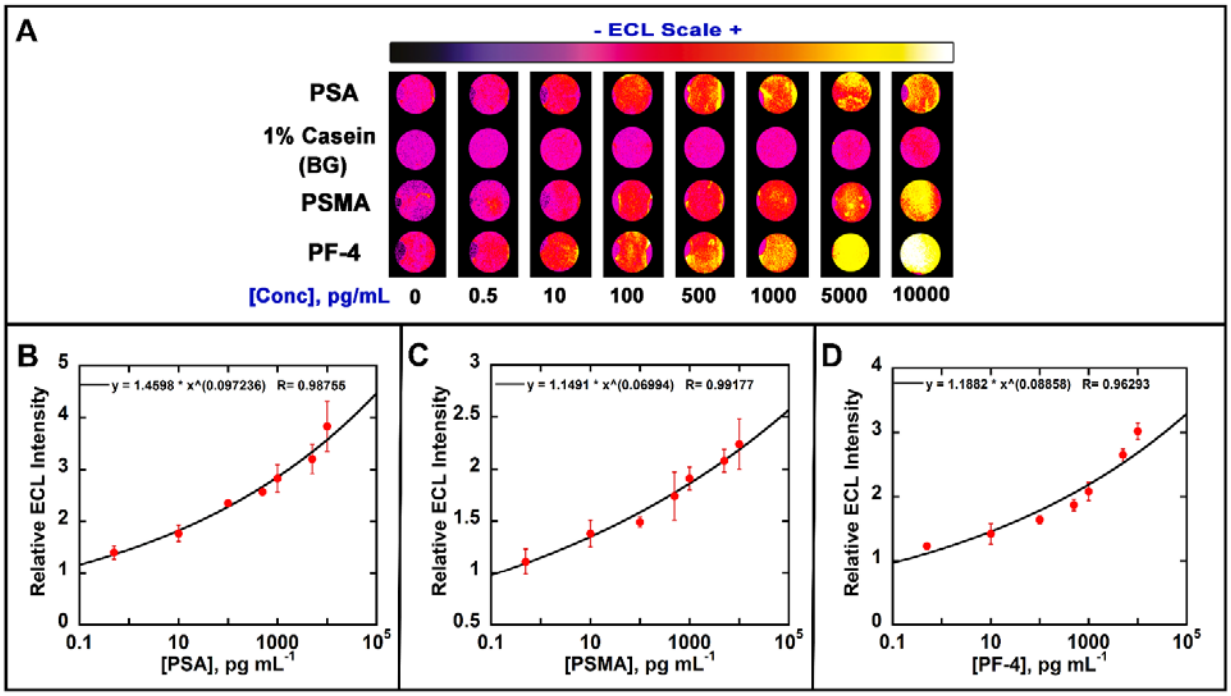

Figure 3-10. Calibration data in undiluted calf serum showing influence of biomarker protein concentration on ECL response: (A) Recolorized ECL images of 8 arrays with showing increase in ECL intensity with increased concentration. ECL signals digitized for (B) PSA, (C) PSMA and (D) PF-4 in calf serum. Error bars show standard deviation for n = 4.

We tested the immunoarrays by determining several proteins simultaneously using mixtures of 3 protein standards in undiluted calf serum Figure 3-10A. Calibration curves were obtained by assigning sensor 1 to detect PSA, Figure 3-10B, 2 to background, 3 to PSMA (Figure 3-10C) and 4 to PF-4, Figure 3-10D. Specific capture antibodies (Ab_1) were first immobilized on the carbon sensors by adding 3 µL of Ab_1 and incubating for 2.5 hr at room temperature followed by adding 1 % casein and incubated for 1 hr. Then, protein mixtures were introduced onto these sensors,

followed by the delivery of multiplexed RuBPY-SiNP ECL labels and development reagents from the prefilled chambers.

Calibration curves for multiplexed detection were obtained by dividing average ECL signal for each concentration by control signals on each sensor chip (n=4). Dynamic ranges were from 500 fg mL^{-1} to 10 ng mL^{-1} for all protiens and detection limits as 3 times the standard deviations of zero protien controls were 300 fg mL^{-1} for PSA, 535 fg mL^{-1} for PSMA and 420 fg mL^{-1} for PF-4.

3-4.3 Assays of Human Serum Samples

We measured the analyte protiens from 4 prostate cancer patient serum samples and 2 cancer free human samples using the calibration curves in Figure 3-10. ECL immunoassay results correlated well with single protein ELISA assays (Figure 3-11. A,B&C). Linear correlation plots obtained for ELISA vs. ECL immunoarray data (Figure 3-12. A,B&C, Table 3-1) had slopes close to 1.0 & intercepts of these plots were close to zero consistent with good correlation.

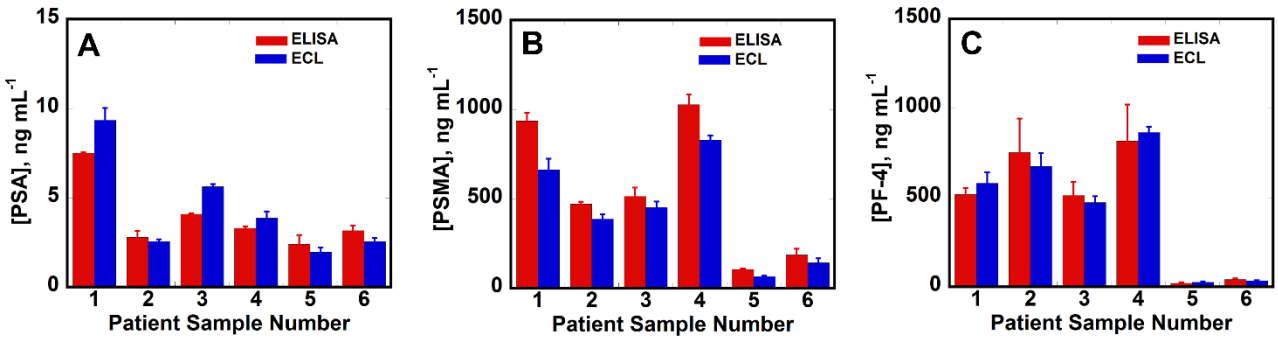

Figure 3-11. Comparisons of ECL vs. ELISA assays on human serum samples. Samples 1-4 are from prostate cancer patients and 5-6 are from cancer free individuals: (A) PSA (B) PSMA (C) PF-4 as bar graphs. Error bars are standard deviations with n=4 for ECL arrays and n=3 for ELISA.

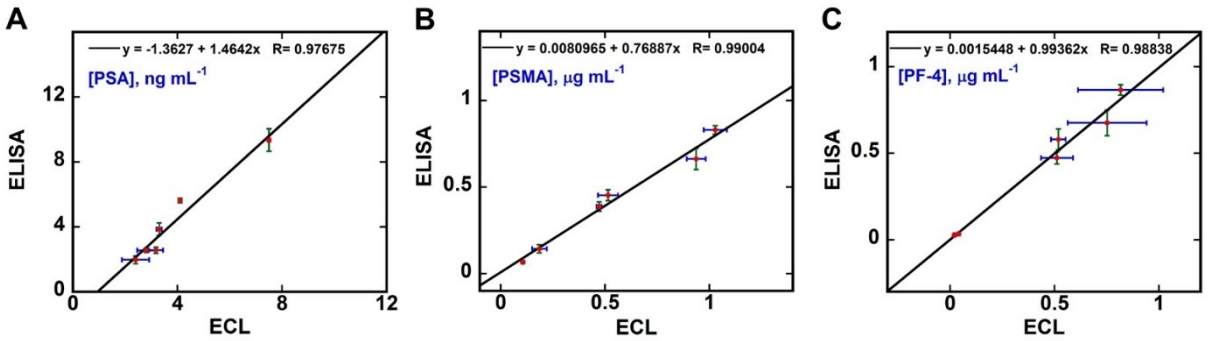

Figure 3-11. Linear correlation plots of ECL vs. ELISA validation studies for (A) PSA, (B) PSMA and (C) PF-4.

Table 3-1. Results from correlation plots of ECL array assays vs. ELISA for patient samples

Protein	Slope	Intercept	Correlation Coefficient
PSA	1.46 ± 0.16	-1.3627 ± 0.681	0.9767
PSMA	0.77 ± 0.05	0.0081 ± 0.035	0.9900
PF-4	0.99 ± 0.08	0.0015 ± 0.041	0.9883

3-5. Discussion

Results above demonstrate successful development of inexpensive, portable, 3D-printed ECL immunoarray capable of measuring three proteins simultaneously. These arrays use light-activated supercapacitors to generate ECL. The cost per assay is ~€0.50 when the arrays are re-used with the replaceable sensor chip. The platform utilizes simple steps to complete the immunoassay in 35 min without external equipment except a CCD camera. Assay time was considered from the time serum proteins were exposed to capture antibodies till detection.

Good repeatability was found between different arrays for finite concentration with RSD ≤ 7 % for single protein detection. RSD for various concentrations of multiplexed detection between different arrays range from 1-13%, which is a little larger than desirable for bioanalytical

devices. However, variability has been compromised somewhat in return for simplicity and very low cost.

Detection limits of 300 fg mL^{-1} for PSA 535 fg mL^{-1} for PSMA and 420 fgmL^{-1} for PF-4 were achieved with dynamic ranges from 500 fg mL^{-1} to 10 ng mL^{-1}, Figure 3-10 that readily correspond to clinical ranges of these proteins in serum after appropriate dilutions.

Accuracy of the ECL immunoassays was confirmed by correlations to standard ELISA (Figure 3-11, 3-12) for prostate cancer patient samples. Sample volumes as low as 5 µL were 500-fold diluted in calf serum to mimic the possibility of determining very low concentrations of proteins in a full serum matrix. These experiments revealed reasonably accurate detection of 3 analyte proteins in the presence of thousands of other proteins[56] in mixed serum media, demonstrating high selectivity. Good correlation between ELISA and the ECL arrays along with relatively small array-to-array standard deviations indicates potential for future clinical applications (Figure 3-11, 3-12 & Table 3-1).

These 3D-printed ECL microfluidic arrays could serve as a simple, low cost diagnostic platform for applications in both low and moderate resource environments. Printed components of the array cost ~€0.90 in materials. The screen-printed 4-sensor chip is a disposable and costs ~€0.20 in materials, whereas the reusable wash module costs ~€0.70. Considering all costs for immunoreagents, a single immunoassay costs ~€1.20, considering the entire platform (€0.90) to be disposable, or ~€0.50 if the wash module is reused. Our 3D printed main arrays can also be reused by detaching and replacing the screen printed carbon sensors. A detailed comparison of cost, time and detection limits between our ECL arrays and ELISA were provided in Table 3-2.

Table 3-2. Comparison between single protein ELISA vs. 3D printed ECL array from this study.

Method	ELISA	3D Printed ECL Array
Number of Proteins & Instrumentation	Single Protein Requires Plate reader and Plate washer	Three Proteins Requires CCD camera in a Dark box.
Cost	409$ for PSA,PF-4 each & 567$ for PSMA Per Plate	~€1.20 Per Array + 10$ Supercapacitor + 12$ Solar panel
Assay Time	4 hours 45 minutes	35 minutes
Dynamic range	10 pg mL^{-1} to 2500pg mL^{-1} PSA 20pg mL^{-1} to 15,000 pg mL^{-1} PF-4 39pg mL^{-1} to 2500pg mL^{-1} PSMA	500fg mL^{-1} to 10ng mL^{-1} for PSA, PF-4 & PSMA.
Detection limits	~8 pg mL^{-1} for PSA, ~19 pg mL^{-1} for PF-4 & ~12 pg mL^{-1} for PSMA	300 fg mL^{-1} for PSA, 420 fg mL^{-1} for PF-4 & 535 fg mL^{-1} for PSMA.

Screen printing of the sensors employs an inexpensive precision desktop craft cutter for patterning templates. Using adhesive-backed patterned vinyl sheets for hand screen printing the electrodes provided acceptably reproducible sensor surface areas (±5%). Lamination after printing

provides an effective hydrophobic boundary when attaching capture antibodies from aqueous solutions.

Solar panels allowed rapid light-driven charging to 1.5 V of the supercapacitor power source to drive the ECL generation step. Integration of this small power source on the immunoarray helps make it portable, avoids potentiostatic equipment, and makes the assay simpler for the operator. Future coupling of our immunosensors with a cell phone digital camera could provide a complete onsite cancer detection array for resource limited settings.

3-6. Summary

In summary, results demonstrate a novel, very low cost, gravity-flow, 3D-printed, portable immunoarray for sensitive detection of proteins. The system results in ECL-based assays for 3 proteins that cost ~€0.50 each and can be completed in 35 min. without high level technical expertise. Using an inexpensive, robust, portable supercapacitor (€10) for power with a solar panel (€12) for recharging, the entire immunoarray costs ~€25, not including the CCD camera. A drawback of this system, however, is that a significant number of sequential tasks must be completed by the operator to complete an immunoassay. Nevertheless, this device is suitable for low and moderate resource clinical environments. This method can be adapted to detect other disease related proteins, nucleic acids or carbohydrates (Hu et al., 2010). We have previously measured other proteins IL-6 with similar strategies.[38,39] This work also suggests that 3D-printing can be used to develop more sophisticated immunoarray devices with a higher level of automation.

3-7. References

1. Gross, B. C.; Erkal, J. L.; Lockwood, S. Y.; Chen, C.; Spence, D. M. *Evaluation of 3D printing and its potential impact on biotechnology and the chemical sciences* **2014**.
2. McDonald, J. C.; Chabinyc, M. L.; Metallo, S. J.; Anderson, J. R.; Stroock, A. D.; Whitesides, G. M. Prototyping of microfluidic devices in poly (dimethylsiloxane) using solid-object printing. *Anal. Chem.* **2002**, *74*, 1537-1545.
3. Symes, M. D.; Kitson, P. J.; Yan, J.; Richmond, C. J.; Cooper, G. J.; Bowman, R. W.; Vilbrandt, T.; Cronin, L. Integrated 3D-printed reactionware for chemical synthesis and analysis. *Nature Chemistry* **2012**, *4*, 349-354.
4. Dragone, V.; Sans, V.; Rosnes, M. H.; Kitson, P. J.; Cronin, L. 3D-printed devices for continuous-flow organic chemistry. *Beilstein journal of organic chemistry* **2013**, *9*, 951-959.
5. Su, C.; Hsia, S.; Sun, Y. Three-dimensional printed sample load/inject valves enabling online monitoring of extracellular calcium and zinc ions in living rat brains. *Anal. Chim. Acta* **2014**, *838*, 58-63.
6. Coskun, A. F.; Wong, J.; Khodadadi, D.; Nagi, R.; Tey, A.; Ozcan, A. A personalized food allergen testing platform on a cellphone. *Lab on a Chip* **2013**, *13*, 636-640.
7. Wei, Q.; Nagi, R.; Sadeghi, K.; Feng, S.; Yan, E.; Ki, S. J.; Caire, R.; Tseng, D.; Ozcan, A. Detection and spatial mapping of mercury contamination in water samples using a smart-phone. *ACS nano* **2014**, *8*, 1121-1129.
8. Coskun, A. F.; Nagi, R.; Sadeghi, K.; Phillips, S.; Ozcan, A. Albumin testing in urine using a smart-phone. *Lab on a Chip* **2013**, *13*, 4231-4238.

9. Roda, A.; Michelini, E.; Cevenini, L.; Calabria, D.; Calabretta, M. M.; Simoni, P. Integrating biochemiluminescence detection on smartphones: mobile chemistry platform for point-of-need analysis. *Anal. Chem.* **2014**, *86*, 7299-7304.

10. Wei, Q.; Luo, W.; Chiang, S.; Kappel, T.; Mejia, C.; Tseng, D.; Chan, R. Y. L.; Yan, E.; Qi, H.; Shabbir, F. Imaging and sizing of single DNA molecules on a mobile phone. *ACS nano* **2014**, *8*, 12725-12733.

11. Femmer, T.; Kuehne, A. J.; Wessling, M. Print your own membrane: direct rapid prototyping of polydimethylsiloxane. *Lab on a Chip* **2014**, *14*, 2610-2613.

12. Kitson, P. J.; Rosnes, M. H.; Sans, V.; Dragone, V.; Cronin, L. Configurable 3D-Printed millifluidic and microfluidic 'lab on a chip'reactionware devices. *Lab on a Chip* **2012**, *12*, 3267-3271.

13. Shallan, , A. I.; Smejkal, P.; Corban, M.; Guijt, R. M.; Breadmore, M. C. Cost-effective three-dimensional printing of visibly transparent microchips within minutes. *Anal. Chem.* **2014**, *86*, 3124-3130.

14. Anderson, K. B.; Lockwood, S. Y.; Martin, R. S.; Spence, D. M. A 3D printed fluidic device that enables integrated features. *Anal. Chem.* **2013**, *85*, 5622-5626.

15. Chen, C.; Wang, Y.; Lockwood, S. Y.; Spence, D. M. 3D-printed fluidic devices enable quantitative evaluation of blood components in modified storage solutions for use in transfusion medicine. *Analyst* **2014**, *139*, 3219-3226.

16. Lee, W.; Kwon, D.; Choi, W.; Jung, G. Y.; Au, A. K.; Folch, A.; Jeon, S. 3D-printed microfluidic device for the detection of pathogenic bacteria using size-based separation in helical channel with trapezoid cross-section. *Scientific reports* **2015**, *5*, 7717.

17. Erkal, J. L.; Selimovic, A.; Gross, B. C.; Lockwood, S. Y.; Walton, E. L.; McNamara, S.; Martin, R. S.; Spence, D. M. 3D printed microfluidic devices with integrated versatile and reusable electrodes. *Lab on a Chip* **2014**, *14*, 2023-2032.

18. Bishop, G. W.; Satterwhite, J. E.; Bhakta, S.; Kadimisetty, K.; Gillette, K. M.; Chen, E.; Rusling, J. F. 3D-printed fluidic devices for nanoparticle preparation and flow-injection amperometry using integrated Prussian blue nanoparticle-modified electrodes. *Anal. Chem.* **2015**, *87*, 5437-5443.

19. Yager,P.; Edwards, T.; Fu, E.; Helton, K.; Nelson, K.; Tam, M. R.; Weigl, B. H. Microfluidic diagnostic technologies for global public health. *Nature* **2006**, *442*, 412-418.

20. Rusling, J. F. Multiplexed electrochemical protein detection and translation to personalized cancer diagnostics. *Anal. Chem.* **2013**, *85*, 5304-5310.

21. Hawkridge, A. M.; Muddiman, D. C. Mass spectrometry–based biomarker discovery: toward a global proteome index of individuality. *Annual Review of Analytical Chemistry* **2009**, *2*, 265-277.

22. Wulfkuhle, J. D.; Liotta, L. A.; Petricoin, E. F. Proteomic applications for the early detection of cancer. *Nature reviews cancer* **2003**, *3*, 267-275.

23. Kingsmore, S. F. Multiplexed protein measurement: technologies and applications of protein and antibody arrays. *Nature reviews Drug discovery* **2006**, *5*, 310-321.

24. Giljohann, D. A.; Mirkin, C. A. Drivers of biodiagnostic development. *Nature* **2009**, *462*, 461-464.

25. Rusling, J. F.; Kumar, C. V.; Gutkind, J. S.; Patel, V. Measurement of biomarker proteins for point-of-care early detection and monitoring of cancer. *Analyst* **2010**, *135*, 2496-2511.

26. Siegel, R.; DeSantis, C.; Jemal, A. Colorectal cancer statistics, 2014. *CA: a cancer journal for clinicians* **2014**, *64*, 104-117.

27. Rusling, J. F. Multiplexed electrochemical protein detection and translation to personalized cancer diagnostics. *Anal. Chem.* **2013**, *85*, 5304-5310.

28. Rusling, J. F.; Bishop, G. W.; Doan, N. M.; Papadimitrakopoulos, F. Nanomaterials and biomaterials in electrochemical arrays for protein detection. *Journal of Materials Chemistry B* **2014**, *2*, 12-30.

29. Weibel, D. B.; Kruithof, M.; Potenta, S.; Sia, S. K.; Lee, A.; Whitesides, G. M. Torque-actuated valves for microfluidics. *Anal. Chem.* **2005**, *77*, 4726-4733.

30. Urbanski, J. P.; Thies, W.; Rhodes, C.; Amarasinghe, S.; Thorsen, T. Digital microfluidics using soft lithography. *Lab on a Chip* **2006**, *6*, 96-104.

31. Hulme, S. E.; Shevkoplyas, S. S.; Whitesides, G. M. Incorporation of prefabricated screw, pneumatic, and solenoid valves into microfluidic devices. *Lab on a Chip* **2009**, *9*, 79-86.

32. Sudarsan, A. P.; Ugaz, V. M. Fluid mixing in planar spiral microchannels. *Lab on a Chip* **2006**, *6*, 74-82.

33. Chin, C. D.; Laksanasopin, T.; Cheung, Y. K.; Steinmiller, D.; Linder, V.; Parsa, H.; Wang, J.; Moore, H.; Rouse, R.; Umviligihozo, G. Microfluidics-based diagnostics of infectious diseases in the developing world. *Nat. Med.* **2011**, *17*, 1015-1019.

34. Laksanasopin, T.; Guo, T. W.; Nayak, S.; Sridhara, A. A.; Xie, S.; Olowookere, O. O.; Cadinu, P.; Meng, F.; Chee, N. H.; Kim, J.; Chin, C. D.; Munyazesa, E.; Mugwaneza, P.; Rai, A. J.; Mugisha, V.; Castro, A. R.; Steinmiller, D.; Linder, V.; Justman, J. E.; Nsanzimana, S.; Sia, S. K. A smartphone dongle for diagnosis of infectious diseases at the point of care. *Sci. Transl. Med.* **2015**, *7*, 273re1.

35. Chikkaveeraiah, B. V.; Mani, V.; Patel, V.; Gutkind, J. S.; Rusling, J. F. Microfluidic electrochemical immunoarray for ultrasensitive detection of two cancer biomarker proteins in serum. *Biosensors and Bioelectronics* **2011**, *26*, 4477-4483.

36. Malhotra, R.; Patel, V.; Chikkaveeraiah, B. V.; Munge, B. S.; Cheong, S. C.; Zain, R. B.; Abraham, M. T.; Dey, D. K.; Gutkind, J. S.; Rusling, J. F. Ultrasensitive detection of cancer biomarkers in the clinic by use of a nanostructured microfluidic array. *Anal. Chem.* **2012**, *84*, 6249-6255.

37. Otieno, B. A.; Krause, C. E.; Latus, A.; Chikkaveeraiah, B. V.; Faria, R. C.; Rusling, J. F. On-line protein capture on magnetic beads for ultrasensitive microfluidic immunoassays of cancer biomarkers. *Biosensors and Bioelectronics* **2014**, *53*, 268-274.

38. Forster, R. J.; Bertoncello, P.; Keyes, T. E. Electrogenerated chemiluminescence. *Annual Review of Analytical Chemistry* **2009**, *2*, 359-385.

39. Sardesai, N. P.; Kadimisetty, K.; Faria, R.; Rusling, J. F. A microfluidic electrochemiluminescent device for detecting cancer biomarker proteins. *Analytical and bioanalytical chemistry* **2013**, *405*, 3831-3838.

40. Kadimisetty, K.; Malla, S.; Sardesai, N. P.; Joshi, A. A.; Faria, R. C.; Lee, N. H.; Rusling, J. F. Automated multiplexed ECL immunoarrays for cancer biomarker proteins. *Anal. Chem.* **2015**, *87*, 4472-4478.

41. Au, A. K.; Bhattacharjee, N.; Horowitz, L. F.; Chang, T. C.; Folch, A. 3D-printed microfluidic automation. *Lab on a chip* **2015**, *15*, 1934-1941.

42. Simon, P.; Gogotsi, Y.; Dunn, B. Materials science. Where do batteries end and supercapacitors begin? *Science* **2014**, *343*, 1210-1211.

43. Aradilla, D.; Gentile, P.; Bidan, G.; Ruiz, V.; Gómez-Romero, P.; Schubert, T. J.; Sahin, H.; Frackowiak, E.; Sadki, S. High performance of symmetric micro-supercapacitors based on silicon nanowires using N-methyl-N-propylpyrrolidinium bis (trifluoromethylsulfonyl) imide as electrolyte. *Nano Energy* **2014**, *9*, 273-281.

44. Wang, G.; Zhang, L.; Zhang, J. A review of electrode materials for electrochemical supercapacitors. *Chem. Soc. Rev.* **2012**, *41*, 797-828.

45. Wang, Y.; Huang, Y.; Chen, H.; Li, L.; Xu, J.; Li, Z.; Zhang, G.; Fan, J.; Zhao, X.; Jia, S. Incidence and correlates of HIV and syphilis in a prospective cohort of men who have sex with men in Mianyang, China, over a 36-month period. *Sexual health* **2015**, *12*, 546-555.

46. Ge, L.; Wang, P.; Ge, S.; Li, N.; Yu, J.; Yan, M.; Huang, J. Photoelectrochemical lab-on-paper device based on an integrated paper supercapacitor and internal light source. *Anal. Chem.* **2013**, *85*, 3961-3970.

47. Telesca, D.; Etzioni, R.; Gulati, R. Estimating lead time and overdiagnosis associated with PSA screening from prostate cancer incidence trends. *Biometrics* **2008**, *64*, 10-19.

48. Lilja, H.; Ulmert, D.; Vickers, A. J. Prostate-specific antigen and prostate cancer: prediction, detection and monitoring. *Nature Reviews Cancer* **2008**, *8*, 268-278.

49. Chikkaveeraiah, B. V.; Bhirde, A.; Malhotra, R.; Patel, V.; Gutkind, J. S.; Rusling, J. F. Single-wall carbon nanotube forest arrays for immunoelectrochemical measurement of four protein biomarkers for prostate cancer. *Anal. Chem.* **2009**, *81*, 9129-9134.

50. Malhotra, R.; Papadimitrakopoulos, F.; Rusling, J. F. Sequential layer analysis of protein immunosensors based on single wall carbon nanotube forests. *Langmuir* **2010**, *26*, 15050-15056.

51. Martin, O.; Averous, L. Poly (lactic acid): plasticization and properties of biodegradable multiphase systems. *Polymer* **2001**, *42*, 6209-6219.

52. Afonso, A. S.; Uliana, C. V.; Martucci, D. H.; Faria, R. C. Simple and rapid fabrication of disposable carbon-based electrochemical cells using an electronic craft cutter for sensor and biosensor applications. *Talanta* **2016**, *146*, 381-387.

53. Miao, W.; Bard, A. J. Electrogenerated chemiluminescence. 77. DNA hybridization detection at high amplification with [Ru (bpy) 3] 2 -containing microspheres. *Anal. Chem.* **2004**, *76*, 5379-5386.

54. Bard, A. J.; Faulkner, L. R. Electrochemical Methods, 2nd. *J.Wiley.New York* **2001**, 669.

55. Lovelock, K. R.; Ejigu, A.; Loh, S. F.; Men, S.; Licence, P.; Walsh, D. A. On the diffusion of ferrocenemethanol in room-temperature ionic liquids: an electrochemical study. *Physical Chemistry Chemical Physics* **2011**, *13*, 10155-10164.

56. Pieper, , R.; Gatlin, C. L.; Makusky, A. J.; Russo, P. S.; Schatz, C. R.; Miller, S. S.; Su, Q.; McGrath, A. M.; Estock, M. A.; Parmar, P. P. The human serum proteome: Display of nearly 3700 chromatographically separated protein spots on two-dimensional electrophoresis gels and identification of 325 distinct proteins. *Proteomics* **2003**, *3*, 1345-1364.

CHAPTER 4

Automated Small Volume Serum Sample Immunoassays using Rapid 3-D Printed Microfluidic ECL Arrays for Prostate Cancer Biomarkers

4-1. Abstract

Multiplexed detection of serum proteins relevant to a diseased state holds promise in accurate diagnosis in early stages. Miniaturized assay platforms are of great demand that require small sample volumes of precious biological sample. There is a need for miniaturized microfluidic arrays that can detect multiple protein markers from serum that is simple, highly sensitive, rapid and high throughput with significant cut down in cost. Automation in microfluidics could provide faster translation of such immunoarrays into personalized public health care as it requires minimal user interference. Herein we report a compact 3-D printed ECL immunoarray that detects 2 prostate cancer biomarkers simultaneously from complex serum matrix with high sensitivity and selectivity. Our proposed method is fast, requires only 18 minutes assay time, accurate and extremely low cost with only 0.75$ per assay, if reused the cost per assay is 0.35$. Our immunoarray just requires sub microliter sample volumes to complete immunoassay with desirable dilutions while total assay volume is just 20 µL. The 3-D printed array here is a clear fluidic device fabricated on an inexpensive desktop SLA 3-D printer. Design includes strategically arranged reagent/sample chambers to facilitate rapid delivery of immunoreagents to detection channels with

minimized dead volumes. We used simple programmable syringe pump to program the immunoassay timing intervals, allowing pump and pause of the reagents as required for completion of sandwich immunoassay. Sandwich immunoassay built on a nanostructured single wall carbon nanotube forest with RuBPY silica nanoparticles as detection labels enabled sensitive detection of both prostate specific antigen (PSA) and prostate specific memberane antigen (PSMA) simultaneously on a same array. Detection limits of 150 fg mL^{-1} for PSA and 230 fg mL^{-1} for PSMA was obtained with dynamic ranges extending up to 5 ng mL^{-1}. Validation assay with human serum samples showed good correlation with single protein ELISA. ROC curve analysis for the human serum samples suggest PSMA can be used as potential marker for prostate cancer in conjunction with PSA. While further studies are warranted with larger patient sample size to establish PSMA as an additional tool to differentiate cancer vs non cancer samples and staging the prostate cancer. Our immunoarray has potential to expand to several markers detection at a time for better personalized public healthcare.

4-2. Introduction

Prostate cancer is the second most frequent cause of cancer death for men in the United States, behind only lung cancer. Roughly 1 man in 39 will die of prostate cancer, and about 1 in 7 will be diagnosed with prostate cancer during his lifetime.[1] Therefore a more sensitive and more accurate test for prostate cancer presence than currently used is a necessity for increasing the survival rate through early detection and monitoring. Currently Prostate specific antigen (PSA) is being widely used as clinical serum biomarker for prostate cancer as early screening tool. PSA levels above 4 ng mL^{-1} suggests possibility of early stage of cancer and often referred to further evaluation by biopsy.[2] PSA test alone has low specificity for cancer, about 75% of men who have a prostate biopsy ordered due to elevated PSA levels 4.0 to 10.0 ng ml^{-1} do not have the cancer[3] reason being the several benign prostate diseases can also elevate PSA leading to false positives.[4] Measuring multiple biomarkers simultaneously can provide improved predictive power in diagnosing the diseased state leading to better personalized therapeutic monitoring.[5,6,7,8] Thus there is great need for the ability to measure multiple proteins in a single device using only a small sample of blood. Prostate specific membrane antigen (PSMA) can be a potential serum marker that can be used in conjunction with PSA to evaluate the prostate cancer in early stages. PSMA is considered to be upregulated by many fold in prostate cancer, metastatic disease and hormone refractory prostate cancers.[9] It's shown that increased levels of PSMA have promoted the progression of prostate cancer.[10] In prostate cancer the average serum PSMA levels for malignant stage (> 620 ng mL^{-1}) vs benign state (>120 ng mL^{-1}) were significantly different.[11] PSA values generally fall to low values post treatment of prostate cancer with surgery, radiation, chemotheraoy etc., whereas it is noticed that elevated levels of PSMA can be used to understand the stage of clinical progression or clinical resistance.[12]

Currently for specific protein marker detection single protein enzyme linked immunosorbent assay (ELISA) function as a gold standard.[13] Quantifying multiple analytes from biological samples using singleplex platforms like ELISA and western blot is time consuming and increased risk of errors between assays. Running parallel assays for multiple proteins besides being expensive and complex, also requires increased sample/analyte volume. Thus sample volume requirements increase with increase in number of proteins to be analyzed which could be major hurdle in establishing protein panels detection for error free diagnosis of a disease. Acquiring biological samples like blood, serum or tissues for multiple protein analysis could provide a greater challenge as they are limited.[14] Hence there is need for miniaturization of assay platforms which can perform multiple analyte analysis simultaneously.[15,16] This ensures use of less sample volume for precious biological samples and more cohesive workflow that minimizes the errors between running different assays for different proteins. Use of miniaturized microfluidics not only helps in reducing use of high sample volume but also helps in minimizing the assay reagent costs, assay times and detection processing times.[17] There is additional need for a clinical device that is inexpensive, fast, reliable, accurate, and user friendly. Possibility of automated liquid handing in microfluidics is an attractive candidate in developing multiplexed immunoarrays as compact diagnostic platforms for resource poor settings.[18]

Microfluidics assists control of fluid reagents within a closed environment with small sample size that carryout reactions and detection with ease, high sensitivity, low operations cost, short analysis time and portability.[19] Microfluidics has been explored in many fields like chemical synthesis,[20] high throughput biological assays,[21] PCR-based DNA analysis,[22] DNA toxicity studies,[23,24] Proteomics[25] and diagnostic assays.[26,27,8] Even with such unique benefits and its multi-disciplinary applications traditional microfluidic manufacturing methods like soft lithography and

sometimes injection molding requires longer prototyping times, specialized skills and specialized equipment which are often not readily available.[28,29,30] We have previously developed such microfluidic devices using simple machining and molded or precision cut microfluidic channels for detection of cancer biomarkers from serum samples. We demonstrated detection of multiple biomarkers simultaneous in such devices using both amperometry[31,32] and electrochemiluminescent (ECL)[33] arrays.[34] Both the approaches successfully demonstrated use of nanostructured electrode surface as detection platform and nanoparticles as detection probes for ultrasensitive detection of multiples proteins with shorter assays times of ~30-40 minutes.[31,32,35] Reducing prototyping costs and array development times along with increasing production scale might lead to faster translation of such diagnostic tools to public health care market.[36]

Three-dimensional (3D) printing of bioanalytical devices can significantly reduce cost and time of prototyping.[37] Current availability of inexpensive bench-top 3-D printers and materials provides great resource for ease of fabrication at much faster pace without need for sophisticated manufacturing facilities.[38] The accessibility of easier consumer technology with 3-D printers and its effortless use in creating custom objects by non experts is creating a shift in paradigm of additive manufacturing in various fields.[39] Some of the applications in bio-analytical field for manufacturing fluidic devices include producing masters for making channels from poly(dimethylsiloxane)(PDMS),[40] reaction ware for chemical synthesis,[41] milli- and microfluidic arrays for nanoparticles synthesis[42,43,44] and metal ion monitoring using flow injection devices.[45] Several sensors and sensor accessories have been printed for detection of food allergens,[46] albumin testing in urine,[47] blood component evaluation,[48] single DNA molecule sizing,[49] and pathogenic bacteria.[50] Since past 2 years we reported use of desktop 3-D printed microfluidic devices based on fused deposition modeling (FDM) and stereolithographic (SLA) 3-D printers for several

sensing purposes and cancer diagnostics. We showcased use of FDM printer based fluidic devices in nanoparticle synthesis and sensitive amperometric sensing of hydrogen peroxide,[44] gravity flow assisted microfluidic immunosensor for detection of prostate cancer biomarkers.[51] SLA printed optically transparent microfluidic sensors were explored for Chemiluminescence (CL) based cancer biomarker detection[52] and Electrochemiluminescence (ECL) based DNA sensors.[53]

Automation along with microfluidics could provide an excellent opportunity to reduce operator errors with simplified assay protocols.[35,54] Currently immunoassays suffer from lack of automation thus require multiple operations by the user to either load or pipette sample or reagent to complete the assay. Significant efforts are essential to achieve streamlining of several steps of immunoassays like adding blocking reagents, sample, wash reagents and detections labels automatically. Such automation efforts could lead to faster translation of immunoassays for better health care and point of care use.[55,56] In order to be most effective point of care devices must be rapid, reproducible with very low device failure rates and able to be operated by technicians with minimal training and operator attention.[57,58] We previously demonstrated ECL based fully automated, microprocessor controlled, microfluidic arrays with reagent/sample loading cassette to complete detection of multiple prostate cancer biomarkers in serum samples. These arrays utilize detection antibody-coated $Ru(bpy)_3^{2+}$ (RuBPY)-doped silica nanoparticles for detection of 4 biomarkers simultaneously on a single wall carbon nanotube forest patterned pyrolytic graphite chip.[35] While we were successful in getting absolute automation until detection step with ultrasensitive detection limits of 10-100 fg mL^{-1} the size of whole immunoarray, sample/reagent volume and assay times were relatively high and thus need to be addressed for achieving futuristic personalized point of care applications.

Here we present a compact packaged (3cm x 4cm x 0.3cm) simple 3-D printed microfluidic array that promises simultaneous and automated detection of two prostate cancer biomarker proteins within 18 min assay time for under $1. Our developed method does not require exclusive training to be operated and require ultralow sample volumes less than 1 µL for diluted sample analysis. Total volume of reagent and sample chambers are 20 ± 2 µL. We were able to run multiple immunoarrays at a time using programmable multi syringe pump. This results in total assay time of 18 minutes for 4 different samples, Figure 4-1. To our knowledge this is the first report of ECL based compact 3-D printed array with ultralow sample volume for detection of multiple cancer biomarkers in serum samples. We demonstrated sensitive detection of two proteins on a nanostructures surface using RuBPY silica nanoparticle coated with detection antibodies as label with detection limits of 150 - 230 fg mL^{-1}. Validation assays on human serum samples from prostate cancer patients showed good correlation with standard single protein ELISA. ROC curves for the patient sample analysis showed PSMA can be used to increase the predictive power of distinguishing the cancer vs cancer free human serum samples.

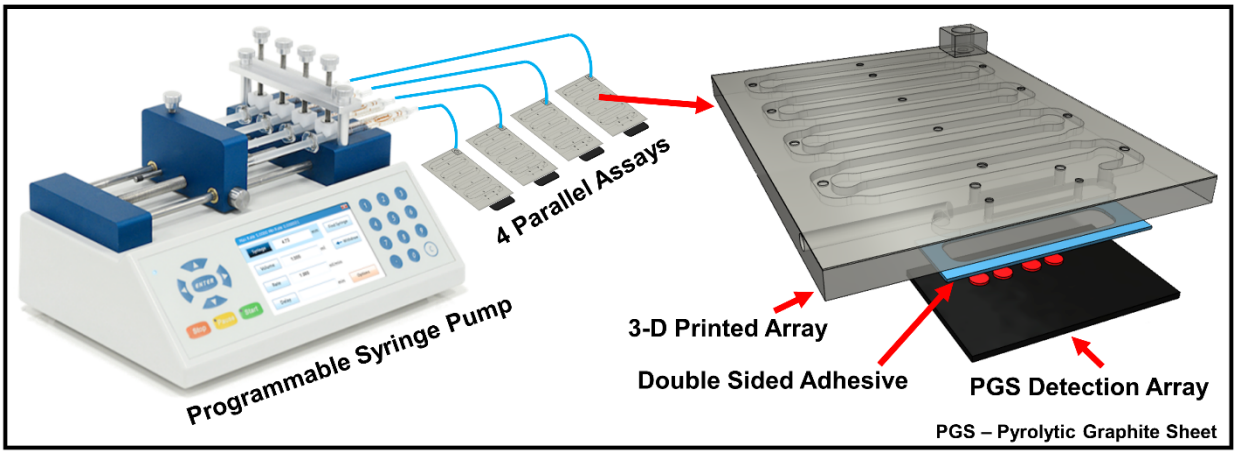

Figure 4-1. Concept image with programmable pump performing four parallel immunoassays on 3-D printed microfluidic immunoarray and 3-D model of the simple and compact immunoarray attached to the pyrolytic graphite sheet (PGS) detection array via double sided adhesive.

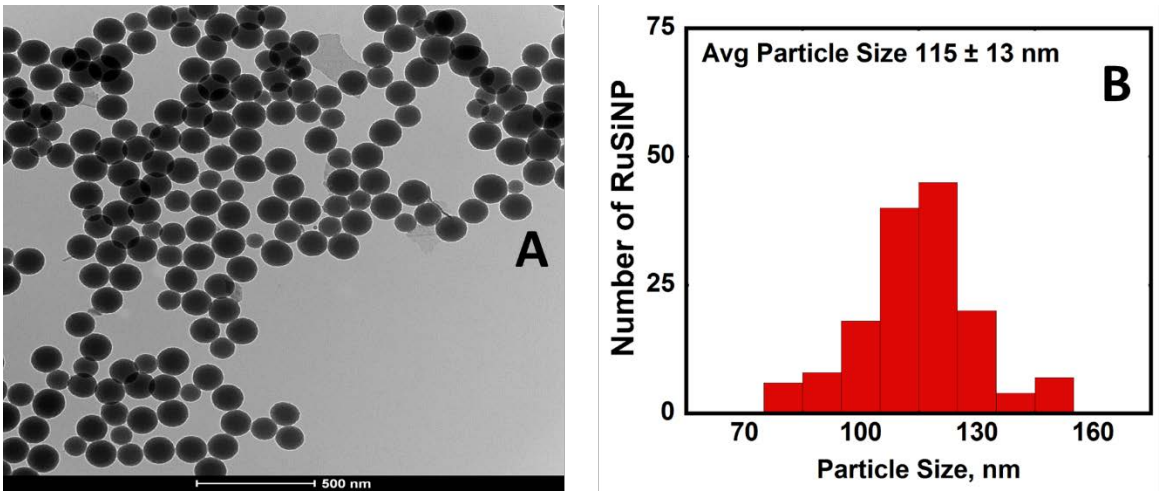

Figure 4-2. (A) TEM image of RuBPY-silica nanoparticles on a 500 nm scale bar. (B) Size distribution of RuBPY silica nanoparticles with an average diameter of 115 ± 13 nm.

4-3. Experimental

4-3.1 Materials. Thin pyrolytic highly oriented graphite sheets (PGS) were obtained from Panasonic Industrial Devices and Solutions. Clear resin (GCPL02) from Formlabs (Somervlle, MA). PSA capture antibodies (M0-T40081A), detection antibodies (M0-T40081B), PSMA capture antibodies (MO-T40086A) and detection antibodies (MO-T40086B) from Anogen. Standard PSA protein (P3235) from Sigma-Aldrich and PSMA standard protein from Novus Biologicals. Single protein ELISA kits for PSA (RAB0331) from Sigma-Aldrich and for PSMA (EL008782HU-96) from Lifeome Biolabs/Cusabio. Human serum samples were obtained from George Washington University Hospital. RuBPY silica nanoparticles used as detection labels were synthesized in our lab as described previously[34] with average diameter of 115 ± 13 nm (Figure 4-2) further coated with layers of polydiallyldimethylammonium chloride (PDDA) and poly(acrylic acid) (PAA) and were then covalently linked to secondary antibodies (Ab2) using 1-(3-(Dimethyla- mino)propyl)-3-ethylcarbodiimidehydrochloride (EDC) and N-

hydroxysulfosuccinimide (NHSS) as described previously.[34] RuBPY-Silica detection nanoparticles were decorated with two different types of antibodies, PSA (PSA-Ab2) and PSMA (PSMA-Ab2). Optimized Ab_2 concentrations of 8 µg mL^{-1} for both PSA and PSMA was used to make the RuBPY-SiNP- Ab_2 conjugate. The Ab_2 / RuBPY –SiNP ratio was measure at 38:1 as shown previously.[51] All immunoreagents were dissolved in pH 7.2 phosphate buffered saline (PBS). Co-reactant solution to develop ECL was 500 mM tripropylamine (TrPA) with 0.05% Tween-20 (T20) and 0.05% Triton-X in 0.2 M phosphate buffer.

The immunoarray was 3D printed on a Form 1+ SLA printer from Formlabs (Somerville, MA). Initially a computer aided design (CAD) with required features were generated using 123D design software (Autodesk), Figure 1 and later converted to 3-D printed splicing software preform to make a print file. Later the preform file with 3-D design was subjected to selected optimized orientation and generated supports to produce final print file. The print orientation was adjusted onto the build platform so that the reagent chambers in the array are longitudinal while printing, this allowed the channels to flush the resin automatically through the reagent loading port holes. This also allowed us to get reproducible prints with no defects and also made easier for post treatment process. The layer height was selected to be 50 µM that gave us faster prints without sacrificing the print quality and resolution. The printed arrays were then removed from the build platform, supports were removed, submerged into isopropanol and subjected to sonication for 15 min to remove any uncured resin present on the outside or inside of the array. The dried arrays were then spray coated with clear acrylic spray (Krylon™) and allowed to air dry for an hour to adjust the transparency to clear for ECL detection.

Microfluidic immunoarray features a unibody design with microfluidic channels that act as chambers to hold reagents and sample for immunoassay. The immunoarray is 3 cm x 4 cm x 0.3

cm in dimensions with 1 inlet port, 1 outlet, 8 chambers inside the array and 1 chamber that is open, present outside at the bottom of the array for electrode attachment, Figure 4-3 A&B. This design allowed us to have the detection chamber complete once sealed with a detection array, thus eliminating need for silicone gasket or PDMS channels. Dimensions of reagent/sample chambers were (Length x Width x Height) 18 mm x 2.5 mm x 0.5 mm, for the detection chamber (L x W x H) were 12 mm x 2.8 mm x 0.5 mm. Out of 8 chambers inside the immunoarray starting from the inlet, chamber 1 and 2 were designated for wash buffer (PBS buffer with 0.05% Tween-20, pH 7.4) followed by air gap chamber 3 to avoid intermixing of reagents. The 4^{th} chamber was designated for RuBPY Si-NP-Ab_2 ECL label, followed by air gap chamber 5. 6^{th} chamber was designated for wash buffer (PBS buffer, pH 7.4) followed by air gap chamber 7. The last chamber, was designated for sample which is right next to detection chamber that was placed downstream at the bottom of the array to facilitate attachment of detection array. Total volume of reagent chambers was 20 ± 2 μL, having very tiny turn to connect to the detection chamber allowed us to have tiny or no dead volume making the detection chamber volume to be slightly less than 20 μL.

The reagents/sample were added through a 0.8 mm hole present at the top of the reagent chamber. We call them injection ports and we also assembled few more ports called vent holes between each turns to facilitate reproducible filling of the chambers, Figure 4-3A & B. The holes on the both ends of the chambers in the turns helps to fill the chambers evenly without choosing a direction. As we are dealing with tiny volume in a confined space, the added reagents will replace the air in the chamber. These vent holes near the ends of each chamber pushes the air out of the chambers as the liquids enter the chamber resulting precise addition of reagents. This is rather an important part of our design and we optimized the position of these vent holes for precision of reagent/sample loading. This also ensured better control over automated reagent delivery to

detection chamber. We used calibrated micropipettes to add the reagents/samples into their respective chambers prior to immunoassay. The detection chamber was equipped with holes and grooves to hold 0.4 mm platinum counter electrode wire and 0.6 mm Ag/AgCl reference electrode wire that run parallel within the detection chamber to complete a 3 electrode setup with pyrolytic graphite sheets as working electrodes.

4-3.2 Detection platforms were prepared from highly conductive, flexible, inexpensive pyrolytic graphite sheets (PG sheets). The PG sheets were initially cut to desired size and placed on adhesive plastic support followed by patterning with microwells using print and peel technology[59] developed in our lab. Microwells formed by hydrophobic toner boundaries allowed us to build single wall carbon nanotube tube (SWCNT) forest[60,61] within them using tiny volumes of reagents. Our detection platforms features 4 microwells with diameter of 1 mm, designated 2 each for PSA and PSMA detection. The template for the 4 microwells were designed using Inkscape software and the pattern was inkjet printed onto glossy paper (Avery ™ 5263) followed by transferring them onto PG sheets via heat press for 60 s at 275 °C. Patterned microwell PG sheet array with SWCNT forest and detection antibody (Ab_1) were then attached onto the 3D printed array using a double sided adhesive. The presence of dense SWCNT forests were confirmed by tapping mode atomic force microscopy previously showing vertically aligned SWCNT forest with increased surface roughness.[34,35] The carboxyl terminal SWCNT's were further activated with 400mM EDC + 100mM NHSS to conjugate primary/capture antibody (Ab_1) by amidization.[62,34]

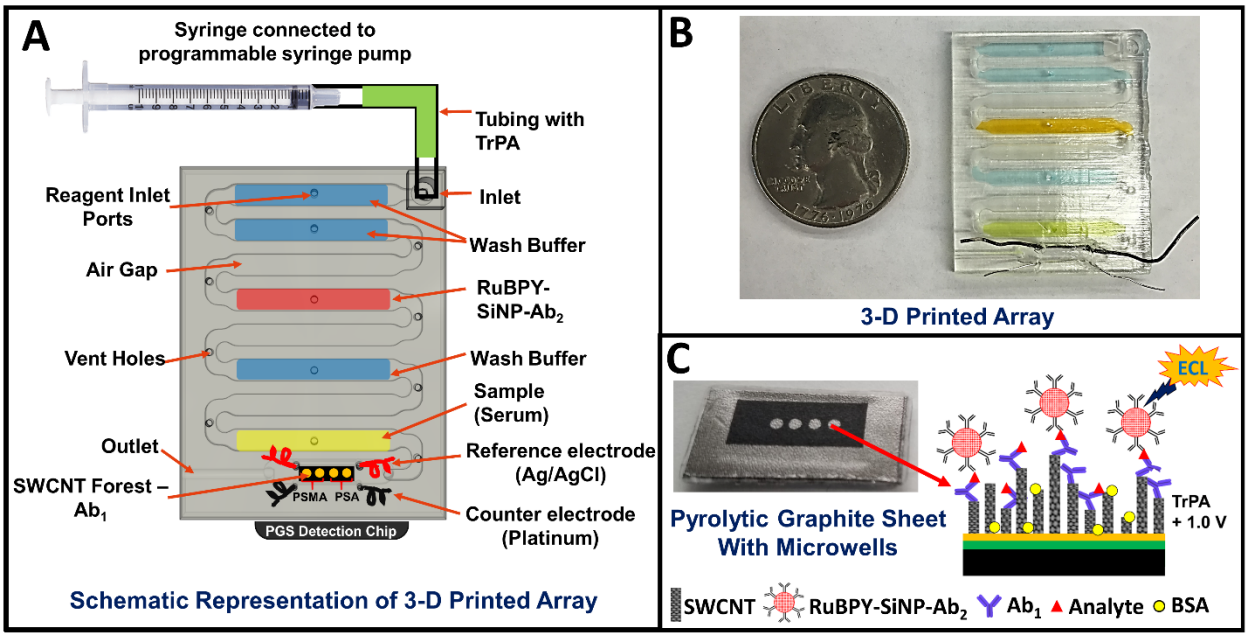

Figure 4-3. Schematic representation of 3-D printed array and Sandwich immunoassay. (A) 3-D printed microfluidic array with reagent chambers designated for sample/analyte, wash buffers, detection label and co-reactant for ECL generation connected to detection platform with pyrolytic graphite detection chip. Programmable pump connected to the microfluidic array via inlet port to sequentially deliver chamber contents to complete the sandwich immunoassay. (B) Image of 3-D printed microfluidic array and fluidic chambers filled with colored food dyes for representation. (C) Disposable pyrolytic graphite sheet with microwells formed by hydrophobic toner print. Insert showing sandwich immunoassay on a single wall carbon nanotube forest (SWCNT).

4-3.3 Immunoassay protocol. SWCNT and Ab1 modified detection platform were attached to 3-D printed array via a precut double sided adhesive. The 3-D printed array was prefilled with reagents and sample through the injection ports to each of the chambers as mentioned earlier. The injection ports and vent holes are then sealed with one-sided transparent scotch tape to make an airtight continuous channel too deliver the reagent sequentially to detection chamber. A flexible

tubing was then inserted into the inlet port of the 3-D printed array and connected to BD Plastic 4.78 mm, 1mL syringe via a luer adaptor. Prior to inserting the tubing into the inlet, 100 µL of 500 mM tripropylamine (TrPA) in 0.2 M phosphate buffer + 0.05% Tween-20 and 0.05% triton-X at pH 7.5 was drawn into the tubing. Excess TrPA was used for additional washing and as co-reactant for ECL generation. Syringe was then placed into a Chemyx Fusion Touch programmable syringe pump that has a three step program loaded. Sample incubation, Label incubation followed by washing and delivery of TrPA. Initial pump cycle at 90 µL/min, delivers 27 µL volume (includes initial pressure buildup delay, slight dead volume and 20 µL sample) to the detection chamber. Program delayed for 8 minutes to allow the sample to incubate on the array. Second pump cycle, delivers 130 µL of volume to wash the array to flush the unreacted sample and leave the detection antibody decorated RuBPY silica nanoparticles on the surface of the detection platform for 7 minutes. Finally 600 µL pump cycle to wash the unreacted detection label and fill the detection chamber with TrPA ECL generation. The immunoarray was then placed under the CCD camera and a potential of 1.0 V was applied vs Ag/AgCl with a handheld potentiostat to generate ECL for 180 s. TrPA in detergent solution as co-reactant allows use of 1.0 V vs Ag/AgCl to oxidize TrPA. This electrochemical oxidation only TrPA enhances production and deprotonation of $TrPA^{*+}$ to drive complex redox process that generates electronically excited $[RuBPY]^{2+*}$ for ECL.[63,61] Acquired ECL images were then processed to get ECL intensities.[34]

4-4. Results

4-4.1 Reproducibility. Relative ECL responses captured by CCD camera from the 3-D printed immunoarray with three trails of controls (undiluted calf serum) and 1 pg mL^{-1} PSMA showed an average relative standard deviation (RSD) of 8 % for spot to spot (n=4) and 6 % for array to array

(n=3). For single protein analysis all the four sensors on the detection PG chip were coated with either PSA or PSMA capture antibodies and the detection label has either PSA or PSMA detection antibodies. Initially the 3-D printed arrays were calibrated by developing single protein calibration curves where increase in ECL responses were observed with increase in concentration of the respective analyte. Obtained ECL signal intensities from CCD camera for different analyte concentrations were further processed by dividing with ECL intensity obtained from control to get relative ECL intensity. Relative ECL intensities were plotted against concentration as show in Figure 4-4.

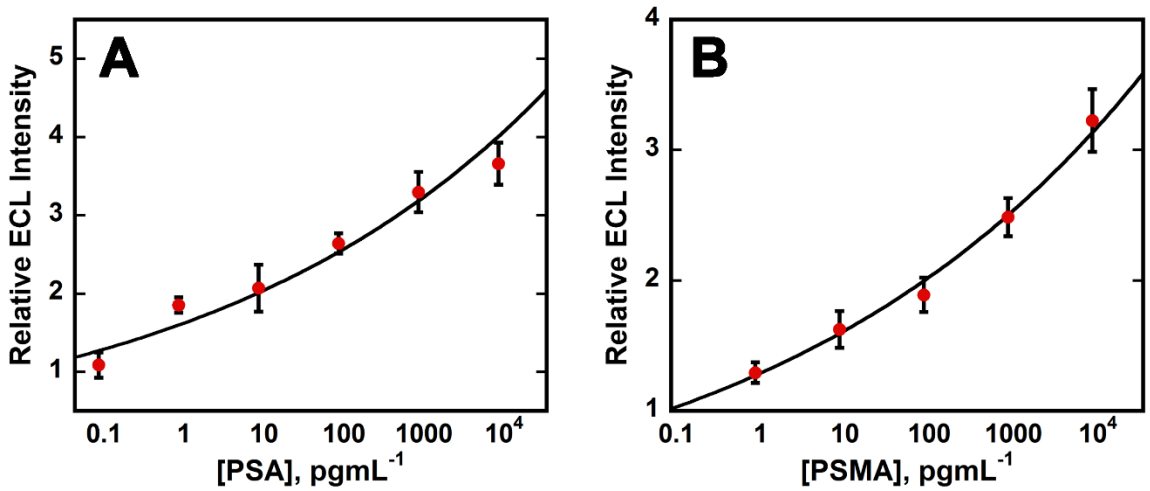

Figure 4-4. Calibration curves in undiluted calf serum with ECL responses captured over 180 s, A) PSA and B) PSMA vs concentration with applied ECL generation potential of 1V vs. Ag/AgCl. Error bars show standard deviation, n=4.

4-4.2 Multiplexed detection. PSMA and PSA were simultaneously detected by using a mixture of standard concentrations of PSA and PSMA in undiluted calf serum. Out of four sensors/microwells on the detection chip, first two sensors were coated with PSMA capture antibodies and the last two sensors were coated with PSA capture antibodies as shown in Figure

4-3 A. The detection label has both PSA and PSMA detection antibodies coated on the RuBPY SiNP. Specific capture antibodies were coated on the single wall carbon nanotube decorated detection sensor wells for 2.5 hours at room temperature followed by adding 2% BSA as a blocking agent to avoid nonspecific binding. The mixture of standard protein samples were then allowed to flow from analyte/sample chamber and incubated for 8 minutes followed by washing with 10 mM PBS buffer, 7.4 pH. Multiplexed detection label, RuBPY SiNP was then flowed on to the detection sensors from reagent chamber and allowed to incubate for 7 minutes, followed by washing with 10 mM PBS and PBS T20 buffer, pH 7.4 from the prefilled chambers. The ECL responses were then captured by CCD camera when 1.0 V vs. Ag/AgCl was applied from a handheld potentiostat and signal was accumulated for 180 s. Obtained ECL responses were further processed as explained earlier to get relative ECL intensities, that were plotted against concentrations to get multiplexed calibration curves as shown in Figure 4-5.

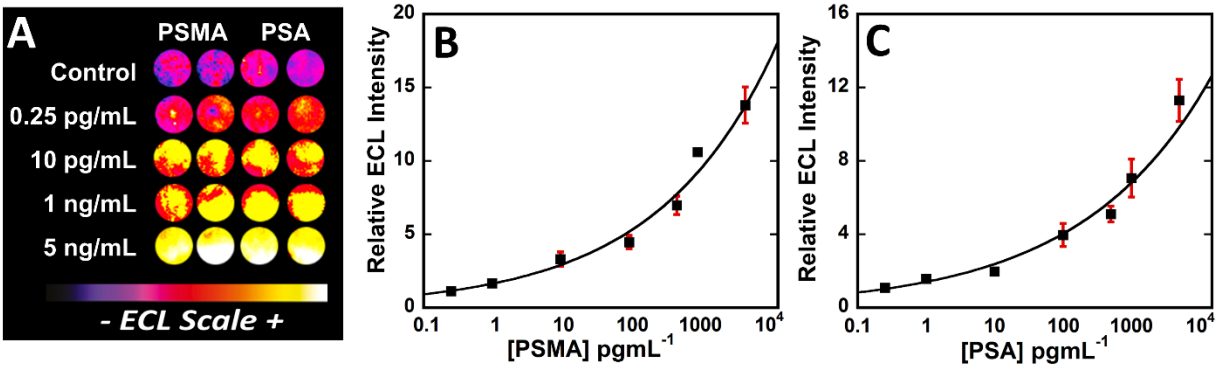

Figure 4-5. Calibration data for multiplexed detection of PSMA and PSA simultaneously in undiluted calf serum with ECL responses integrated over 180 s at 1.0 V vs Ag/AgCl. (A) Recolorized CCD images of 5 arrays showing increase in ECL response with increase in concentration for both PSMA and PSA on a single array. Influence of ECL responses with increase in concentrations for (B) PSMA and (C) PSA, error bars show standard deviation, n=4.

Recolorized CCD images from Figure 4-5A shows ECL responses with increase in concentrations of mixture of proteins (PSMA and PSA). ECL response obtained for specific concentrations were divided with controls and obtained relative ECL intensities were plotted against concentration to get multiplexed calibration curves as show in Figure 4-5B & C. Dynamic range from 250 fg mL^{-1} to 5 ng mL^{-1} was obtained for both the proteins with detection limit of 150 fg mL^{-1} for PSA and 230 fg mL^{-1} for PSMA. Detection limit was measures at 3 times standard deviation of signal from 0 pg mL^{-1} protein control.

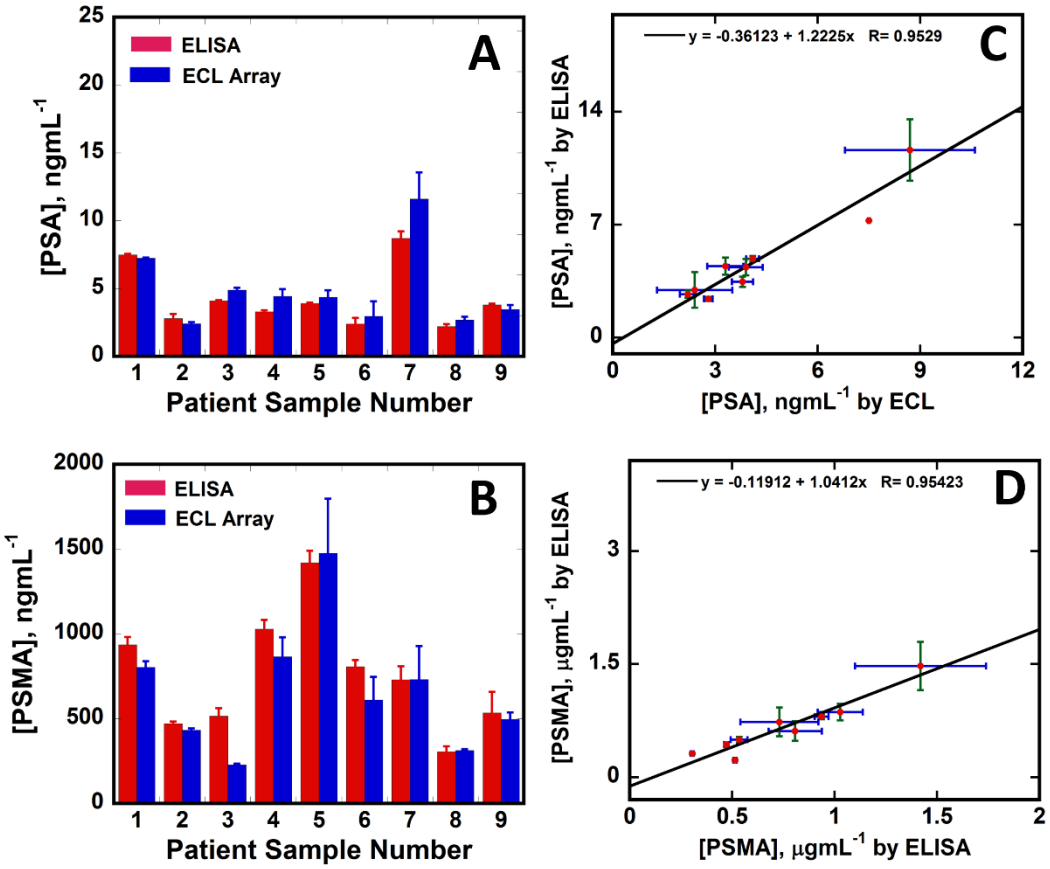

Figure 4-6. Elisa vs ECL immunoarray comparison results for 9 patient human serum samples. Bar graph showing ECL vs ELISA results for (A) PSA and (B) PSMA. Linear correlation plots for (C) PSA and (D) PSMA. Error bars are standard deviations with n=4 for ECL and n=3 for ELISA.

4-4.3 Patient Sample Analysis. 32 cancer patient samples and 6 cancer free individual samples were analyzed using our 3-D printed array. 9 patient samples were compared with gold standard single protein ELISA for both PSA and PSMA to establish the correlation between the two methods. Considering the dynamic range of the calibration curves, patient and cancer free individual samples were diluted from 100-500 fold in undiluted calf serum prior to analysis to bring the ECL responses to acceptable range. Obtained ECL immunoarray responses were corresponded well with ELISA results as shown in Figure 4-6. Linear correlation plots, Figure 4-6 C&D with slopes close to 1.0, PSA 1.22 ± 0.14 and for PSMA 1.04 ± 0.12 whereas intercepts were close to zero, -0.36 ± 0.70 and -0.12 ± 0.10 suggest a good correlation between our automated ECL immunoarray and ELISA.

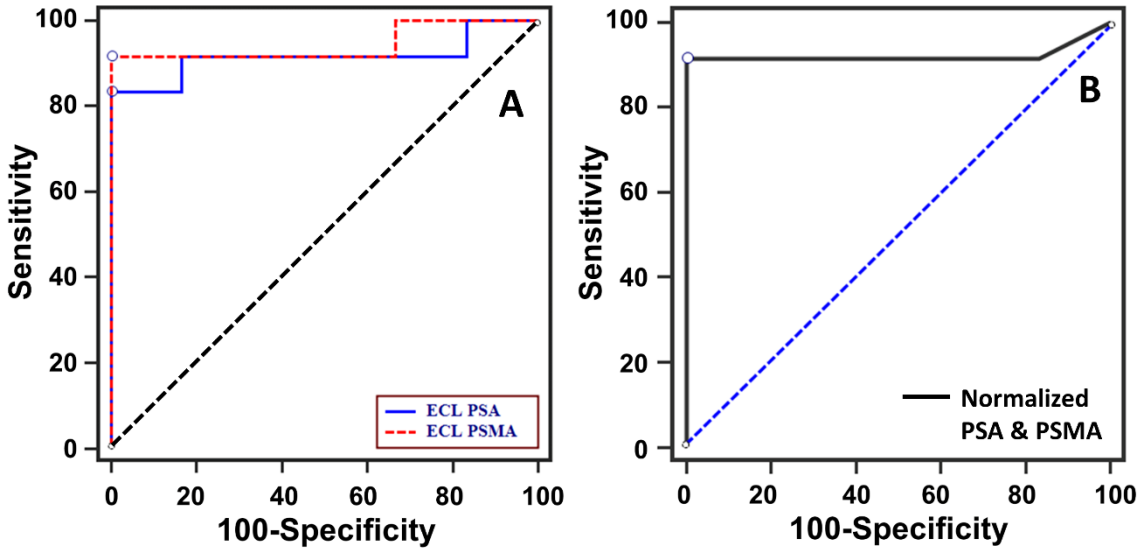

Figure 4-7. Receiver operating characteristic curves (ROC) for 18 human serum samples. (A) Red line for PSMA and Blue line for PSA shows AUC to be 0.92 for PSA, 100 % specificity and 83.3 % sensitivity and for PSMA, AUC was calculated to be 0.94, 100 % specificity and 91.7 % sensitivity. (B) Normalized PSA and PSMA results suggest 0.92 AUC, 100 % specificity and 91.7 % sensitivity.

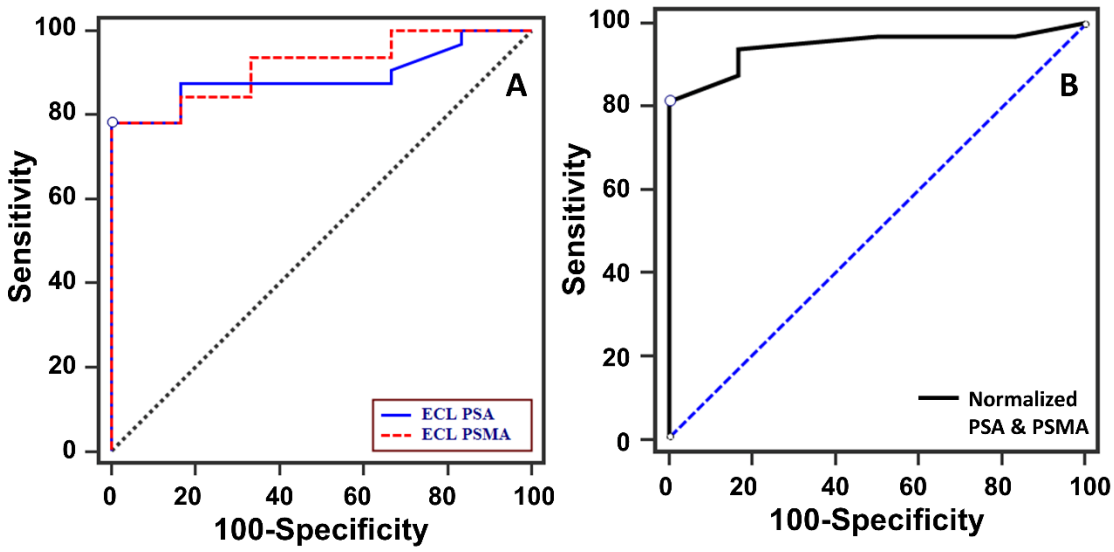

Figure 4-8. Receiver operating characteristic curves (ROC) for 38 human serum samples. (A) Red line for PSMA and Blue line for PSA shows AUC to be 0.89 for PSA, 100 % specificity and 78.1 % sensitivity and for PSMA, AUC was calculated to be 0.92, 100 % specificity and 78.1 % sensitivity. (B) Normalized PSA and PSMA results suggest 0.95 AUC, 100 % specificity and 81.3 % sensitivity.

Receiver operating characteristic (ROC) plots were utilized to predict the diagnostic accuracy for 12 patient samples and 6 cancer free individual samples for which Gleason score were available, Figure 4-7. For the rest of the 20 patient samples ROC analysis was performed assuming them to be cancer patient samples as Gleason score data was not available, Figure 4-8. In ROC analysis the true positive rate (sensitivity) was plotted against false positive rate (specificity). In an ideal scenario the test with perfect discrimination between cancerous and cancer free samples has an ROC curve that passes through the upper left corner with 100 % sensitivity and 100 % specificity.[64] The area under the curve from ROC analysis helps to quantify the ability of the test to distinguish between healthy individuals and individuals with diseased state. If the observed data has zero false positives and zero false negatives the area under the curve will be 1.0. ROC analysis for PSA show AUC to be 0.92 with specificity to be 100 % and sensitivity to be 83.3 % whereas

for PSMA AUC was 0.94 with 100 % specificity and 91.7 % sensitivity. Normalized mean ROC values for combined PSA and PSMA for 18 human serum samples were 0.92 for AUC with 100 % specificity and 91.7 % sensitivity. Normalized values showed slightly improved sensitivity. Associated criteria for cancer vs non cancer based on the obtained sensitivity and specificity values for PSA > 2.7 ng mL^{-1} and for PSMA > 86 ng mL^{-1}. Normalized mean ROC values for combined PSA and PSMA for 38 human serum samples were 0.95 for AUC with 100 % specificity and 81.3 % sensitivity. Normalized values showed slightly improved AUC and similar specificity.

4-5. Discussion

Results achieved using our low cost, automated, 3-D printed array show simultaneous detection of both PSA and PSMA in complex serum matrix that contains thousands of other proteins.[65] Our goal was to detect ultralow levels of prostate cancer biomarkers within 20 min assay time and low sample volume on a compact 3-D printed fluidic array. Utilizing 3-D printing we established rapid prototyping of transparent miniaturized immunoarrays with microfluidic structures of dimensions 500 microns resulting in the use of low sample/reagent volumes. We arranged the reagent reservoirs on the same microfluidic array, Figure 4-3A that allows their sequential pumping to the detection sensor to complete the sandwich assay. Non-complex layout of our sample/reagent chambers in a confined space allowed greater control of all immunoreagents to reach downstream detection sensor efficiently. Programmable pump allowed precise control on timing the pumping events either ON/OFF to deliver or wash off immunoreagnets to facilitate incubation and washing excess reagents with minimal user interference. Use of small portable programmable pump that has non-complex operations with total assay cost of 0.75 $ with detection

limits in low fg mL^{-1} for reliable detection of two markers in complex serum matrix makes it an ideal candidate for its application in resource poor settings.

Detection limits of 150 fg mL^{-1} for PSA and 230 fg mL^{-1} for PSMA was achieved with dynamic ranges extending from 250 fg mL^{-1} to 5 ng mL^{-1} for both the proteins, Figure 4-5. These dynamic ranges are acceptable and matches to the clinical ranges of selected proteins in assay within 500X dilution eliminating the need for excessive serial dilutions. The relative standard deviations ranged from 2 to 11 % for both the proteins between all the assayed concentrations. Good repeatability was obtained in reproducibility assays performed with controls and 1 pg mL^{-1} concentration of PSMA. We found acceptable standard deviations of 8% (n=4) in spot to spot variability and 6% between assays (n=3) for the defined concentration.

ECL immunoarrays were validated by accurately measuring both PSA and PSMA in 38 human serum samples further compared to standard single protein ELISA. Comparison studies between our immunoarray results and ELISA for human serum samples showed very good correlation, Figure 4-6. Quantifying both PSA and PSMA in full serum matrix accurately demonstrated high selectivity and specificity of our immunoarray. ROC curves from the human serum sample data suggest that both PSA and PSMA as serum protein markers have diagnostic potential in differentiating the cancer vs Non-cancerous individual with 100 % specificity and 83 % - 92 % sensitivity.

3-D printing allowed us to achieve compact design with both reagent chambers and detection channels on the same array. This allowed us to eliminate any external tubing for connectivity and leaking issues. Adding detection channel very close to sample chamber allowed us to eliminate dead volumes that usually comes with the connectors. Efficient transfer of sample/reagents sequentially as intended with optimized times results in reproducible ECL

responses. Using this parallel alignment of fluidic chambers with optimized minimal distances resulted in rapid completion of assays. Pyrolytic graphite sheets were used as an alternative for traditionally used bulky expensive pyrolytic graphite chip or screen printed carbon electrodes. These pyrolytic graphite sheets are inexpensive, disposable, robust, highly conductive and can withstand harsh organic solvent conditions. This enabled us to grow our nano-structured surface single walled carbon nanotubes forest on the surface for much efficient coating of capture antibody that in turn facilitated high capture efficiency of selective proteins from the serum. The PG sheets costs 6 $ for a 7 inch X 5 inch sheet with thickness of 0.0028 inch. These extremely flexible and tough PG sheets can make up to 75 detection sensor chips with 4 detection spots on each of them costing only 8 cents per array. 3-D printing costs 0.40 $ in materials to print our 3-D printed immunoarray. Including all the immunoreagents the total cost per assay is just 0.75 $. Our compact design plan made them disposable arrays that leave a low ecological foot print. Our arrays are reusable, assuming the 3-D printed devices are not disposed and used for multiple assays the cost per assay comes down to as low as 35 cents.

4-6. Summary

In summary we demonstrated use of inexpensive desktop stereolithographic 3-D printer that can fabricate compact microfluidic array that is optically transparent for ECL detection. Our immunoarray is low cost and portable with sensitive and selective detection of two prostate cancer biomarkers from human serum samples. Using commercially available programmable pump we automated the complex immunoassay process to be easily operated with minimal manual interference. The assay is cost effective and rapid with good detection limits and dynamic ranges that are acceptable for clinical analysis. Our fabrication methods enabled our assays as print and

go method. We minimized the complex operations of microfluidic immunoassay where there is need for mixing units, connectors, valves etc. Our print and go method just requires a 3-D printed fluidic device with prefilled immunoreagents, followed by simply attaching capture antibody coated PG sheet via a double sided adhesive and connected to a preprogrammed syringe pump. In principle this device can be extended to many other disease related markers and multiple markers at a time with few changes in the array fabrication.

4-7. References

1. http://www.cancer.org/cancer/prostatecancer/detailedguide/prostate-cancer-key-statistics , Accessed April, 2017.
2. Smith, R. A.; Cokkinides, V.; Brawley, O. W. Cancer screening in the United States, 2012. *CA: a cancer journal for clinicians* **2012**, *62*, 129-142.
3. Barry, M. J. Prostate-specific–antigen testing for early diagnosis of prostate cancer. *N. Engl. J. Med.* **2001**, *344*, 1373-1377.
4. Ward, A. M.; Catto, J.; Hamdy, F. Prostate specific antigen: biology, biochemistry and available commercial assays. *Ann. Clin. Biochem.* **2001**, *38*, 633-651.
5. Hawkridge, A. M.; Muddiman, D. C. Mass spectrometry–based biomarker discovery: toward a global proteome index of individuality. *Annual Review of Analytical Chemistry* **2009**, *2*, 265-277.
6. Wulfkuhle, J. D.; Liotta, L. A.; Petricoin, E. F. Proteomic applications for the early detection of cancer. *Nature reviews cancer* **2003**, *3*, 267-275.
7. Kingsmore, S. F. Multiplexed protein measurement: technologies and applications of protein and antibody arrays. *Nature reviews Drug discovery* **2006**, *5*, 310-321.
8. Rusling, J. F.; Kumar, C. V.; Gutkind, J. S.; Patel, V. Measurement of biomarker proteins for point-of-care early detection and monitoring of cancer. *Analyst* **2010**, *135*, 2496-2511.
9. Ghosh, A.; Heston, W. D. Tumor target prostate specific membrane antigen (PSMA) and its regulation in prostate cancer. *J. Cell. Biochem.* **2004**, *91*, 528-539.
10. Caromile, L. A.; Dortche, K.; Rahman, M. M.; Grant, C. L.; Stoddard, C.; Ferrer, F. A.; Shapiro, L. H. PSMA redirects cell survival signaling from the MAPK to the PI3K-AKT

pathways to promote the progression of prostate cancer. *Sci. Signal.* **2017**, *10*, 10.1126/scisignal.aag3326.

11. Xiao, Z.; Adam, B. L.; Cazares, L. H.; Clements, M. A.; Davis, J. W.; Schellhammer, P. F.; Dalmasso, E. A.; Wright, G. L.,Jr Quantitation of serum prostate-specific membrane antigen by a novel protein biochip immunoassay discriminates benign from malignant prostate disease. *Cancer Res.* **2001**, *61*, 6029-6033.
12. Murphy, G.; Ragde, H.; Kenny, G.; Barren, R.,3rd; Erickson, S.; Tjoa, B.; Boynton, A.; Holmes, E.; Gilbaugh, J.; Douglas, T. Comparison of prostate specific membrane antigen, and prostate specific antigen levels in prostatic cancer patients. *Anticancer Res.* **1995**, *15*, 1473-1479.
13. Wang, J. Electrochemical biosensors: towards point-of-care cancer diagnostics. *Biosensors and Bioelectronics* **2006**, *21*, 1887-1892.
14. Cox, K. L.; Devanarayan, V.; Kriauciunas, A.; Manetta, J.; Montrose, C.; Sittampalam, S. In *Immunoassay Methods;* Sittampalam, G. S., Coussens, N. P., Brimacombe, K., Grossman, A., Arkin, M., Auld, D., Austin, C., Baell, J., Bejcek, B., Chung, T. D. Y., Dahlin, J. L., Devanaryan, V., Foley, T. L., Glicksman, M., Hall, M. D., Hass, J. V., Inglese, J., Iversen, P. W., Lal-Nag, M., Li, Z., McGee, J., McManus, O., Riss, T., Trask OJ, J., Weidner, J. R., Xia, M. and Xu, X., Eds.; Assay Guidance Manual; Bethesda (MD), 2004; .
15. Haeberle, S.; Zengerle, R. Microfluidic platforms for lab-on-a-chip applications. *Lab on a Chip* **2007**, *7*, 1094-1110.
16. Fernandes, T. G.; Diogo, M. M.; Clark, D. S.; Dordick, J. S.; Cabral, J. M. High-throughput cellular microarray platforms: applications in drug discovery, toxicology and stem cell research. *Trends Biotechnol.* **2009**, *27*, 342-349.

17. Schroeder, H.; Adler, M.; Gerigk, K.; Müller-Chorus, B.; Götz, F.; Niemeyer, C. M. User configurable microfluidic device for multiplexed immunoassays based on DNA-directed assembly. *Anal. Chem.* **2009**, *81*, 1275-1279.

18. Sia, S. K.; Linder, V.; Parviz, B. A.; Siegel, A.; Whitesides, G. M. An Integrated Approach to a Portable and Low-Cost Immunoassay for Resource-Poor Settings. *Angewandte Chemie International Edition* **2004**, *43*, 498-502.

19. Whitesides, G. M. The origins and the future of microfluidics. *Nature* **2006**, *442*, 368-373.

20. Günther, A.; Jensen, K. F. Multiphase microfluidics: from flow characteristics to chemical and materials synthesis. *Lab on a Chip* **2006**, *6*, 1487-1503.

21. Guo, M. T.; Rotem, A.; Heyman, J. A.; Weitz, D. A. Droplet microfluidics for high-throughput biological assays. *Lab on a Chip* **2012**, *12*, 2146-2155.

22. Khandurina, J.; McKnight, T. E.; Jacobson, S. C.; Waters, L. C.; Foote, R. S.; Ramsey, J. M. Integrated system for rapid PCR-based DNA analysis in microfluidic devices. *Anal. Chem.* **2000**, *72*, 2995-3000.

23. Wasalathanthri, D. P.; Malla, S.; Bist, I.; Tang, C. K.; Faria, R. C.; Rusling, J. F. High-throughput metabolic genotoxicity screening with a fluidic microwell chip and electrochemiluminescence. *Lab on a Chip* **2013**, *13*, 4554-4562.

24. Hvastkovs, E. G.; Rusling, J. F. *State-of-the-Art Metabolic Toxicity Screening and Pathway Evaluation* **2016**.

25. Lion, N.; Rohner, T. C.; Dayon, L.; Arnaud, I. L.; Damoc, E.; Youhnovski, N.; Wu, Z.; Roussel, C.; Josserand, J.; Jensen, H. Microfluidic systems in proteomics. *Electrophoresis* **2003**, *24*, 3533-3562.

26. Yager, P.; Edwards, T.; Fu, E.; Helton, K.; Nelson, K.; Tam, M. R.; Weigl, B. H. Microfluidic diagnostic technologies for global public health. *Nature* **2006**, *442*, 412-418.

27. Malhotra, R.; Patel, V.; Chikkaveeraiah, B. V.; Munge, B. S.; Cheong, S. C.; Zain, R. B.; Abraham, M. T.; Dey, D. K.; Gutkind, J. S.; Rusling, J. F. Ultrasensitive detection of cancer biomarkers in the clinic by use of a nanostructured microfluidic array. *Anal. Chem.* **2012**, *84*, 6249-6255.

28. Weibel, D. B.; Kruithof, M.; Potenta, S.; Sia, S. K.; Lee, A.; Whitesides, G. M. Torque-actuated valves for microfluidics. *Anal. Chem.* **2005**, *77*, 4726-4733.

29. Urbanski, J. P.; Thies, W.; Rhodes, C.; Amarasinghe, S.; Thorsen, T. Digital microfluidics using soft lithography. *Lab on a Chip* **2006**, *6*, 96-104.

30. Laksanasopin, T.; Guo, T. W.; Nayak, S.; Sridhara, A. A.; Xie, S.; Olowookere, O. O.; Cadinu, P.; Meng, F.; Chee, N. H.; Kim, J.; Chin, C. D.; Munyazesa, E.; Mugwaneza, P.; Rai, A. J.; Mugisha, V.; Castro, A. R.; Steinmiller, D.; Linder, V.; Justman, J. E.; Nsanzimana, S.; Sia, S. K. A smartphone dongle for diagnosis of infectious diseases at the point of care. *Sci. Transl. Med.* **2015**, *7*, 273re1.

31. Chikkaveeraiah, B. V.; Mani, V.; Patel, V.; Gutkind, J. S.; Rusling, J. F. Microfluidic electrochemical immunoarray for ultrasensitive detection of two cancer biomarker proteins in serum. *Biosensors and Bioelectronics* **2011**, *26*, 4477-4483.

32. Otieno, B. A.; Krause, C. E.; Latus, A.; Chikkaveeraiah, B. V.; Faria, R. C.; Rusling, J. F. On-line protein capture on magnetic beads for ultrasensitive microfluidic immunoassays of cancer biomarkers. *Biosensors and Bioelectronics* **2014**, *53*, 268-274.

33. Forster, R. J.; Bertoncello, P.; Keyes, T. E. Electrogenerated chemiluminescence. *Annual Review of Analytical Chemistry* **2009**, *2*, 359-385.

34. Sardesai, N. P.; Kadimisetty, K.; Faria, R.; Rusling, J. F. A microfluidic electrochemiluminescent device for detecting cancer biomarker proteins. *Analytical and bioanalytical chemistry* **2013**, *405*, 3831-3838.

35. Kadimisetty, K.; Malla, S.; Sardesai, N. P.; Joshi, A. A.; Faria, R. C.; Lee, N. H.; Rusling, J. F. Automated multiplexed ECL Immunoarrays for cancer biomarker proteins. *Anal. Chem.* **2015**, *87*, 4472-4478.

36. Au, A. K.; Bhattacharjee, N.; Horowitz, L. F.; Chang, T. C.; Folch, A. 3D-printed microfluidic automation. *Lab on a chip* **2015**, *15*, 1934-1941.

37. Gross, B. C.; Erkal, J. L.; Lockwood, S. Y.; Chen, C.; Spence, D. M. *Evaluation of 3D printing and its potential impact on biotechnology and the chemical sciences* **2014**.

38. Mathieson, J. S.; Rosnes, M. H.; Sans, V.; Kitson, P. J.; Cronin, L. Continuous parallel ESI-MS analysis of reactions carried out in a bespoke 3D printed device. *Beilstein journal of nanotechnology* **2013**, *4*, 285-291.

39. Morgan, A. J.; San Jose, L. H.; Jamieson, W. D.; Wymant, J. M.; Song, B.; Stephens, P.; Barrow, D. A.; Castell, O. K. Simple and versatile 3D printed microfluidics using fused filament fabrication. *PloS one* **2016**, *11*, e0152023.

40. McDonald, J. C.; Chabinyc, M. L.; Metallo, S. J.; Anderson, J. R.; Stroock, A. D.; Whitesides, G. M. Prototyping of microfluidic devices in poly (dimethylsiloxane) using solid-object printing. *Anal. Chem.* **2002**, *74*, 1537-1545.

41. Symes, M. D.; Kitson, P. J.; Yan, J.; Richmond, C. J.; Cooper, G. J.; Bowman, R. W.; Vilbrandt, T.; Cronin, L. Integrated 3D-printed reactionware for chemical synthesis and analysis. *Nature Chemistry* **2012**, *4*, 349-354.

42. Femmer, T.; Kuehne, A. J.; Wessling, M. Print your own membrane: direct rapid prototyping of polydimethylsiloxane. *Lab on a Chip* **2014**, *14*, 2610-2613.

43. Kitson, P. J.; Rosnes, M. H.; Sans, V.; Dragone, V.; Cronin, L. Configurable 3D-Printed millifluidic and microfluidic 'lab on a chip'reactionware devices. *Lab on a Chip* **2012**, *12*, 3267-3271.

44. Bishop, G. W.; Satterwhite, J. E.; Bhakta, S.; Kadimisetty, K.; Gillette, K. M.; Chen, E.; Rusling, J. F. 3D-Printed Fluidic Devices for Nanoparticle Preparation and Flow-Injection Amperometry Using Integrated Prussian Blue Nanoparticle-Modified Electrodes. *Anal. Chem.* **2015**, *87*, 5437-5443.

45. Su, C.; Hsia, S.; Sun, Y. Three-dimensional printed sample load/inject valves enabling online monitoring of extracellular calcium and zinc ions in living rat brains. *Anal. Chim. Acta* **2014**, *838*, 58-63.

46. Coskun, A. F.; Wong, J.; Khodadadi, D.; Nagi, R.; Tey, A.; Ozcan, A. A personalized food allergen testing platform on a cellphone. *Lab on a Chip* **2013**, *13*, 636-640.

47. Coskun, A. F.; Nagi, R.; Sadeghi, K.; Phillips, S.; Ozcan, A. Albumin testing in urine using a smart-phone. *Lab on a Chip* **2013**, *13*, 4231-4238.

48. Chen, C.; Wang, Y.; Lockwood, S. Y.; Spence, D. M. 3D-printed fluidic devices enable quantitative evaluation of blood components in modified storage solutions for use in transfusion medicine. *Analyst* **2014**, *139*, 3219-3226.

49. Wei, Q.; Luo, W.; Chiang, S.; Kappel, T.; Mejia, C.; Tseng, D.; Chan, R. Y. L.; Yan, E.; Qi, H.; Shabbir, F. Imaging and sizing of single DNA molecules on a mobile phone. *ACS nano* **2014**, *8*, 12725-12733.

50. Lee, W.; Kwon, D.; Choi, W.; Jung, G. Y.; Au, A. K.; Folch, A.; Jeon, S. 3D-printed microfluidic device for the detection of pathogenic bacteria using size-based separation in helical channel with trapezoid cross-section. *Scientific reports* **2015**, *5*, 7717.

51. Kadimisetty, K.; Mosa, I. M.; Malla, S.; Satterwhite-Warden, J. E.; Kuhns, T. M.; Faria, R. C.; Lee, N. H.; Rusling, J. F. 3D-printed supercapacitor-powered electrochemiluminescent protein immunoarray. *Biosensors and Bioelectronics* **2016**, *77*, 188-193.

52. Tang, C.; Vaze, A.; Rusling, J. Automated 3D-printed unibody immunoarray for chemiluminescence detection of cancer biomarker proteins. *Lab on a Chip* **2017**.

53. Bishop, G. W.; Satterwhite-Warden, J. E.; Bist, I.; Chen, E.; Rusling, J. F. Electrochemiluminescence at bare and DNA-coated graphite electrodes in 3D-printed fluidic devices. *ACS sensors* **2015**, *1*, 197-202.

54. Park, M. C.; Kim, M.; Lim, G. T.; Kang, S. M.; An, S. S. A.; Kim, T. S.; Kang, J. Y. Droplet-based magnetic bead immunoassay using microchannel-connected multiwell plates (μCHAMPs) for the detection of amyloid beta oligomers. *Lab on a Chip* **2016**, *16*, 2245-2253.

55. Rusling, J. F. Multiplexed electrochemical protein detection and translation to personalized cancer diagnostics. *Anal. Chem.* **2013**, *85*, 5304-5310.

56. Yager, P.; Edwards, T.; Fu, E.; Helton, K.; Nelson, K.; Tam, M. R.; Weigl, B. H. Microfluidic diagnostic technologies for global public health. *Nature* **2006**, *442*, 412-418.

57. Chin, C. D.; Laksanasopin, T.; Cheung, Y. K.; Steinmiller, D.; Linder, V.; Parsa, H.; Wang, J.; Moore, H.; Rouse, R.; Umviligihozo, G. Microfluidics-based diagnostics of infectious diseases in the developing world. *Nat. Med.* **2011**, *17*, 1015-1019.

58. Linder, V.; Sia, S. K.; Whitesides, G. M. Reagent-loaded cartridges for valveless and automated fluid delivery in microfluidic devices. *Anal. Chem.* **2005**, *77*, 64-71.

59. Tang, C. K.; Vaze, A.; Rusling, J. F. Fabrication of immunosensor microwell arrays from gold compact discs for detection of cancer biomarker proteins. *Lab on a Chip* **2012**, *12*, 281-286.

60. Yu, X.; Munge, B.; Patel, V.; Jensen, G.; Bhirde, A.; Gong, J. D.; Kim, S. N.; Gillespie, J.; Gutkind, J. S.; Papadimitrakopoulos, F.; Rusling, J. F. Carbon nanotube amplification strategies for highly sensitive immunodetection of cancer biomarkers. *J. Am. Chem. Soc.* **2006**, *128*, 11199-11205.

61. Sardesai, N.; Pan, S.; Rusling, J. Electrochemiluminescent immunosensor for detection of protein cancer biomarkers using carbon nanotube forests and [Ru-(bpy) 3] 2 -doped silica nanoparticles. *Chemical Communications* **2009**, 4968-4970.

62. Malhotra, R.; Papadimitrakopoulos, F.; Rusling, J. F. Sequential layer analysis of protein immunosensors based on single wall carbon nanotube forests. *Langmuir* **2010**, *26*, 15050-15056.

63. Miao, W.; Choi, J.; Bard, A. J. Electrogenerated Chemiluminescence 69: The Tris (2, 2 '-bipyridine) ruthenium (II),(Ru (bpy) 32)/Tri-n-propylamine (TPrA) System Revisited A New Route Involving TPrA• Cation Radicals. *J. Am. Chem. Soc.* **2002**, *124*, 14478-14485.

64. Zweig, M. H.; Campbell, G. Receiver-operating characteristic (ROC) plots: a fundamental evaluation tool in clinical medicine. *Clin. Chem.* **1993**, *39*, 561-577.

65. Pieper, R.; Gatlin, C. L.; Makusky, A. J.; Russo, P. S.; Schatz, C. R.; Miller, S. S.; Su, Q.; McGrath, A. M.; Estock, M. A.; Parmar, P. P. The human serum proteome: Display of nearly 3700 chromatographically separated protein spots on two-dimensional electrophoresis gels and identification of 325 distinct proteins. *Proteomics* **2003**, *3*, 1345-1364.

CHAPTER 5

Automated 3-D Printed ECL Immunoarrays for 8-Protien Prostate Cancer Panel

5-1.Abstract

Automated low cost microfluidic diagnostic platforms have great potential to transform current conventional and reliable methodologies to personalized point of care diagnosis. Prostate cancer is one of leading cause of death in men, and current diagnostic strategy to detect PSA alone should be replaced by multiple biomarker detection for reliable conclusions and provide better therapeutic options for the patients. Here we developed a low cost 3-D printed sensitive microfluidic platform that could simultaneously detect 8 proteins selectively from human serum samples. We engineered a touch screen user interface master controller with simple user commands to operate the diagnostic platform without need for technical expertise. The miniaturized 3-D printed platform have all the reagent/sample reservoirs required to complete the immunoassay without need for intermediate manual operations. Patterned pyrolytic graphite sensor features 16 micro well nanostructured sensors that are selectively coated with capture antibodies relevant to prostate cancer to efficiently capture the proteins of high diagnostic significance from the serum sample. The multiplexed platform, we integrated all the digital and analog commands to simple user friendly options like start/stop and detect with prompts that assure the stages of the immunoassay. We successfully demonstrated detection of 8 proteins on a single platform using sample volumes less 1 µL in diluted samples where the detection chamber volumes were less than 50 µL. We used ECL based immunoassays on a single walled carbon nanotube forest sensor achieving low detection limits of <500 fg mL^{-1} from complex serum matrix. We

validated our analytical precision using spiked human serum samples and found the excellent analytical performance by recovering the spiked proteins ranging from 88 % to 110%.

5-2 Experimental

We developed our low cost 3-D printed ECL immunoarrays using stereolithographic desktop 3-D printer *Form 2* (Formlabs). These printers are inexpensive and can produce high resolution objects (~25 μm) with low surface roughness. Briefly a CAD design with desired structures was prepared using 123 D design software (Autodesk) and transformed later to stereolithography printing compatible format using printer software called preform. These files were uploaded to the printer to fabricate the desired object. A clear photo curable resin (GPCL02 formlabs clear resin) was used to produce these 3-D objects. The obtained 3-D objects are compact plastic devices with internal structures that hold the reagents and sample. These 3-D objects are optically clear and well suited for Electrochemiluminescence detection. The printed objects were removed from build platform and subjected slight post treatment procedures to obtain immunoassay ready platforms. The freshly printed objects were cleaned by flushing, bathing and sonicating them in isopropanol bath for 10-15 minutes to remove any uncured resins followed by air drying to reveal all the detailed structures as desired. Later the arrays were spray coated with acrylic spray (Krylon™) to adjust the optical clarity from slightly opaque to completely clear. These prepared arrays were then inserted with counter and reference electrode wires in the grooves and holes that were are already present on the array. The reference Ag/AgCl and counter platinum wires were used to complete the ECL electrochemical cell when a nanostructured sensor patterned pyrolytic graphite chip is used as a working electrode.

The 3-D printed array is a miniaturized platform with dimensions (L) length 40 mm x (W) width 35 mm x (H) height 3.5 mm. Internal structures the reagent/sample chambers have dimensions of (L x W x H) 25 mm x 2 mm x 1mm resulting in volumes of 48 ± 2 µL. The detection chamber is a open bottom channel converted into an closed microfluidic detection chamber when attached a pyrolytic graphite detection platform. The detection chamber is of 30 mm x 2 mm x 0.6 mm (L x W x H) in dimensions to accommodate the sample and reagents coming from upstream. The detection chamber volumes were designed and optimized to efficiently fill the contents of reagent/sample chambers with low dead volumes. So the volume of the detection chamber is slightly less than 50 µL. The detection channels is designed to accommodate 16 microweel detection sensor spots with 2 spots for each prostate cancer biomarker detection. The sample and reagents were preloaded into the 3-D printed array prior to the immunoassay and stored at 4 °C until use. The reagents and sample were loaded onto to the array using a graduated 50 µL micropipette. To demonstrate the applicability of our array design to commercial purposes we used the array with preloaded samples and reagents prior and stored them until use at 4 °C. To ensure the non-specific adsorption of assay constituents to the 3-D printed immunorray, we incubated all the 3-D arrays with bovine serum albumin at 2 mg mL^{-1} concentration prior to use. The assay reagents and samples were added into the inter structures of the 3-D array called reagent and sample chambers via loading ports present on the top of the array. By placing the pipette's tip into the loading ports the assay reagents were simply loaded with good reproducibility. To appeal to non-expert users we took extreme care in designing the array, we placed vent holes at the end of each chambers to fill reagents efficiently with absolutely no training. The reagents can be easily loaded by simply pipetting the desired solutions and placing the pipette upright into the loading port to deliver the reagents. These vent holes strategically placed to efficiently load the reagents

and samples every time. All the vent holes and loading ports were closed with a single sided transparent tape to complete the airtight continuous channel to sequentially deliver the reagents to downstream detection chamber.

The detection channel that is open at the bottom of the array to deliver the contents placed in the 3-D array, it is completed by attaching out nanostructured detection platform pyrolytic graphite chips. The pyrolytic graphite chips were prepared by cutting the pyrolytic graphite sheets (Panasonic Industrial Devices and Solutions) to desired sizes and attached on to plastic support. The pyrolytic graphite chip is then patterned with Ink-jet printed toner template to get desired microwells. We used our lab's print and peel technology [1] to heat transfer a printed toner design from a glossy paper to the pyrolytic graphite chip. The patterned array has 16 microwells that can accommodate tiny volumes of reagents for building single walled carbon nanotube (SWCNT) forest[2] and coated them with capture antibodies for capturing the selective proteins from serum samples. The SWCNT forest provided enhanced density of capture antibodies immobilization on the surface due to increased surface area from SWCNT forest.[3] This allowed ultralow detection limits of specific cancer biomarker proteins from complex serum matrix. The capture antibody coated pyrolytic graphite chips were then attached to 3-D printed array via a patterned double sided adhesive (DSA). Out of 16 sensor spots on the detection platform, 2 sensors spots each were coated with 8 different capture antibodies. The 8 proteins under study as prostate cancer panel are Insulin like Growth Factor -1 (IGF-1),[4] Prostate specific antigen (PSA),[5] Platelet Factor-4 (PF-4),[6] cluster of differentiation protein 14 (CD-14),[7,8] Vascular Endothelial Growth Factor - D (VEGF-D),[9,10] Golgi membrane protein 1(GOLM-1),[11,12] Prostate specific membrane antigen (PSMA)[13] and Insulin like Growth Factor Binding Protein-3 (IGFBP-3).[14] The capture antibodies for IGF-1, PSA, PF-4, CD-14, VEGF-D, GOLM-1, PSMA and IGFBP-3 were coated on the array via EDC-NHSS

amidization and stored at 4°C until use. Before storing the antibody coated arrays were allowed to incubate with non-specific blocking agent 2% BSA for 1 hr at room temperature to avoid non-specific binding.

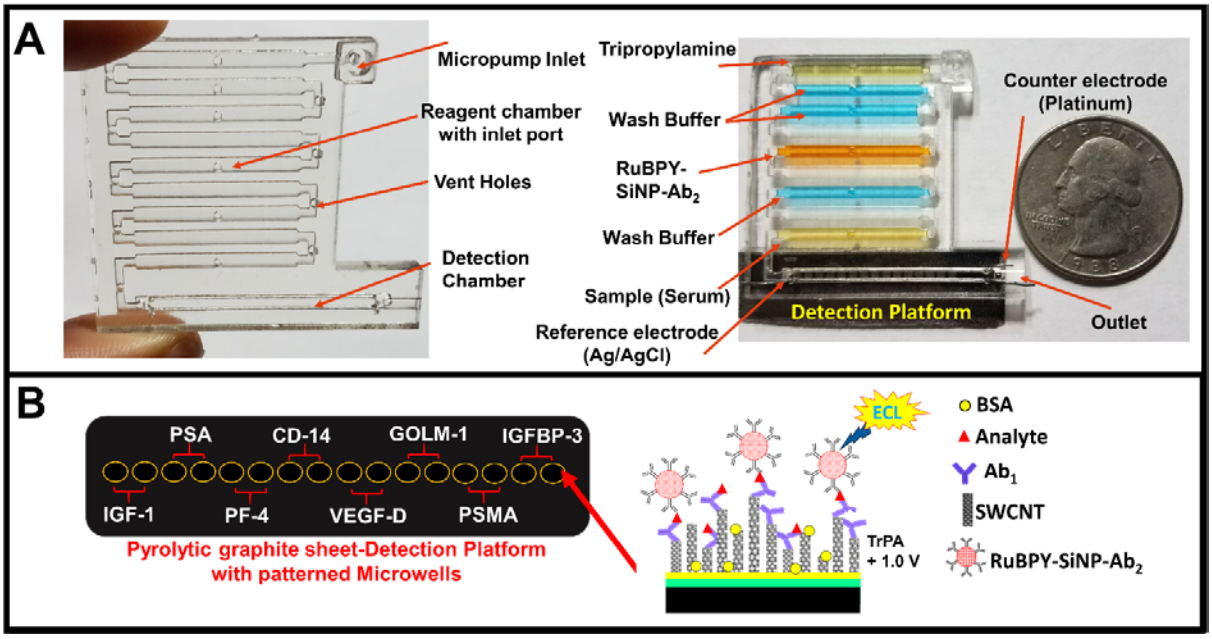

Figure 5-1. Schematic representation of 3-D printed array and Sandwich immunoassay. (A) 3-D printed microfluidic array with reagent chambers designated for sample/analyte, wash buffers, detection label and co-reactant for ECL generation connected to detection platform with pyrolytic graphite detection chip. (B) Disposable pyrolytic graphite sheet with microwells formed by hydrophobic toner print. Insert showing sandwich immunoassay on a single wall carbon nanotube forest (SWCNT).

The 3-D printed array features 9 reagent/sample chambers, one inlet port and one out let port leading to interconnected detection chamber. The each reagent chamber is followed by a empty air gap chamber to avoid mixing of reagents. The 1st reagent chamber next to pump inlet port is filled with Tripropylamine (TrPA) our ECL co-reactant followed by 2nd and 3rd chambers filled with wash reagent (10 mM PBS Buffer + 0.05% Tween 20, pH 7.4). These 2 chambers are

not separated by air gap chamber as intermixing of wash buffers not adversely effect the assay and save the real estate space on the array. The 4th chamber is air gap chamber followed by 5th chamber to be our ECL detection label, detection antibody coated RuBPY doped silica nanoparticles. 6th chamber is again a air gap chamber followed by a wash buffer chamber. The 8th chamber is again air gap chamber followed by final 9th chamber sample/serum. The 9th chamber directly leads to outlet via the detection chamber, Figure 1. The inlet port is connect to micro pump operated digital analog user interface where all the automated commands are integrated for completion of sandwich immunoassay by sequential delivery of prefilled reagents.

Automation and User Interface a master controller system that enables simple user commands. Briefly the construction of the micropump user interface was established by using voltage controlled oscillator (VCO) latch to control on and off cycles of micropumps and times assay events. A digital to analog convertor (DAC) latch controls the voltage, amplitude and frequency for the micropump flow rates. In all, 3 DAC's are connected to 3 sub-microcontrollers for three micropumps. An extra DAC with a potentiometer applies 1.0 V precisely to drive the ECL detection reaction. All components are integrated onto one Arduino microcontroller and a touch LED screen is used to give digital commands. A small 4.5 V rechargeable lithium ion battery 4.5 V is used to power the control system and drive ECL. Three sequential displays appear on an LED screen after the user adds sample. Screen 1 presents a settings display with digital commands to control flow rates and timing. If all settings are optimized, users simply confirm settings. Screen 2 is the start command screen, and the assay is initiated by touching the start button. A digital timer in terms of step number is displayed for each step of the assay so the user can monitor assay progress. Screen 3 showing "**Done**" and Measure OFF, when the immunoassay is complete, and prompts the user to touch the detect button to drive the ECL reaction and camera data collection,

Figure 2. When the ECL potential is being applied Measure ON is displayed for given time to promt the user about ECL detection in progress. In developing assays for the immunoarrays using this control system, we optimized conditions to attain the best analytical performance characteristics including high sensitivity, good dynamic range and ultralow detection limits and optimize assay protocols and device-to-device reproducibility.

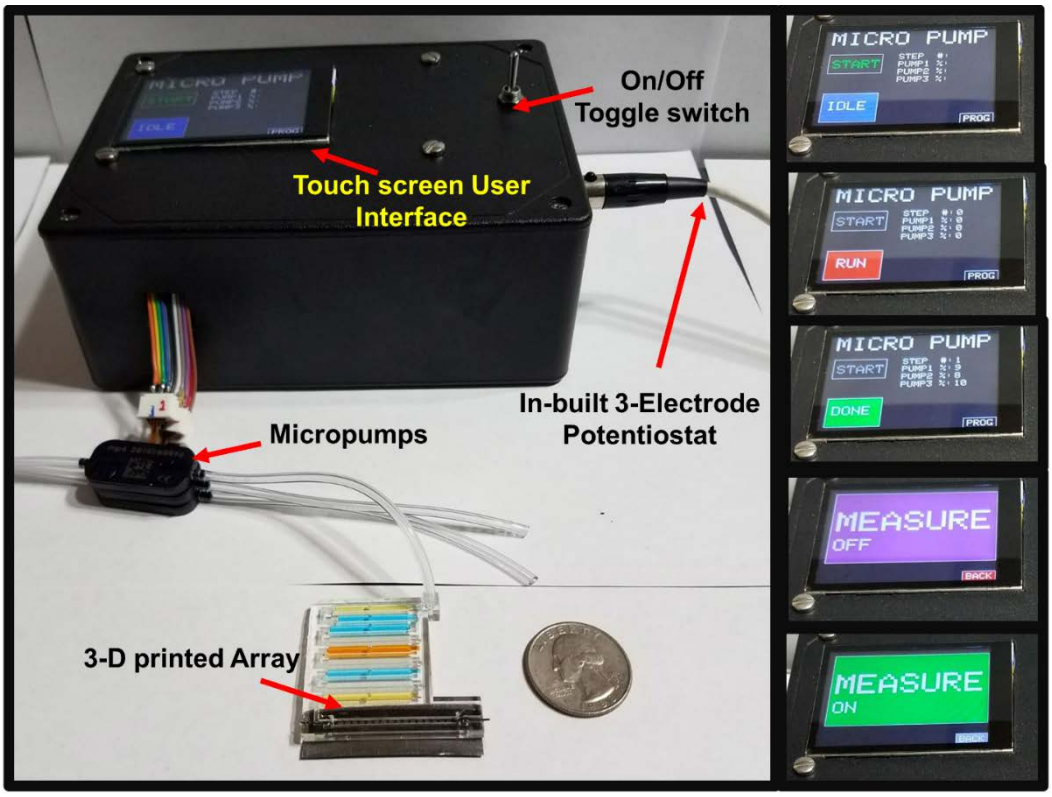

Figure 5-2. Immuoassay setup of 3-D printed array with automation platform and touch screen user interface. 3-D printed microfluidic array with reagent chambers designated for sample/analyte, wash buffers, detection label and co-reactant for ECL generation connected to detection platform with pyrolytic graphite detection chip connected to micropumps. Inset figures showing multiple steps that are automatically completed to perm the immunoassay as designed. Starting from Start the reaction to completing the assay by measuring ECL under a CCD camera in a darkbox.

Assay Procedure The 3-D microfluidic arrays were filled with immunoreagents and sample and connected to the automated pump user interface module. The pumps and pumping cycles were initiated by pressing start. The steps to pumps sample and incubation followed by pushing wash reagents to wash off the excess sample out of the detection channel. Followed by step 2 to deliver ECL RuBPY label to form ECL sandwich immunoassay. When 1.0 vs Ag/AgCl was applied from the onboard potentiostat when place under a CCD camera in a dark box results in ECL generation. The captured ECL light is analyzed to determine the light intensities that relate to concentration of the analyte. 50 µL of sample and other immunoreagents were filled using a pipette and 3-D array sealed with a single sided tape. The micro pumps were optimized to deliver the reagents reproducibly at designated timed intervals at 130 ± 5 µL mL^{-1} flow rates. When more than one assay is being performed we ensure synchronization of the 3 pumps by carefully adjusting their frequency and amplitude via the user interface. The immunoassay incubation times for both sample incubation and RuBPY incubation were optimized to get desired reproducible ECL signals. The incubation times for sample and label for multiplexed detection were 10 min each, whereas for the duplex protein detection the incubation times for sample is 14 min and for RuBPY label is 12 min. ECL is captured at 1.0 V vs Ag/AgCl for 3 min accumulation times in presence of 500 mM tripropylamine in 200mM phosphate buffer + 0.05% Tween 20 + 0.05% Triton-X at pH 7.5. Relative ECL intensities were obtained by analyzing the light intensities of sample concentrations and dividing by signal for control. Plotting the relative ECL intensities on Y axis and concentration of X-axis results in calibration curves that are further used to analyze spike human serum samples.

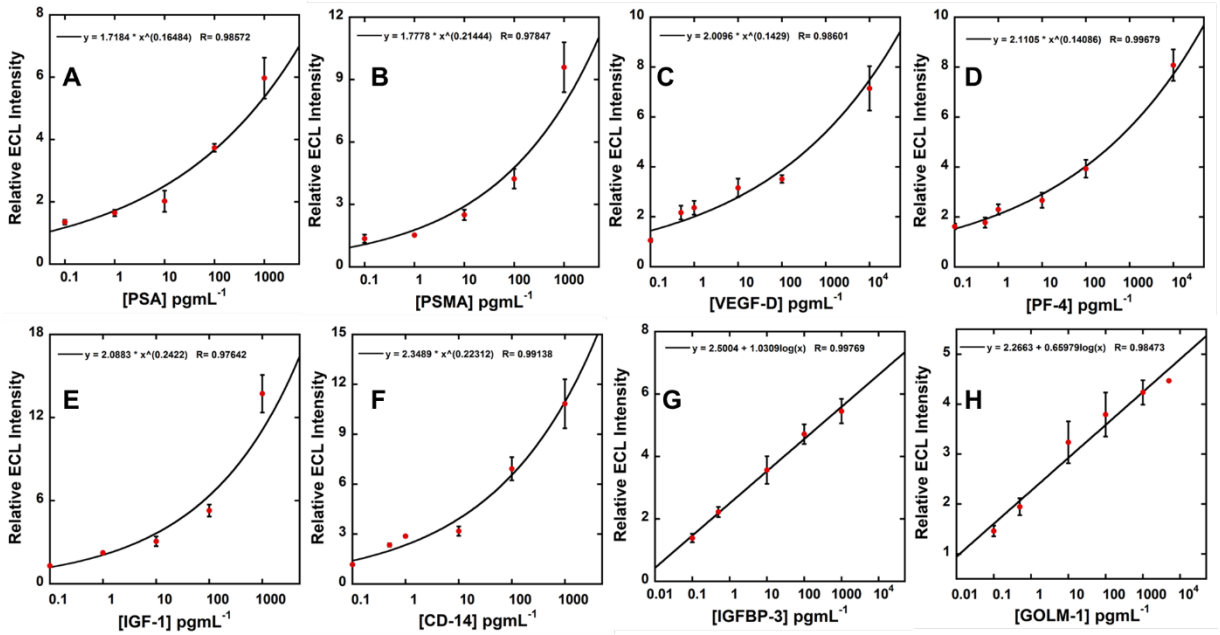

Figure 5-3. Calibration data for duplex detection platforms simultaneously in undiluted calf serum with ECL responses integrated over 180 s at 1.0 V vs Ag/AgCl. (A&B) Duplex assay calibration curves for PSA and PSMA. (C&D) Duplex assay calibration curves for VEGF-D and PF-4. (E&F) Duplex assay calibration curves for IGF-1 and CD-14. (G&H) Duplex assay calibration curves for IGFBP-3 and GOLM-1. Standard deviation for ECL responses at n=4.

5-3 Results

Relative ECL responses captured by CCD camera from the 3-D printed immunoarray with three trails of controls (undiluted calf serum) and 1 pg mL^{-1} PSA and PSMA duplex array showed an average relative standard deviation (RSD) of 5 % for spot to spot (n=8) and 8 % for array to array (n=3). Initially we performed duplex array where we simultaneously detected 2-proteins at a time. We did the duplex array to ensure antibody concentrations for sandwich immunoassay and see reproducible signal from the antibody pairs selected. On the 16 sensor microfluidic chip 4 sensors were addressed for each of the duplex proteins. We calibrated our ECL arrays by

developing calibration curves for all the 8 proteins in duplexes. We found reproducible ECL signals with RSDs ranging for 7 to 13%. Increased ECL responses were observed with increase in concentration of the respective analyte, obtained ECL signal intensities from CCD camera for different analyte concentrations were further processed by dividing with ECL intensity obtained from control to get relative ECL intensity. Relative ECL intensities were plotted against concentration as show in Figure 3. The duplex array formats we coupled PSA and PSMA, VEGF-D and PF-4, IGF-1 and CD-14, IGFBP-3 and GOLM-1 as pairs and detected simultaneously. Dynamic ranges from 0.1 pg mL^{-1} to 1000 pg mL^{-1} was obtained for PSA, PSMA, VEGF-D, IGF-1, CD-14 and IGFBP-3, 0.1 pg mL^{-1} to 10,000 pg mL^{-1} was obtained for GOLM-1 and PF-4. Detection limits of 78 fg mL^{-1} to 100 fg mL^{-1} was obtained for all the 8 proteins.

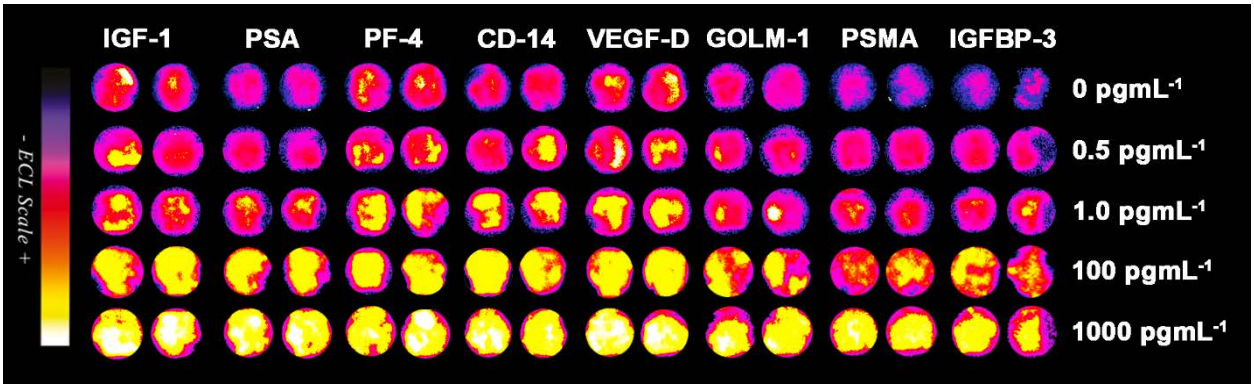

Figure 5-4. Recolorized CCD images of 5 arrays showing increase in ECL response with increase in concentration for all the 8 proteins on a single array with ECL aqasition times of 180 sec in presence of 500 mM TrPA with applied voltage of 1.0 V Ag/AgCl. Influence of ECL responses with increase in concentrations was shown for 0 pg mL^{-1} to 1000 pg mL^{-1}.

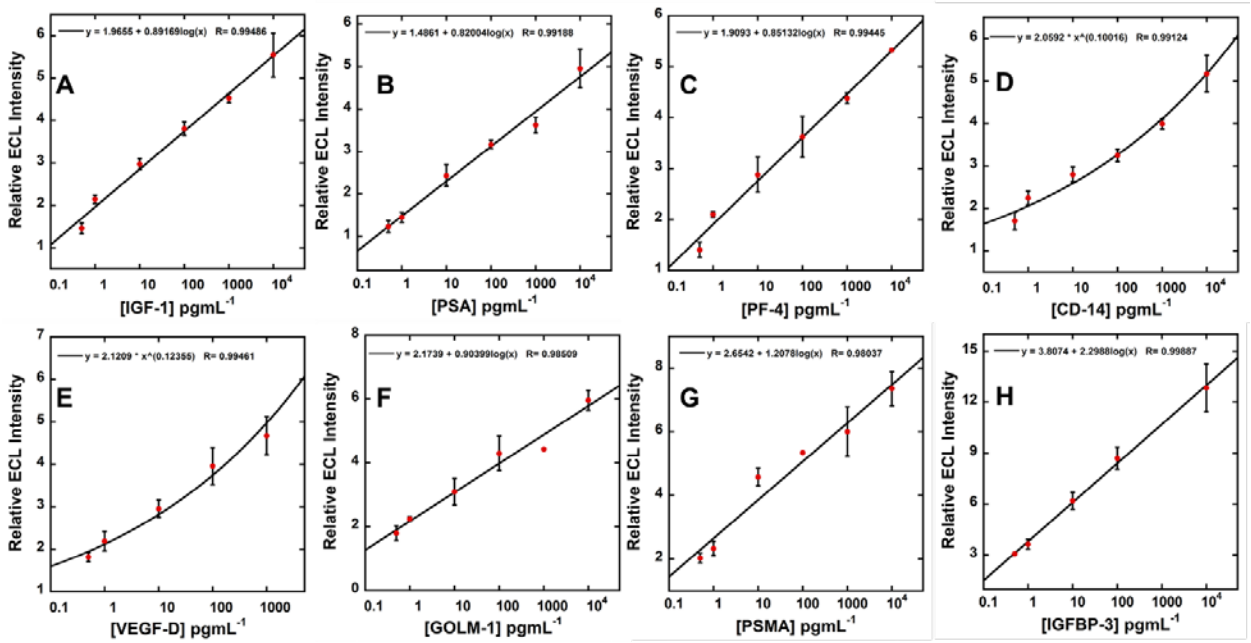

Figure 5-5. Calibration data for multiplexed detection platforms simultaneously in undiluted calf serum with ECL responses integrated over 180 s at 1.0 V vs Ag/AgCl. (A to H) multiplex assay calibration curves for IGF-1, PSA, PF-4, CD-14, VEGF-D, GOLM-1, PSMA and IGFBP-3. Standard deviation for ECL responses at n=4.

Multiplexed detection. All the 8 proteins were detected simultaneous on our detection platforms with 2 sensors allocated for each biomarker. The 8 different capture antibodies were immobilized onto our single walled carbon nanotube forest sensor microwells. The capture antibodies were placed in the order of IGF-1, PSA, PF-4, CD-14, VEGF-D, GOLM-1, PSMA and IGFBP-3 as shown in Figure 1B. The detection label with all the 8 detection antibodes was prepared by mixing duplex assay labels. 4 duplex assay labels where label 1 with PSA and PSMA, label 2 VEGF-D and PF-4, label 3 CD-14 and IGF-1, label 4 GOLM-1 and IGFBP-3 were mixed in equal proportions and sent onto detection platform to complete the sandwich immunoassay. The

mixture of standard protein samples were then allowed to flow from analyte/sample chamber and incubated for 10 minutes followed by washing with 10 mM PBS buffer, 7.4 pH. Multiplexed detection label, RuBPY SiNP was then flowed on to the detection sensors from reagent chamber and allowed to incubate for 10 minutes, followed by washing with 10 mM PBS and PBS T20 buffer, pH 7.4 from the prefilled chambers. ECL responses were accumulated using CCD camera as explained before. The relative ECL intensities were plotted against specific concentrations showing ECL increase with increase in concentration Figure 4 and 5. Acceptable dynamic ranges from 0.5 pg mL^{-1} to 10 ng mL^{-1} was obtained for all the proteins with detection limits ranging from 110 fg mL^{-1} to 500 fg mL^{-1} was obtained for all the proteins in multiplexed detection.

To validate our array for using with human serum samples we performed spike and recovery test to demonstrate the accuracy and reproducibility of our developed method. Spike and recovery tests were performed for concentrations ranging from 5 ng mL^{-1} to 0.75 pg ng mL^{-1}. Spike, recovery and patient samples study will be done to evaluate the validity of the developed platform.

5-4. References

1. Tang, C. K.; Vaze, A.; Rusling, J. F. Fabrication of immunosensor microwell arrays from gold compact discs for detection of cancer biomarker proteins. *Lab on a Chip* **2012**, *12*, 281-286.

2. Chattopadhyay, D.; Galeska, I.; Papadimitrakopoulos, F. Metal-assisted organization of shortened carbon nanotubes in monolayer and multilayer forest assemblies. *J. Am. Chem. Soc.* **2001**, *123*, 9451-9452.

3. Sardesai, N. P.; Kadimisetty, K.; Faria, R.; Rusling, J. F. A microfluidic electrochemiluminescent device for detecting cancer biomarker proteins. *Analytical and bioanalytical chemistry* **2013**, *405*, 3831-3838.

4. Allen, N. E.; Key, T. J.; Appleby, P. N.; Travis, R. C.; Roddam, A. W.; Rinaldi, S.; Egevad, L.; Rohrmann, S.; Linseisen, J.; Pischon, T.; Boeing, H.; Johnsen, N. F.; Tjonneland, A.; Gronbaek, H.; Overvad, K.; Kiemeney, L.; Bueno-de-Mesquita, H. B.; Bingham, S.; Khaw, K. T.; Tumino, R.; Berrino, F.; Mattiello, A.; Sacerdote, C.; Palli, D.; Quiros, J. R.; Ardanaz, E.; Navarro, C.; Larranaga, N.; Gonzalez, C.; Sanchez, M. J.; Trichopoulou, A.; Travezea, C.; Trichopoulos, D.; Jenab, M.; Ferrari, P.; Riboli, E.; Kaaks, R. Serum insulin-like growth factor (IGF)-I and IGF-binding protein-3 concentrations and prostate cancer risk: results from the European Prospective Investigation into Cancer and Nutrition. *Cancer Epidemiol. Biomarkers Prev.* **2007**, *16*, 1121-1127.

5. Lilja, H.; Ulmert, D.; Vickers, A. J. Prostate-specific antigen and prostate cancer: prediction, detection and monitoring. *Nature Reviews Cancer* **2008**, *8*, 268-278.

6. Chikkaveeraiah, B. V.; Bhirde, A.; Malhotra, R.; Patel, V.; Gutkind, J. S.; Rusling, J. F. Single-wall carbon nanotube forest arrays for immunoelectrochemical measurement of four protein biomarkers for prostate cancer. *Anal. Chem.* **2009**, *81*, 9129-9134.

7. Butkus de Aguiar, B.; Girardi, I.; D'Avila Paskulin, D.; de França, E.; Dornelles, C.; Suparregui Dias, F.; Bonorino, C.; Sampaio Alho, C. CD14 Expression in the First 24h of Sepsis: Effect of− 260C> T CD14 SNP. *Immunol. Invest.* **2008**, *37*, 752-769.

8. Kim, J. I.; Lee, C. J.; Jin, M. S.; Lee, C. H.; Paik, S. G.; Lee, H.; Lee, J. O. Crystal structure of CD14 and its implications for lipopolysaccharide signaling. *J. Biol. Chem.* **2005**, *280*, 11347-11351.

9. Woollard, D. J.; Opeskin, K.; Coso, S.; Wu, D.; Baldwin, M. E.; Williams, E. D. Differential expression of VEGF ligands and receptors in prostate cancer. *Prostate* **2013**, *73*, 563-572.

10. Zeng, Y.; Opeskin, K.; Baldwin, M. E.; Horvath, L. G.; Achen, M. G.; Stacker, S. A.; Sutherland, R. L.; Williams, E. D. Expression of vascular endothelial growth factor receptor-3 by lymphatic endothelial cells is associated with lymph node metastasis in prostate cancer. *Clin. Cancer Res.* **2004**, *10*, 5137-5144.

11. Wei, S.; Dunn, T. A.; Isaacs, W. B.; De Marzo, A. M.; Luo, J. GOLPH2 and MYO6: putative prostate cancer markers localized to the Golgi apparatus. *Prostate* **2008**, *68*, 1387-1395.

12. Gu, Y.; Chen, W.; Zhao, Y.; Chen, L.; Peng, T. Quantitative analysis of elevated serum Golgi protein-73 expression in patients with liver diseases. *Ann. Clin. Biochem.* **2009**, *46*, 38-43.

13. Sardana, G.; Dowell, B.; Diamandis, E. P. Emerging biomarkers for the diagnosis and prognosis of prostate cancer. *Clin. Chem.* **2008**, *54*, 1951-1960.

14. Meinbach, D. S.; Lokeshwar, B. L. In *In Insulin-like growth factors and their binding proteins in prostate cancer: Cause or consequence?;* Urologic Oncology: Seminars and Original Investigations; Elsevier: 2006; Vol. 24, pp 294-306.

Chapter 6

Genotoxic Screening Assays Using Eletrochemiluminiscence and LC-MS/MS

6-1. Goal & Significance

Cancer is the second leading cause of death in the United States and in 2017, 1,688,780 new cancer cases and 600,920 cancer deaths are projected. American Cancer Society estimates the number of new cancer cases and deaths every year according to the data collected from the national Program of Cancer Registries and the North American Association of Central Cancer Registries.[1] Cancer is caused by both exogenous and endogenous factors whose mechanism and management still has a lot of unresolved factors.[2] Pharmaceutical and academic institutions are constantly driving their efforts towards cure and management of cancer.

Toxicity screening plays a significant role in drug development. 95 % of drugs that enter into clinical trials do not make it to market. 20-40 % of these failures are associated with toxicology and pharmacological reasons.[3] Idiosyncratic adverse drug reactions of pharmaceutical drugs and their metabolites is a major reason for market withdrawals of many pharmaceutical drugs.[4] Toxicity screening assays estimating the adverse reaction of both drugs and their metabolites is essential before clinical trials to save millions of dollars associated with drug development. Animal models and in-silico studies are not always designed keeping in mind the predictive result in humans. More over even if these experiments were designed as a predictive tool for equivalent response in humans is not always accurate.[5] Transition from animal models to clinical trials is less than 8 %.[6]

Current research focuses of development of high throughput toxicity screening assays for both the drugs/chemicals and their metabolites that can complement the currently available assays for getting more information of the drug under study at molecular level and also taking into consideration of their metabolic transformations. Developed methods are simple and inexpensive. Efforts are also directed towards making these assays automated and

thus making them adaptive to people with minimum expertise. In addition to drug toxicity these assays can also be used for estimating the genotoxic assessment of environmental samples.

6-2. Genotoxicity &Current Assays

Ability of chemicals, drugs or environmental pollutants to cause damage to genetic material is known as genotoxicity. These damages often lead to mutations that can eventually lead to cancer in the absence of inherent repair mechanism of gene damage. There are number of mechanisms involved in damage to genetic material. Some of them include DNA hydrolysis, deamination, covalent adduct formation, DNA oxidation, abasic site formation, strand breaks etc.,[7,8]

Ames test, comet assay, chromosomal aberration, micronucleus assay, mouse lymphoma test etc., are some of the commercial assays used for genotoxic testing. Ames test uses biological assays with bacteria to test a potential chemical/drug for its mutagenicity.[9] Comet assay uses DNA strand breaks in eukaryotic organisms as a measure of genotoxic potential.[10] Micronucleus test involves the study of chromosomal fragments in erythrocytes as a measure of genotoxic potential.[11]

These tests give valuable information wither stand alone or in combination. Most of these assays focus on one single mechanism of genetic material damage or does not give the mechanism of DNA damage involved. More over the effect reactive metabolites in not known. Hence there is a need of in-vitro method that can complement the current commercial methods that gives mechanism of DNA damage and also takes into consideration of multiple mechanisms of DNA damage and accounts for reactive metabolites formed during biotransformation of drugs or chemicals.

6-3. ECL based toxicity assays

Microfluidic electrochemical arrays have been developed in our lab for over the past decade. Briefly microfluidic arrays for DNA damage have been developed for DNA oxidation, DNA adduct formation, strand breaks etc., These microfluidic arrays contain thin films of DNA, ECL-active polymer [Ru(bpy)2(PVP)10(ClO4)2] and

microsomal enzyme sources. A negative potential of -0.65 V was initiated first to activate/mimic the fast electron injection from electrode to microsomal CPR required for transfer of electrons to cyt P450 enzymes which in presence of oxygen activate the catalytic cycle. This generates metabolites from drugs/chemicals/pollutants. DNA damage detection then involves oxidation of RuPVP in thin films at +1.25 V, which in turn oxidizes DNA to produce excited $Ru^{II}PVP^*$ that emits ECL light. Thus, +1.25 V vs. Ag/AgCl was applied for 240 s, at which time the catalytic current for the process was saturated, to generate 610 nm light that was captured by a CCD camera in a dark box.[12]

6-4. LC-MS/MS based Genotoxicity assays

LC-MS/MS based approaches give a more elaborate information for specific chemicals under study. LC-MS/MS is a valuable tool for predicting the structural and mechanisms of DNA damage. Molecular level of information regarding the structure of the drug/chemicals, possible metabolites formed upon bioactivation and the mechanism of DNA damage can be studied using LC-MS/MS. When this approach used in combination of other genotxic assays can give valuable information in drug development and toxicity screening.

6-5. Summary

In this thesis development of automated 3-D printed microfluidic arrays for high throughput ECL based genotoxic assays for environmental pollutants was studied and also LC-MS/MS based approaches for sequence specific DNA damage on P53 tumor suppressor gene for predicting organ specific cancer has been studied in detail.

6-7. References

1. Siegel, R. L.; Miller, K. D.; Jemal, A. Cancer statistics, 2016. *CA: a cancer journal for clinicians* **2016**, *66*, 7-30.
2. Feigelson, H. S.; Ross, R. K.; Yu, M. C.; Coetzee, G. A.; Reichardt, J. K.; Henderson, B. E. Genetic susceptibility to cancer from exogenous and endogenous exposures. *J. Cell. Biochem.* **1996**, *63*, 15-22.
3. Hartung, T. Look back in anger - what clinical studies tell us about preclinical work. *ALTEX* **2013**, *30*, 275-291.
4. Thompson, R. A.; Isin, E. M.; Ogese, M. O.; Mettetal, J. T.; Williams, D. P. Reactive metabolites: current and emerging risk and hazard assessments. *Chem. Res. Toxicol.* **2016**, *29*, 505-533.
5. Herati, R. S.; Wherry, E. J. What Is the Predictive Value of Animal Models for Vaccine Efficacy in Humans? Consideration of Strategies to Improve the Value of Animal Models. *Cold Spring Harb Perspect. Biol.* **2017**.
6. Mak, I. W.; Evaniew, N.; Ghert, M. Lost in translation: animal models and clinical trials in cancer treatment. *Am. J. Transl. Res.* **2014**, *6*, 114-118.
7. Gates, K. S. An overview of chemical processes that damage cellular DNA: spontaneous hydrolysis, alkylation, and reactions with radicals. *Chem. Res. Toxicol.* **2009**, *22*, 1747-1760.
8. Sancar, A.; Lindsey-Boltz, L. A.; Ünsal-Kaçmaz, K.; Linn, S. Molecular mechanisms of mammalian DNA repair and the DNA damage checkpoints. *Annu. Rev. Biochem.* **2004**, *73*, 39-85.

9. Ames, B. N.; McCann, J.; Yamasaki, E. Methods for detecting carcinogens and mutagens with the Salmonella/mammalian-microsome mutagenicity test. *Mutation Research/Environmental Mutagenesis and Related Subjects* **1975**, *31*, 347-363.

10. Fairbairn, D. W.; Olive, P. L.; O'Neill, K. L. The comet assay: a comprehensive review. *Mutation Research/Reviews in Genetic Toxicology* **1995**, *339*, 37-59.

11. Schmid, W. The micronucleus test. *Mutation Research/Environmental Mutagenesis and Related Subjects* **1975**, *31*, 9-15.

12. Hvastkovs, E. G.; Rusling, J. F. *State-of-the-Art Metabolic Toxicity Screening and Pathway Evaluation*. Anal. Chem. **2016,** *88*, 4584-4599.

Chapter 7

Automated 3-D Printed Arrays to Evaluate Genotoxic Chemistry: E-Cigarettes and Water Samples

7-1. Abstract

A novel, automated, low cost, 3-D printed microfluidic array was developed to detect DNA damage from metabolites of chemicals in environmental samples. The electrochemiluminescent (ECL) detection platform incorporates layer-by-layer (LbL) assembled films of microsomal enzymes, DNA and an ECL-emitting ruthenium metallopolymer in ~10 nm deep microwells. Liquid samples are introduced into the array, metabolized by the human enzymes, products react with DNA if possible, and DNA damage is detected by ECL with a camera. Measurements of relative DNA damage by the array assess the genotoxic potential of the samples. The array analyses 3 samples simultaneously in 5 min. Measurement of cigarette and e-cigarette smoke extracts and polluted water samples was used to establish proof of concept. Potentially genotoxic reactions from e-cigarette vapor similar to smoke from conventional cigarettes were demonstrated. Untreated waste water showed a high genotoxic potential compared to negligible values for treated waste water from a pollution control treatment plant. Reactivity of chemicals known to produce high rates of metabolite-related DNA damage were measured and array results for environmental samples were expressed in terms of equivalent responses from these standards to assess severity of possible DNA damage. Genotoxic assessment of waste water samples during processing also highlighted future on-site monitoring applications.

7-2. Introduction

Genotoxicity refers to the ability of chemicals or their metabolites to interact with genetic material. Reactions with DNA include covalent adduct formation, oxidation, strand breaks and non-covalent intercalations. When damage to DNA is not repaired, subsequent mutations occur that may lead to cancer.[1] For environmental chemicals and drugs, a battery of tests is typically used to predictively assess potential genotoxicity and other toxicities. Genotoxicity tests such as Comet, Ames, micronucleus, and mouse lymphoma assays are very useful for toxicity predictions, but are limited by ease of use and metabolic generality.[2] We previously developed microfluidic toxicity screening arrays with the ability to uncover multiple chemical pathways of genotoxicity by measuring DNA damage.[2] These high throughput electrochemiluminescent (ECL) and electrochemical assays include DNA and human metabolic enzymes that convert chemicals to metabolites, which are most often the DNA-reactive species in genotoxic pathways. [2]

Automated, disposable devices that rapidly detect genotoxic chemistry in environmental samples can serve to evaluate the potential influence of toxic chemicals and on-site risks to human health.[2,3] We recently reported a paper microfluidic device that estimated the genotoxic potential of water samples.[4] In this paper, 3-D printing is used to develop a more sophisticated and sensitive general automated array to assess genotoxic potential of environmental samples. 3D printing was used to afford cheap, fast design and optimization. It has been used to print fluidic devices that detect pathogenic bacteria, biomedical markers, food allergens, and heavy metals, as well as in nanoparticle and chemical synthesis.[5,6] 3D printed flow cells were designed for microdroplet generation, electrochemical sensing, and microfluidic devices.[7] We used desktop 3D printers to develop devices for flow injection amperometry, flow cells to measure ECL,[8] and microfluidic immunoarrays to detect cancer biomarker proteins.[9]

The current device is designed for rapid assays of liquid samples. We focus here on two types of samples for reasons outlined below. The first is cigarette and e-cigarette smoke, since smoking is a major contributor to heart disease and cancer.[10] The second is contaminated water, a major public health concern.

Smoking causes more deaths than human immunodeficiency virus, illegal drug use, alcohol, motor vehicle accidents, and fire related deaths combined.[11] Electronic (e-)cigarettes, are battery powered devices that vaporize nicotine, and were designed as an alternative to tobacco cigarettes. Additives in recent e-cigarettes make the vapor less harsh and more rapidly deliver nicotine to the brain, fostering use and increasing chances of addiction. Between 2011 and 2015 e-cigarette use increased from 1.5 to 16 % among US high school students and from 0.6 to 5.3% among middle school children.[12] In addition, e-cigarette vapor contains toxic metals such as cadmium, lead and nickel at levels of 0.022-0.057 ng in 15 puffs of the aerosol.[13]

Currently one-third of available fresh water is used for agriculture, industrial and domestic purpose.[14] Chemical pollution of fresh water lakes and rivers is endemic in populated areas.[15] Toxic pollutants found in water bodies include nitrogenous and phosphorous species, organic chemicals, metals, and biologically generated compounds.[16] Co-existence of these chemicals in a mixture has been suggested as an origin of elevated genotoxic effects.[14,17]

In this paper, we report the first disposable, fully automated 3D-printed array designed to assess genotoxic potential of liquid environmental samples. This device can analyze vapor extract samples from cigarettes and water samples in 5 min for less than $1.00 (Figure 7-1). The arrays assess potential genotoxicity based on DNA reactivity of metabolites generated by enzymes on the array. To our knowledge, this is the first low cost 3-D printed microfluidic array capable of evaluating the metabolite-dependent genotoxic potential of environmental samples. Results

suggest that e-cigarettes can have similar or enhanced genotoxic potential compared to tobacco cigarettes, depending on use patterns. The genotoxic potential of untreated waste water was high, but was decreased to very low levels by reclamation in a sewage treatment facility.[18]

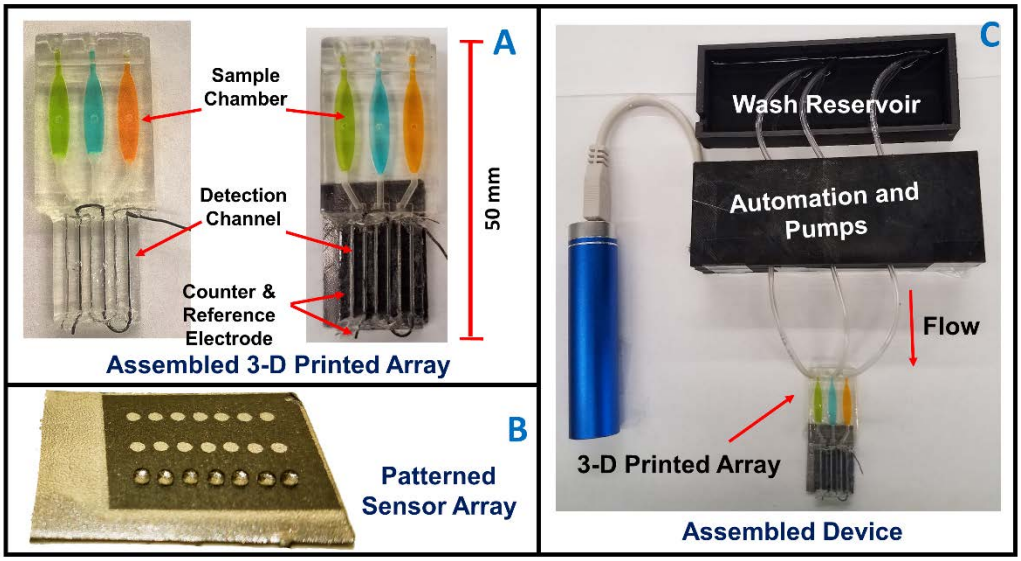

Figure 7-1. Automated genotoxicity screening array: (A) 3D printed devices without (left) and with (right) microwell chip and counter electrode wires inserted showing sample chambers containing dye solutions; coin for size comparison is US 10 cent piece; (B) microwell-patterned pyrolytic graphite detection array showing the first row holding 1 µL water droplets retained by the hydrophobic microwell boundaries. Each row is fed by a separate sample line. The working array features films of DNA, metabolic enzymes, and RuPVP in each microwell; (C) Assembled array system showing box enclosing electronic microprocessors and micropumps driven by a rechargeable battery and connected to the 3D printed array below with a wash reservoir (top) containing pH 7.4 buffer.

7-3. Experimental Section

Safety note: Benzo[a]pyrene (B[a]P), 4-[methyl(nitroso)amino]-1-(3-pyridinyl)-1-butanone (NNK), N'-Nitroso-2-(3-pyridyl)pyrolidine (NNN), 2-Acetylaminofluorene (2-AAF), 2-

Naphthylamine (2-NA), Aflatoxin-B_1 (AFB1) and their metabolites are potential carcinogens. Handling these chemicals involved protective measures including wearing gloves, safety glasses and working in a hood.

7-3.1 Chemicals and Materials. B[a]P (MW 252.31), NNK (MW 207.23), NNN (MW 177.20), 2-AAF (MW 223.28), 2-NA (MW 143.19), AFB1 (MW 312.28), poly(diallyldimethylammonium chloride) (PDDA, avg. MW= 100,000-200,000), poly(acrylic acid) (PAA, avg. MW= 1800), calf thymus DNA (Type I), and other chemicals were from Sigma Aldrich. Pooled male human liver microsomes were from BD Gentest. $[Ru(bpy)_2(PVP)_{10}]^{2+}$ {RuPVP; (bpy=2,2-bipyridyl; PVP=poly(4-vinylpyridine)} was synthesized and characterized as described previously.[19] Pyrolytic graphite (PG) sheets are from Panasonic PGS-P13689-ND 70 µm thick.

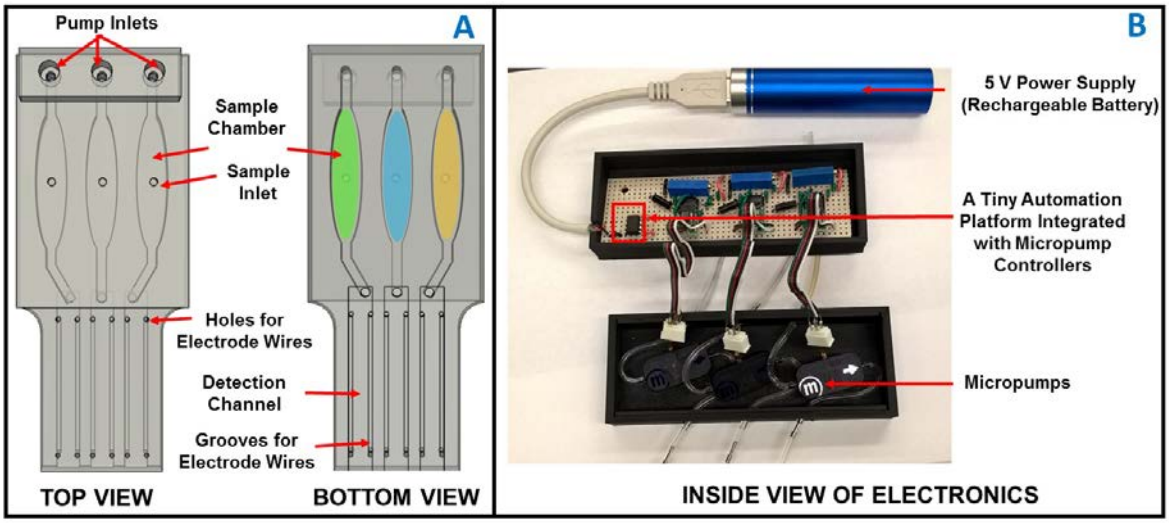

Figure 7-2. 3-D Printed PG array: (A) CAD design showing top and bottom view of 3-D printed arrays with pump inlets, sample chambers, detection channels and grooves for counter and reference electrodes; (B) Inside view of micropump and microcontrollers along with automation platform connected to 3-D printed array and operated via 5 V rechargeable battery.

7-3.2 3-D Printed Microfluidic Arrays. Microfluidic arrays were printed from clear acrylate resin using a Formlabs Form1+ stereolithographic 3D printer. Design files are available on our website.[20] Briefly, CAD files incorporating the design were converted to printer instruction files for input to the printer (details in SI). After printing, devices were rinsed internally and externally successively with isopropanol and water, then spray coating with clear acrylic spray (Krylon™).

Arrays were printed with 3 sample chambers that feed 3 detection channels designed so that sample solutions flow directly across shallow 1 mm wide, 10 nm deep microwells on the detection chip to facilitate reactions with enzyme/DNA films in the wells (Figures 7-1A,B and 7-2). Detection chips were made from conductive pyrolytic graphite (PG) sheets cut to desired sizes. PG sheets were patterned with microwells using our print and peel technology[21] to accommodate tiny volumes of reagents during layer-by-layer (LbL) film assembly (Figure 7-1B).[22] A microwell template featuring 21 spots of diam. 1 mm in 3 rows with 7 spots per flow channel was inkjet printed onto glossy paper (Avery ™ 5263) and heat pressed for 45 s at 275 °C to transfer onto these PG sheets (Figure 7-3, SEM). Patterned PG sheets were attached onto the 3D printed array using double sided adhesive.

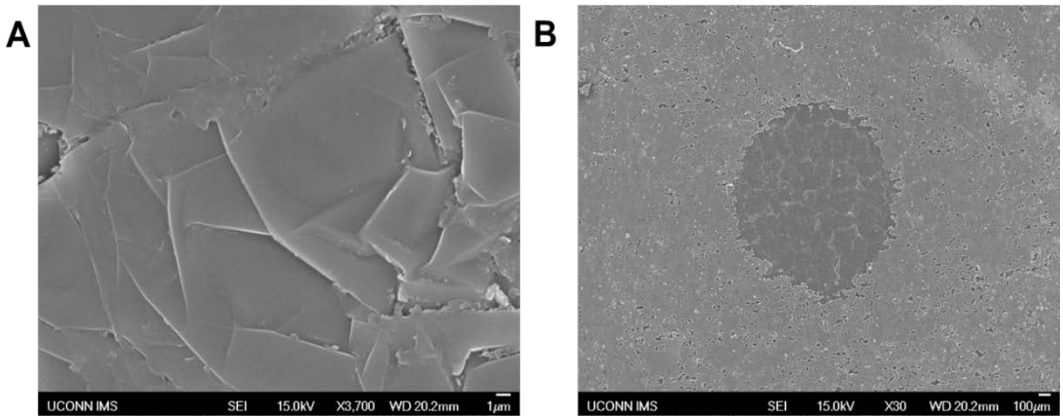

Figure 7-3. SEM images for A) bare pyrolytic graphite sheets and B) Microwell that hold 1 µL volumes of reagent required to complete layer by layer assembly.

Array were 3D printed in less than 1 hr using 6 mL resin at fabrication cost $0.80. They have dimensions 50 mm (length (L)) X 22 mm (width (W)) X 5 mm (height (H)). Sample chamber dimensions are 17 mm (L) X 5 mm (W) X 2.5 mm (H) and maximum sample or reagent volume 170 ± 5 µL. Sample volume was 150 µL, and detection channels are 23 mm (L) X 3 mm (W) X 0.65 mm (H) with volume 45 ± 5 µL, and are provided with holes and grooves to accommodate stainless steel wire counter (0.4 mm diam.) and Ag/AgCl wire reference (0.6 mm diam.) electrodes to complete the ECL electrochemical detection cell (Figure 7-1A).

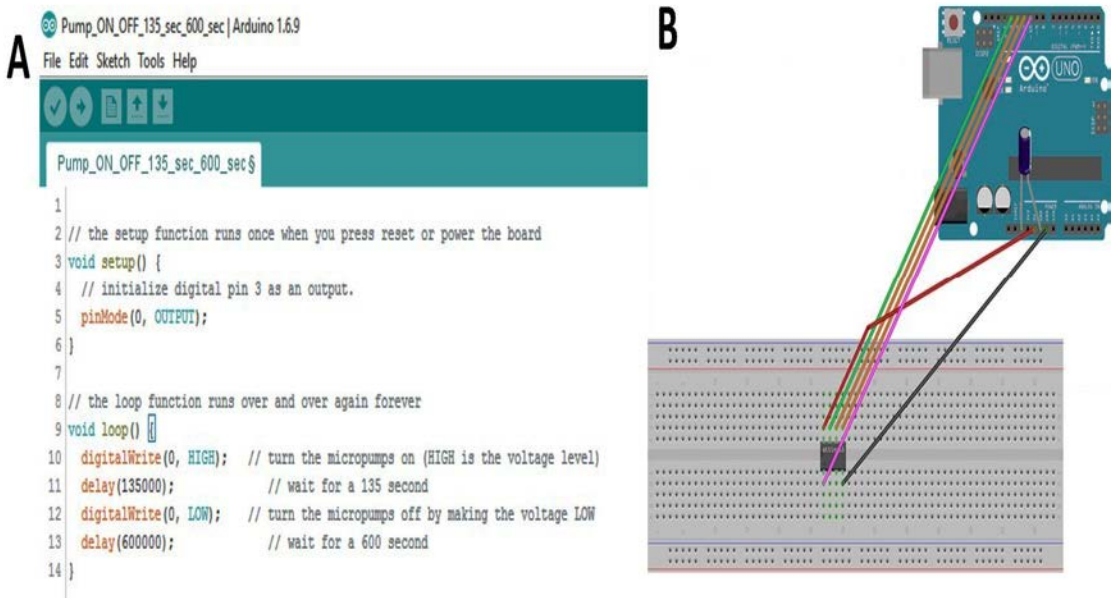

Figure 7-4. A) Arduino program for pumps automation B) Schematic upload of Arduino program to ATtiny85 chip.

7-3.3 Automation. Automation was achieved by interfacing three Mp6 micropumps (Bartels) with an "ATtiny85" microprocessor chip via Bartels OEM microcontrollers (Figure 7-4). Micropump control features printed-circuit board (PCB)-linked microcontrollers independently connected to the ATtiny85 chip. The inexpensive 8-bit ATtiny microcontroller chip runs Arduino programs for pump control at low power consumption (Figure 7-4),[23] and provides ON/OFF commands to

control voltage input to micropumps from a rechargeable lithium ion battery. Micropumps were adjusted to flow rate 120 ± 3 µL/min.

7-3.4 Layer by layer film assembly. Sequential layers of ECL metallopolymer RuPVP, human liver microsome (HLM) enzyme source and DNA were grown in microwells on the PG chip by layer-by-layer (LbL) alternate electrostatic assembly,[22] depositing appropriate solutions sequentially and incubating 20 min for polyion layers and 30 min for enzyme and DNA layers at 4°C with water washing between adsorption steps.[24] Film architecture optimized for best signal/noise was PDDA/PAA/$(RuPVP/DNA)_2$/RuPVP/Enzyme/DNA.

7-3.5 Detection of genotoxic reactions. The assay protocol involves two steps. First, the natural cyt P450 catalytic cycle is activated by applying -0.65 V vs Ag/AgCl while flowing oxygenated solutions of test samples in 10 mM phosphate buffer pH 7.4 + 1 % DMSO for 45 s. This generates metabolites from the test compounds that can react with DNA.[25] Second, after washing the array with buffer, 1.25 V vs Ag/AgCl is applied for 180 s to generate ECL proportional to damage of co-reactant DNA. This oxidizes $Ru^{II}PVP$ to $Ru^{III}PVP$, and $Ru^{III}PVP$ reacts with guanine in a complex pathway to form excited state $*Ru^{II}PVP$ that emits ECL light at 610 nm which is captured with a CCD camera in a dark box. [2] Briefly the complex reaction between $Ru^{III}PVP$ and guanine involves oxidation of guanine by $Ru^{III}PVP$ in an electrochemical catalytic pathway resulting in a guanine radical. Guanine radical further reacts with $Ru^{III}PVP$ to form $*Ru^{II}PVP$ that emits ECL light.[19] Covalent metabolite-nucleobase adducts disrupt the DNA double helix and can also form abasic sites or strand breaks, which all result in more accessible guanines to generate more ECL light. Electrodes are disposable and are discarded after each use.

Prior to assays, sample chambers in the microarray (Figure 7-1A) were pre-filled with 150 µL of test solution through the sample injection ports, which are then closed. The micropumps are connected to inlets with common feed at the back from a wash buffer reservoir (Figure 7-1C). Application of voltage to the array was controlled by a 3-electrode handheld potentiostat. The entire device resides inside a dark box. Initially pumps are off, then the program initiates a 135 s pumping cycle for three steps, 10 s filling the detection channel, 45 s electrolysis and 80 s washing. Samples were pumped into the 3 separate detection channels and 45 s electrolysis was done at -0.65 V vs Ag/AgCl once channels were full (while continuing flow) to activate the natural catalytic cycle of cyt P450s.[25] After a subsequent 80 s wash cycle, pumps turn off and visible ECL light is generated by applying 1.25 V vs Ag/AgCl for 180 s and capturing light with a CCD camera. Timing was optimized for the best ECL signal/noise.

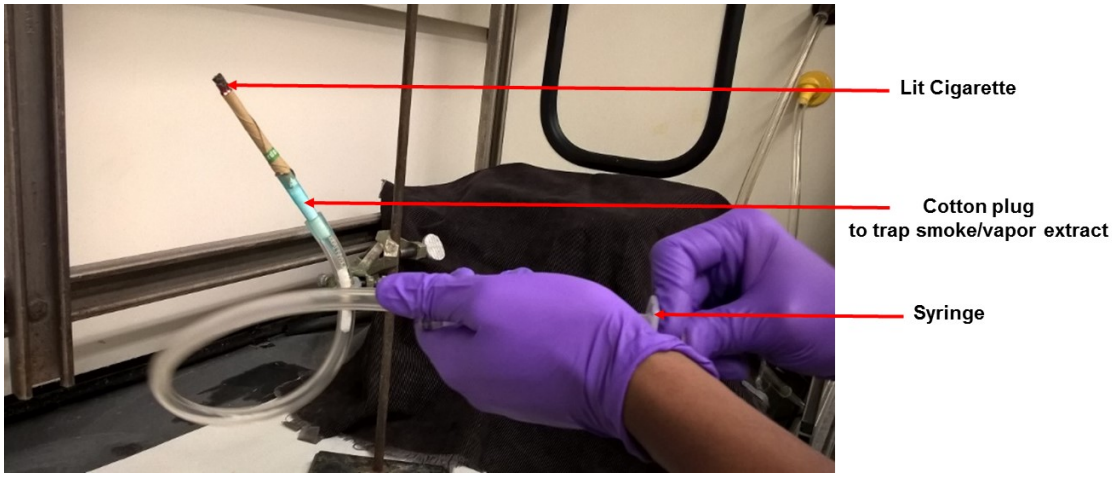

Figure 7-5. Artificial inhalation setup to extract smoke/vapor from cigarettes on to a cotton plug.

7-3.6 Sample analyses. Smoke (vapor) extracts from e-cigarettes and filtered and non-filtered tobacco cigarettes were collected using an artificial inhalation device (Figure 7-5). Tubing connecting a syringe and the cigarette or e-cigarette was attached via a pipette tip plugged with cotton so that smoke passes through it and chemicals are trapped. This cotton was subsequently

extracted with 2 mL DMSO. To keep experimental conditions representative and relevant for vaping usage by smokers we extracted 100 puffs and smoke from 5 tobacco cigarettes for comparison. Vaping anywhere from 75-175 puffs from e-cigarettes is equivalent on average to 5-6 tobacco cigarettes per day.[26] Approximately 15-30 puffs from an e-cigarette is considered equivalent to smoke from one tobacco cigarette.[13,28]

Polyaromatic hydrocarbons and tobacco specific nitrosamines 4-(methylnitrosamino)-1-(3-pyridyl)-1-butanone (NNK) and N'-nitrosonornicotine (NNN) are major carcinogens present in cigarette smoke.[27] Most chemicals in tobacco cigarettes and e-cigarettes are similar with slightly lower concentrations reported for e-cigarettes.[13,28] Usually contents of e-cigarettes are loaded into a cartridge and used with a battery operated inhalation device that heats and converts a nicotine solution with additives into an aerosol.[13] The contents of the e-cigarette liquid quoted by manufacturer content lists show tobacco derived nicotine, propylene glycol, vegetable glycerin and natural and artificial flavoring agents.

Our second test targets featured untreated sewage water, partially treated water and completely treated reclaimed water as collected from University of Connecticut water pollution control facility.[18] Water samples were passed through a 0.2 µM syringe filters (Thermo Scientific F2504-6) prior to genotoxic evaluation to remove particulate matter. Genotoxic chemicals present in waste water 2-acetylaminofluorene (2-AAF),[29] 2-naphthylamine (2-NA)[30] and aflatoxin-B_1 (AFB1)[31] were used as reference standards.

7-4. Results

Cigarettes and e-cigarettes. Responses to tobacco smoke components B[a]P, NNK and NNN were measured first. One channel in the microfluidic array was used for each specific

compound (Figure 7-6). Plots of % ECL increase over the blank (1% DMSO in 10 mM phosphate buffer, pH 7.4) vs. concentration of standard (Figure 7-6B) serve as standard calibration curves and their slopes reflect relative rates of DNA damage.[2] Dynamic range was from 3 to 150 µM for all standards. Increase in ECL intensity was observed with increase in test chemical concentration (Figure 7-6). ECL increases in earlier versions of related genotoxicity arrays were confirmed as directly related to amounts of specific metabolite-DNA adducts detected by LC-MS/MS.[2,4,24] In the present array, spot-to-spot variability was ±6 % (n=21) and array-to-array variability was ±7% (n=3) (Figure 7-7). Toluene, with poorly DNA-reactive metabolites,[32] was used as a negative control with negligible ECL change (Figure 7-6).

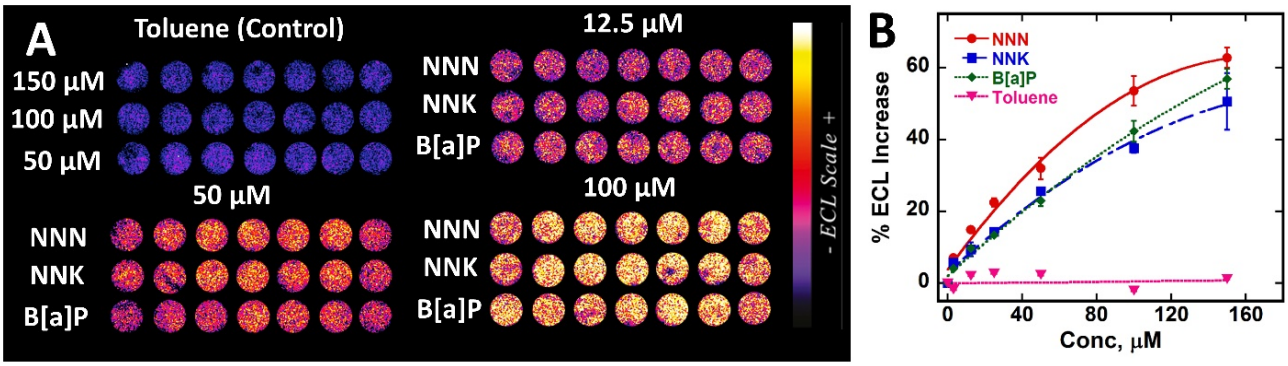

Figure 7-6. Array results for tobacco-related standards with DNA-reactive metabolites: (A) recolorized ECL data using arrays featuring RuPVP/enzyme/DNA microwells treated with oxygenated solutions of carcinogens B[a]P, NNK and NNN and negative control toluene in 1 % DMSO + 10 mM phosphate buffer pH 7.4 for 45 s at -0.65 V vs. Ag/AgCl, with ECL captured by CCD camera after subsequently applying 1.25 V vs Ag/AgCl for 180 s. (B) Calibration plots of % ECL increase over 1% DMSO control vs. concentration of standards. ECL intensity increases proportional to DNA damage that disorders ds-DNA and allows co-reactant guanines in the DNA better access to Ru^{III} sites of RuPVP.[2]

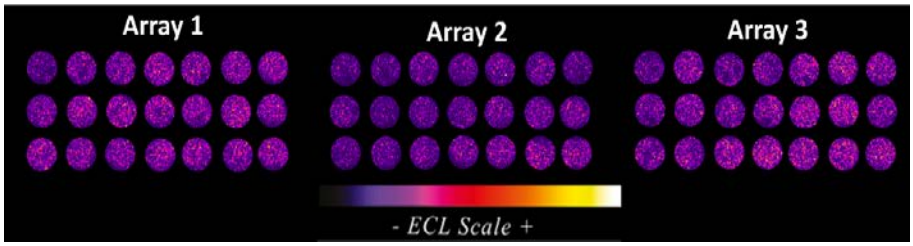

Figure 7-7. Recolorized ECL images from PDDA/PAA/(Ru/DNA)$_2$/RuPVP/Enzyme/DNA films in microwells captured by CCD camera in 10mM phosphate buffer, pH 7.4 upon application of 1.25 V against Ag/AgCl reference electrode for 180 s.

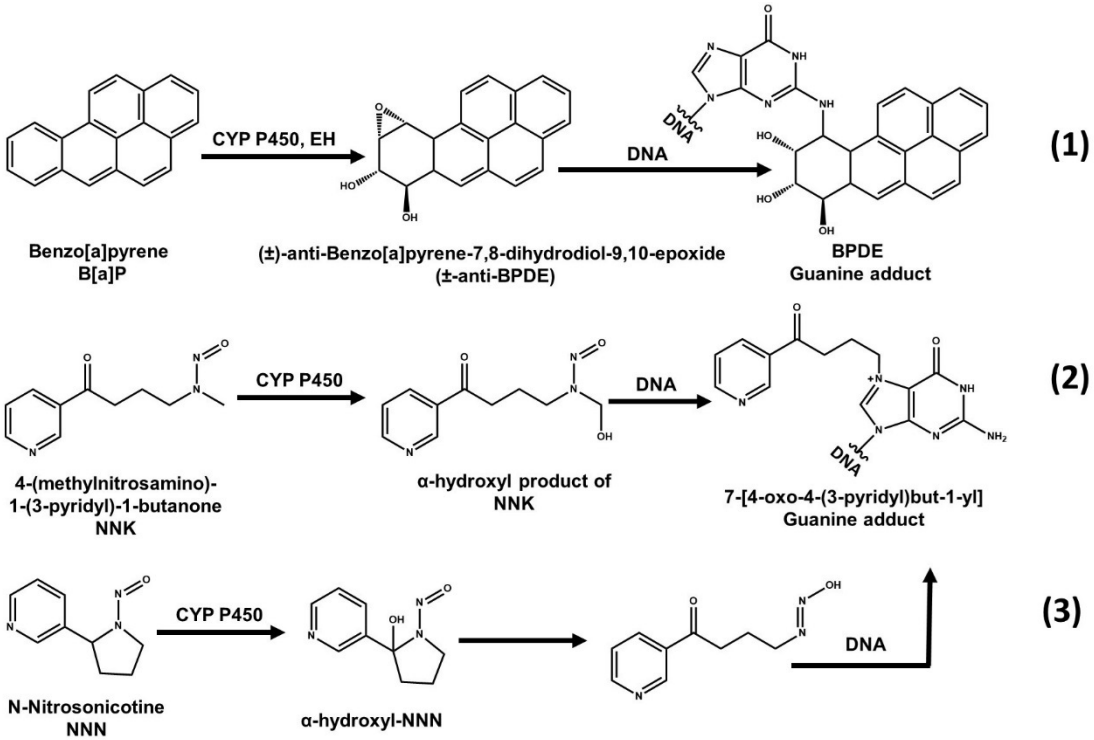

Scheme 1. Cytochrome P450 mediated bioactivation and DNA reactivity of standard chemicals used for cigarette studies ((1) Benzo[a]pyrene (B[a]P), metabolized to benzo[a]pyrene-7,8-dihydrodiol-9,10-epoxide that intercalates and covalently binds predominantly with guanine base in DNA,[33] Adapted from information in ref.33 (2) 4-(methylnitrosoamino)-1-(3-pyridyl)-1-

butanone (NNK) and (3) N-nitrosonicotine (NNN) form hydroxyl forms before binding to nucleobases within DNA.[34] Adapted from information in ref.34.

Previous studies of B[a]P, NNK and NNN confirmed that reactive metabolites of these pro-carcinogens react with DNA to form covalent DNA adducts (Scheme 7-1). B[a]P is a polyaromatic hydrocarbon present in coal tar, cigarette smoke, and grilled meat, Metabolic cyt P450s catalyze B[a]P oxidation to a 7,8 epoxide that is rapidly hydrolyzed to a diol by epoxide hydrolase. The diol is further oxidized by cyt P450 to an epoxide to form ±-anti-benzo[a]pyrene-7,8-dihydrodiol-9.10-epoxide (±-anti-BPDE, eq 1).[33] Major metabolite ±-anti-BPDE is classified as a Group I carcinogen by the International Agency of Research on Cancer (IARC). It is a strong electrophile that reacts with DNA nucleobases of to form covalent adducts. The major covalent adduct is formed by ±-anti-BPDE reaction with the exocyclic amine of nucleobase guanine to form a stable covalent adduct (Scheme 7-1, eq. 1). Similarly, the tobacco specific nitroso amines NNK and NNN undergo α-hydroxylation catalyzed by cyt P450s to form reactive metabolites that react with DNA to form adducts at the N7 position of guanine (Scheme 7-1, eqs 2 and 3).[2,34,35]

Cigarette smoke and E-cigarette vapor trapped in the inhalation device Figure 7-5 was extracted into DMSO, and diluted 100-fold in pH 7.4 buffer prior to analysis. Vapor extract from 20 puffs of e-cigarettes was taken as equivalent to smoke from one tobacco cigarette.[13,28] We found large increases in ECL intensity with increases in amount of extracted cigarette smoke and e-cigarette vapor (Figure 7-8A), suggesting increased amounts of DNA damage[2,4] (Figure 7-8A,B). The most important finding is that %ECL values for equivalent numbers of puffs are slightly larger for e-cigarettes than for tobacco cigarettes, and much larger than for filtered tobacco cigarettes and non-nicotine e-cigarettes. These differences are significant at 95% confidence levels

(t-tests) and suggest that chemicals in the vapor of nicotine e-cigarettes metabolized in the array are at least as DNA-reactive as those in smoke of unfiltered tobacco cigarettes.

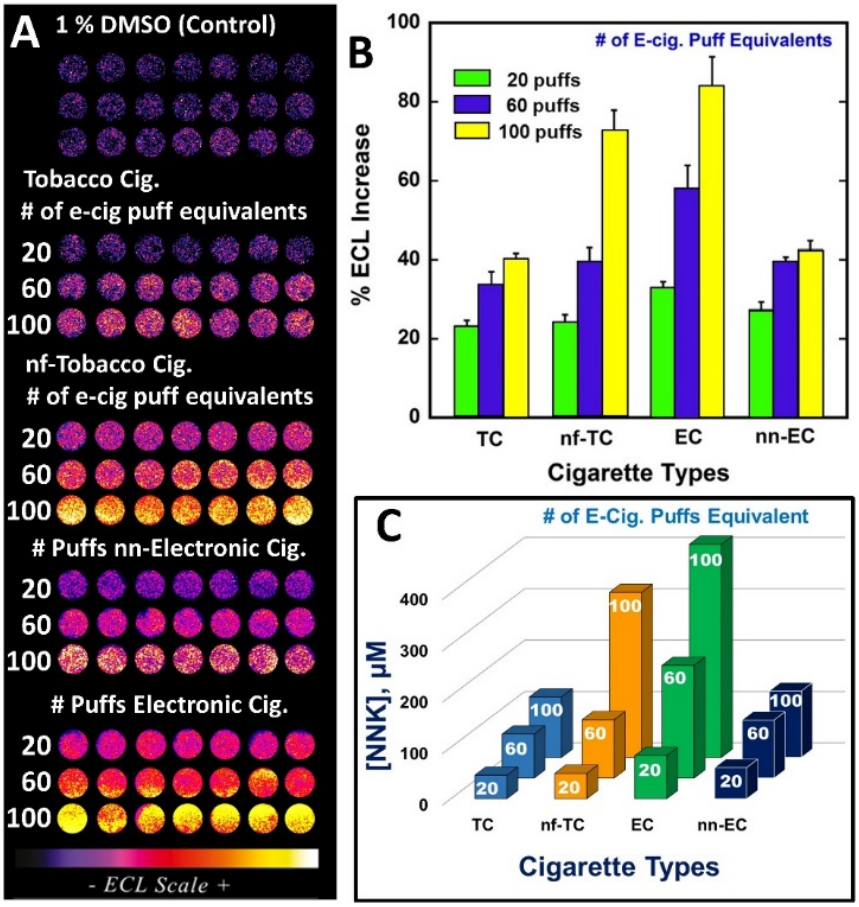

Figure 7-8. ECL array results comparing extracted vapor from e-cigarettes with extracted smoke from tobacco cigarettes using the conversion that 20 e-cigarette puffs equals smoke from one tobacco cigarette {Abbrev.: Tobacco Cigarettes (TC), e-Cigarettes (EC), non filtered (nf) and non-nicotine (nn)}: [13,28] **(**A) Recolorized ECL data from arrays. Each row represents microwells containing RuPVP/Enzyme/DNA layers treated with smoke extracted from 1, 3 and 5 TC & nf-TC (equivalent to 20, 60 and 100 puffs of e-cig.) and 20, 60 and 100 puffs of EC & non-nicotine (nn)-EC in 1% DMSO containing buffer for 45 s under potential of -0.65 V vs. Ag/AgCl. ECL captured while applying 1.25 V vs Ag/AgCl for 180 s. (B) % ECL increase over control (1%

DMSO in buffer) vs. cigarette samples. C) NNK equivalents from %ECL for different cigarette samples.

The difference in %ECL increase between filtered and non-filtered tobacco cigarettes for 20 puff e-cig. equivalents was not statistically different at the 95 % confidence interval. However, for 60 and 100 e-cig. puff equivalents, %ECL was statistically larger for unfiltered cigarettes at the 95% confidence level (Figure 7-8B). DNA reactivity of the non-nicotine e-cigarettes and the filtered tobacco cigarettes denoted by array signals were comparable, and ~1.8-fold smaller than from unfiltered tobacco cigarettes.

Table S1. Genotoxic reactivity of cigarette sample assessed in terms of known carcinogen concentration

Sample	% ECL	NNK		NNN		BaP	
		[Conc.]	STDEV	[Conc.]	STDEV	[Conc.]	STDEV
1 Gen Cig	23.32	45.74	2.58	26.40	1.49	45.54	2.56
3 Gen Cig	33.58	85.52	8.50	49.74	4.94	77.84	7.74
5 Gen Cig	40.46	117.76	3.36	68.77	1.96	102.37	2.92
1 nf-Gen Cig	24.35	49.25	3.43	28.45	1.98	48.52	3.38
3 nf-Gen Cig	39.58	113.41	10.10	66.20	5.90	99.12	8.83
5 nf-Gen Cig	72.57	320.99	23.45	189.80	13.86	241.63	17.65
15 puff e-cig	32.16	79.39	10.52	46.13	6.11	73.03	9.67
30 puffs e- cig	44.83	140.42	11.38	82.18	6.66	119.02	9.64
60 puffs e-cig	60.66	235.95	13.85	138.99	8.16	185.64	10.90
15 puffs nn e-cig	27.74	61.62	3.70	35.70	2.14	58.79	3.53
30 puffs nn e-cig	34.55	89.80	4.34	52.27	2.53	81.16	3.92
60 buffs nn e-cig	37.44	103.10	12.86	60.11	7.50	91.35	11.40
1 e-cig cartridge	35.74	95.19	7.88	55.44	4.59	85.32	7.07
3 e-cig cartridges	166.15	1330.50	169.94	800.78	102.28	816.67	104.31
5 e-cig cartridges	218.43	2127.83	209.67	1288.16	126.93	1220.95	120.31

To link these results to known DNA-reactive chemical metabolites, DNA-reactivity of the samples was expressed in terms of array responses of known tobacco component concentrations of B[a]P, NNK and NNN using Figure 7-6B. This approach puts the results on a common footing related to major genotoxic components in tobacco smoke. Figure 7-8C shows the NNK-equivalent concentration in each of the cigarette types and suggest that nicotine e-cigarettes and unfiltered cigarettes are equivalent to quite significant levels of the potent tobacco carcinogen NNK. Equivalence of sample responses in terms of B[a]P and NNN are reported in Table 7-1, and lead to qualitatively similar conclusions.

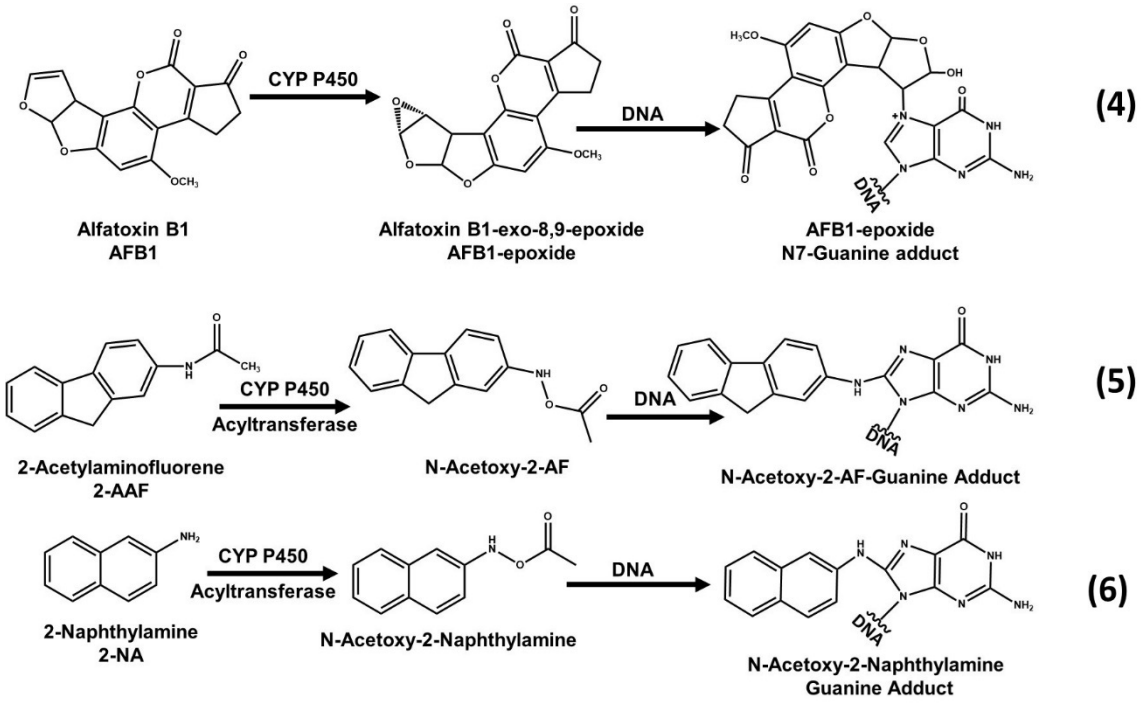

Scheme 7-2. Cytochrome P450 mediated bioactivation and DNA reactivity of standard chemicals used for water samples. (4) Aflatoxin B1 (AFB1), metabolically activated to its epoxide form that forms covalent adducts with DNA nucleobases.[37] Adapted from information in ref.37 (5) 2-acetylaminofluorene (2-AAF)[38] Adapted from information in ref.38 and (6) 2-

naphthylamine (2-NA) form acetoxy forms upon bioactivation that form covalent adducts with DNAnucleobases.[40] Adapted from information in ref.40.

Water samples. Known water pollutants 2-AAF, 2-NA, AFB1 were first tested as reference standards to assess genotoxic potential. Aflatoxins are metabolites of fungal organisms in polluted food and environmental samples and are associated with liver cancer.[36] Aflatoxin B1 is one of the most potent aflatoxins, and requires cyt P450 bioactivation to become carcinogenic. It is oxidized by cyt P450s to the 8,9-epoxide, which reacts with the N7 position of guanine to form covalent adducts (Scheme 7-2, eq. 4).[37] Arylamines are commonly associated with bladder cancer.[38] 2-acetylaminofluorene (2-AAF) and 2-naphthylamine are converted by sequential reactions catalyzed by cyt P450s and acetyl transferase to arylnitrenium ions that react with nucleobases of DNA to form covalent adducts. A major adduct on the C8 position of guanine is shown in Scheme 7-2 (eqs 5,6). [35,39,40]

Array results for these 3 compounds and toluene negative control are shown in Figure 7-9A. Plots of % ECL increase over blank (1% DMSO in pH 7.4 buffer) vs. concentration of standard (Figure 7-9B) serve as calibration curves for water samples. Again, slopes reflect relative rates of DNA damage.[2] Dynamic ranges were from 3 to 100 µM. Limits of detection as %ECL increase 3x the avg. noise were ~3 µM for these genotoxic compounds.

Samples from the University of Connecticut water treatment facility were assayed on the array. Figure 7-9C shows a significant increase in ECL for untreated water samples compared to reclaimed and partially treated water samples. Results from Figure 7-9C are also expressed in terms of equivalent concentrations of the reference standards (Figure 7-9D) to provide comparisons of the relative genotoxicity potential of the samples. E.g. the untreated waste water is equivalent to about 10 µM of the parent chemical 2-AAF.

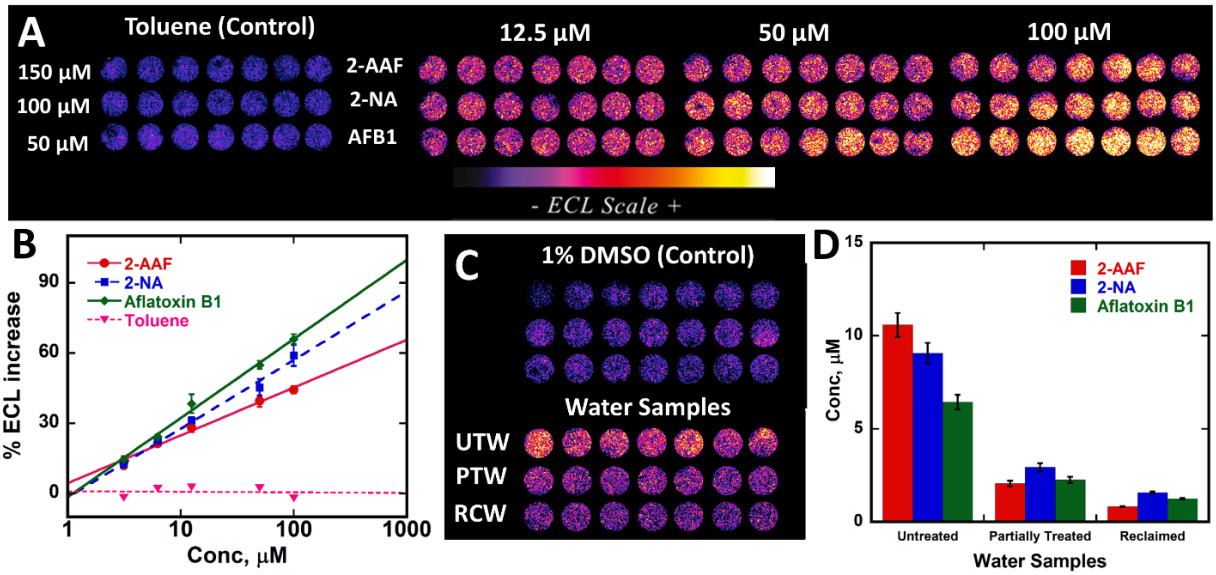

Figure 7-9. Array results for standards with known DNA-reactive metabolites: (A) Recolorized ECL data using arrays featuring RuPVP/enzyme/DNA microwells treated with oxygenated solutions of carcinogens (2-AAF, 2-NA and Aflatoxin B1 and negative control toluene in 1 % DMSO + 10 mM phosphate buffer pH 7.4 for 45 s at -0.65 V vs. Ag/AgCl, with ECL captured by CCD camera after subsequently applying 1.25 V vs Ag/AgCl for 180 s. (B) Calibration plots of % ECL increase over the blank vs. concentration of standards. ECL intensity increases proportional to DNA damage. (C) ECL array results comparing ECL intensities obtained from untreated water (UTW), partially treated water (PTW) and fully treated reclaimed water (RCW) with respect to 1% DMSO controls. Recolorized ECL data from arrays with each row representing microwells containing RuPVP/Enzyme /DNA layers treated with UTW, PTW, RCW& 1% DMSO in buffer for 45 s at -0.65 V vs. Ag/AgCL with ECL captured after subsequent application of 1.25 V vs Ag/AgCl for 180 s. (D) Bar graph showing chemical equivalents from %ECL response for different water samples.

Compared to the untreated waste water, the difference from the treated reclaimed water is significant at the 95% confidence level. Results suggest that more potentially genotoxic chemicals in the untreated waste water are converted on the array to metabolites that are reactive with DNA compared to reclaimed or partially treated water samples. The larger % ECL for partially treated water compared to fully reclaimed water was also statistically significant at 95 % confidence (Figure 7-9C, D). Genotoxic potential in terms of DNA reactivity of untreated water samples was ~10 fold larger than fully reclaimed water and ~2.4 fold larger than partially treated water.

7-5. Discussion.

Results above illustrate a novel, low cost, 3D-printed microfluidic array capable of assessing the genotoxic potential of environmental samples. The 3D printed device with disposable microwell array containing enzyme/DNA/RuPVP films costs less than **$**1.00 to fabricate. Advantages of this device include, multi analyte analysis, complete automation, on chip metabolite generation, and rapid detection of DNA damage (5 min). These disposable arrays are designed to "plug-in" to a reusable automation platform featuring microcontrollers, micropumps, and battery that costs **$**150. The array here was equipped with 21 detection microwells, but is possible to expand to larger size to accommodate multiple enzymes, multiple analytes, and higher sample throughput.

DNA-reactivity related to metabolites from smoke or vapor extracts measured by the array clearly suggests comparable genotoxic potential of tobacco and nicotine e-cigarettes when assayed by the same protocol (Figure 7-8). Expression of the signals in terms of levels of known tobacco chemicals with metabolites having high rates of DNA damage, e.g. NNK (Figure 7-8D) provides a reference point to assess the severity of possible genotoxicity, without having to determine

individual DNA adducts by expensive LC-MS/MS assays. E-cigarette vapor was reported to have low concentrations of chemicals with potential to cause DNA damage[13] and could be assumed by some to be a safer alternative to tobacco cigarettes. However, our results suggest similar DNA damage from e-cigarette vapors and tobacco cigarette smoking.

Results also showed that genotoxic potential for non-nicotine e-cigarettes is about the same as for filtered tobacco cigarettes, and 1.5-2 fold lower than for e-cigarettes. DNA reactivity for 20 puffs of an e-cigarette was equivalent to about 83 µM NNK (1.6 µg/mL) (Figure 7-8C) compared to estimated levels of NNK in one tobacco cigarette of 46 µM (0.9 µg/mL). Unfiltered tobacco cigarettes gave DNA reactivity nearly 2 times greater than filtered tobacco cigarettes (Figure 7-8B&C). Even non-nicotine e-cigarettes showed significant DNA reactivity, similar to that of filtered tobacco cigarettes (Figure 7-8C).

The above results are consistent with recent reports using conventional assays that found significant DNA strand breaks, cytotoxic effects, and cell death caused by e-cigarette vapor with and without nicotine.[41,42] Ease of use of e-cigarettes may also result in elevated use compared to tobacco cigarettes, which can result in escalated DNA damage. For example, DNA reactivity as NNK equivalents in vapor extract from 2 full e-cigarette cartridges was 1.1 mM, roughly equivalent to 0.9 mM for 20 tobacco cigarettes (Table 7-1).

The arrays also revealed genotoxic potential of water samples (Figure 7-9). ECL responses from the untreated waste water were about 9 times larger than fully recovered water suggesting significant presence of genotoxic chemicals. Successful analysis of samples during mid-treatment suggests that the array can be used to monitor the success of intermediate stages of water treatment. Expression of these results in terms of water polluting chemicals that cause metabolite-related DNA damage again provide a rapid assessment of relative severity of the contamination (Figure

7-9D). Calibration range and LOD of 3 μM for standard water pollutants (Figure 7-9B) suggests applications in rapid identification of seriously polluted water. Array results for the untreated water samples are consistent with reports of genotoxic chemicals in domestic and industrial waste water.[43] ECL responses from fully reclaimed water did not show significant genotoxic potential when compared to controls suggesting significant removal of genotoxic chemicals.

7-6. Summary

In summary, we described here a new, portable low cost, automated, toxicity screening tool to detect metabolite-related genotoxicity chemistry from environmental samples. The 3-D printed array is fast and accurate in sensing effects of possible genotoxic chemicals. A unique feature is that test chemicals are converted to their metabolites so that metabolite reactivity towards genetic material can be measured rapidly and efficiently. This is a major attribute for assessment of possible genotoxic consequences of pollutant exposure from relevant samples.

7-7. References

1. (a) Caldwell, J. C. DEHP: Genotoxicity and potential carcinogenic mechanisms—A review. *Mutation Research/Reviews in Mutation Research* **2012**, *751*, 82-157. (b) Chen, R. J.; Chang, L. W.; Lin, P.; Wang, Y. J. Epigenetic effects and molecular mechanisms of tumorigenesis induced by cigarette smoke: an overview. *J. Oncol.* **2011**, *2011*, 654931.
2. (a) Hvastkovs, E. G.; Schenkman, J. B.; Rusling, J. F. Metabolic toxicity screening using electrochemiluminescence arrays coupled with enzyme-DNA biocolloid reactors and liquid chromatography-mass spectrometry. *Annu. Rev. Anal. Chem. (Palo Alto Calif)* **2012**, *5*, 79-105. (b) Hvastkovs, E. G.; Rusling, J. F. State-of-the-Art Metabolic Toxicity Screening and Pathway Evaluation. *Anal. Chem.* **2016**, *88*, 4584-4599.
3. (a) Rogers, K. Recent advances in biosensor techniques for environmental monitoring. *Anal. Chim. Acta* **2006**, *568*, 222-231. (b) Long, F.; Zhu, A.; Shi, H. Recent advances in optical biosensors for environmental monitoring and early warning. *Sensors* **2013**, *13*, 13928-13948.
4. Mani, V.; Kadimisetty, K.; Malla, S.; Joshi, A. A.; Rusling, J. F. Paper-based electrochemiluminescent screening for genotoxic activity in the environment. *Environ. Sci. Technol.* **2013**, *47*, 1937-1944.
5. (a) Gross, B. C.; Erkal, J. L.; Lockwood, S. Y.; Chen, C.; Spence, D. M. Evaluation of 3D printing and its potential impact on biotechnology and the chemical sciences. *Anal. Chem.* **2014**, *86*, 3240-3253. (b) Bishop, G. W.; Satterwhite-Warden, J. E.; Kadimisetty, K.; Rusling, J. F. 3D-printed bioanalytical devices. *Nanotechnology* **2016**, *27*, 284002.
6. (a) Lee, W.; Kwon, D.; Choi, W.; Jung, G. Y.; Au, A. K.; Folch, A.; Jeon, S. 3D-printed microfluidic device for the detection of pathogenic bacteria using size-based separation in helical channel with trapezoid cross-section. *Scientific reports* **2015**, *5*, 7717. (b) Coskun, A.

F.; Nagi, R.; Sadeghi, K.; Phillips, S.; Ozcan, A. Albumin testing in urine using a smart-phone. *Lab on a Chip* **2013**, *13*, 4231-4238. (c) Wei, Q.; Luo, W.; Chiang, S.; Kappel, T.; Mejia, C.; Tseng, D.; Chan, R. Y. L.; Yan, E.; Qi, H.; Shabbir, F. Imaging and sizing of single DNA molecules on a mobile phone. *ACS nano* **2014**, *8*, 12725-12733. (d) Coskun, A. F.; Wong, J.; Khodadadi, D.; Nagi, R.; Tey, A.; Ozcan, A. A personalized food allergen testing platform on a cellphone. *Lab on a Chip* **2013**, *13*, 636-640. (e) Wei, Q.; Nagi, R.; Sadeghi, K.; Feng, S.; Yan, E.; Ki, S. J.; Caire, R.; Tseng, D.; Ozcan, A. Detection and spatial mapping of mercury contamination in water samples using a smart-phone. *ACS nano* **2014**, *8*, 1121-1129. (f) Kitson, P. J.; Rosnes, M. H.; Sans, V.; Dragone, V.; Cronin, L. Configurable 3D-Printed millifluidic and microfluidic 'lab on a chip'reactionware devices. *Lab on a Chip* **2012**, *12*, 3267-3271. (g) Kitson, P. J.; Symes, M. D.; Dragone, V.; Cronin, L. Combining 3D printing and liquid handling to produce user-friendly reactionware for chemical synthesis and purification. *Chemical Science* **2013**, *4*, 3099-3103. (h) Dragone, V.; Sans, V.; Rosnes, M. H.; Kitson, P. J.; Cronin, L. 3D-printed devices for continuous-flow organic chemistry. *Beilstein journal of organic chemistry* **2013**, *9*, 951-959.

7. (a) Bhargava, K. C.; Thompson, B.; Malmstadt, N. Discrete elements for 3D microfluidics. *Proc. Natl. Acad. Sci. U. S. A.* **2014**, *111*, 15013-15018. (b) Snowden, M. E.; King, P. H.; Covington, J. A.; Macpherson, J. V.; Unwin, P. R. Fabrication of versatile channel flow cells for quantitative electroanalysis using prototyping. *Anal. Chem.* **2010**, *82*, 3124-3131. (c) Erkal, J. L.; Selimovic, A.; Gross, B. C.; Lockwood, S. Y.; Walton, E. L.; McNamara, S.; Martin, R. S.; Spence, D. M. 3D printed microfluidic devices with integrated versatile and reusable electrodes. *Lab on a Chip* **2014**, *14*, 2023-2032. (d) Saggiomo, V.; Velders, A. H. Simple 3D printed scaffold-removal method for the fabrication of intricate microfluidic

devices. *Advanced Science* **2015**, *2*, DOI: 10.1002/advs.201500125. (e) Lee, K. G.; Park, K. J.; Seok, S.; Shin, S.; Park, J. Y.; Heo, Y. S.; Lee, S. J.; Lee, T. J. 3D printed modules for integrated microfluidic devices. *RSC Advances* **2014**, *4*, 32876-32880.

8. (a) Bishop, G. W.; Satterwhite, J. E.; Bhakta, S.; Kadimisetty, K.; Gillette, K. M.; Chen, E.; Rusling, J. F. 3D-printed fluidic devices for nanoparticle preparation and flow-injection amperometry using integrated prussian blue nanoparticle-modified electrodes. *Anal. Chem.* **2015**, *87*, 5437-5443. (b) Bishop, G. W.; Satterwhite-Warden, J. E.; Bist, I.; Chen, E.; Rusling, J. F. Electrochemiluminescence at bare and DNA-coated graphite electrodes in 3D-printed fluidic devices. *ACS sensors* **2015**, *1*, 197-202.
9. Kadimisetty, K.; Mosa, I. M.; Malla, S.; Satterwhite-Warden, J. E.; Kuhns, T. M.; Faria, R. C.; Lee, N. H.; Rusling, J. F. 3D-printed supercapacitor-powered electrochemiluminescent protein immunoarray. *Biosensors and Bioelectronics* **2016**, *77*, 188-193.
10. Thun, M. J.; Carter, B. D.; Feskanich, D.; Freedman, N. D.; Prentice, R.; Lopez, A. D.; Hartge, P.; Gapstur, S. M. 50-year trends in smoking-related mortality in the United States. *N. Engl. J. Med.* **2013**, *368*, 351-364. (b) Alexandrov, L. B.; Ju, Y. S.; Haase, K.; Van Loo, P.; Martincorena, I.; Nik-Zainal, S.; Totoki, Y.; Fujimoto, A.; Nakagawa, H.; Shibata, T. Mutational signatures associated with tobacco smoking in human cancer. *bioRxiv* **2016**, 051417.
11. Mokdad, A. H.; Marks, J. S.; Stroup, D. F.; Gerberding, J. L. Actual causes of death in the United States, 2000. *JAMA* **2004**, *291*, 1238-1245.
12. (a) Singh, T. Tobacco use among middle and high school students—United States, 2011–2015. *MMWR.Morbidity and mortality weekly report* **2016**, *65*, 361-367. (b) McMillen, R. C.; Gottlieb, M. A.; Shaefer, R. M.; Winickoff, J. P.; Klein, J. D. Trends in Electronic Cigarette

Use Among U.S. Adults: Use is Increasing in Both Smokers and Nonsmokers. *Nicotine Tob. Res.* **2015**, *17*, 1195-1202.

13. (a) Grana, R.; Benowitz, N.; Glantz, S. A. E-cigarettes: a scientific review. *Circulation* **2014**, *129*, 1972-1986. (b) Trtchounian, A.; Williams, M.; Talbot, P. Conventional and electronic cigarettes (e-cigarettes) have different smoking characteristics. *Nicotine Tob. Res.* **2010**, *12*, 905-912.

14. Schwarzenbach, R. P.; Escher, B. I.; Fenner, K.; Hofstetter, T. B.; Johnson, C. A.; von Gunten, U.; Wehrli, B. The challenge of micropollutants in aquatic systems. *Science* **2006**, *313*, 1072-1077.

15. Schwarzenbach, R. P.; Egli, T.; Hofstetter, T. B.; von Gunten, U.; Wehrli, B. Global water pollution and human health. *Annual Review of Environment and Resources* **2010**, *35*, 109-136.

16. a) Gruber, N.; Galloway, J. N. An Earth-system perspective of the global nitrogen cycle. *Nature* **2008**, *451*, 293-296; b) Filippelli, G. M. The global phosphorus cycle: past, present, and future. *Elements* **2008**, *4*, 89-95; c) Jorgenson, A. K. Political-economic Integration, Industrial Pollution and Human Health: A Panel Study of Less-Developed Countries, 1980—2000. *International Sociology* **2009**, *24*, 115-143; d) Watson, S. B. Aquatic taste and odor: a primary signal of drinking-water integrity. *Journal of Toxicology and Environmental Health, Part A* **2004**, *67*, 1779-1795.

17. Ohe, T.; Watanabe, T.; Wakabayashi, K. Mutagens in surface waters: a review. *Mutation Research/Reviews in Mutation Research* **2004**, *567*, 109-149.

18. University of Connecticut (UCONN) water treatment facility http://ecohusky.uconn.edu/water/rwf.html; last accessed 13 Feb 2017.

19. Dennany, L.; Forster, R. J.; Rusling, J. F. Simultaneous direct electrochemiluminescence and catalytic voltammetry detection of DNA in ultrathin films. *J. Am. Chem. Soc.* **2003**, *125*, 5213-5218.

20. http://web2.uconn.edu/rusling/3D_printing.html; last accessed 13 Feb 2017.

21. Tang, C. K.; Vaze, A.; Rusling, J. F. Fabrication of immunosensor microwell arrays from gold compact discs for detection of cancer biomarker proteins. *Lab on a Chip* **2012**, *12*, 281-286.

22. Rusling, J. F.; Wasalathanthri, D. P.; Schenkman, J. B. Thin multicomponent films for functional enzyme devices and bioreactor particles. *Soft matter* **2014**, *10*, 8145-8156.

23. http://www.atmel.com/devices/attiny85.aspx; last accessed 13 Feb 2017.

24. Krishnan, S.; Hvastkovs, E. G.; Bajrami, B.; Choudhary, D.; Schenkman, J. B.; Rusling, J. F. Synergistic metabolic toxicity screening using microsome/DNA electrochemiluminescent arrays and nanoreactors. *Anal. Chem.* **2008**, *80*, 5279-5285.

25. (a) Krishnan, S.; Wasalathanthri, D.; Zhao, L.; Schenkman, J. B.; Rusling, J. F. Efficient bioelectronic actuation of the natural catalytic pathway of human metabolic cytochrome P450s. *J. Am. Chem. Soc.* **2011**, *133*, 1459-1465. (b) Wasalathanthri, D. P.; Faria, R. C.; Malla, S.; Joshi, A. A.; Schenkman, J. B.; Rusling, J. F. Screening reactive metabolites bioactivated by multiple enzyme pathways using a multiplexed microfluidic system. *Analyst* **2013**, *138*, 171-178.

26. (a) Etter, J.; Bullen, C. A longitudinal study of electronic cigarette users. *Addict. Behav.* **2014**, *39*, 491-494. (b) Etter, J.; Bullen, C. Electronic cigarette: users profile, utilization, satisfaction and perceived efficacy. *Addiction* **2011**, *106*, 2017-2028. (c) Etter, J. Electronic cigarettes: a survey of users. *BMC Public Health* **2010**, *10*, 231.

27. Shihadeh, A.; Saleh, R. Polycyclic aromatic hydrocarbons, carbon monoxide,"tar", and nicotine in the mainstream smoke aerosol of the narghile water pipe. *Food and Chemical Toxicology* **2005**, *43*, 655-661.

28. (a) Grana, R. A.; Ling, P. M. "Smoking revolution": a content analysis of electronic cigarette retail websites. *Am. J. Prev. Med.* **2014**, *46*, 395-403. (b) Goniewicz, M. L.; Kuma, T.; Gawron, M.; Knysak, J.; Kosmider, L. Nicotine levels in electronic cigarettes. *Nicotine Tob. Res.* **2013**, *15*, 158-166.

29. López-Barea, J.; Pueyo, C. Mutagen content and metabolic activation of promutagens by molluscs as biomarkers of marine pollution. *Mutation Research/Fundamental and Molecular Mechanisms of Mutagenesis* **1998**, *399*, 3-15.

30. Le Curieux, F.; Marzin, D.; Erb, F. Comparison of three short-term assays: results on seven chemicals: Potential contribution to the control of water genotoxicity. *Mutation Research/Genetic Toxicology* **1993**, *319*, 223-236.

31. Žegura, B.; Heath, E.; Černoša, A.; Filipič, M. Combination of in vitro bioassays for the determination of cytotoxic and genotoxic potential of wastewater, surface water and drinking water samples. *Chemosphere* **2009**, *75*, 1453-1460.

32. Pan, S.; Zhao, L.; Schenkman, J. B.; Rusling, J. F. Evaluation of electrochemiluminescent metabolic toxicity screening arrays using a multiple compound set. *Anal. Chem.* **2011**, *83*, 2754-2760.

33. (a) Xue, W.; Warshawsky, D. Metabolic activation of polycyclic and heterocyclic aromatic hydrocarbons and DNA damage: a review. *Toxicol. Appl. Pharmacol.* **2005**, *206*, 73-93. (b) Straif, K.; Baan, R.; Grosse, Y.; Secretan, B.; El Ghissassi, F.; Cogliano, V. Carcinogenicity of polycyclic aromatic hydrocarbons. *Lancet Oncology* **2005**, *6*, 931.

34. Hecht, S. S. Tobacco carcinogens, their biomarkers and tobacco-induced cancer. *Nature Reviews Cancer* **2003**, *3*, 733-744.

35. Wasalathanthri, D. P.; Li, D.; Song, D.; Zheng, Z.; Choudhary, D.; Jansson, I.; Lu, X.; Schenkman, J. B.; Rusling, J. F. Elucidating organ-specific metabolic toxicity chemistry from electrochemiluminescent enzyme/DNA arrays and bioreactor bead-LC-MS/MS. *Chemical Science* **2015**, *6*, 2457-2468.

36. Warth, B.; Sulyok, M.; Krska, R. LC-MS/MS-based multibiomarker approaches for the assessment of human exposure to mycotoxins. *Analytical and bioanalytical chemistry* **2013**, *405*, 5687-5695.

37. Phillips, D. H.; Farmer, P. B.; Beland, F. A.; Nath, R. G.; Poirier, M. C.; Reddy, M. V.; Turteltaub, K. W. Methods of DNA adduct determination and their application to testing compounds for genotoxicity. *Environ. Mol. Mutagen.* **2000**, *35*, 222-233.

38. Mimi, C. Y.; Skipper, P. L.; Tannenbaum, S. R.; Chan, K. K.; Ross, R. K. Arylamine exposures and bladder cancer risk. *Mutation Research/Fundamental and Molecular Mechanisms of Mutagenesis* **2002**, *506*, 21-28.

39. Wasalathanthri, D. P.; Faria, R. C.; Malla, S.; Joshi, A. A.; Schenkman, J. B.; Rusling, J. F. Screening reactive metabolites bioactivated by multiple enzyme pathways using a multiplexed microfluidic system. *Analyst* **2013**, *138*, 171-178.

40. Arlt, V. M.; Schmeiser, H. H.; Osborne, M. R.; Kawanishi, M.; Kanno, T.; Yagi, T.; Phillips, D. H.; Takamura-Enya, T. Identification of three major DNA adducts formed by the carcinogenic air pollutant 3-nitrobenzanthrone in rat lung at the C8 and N2 position of guanine and at the N6 position of adenine. *International journal of cancer* **2006**, *118*, 2139-2146.

41. Yu, V.; Rahimy, M.; Korrapati, A.; Xuan, Y.; Zou, A. E.; Krishnan, A. R.; Tsui, T.; Aguilera, J. A.; Advani, S.; Alexander, L. E. C. Electronic cigarettes induce DNA strand breaks and cell death independently of nicotine in cell lines. *Oral Oncol.* **2016**, *52*, 58-65.

42. (a) Wei, B.; Blount, B. C.; Xia, B.; Wang, L. Assessing exposure to tobacco-specific carcinogen NNK using its urinary metabolite NNAL measured in US population: 2011–2012. *Journal of Exposure Science and Environmental Epidemiology* **2015,** *26*, 249-256. (b) Zhong, Y.; Carmella, S. G.; Upadhyaya, P.; Hochalter, J. B.; Rauch, D.; Oliver, A.; Jensen, J.; Hatsukami, D.; Wang, J.; Zimmerman, C. Immediate consequences of cigarette smoking: rapid formation of polycyclic aromatic hydrocarbon diol epoxides. *Chem. Res. Toxicol.* **2010**, *24*, 246-252.

43. (a) White, P. A.; Rasmussen, J. B. The genotoxic hazards of domestic wastes in surface waters. *Mutation Research/Reviews in Mutation Research* **1998**, *410*, 223-236. (b) Thewes, M. R.; Endres Junior, D.; Droste, A. Genotoxicity biomonitoring of sewage in two municipal wastewater treatment plants using the Tradescantia pallida var. purpurea bioassay. *Genetics and molecular biology* **2011**, *34*, 689-693. (C) Žegura, B.; Heath, E.; Černoša, A.; Filipič, M. Combination of in vitro bioassays for the determination of cytotoxic and genotoxic potential of wastewater, surface water and drinking water samples. *Chemosphere* **2009**, *75*, 1453-1460.

Chapter 8

Sequence Specific Genotoxic Assessment Using LC-MS/MS

8-1. Introduction.

The p53 (or TP53) tumor suppressor gene codes for p53 protein that regulates cell division, cell death, genomic stability and suppresses cancer. P53 gene mutations occur in over 50% of human cancers,[1] and are located selectively in exons 5-8, and alter the p53 protein so as to minimize cancer protection. *TP53* (or p53) was confirmed as a tumor suppressor gene in the 1980s,[2] and other tumor suppressor genes such as retinoblastoma (RB), Wilms Tumor 1 (WT1), Adenomatosis Polyposis Coli (APC), and p16 have also been discovered. Furthermore, mutation sites within P53 gene are correlated with specific cancers,[3,4] so that prediction of the most reactive p53 codons toward new chemicals and their metabolites could be a valuable tool to aid in toxicity and cancer prediction.

Xenobiotic chemicals and their metabolites can damage tumor suppressor genes. More than 50 % of human cancers are known to have mutations in the *p53* gene.[5-9] Human exposure to various carcinogens and specific mutated codons in the *p53* gene leading to the development of specific cancers.[3] Exon 5-8 are most mutated codons in the P53 gene[10,11] Mutational spectra on the *p53* gene are correlated with the incidence of tissue specific cancers. For example, data in the p53 database handbook shows that highly mutated reactive *hot spots* include codons 157, 158, 248, 249 in lung cancer, codon 273 in brain and prostate cancer, codons 175, 248 and 273 in breast cancer and codons 175, 282 and 248 in liver cancer.[12] Codon *hot spots* for reactions of metabolites on the *p53* gene have been linked to human exposure to particular carcinogens. Specifically, components of tobacco smoke are related to lung cancer, tobacco smoke and alcohol to head and

neck cancers, aromatic amines to bladder cancer, aflatoxine-B1 and hepatitis B virus to liver cancer and ultraviolet light to skin cancer. Thus, exposure to specific carcinogens that lead to damage to the *p53* gene can be correlated with organ-specific cancers.

These relationships between the mutational spectra of p53 to organ-specific cancers are clearly indicated in large databases integrating extensive p53 research.[13] These data include genomic studies of patient tumors and cell lines, and show that **the** *p53* gene has 7 reactive hot spots between bases 361 and 920 of the reading frame, one in exon 5, one in exon 6, five in exon 7 and two in exon 8. Screening of a wide range of carcinogens by assessing reactive hot spots on p53 in vitro could identify reactive nucleobases within codons that, if correlated with mutational spectra, could be used to predict tissue specific cancers. This sort of information is not available for large libraries of potentially reactive compounds or metabolites on p53, and is almost non-existent for other tumor suppressor genes.[14] New methods for screening reactive metabolites for sequence specific tumor suppressor gene damage would be valuable tools to assess the potential of new drugs and environmental chemicals for organ-specific carcinogenicity.

Reactants such as benzo[a]pyrene-7,8-dihydrodiol-9,10-epoxide (BPDE), 7,12-dimethylbenz(a)anthracene diol epoxide, acrolein, and mitocin C, are more reactive towards MeCpG sites on the genes.[19,20] Limited repair of these reacted sites contributes to their role as mutational hot spots. Polyaromatic hydrocarbon (PAHs) metabolites preferentially react with MeCpG sites.[15] E.g., benzo[a]pyrene is metabolized to BPDE by a sequential pathway involving cytochrome P450s and epoxide hydrolase,[16,17] and reacts with DNA in S_N2 reactions to form nucleobase adducts that lead to mutations.[18] Within the p53 gene, 42 CpG sites are methylcytosines (MeC),[19,20] and are the most frequently mutated codons or *hot spots*.[21,22] Non-CpG MeC related to GC>AT transitions are known in lung, head and neck cancer.[23]

Mass spectrometry (MS) is a valuable tool for structural analysis of DNA, and LC-MS/MS methodologies have been developed over the past decade for sizing and sequencing oligonucleotides of up to 20 base pairs (bp).[24-28] Harsch, reacted a 10 base pair oligonucleotide derived from hypoxanthine-guanine phosphoribosyltransferase gene (HPRT gene) with benzo[c]phenanthrene and determined positional isomers in the product.[29] Chowdhury and Guengerich reacted a 15 base pair oligonucleotide incorporating hot spot codon 157 on exon 5 of p53 gene with mutagenic molecules benzo[a]pyrene-7,8-dihydrodiol-9,10-epoxide (BPDE) and N-hydroxy-4-aminobiphenyl (N-OH-4ABP) and used MS/MS to determine site reactivity.[30] They also determined C-4 oxidized abasic sites on a 15-mer oligonucleotide.[26] Sharma et. al., reacted a 17-mer incorporating codon 135 of p53 with 2-acetylAminofluorene (AAF), and observed multiple adducts formed from reactions with guanosines.[31] Satterwhite et. al., reacted a 21-mer of p53 containing codon 273 with BPDE.[32] Xiong et. al., reacted a 14 mer ds DNA containing hot spot codons 157 and 158 with BPDE. Xiong et. al., reacted a 14 mer ds DNA containing hot spot codons 157 and 158 with BPDE.[24] Sharma et. al., studied a 15 base pair DNA containing codon 135 with 2-AAF [31] and also investigated 14 mer ds DNA with codons 157 and 158 [33] in reactions with BPDE, AAF and N-OH-4ABP.

Previous studies of alkylated CpGs on DNA exon 5 analogs using [$^{15}N_3$, $^{13}C_1$]-labeled guanines and oligonucleotide hydrolysis revealed 2-3 fold increases in yields of BPDE adduction for MeCs.[34] MeCpG's also enhanced DNA-acrolein adduction 2-fold.[35,36] A 21-base pair (bp) oligonucleotide with a CpG site gave MeC-dependent voltammetry suggesting enhanced BPDE reactivity.[37] A 14 bp oligonucleotide with four MeCpG sites gave 3-4 fold increased adduction yields compared to unmethylated CpG.[38] In the 1990s, Geacintov measured strong non-covalent binding between BPDE and ds-poly(dG-dC).(dG-dC) oligonucleotides and proposed enhanced

subsequent coupling with MeCs related to stronger binding in a preceding step.[39,40] This model was supported by the studies of alkyl-C exon 5 analogs.[34]

Previous studies have been restricted to ds-oligonucleotides smaller than 20 bp to enable direct LC-MS/MS sequencing. The short strands studies thus far contained only a single reaction site, and thus did not address relative reactivity between different sites or correlations with mutation frequencies in tumors. Further, short strands may exhibit altered structural specificity in nucleophilic addition compared to natural tumor suppressor genes that may show tertiary and quaternary structural influences on codon reactivity.[41-45]

In this paper, we report an LC-MS/MS study of ds fragment of 32 bp of p53 gene exon 7, from codon 242 to 253. This fragment exhibits up to 5 reactive hot spots[13] and our work represents metabolite reactivity of a p53 strand (>20base pairs) with multiple mutation sites. The 32 bp fragment was chosen to be long enough to mimic higher order structure-reactivity of DNA.[43] This fragment was reacted with BPDE, the major DNA-reactive metabolite of benzo[a]pyrene,[46-48] and then a restriction enzyme was used to cleave the fragment into smaller fragments to enable LC-MS/MS sequencing.

Mutational hot spots within this 32 bp fragment include 248, 245, and 249 associated with non-small cell lung cancer, 248, 249 and 244 for small cell lung cancer, 248 for head and neck cancer, 248 and 245 for colorectal cancer, 248 and 247 for skin cancer.[10,11,14] Using the approaches described herein, we found that the most frequently BPDE-adducted guanines were within codons 244 and 248, which correlate with frequently mutated p53 sites in several cancers.

For a 32 bp exon 7 p53 duplex fragment, we found adduct yields for reaction with BPDE in the order of codons 248>243>244. In the present paper, we adapt this method for the first time to elucidate relationships between codon-specific reaction kinetics with metabolites, and evaluate the

influence of subtle but important MeC-related p53 gene structure changes on reaction kinetics. This approach enabling studies of longer nucleotides that have been previously possible are amenable to uncover the influence of important structural changes relevant to the reactivity of the entire gene.

We compared a MeC form (19 MeCs) with a non-MeC form (Scheme 8-1) of the 32-bp exon 7 p53 fragment. G in codon 248 CpG had the largest rate constant, which was 3-fold for the MeC version compared to all-C. Rate constants for reactive G's in non-CpG codons were 5-8 fold smaller than codon 248 MeCpG. Conformational and hydrophobicity changes in the MeC-p53 fragment revealed by circular dichroism (CD) and molecular modeling combine to increase the binding constant of BPDE at the codon 248 site to greatly facilitates the rate of the S_N2 coupling reaction in line with the preceding non-covalent binding pathway.

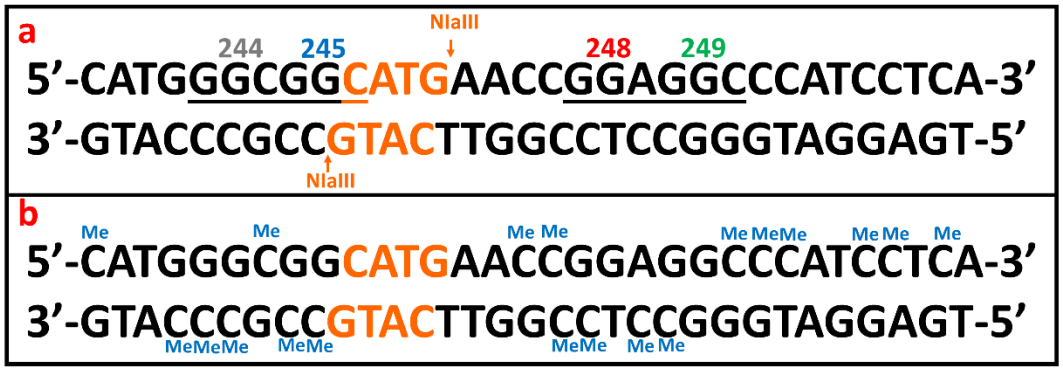

Scheme 8-1. Exon 7 32 bp fragment of p53 gene with major hot spots 244, 245, 248 and 249 labeled grey, blue, red and green. Restriction enzyme cleavage site CATG in orange a) all-C version b) MeC version, all Me except C in restriction enzyme cleavage site.

8-2. Experimental Section

Caution. *Benzo[a]pyrene-r-7,t-8-dihydrodiol-t-9,10-epoxide (+/-) (anti) (anti BPDE) is a chemical carcinogen. Protective measures including wearing gloves and protective eyewear and doing experiments in a closed hood were taken.*

8-2.1 Chemicals and Reagents. Benzo[a]pyrene-r-7,t-8-dihydrodiol-t-9,10-epoxide (+/-) (anti) (anti BPDE) was from National Cancer Institute Chemical Carcinogen Reference Standard Repository. Triethylammonium bicarbonate (TEAB, 1.0 M, pH 8.4-8.6) and 4-nitrobenzyl alcohol were from Sigma-Aldrich. Custom made single stranded DNA oligomers and the 32-base pair oligonucleotide were from Sigma-Aldrich. HPLC grade solvents, methanol, tetrahydrofuran and water were from Fischer Scientific. Restriction enzyme, NIaIII was from New England Biolabs.

8-2.2 Reactions of Oligonucleotides with BPDE. Reactions with BPDE were done with 4 single stranded (ss) oligonucleotides and the double stranded (ds) 32 bp portion of P53 gene representing codons 242 to 253. 0.1 nmol of each of the 4 ss oligonucleotides were treated with 100 nmol BPDE in a reaction volume of 150 µL at 37°C for 48 hours in dark, 10 mM Tris buffer, pH 7.4. 2.5 µmol of ds 32 bp fragment was reacted with 0.1 µmole of BPDE in volume of 150 µL at 37°C for 48 hours in dark, 10 mM Tris buffer, pH 7.4. A minimum of three replicates of DNA and BPDE reactions were done.

8-2.3 Removal of excess BPDE. ss DNA fragments were extracted from the BPDE-ss DNA mixture by extracting with 150 µL of ethylacetate for three times. DNA was recovered from the aqueous phase. Samples were then dried and reconstituted in 100 µL of pure water to make a final concentration of 1 µM ss DNA.

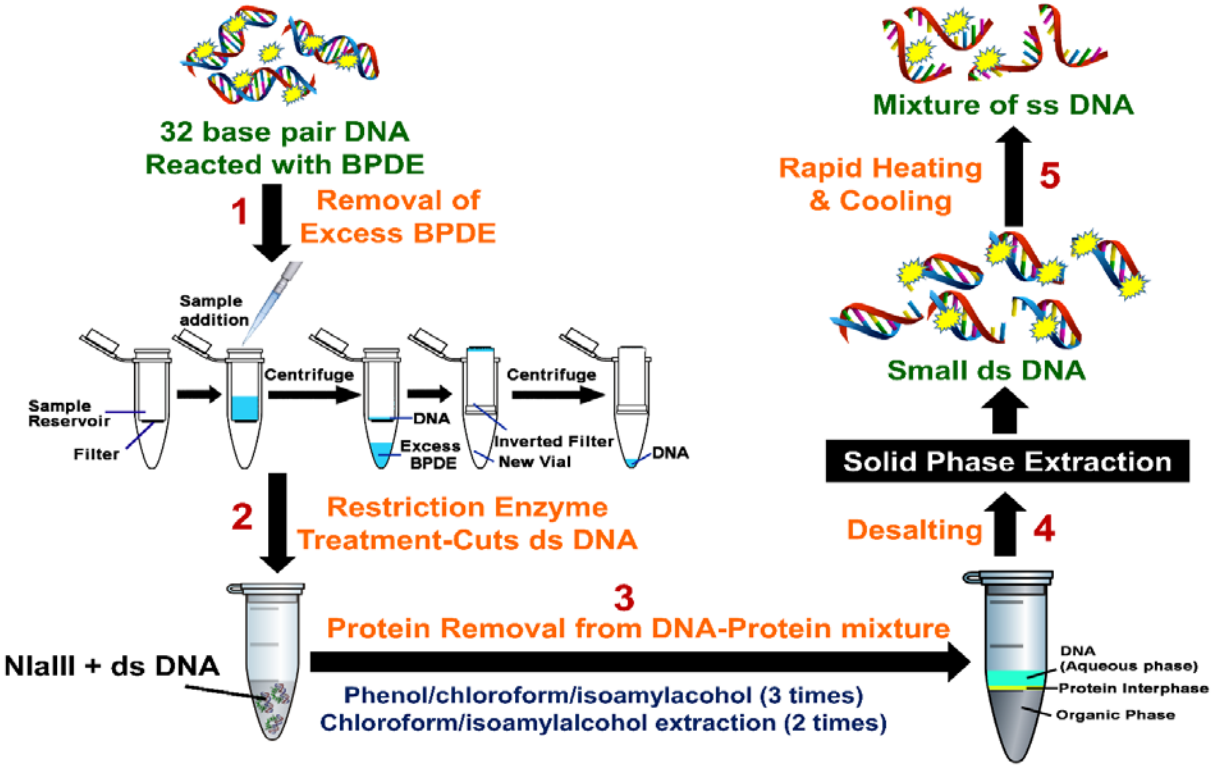

Scheme 8.2 Protocol for sample preparation of 32-base pair p53 fragment reacted with BPDE involving steps: (1) removal of excess BPDE from DNA reaction mixture; (2) restriction enzyme treatment to cut DNA into smaller fragments; (3) protein removal; (4) desalting and (5) rapid heating and cooling to give ss DNA.

For the ds-DNA-BPDE mixtures, Millipore 3000 Dalton mass cutoff filter vials were used to remove unreacted BPDE (Scheme 8-2). Reaction mixture from above was put into a 3000 Da mass cutoff filter, (catalog # UFC500396) and centrifuged at 13000 rpm for 30 min. ds-DNA was retained on the filter, while the smaller BPDE molecules pass through. The filter was then

removed, inverted and placed into a new centrifuge vial, and centrifuged for another 30 min. Approximately 50 µL of the DNA solution was recovered. Recovered solutions of ds oligonucleotides were subjected to restriction enzyme treatment (Scheme 8-2).

8-2.4 Restriction enzyme treatment on ds DNA. Approximately 50 µg (2.5 µmol) of DNA was recovered from above step. 50 units (5 µL) of restriction enzyme, NIaIII was added to 50 µg of the ds 32 bp oligonucleotides to which 20 µL of 10X NE buffer supplied by New England Biolabs, was added and the reaction volume made up to 200 µL with pure water. This reaction mixture was incubated at 37 °C for 8 hours. The resulting solution is mixture of DNA fragments, protein and salt from the NE reaction buffer given by the manufacturer**.**

8-2.5 Removal of Proteins from DNA-Protein-Salt mixture. Proteins were removed from the DNA samples by extraction using 200 µL of water-saturated phenol/chloroform/isoamylalcohol, 25/24/1. Each extraction step involves vortexing on a rotor for 10 min followed by centrifugation for 10 min prior to aqueous phase collection. DNA in the aqueous phase was collected and the extraction procedure was repeated twice more. Further extraction of DNA contained in the aqueous phase was done twice with 200 µL of water-saturated chloroform/isoamylalcohol, 24/1. Finally the aqueous phases were combined and organic phase was discarded. The resulting sample containing DNA and salt was approximately 200 µL.

8-2.6 Desalting. Solid phase extraction (SPE) was performed to remove salt from DNA-salt mixtures to obtain samples suitable for LC-MS/MS analysis. Waters Oasis HLB cartridges were

used for desalting. The method involves initial equilibration of the cartridge with methanol and water. Sample was loaded and then washed with 5% methanol in water to remove salts followed by elution with 100 % methanol. The resultant DNA sample was dried and reconstituted in 100 µL pure water. The ds DNA samples were heated and cooled rapidly to convert ds DNA to ss DNA and stored at -20 ºC until LC-MS/MS analysis.

8-2.6 LC-MS/MS analysis. A Waters Capillary LC-XE (Milliford, MA) chromatograph with a Gemini C-18 column (0.3 mm X 150 mm, 5µ for ds DNA fragments & 0.5 mm X 150 mm, 3µ for ds DNA fragments) and photodiode array detector were used. Separation featured a binary solvent consisting of A - 25 mM TEAB and B - methanol. Separation was achieved with a gradient of 0 % to 10% B for 10 min followed by increase from 10 to 50 % B for 100 min and 50 to 100 % B for the final 10 min at flow rate 10 µL/min. m-Nitrobenzylalcohol increases signal intensity and charge states of oligonucleotide fragments in negative mode, which enhances the fragmentation of oligonucleotides in tandem mass spectrometry.[49] Thus, 0.1 % m-nitrobenzyl alcohol was infused at a flow rate of 3 µL/min to mix with the LC flow post-column using a three way connector before entering the mass spectrometer to produce supercharged oligonucleotide fragments.

ss-DNA fragments were analyzed with an AB Sciex Qtrap 4000 mass spectrometer interfaced to the capillary LC. Enhanced multiple charge (EMC) mode for sizing (molecular weight measurement) and enhanced product ion mode (EPI) for sequencing of ss-DNA fragments in negative mode were employed. Potentials -4500 V (ion spray voltage), 130 V (declustering potential), -60 eV (collision energy), and 20eV (collision energy spread) were used while GS1, GS2, and temperature were kept at 35, 20, and 350°C, respectively.

For analysis of ds-DNA samples, an AB Sciex QSTAR mass spectrometer was interfaced with the capillary LC. Negative ion mode with a -4500 V ion spray voltage, -130 V declustering potential and 300°C temperature was used. DNA fragments were subjected to time of flight mass scan (TOF-MS) mode for sizing of unreacted and adducted DNA fragments and product ion scan mode was used at -45 eV collision energy for MS/MS sequencing. Only singly adducted fragments were discussed in this study.

8-2.8 Circular Dichroism. Circular dichroism experiments on the C and MeC ds-32 base pair exon 7 oligonucleotides were performed on Jasco spectrophotometer (J-710), in 10mM Tris buffer pH 7.4 and 50 mM sodium chloride. Parameter used within the spectrophotometer include sensitivity of 100mdeg, wavelength range 195nm to 230nm with a bandwidth of 5.0 nm.

8-2.9 Molecular Modeling. A and B form's of 32-base pair P53 DNA was modeled using make-na software[50] and modified with cytosines methylated using Maestro software and minimized.[51] Solvated models of these modified oligonucleotides were created using CHIMERA software.[52,53] Amber solvation model was used for solvation with a box size of 1Å to accommodate water molecules. Autodock 4.2.6 was used for docking studies. Prepared biomolecule (Solvated MeC and C 32 base pair exon 7 fragment) were imported into the software. Lamarckian genetic algorithm (LGA) was used in Autodock 4.2.6 to find binding energy between the gene fragments and BPDE. Grid or volume for docking studies were kept constant for all the confirmations and set to be at maximum. Binding energies, binding constants and the distance between the exocyclic amine of the reactive guanine and epoxide carbon of BPDE were calculated.[90] Steps for molecular modeling are given below.

STEPS

A and B form's of 32-base pair P53 DNA was modelled using make-na software and modified with cytosines methylated using Maestro software and minimized. Solvated models of these modified olignucloetides were created using CHIMERA software. Amber solvation model was used for solvation with a box size of 1Å to accommodate water molecules.

Autodock 4.2.6 was used for docking studies. Prepared biomolecule (Solvated MeC and C 32 base pair exon 7 fragment) were imported into the software. Lamarckian genetic algorithm (LGA) was used in Autodock 4.2.6 to find binding energy between the gene fragments and BPDE. Grid or volume for docking studies were kept constant for all the confirmations and set to be at maximum (126X x 126Y x 126Z dimensions). Binding energies, binding constants and the distance between the exocyclic amine of the reactive guanine and epoxide carbon of BPDE were calculated.[54]

Procedure for Docking

1. Import the biomolecule
2. Add Hydrogens to the biomolecule
3. Compute gasteiger charges
4. Now input the Ligand
5. Save the output format of the ligand to be in PDBQT (autodock suitable format)
6. Preparation for grid
    a. Choose Macromolcule (32 bp DNA)
    b. Save as PDBQT

c. Choose ligand (from set map types)

d. Set grid size (maximum grid size used for our study 126 X 126 X 126).

e. Save out put file as .gpf (grid format for autodock).

f. Run autogrid from run option.

7. Docking

a. Select macromolecule and ligand similar to above from docking menu.

b. Search Paparmeters given as # of GA runs to be 100, population size 150, maximum evaluations 250000, maximumber of generations 27000 and other factors kept default. Accept the parameters.

c. Docking parameter kept default.

d. Output saved as default.

e. Run autodock from run menu.

8-3. Results

Initial studies centered on reacting single-strand fragments GGCGGCATG (ss-DNA Fragment 1), including hot spot codon 244 and 245, AACCGGAGGCCCATCCTCA (ss-DNA Fragment 2), including hot spot codon 248 and 249, TGAGGATGGGCCTCCGGTTCATG (ss-DNA Fragment 3, complementary to fragment 2) and CCGCCCATG (ss-DNA Fragment 4, complementary to fragment 1) with BPDE to optimize the LC-MS/MS methodology without using the restriction enzyme.

Our protocol for the 32 base pair exon 7 fragment involves reacting p53 oligonucleotide sequences with BPDE, then using restriction enzymes to cut the reacted fragment into smaller fragments suitable for LC-MS/MS (Scheme 8-3). Our 32 bp exon 7 fragment extends from codon

242 to 253 and includes possible reactive hot spots at codons 244, 245, 247, 248 and 249 related to the various cancers described above. All codons contain guanine except 247 (ACC), which contains a possible reactive adenine. Within this sequence, codon 248 is the most frequently mutated in all cancers. Codons 245, 248 and 249 are adducted for most cancers related to BPDE, which adds to DNA bases by nucleophilic substitution. Our 32 base pair fragment is a combination of ss-DNA fragment 1 and ss-DNA fragment 2 with four additional bases CATG added before the ss-DNA fragment 1. This was done in order to eliminate the possibility of having terminal guanines with enhanced reactivity.

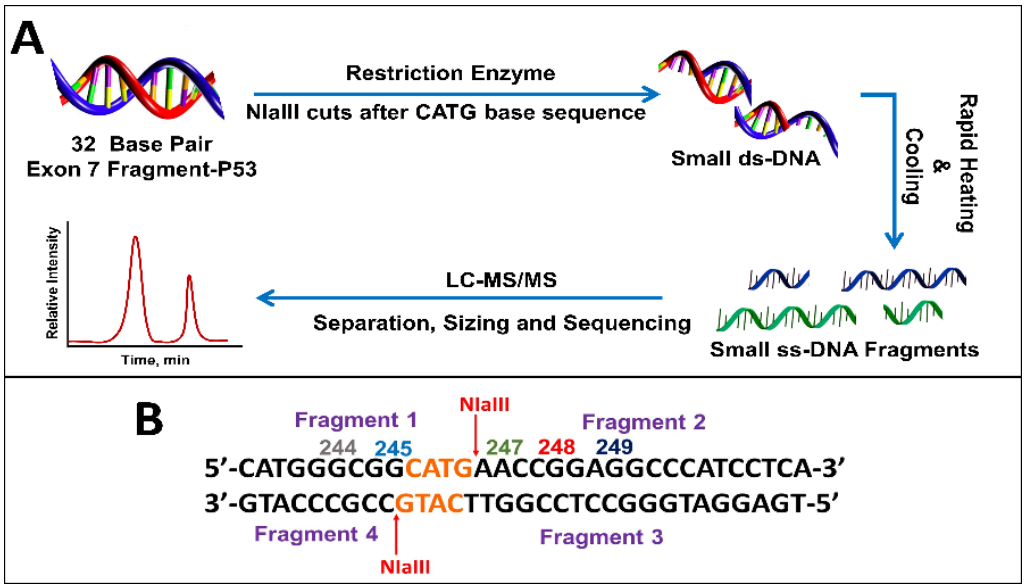

Scheme 8-3. (A) Sample preparation for LC-MS/MS sizing and sequencing of fragment. (B) 32 bp exon 7 fragment showing cut points for restriction enzyme NIaIII along with resulting fragments obtained.

In order to sequence products of 32 base pair oligonucleotide reactions with BPDE by LC-MS/MS, we used the restriction enzyme NlaIII, which cuts DNA after the sequence CATG (Scheme 8-3). For our 32 bp fragment, this results in two fragments of 13 and 19 bases that are double stranded except for 4 bases at their ends (Scheme 8-3B). 13 mer was obtained instead of

the expected 9 mer since the efficiency of restriction enzymes to cut the dsDNA decreases drastically when the recognition site in closer to the 5' end. A minimum of 3-4 extra bases flanking the recognition site on the 5' prime end was required for restriction enzyme to act on ds-DNA.[55] These two ds-fragments were rapidly heated and cooled to give in 4 ss-oligonucleotide fragments (Scheme 8-3A).

We used enhanced multiple charge scanning to size the ss-oligonucleotides, followed by collision-induced dissociation (CID) MS/MS for sequencing. CID of oligonucleotides shows a characteristic fragmentation pattern (**Scheme 8-4**) featuring a_n-b_n and w_n ions.[56-59] Adduction of BPDE to specific nucleobases within codons was monitored by comparing un-adducted oligonucleotides to those reacted with BPDE, and detecting the difference in m/z of the a_n-b_n and w_n ions.

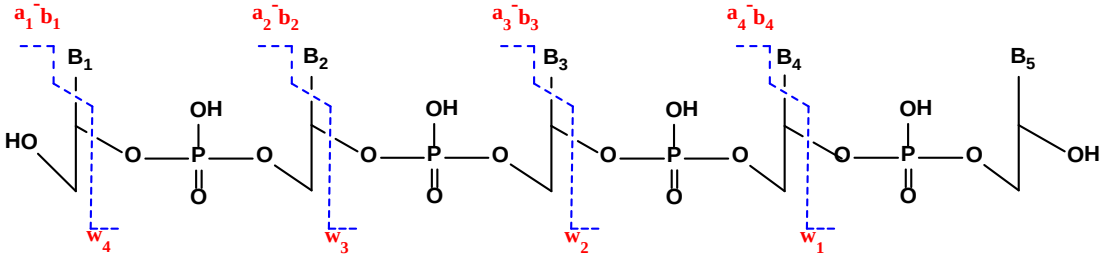

Scheme 8-4. Collision Induced Dissociation (MS/MS or tandem MS) of DNA fragments resulting in the generation of w_n and a_n-b_n ions.

Enhanced multiple charge scans (EMC) were used to determine the m/z of standard and BPDE-adducted DNA fragments that have an additional mass of 302.323. Expected multiple charged species possible were calculated using the online database Mongo oligomass calculator.[60] We first present results for the ss-Fragments. With the ionization conditions used, we observed an m/z of 1388.9 for unreacted ss-Fragment 1 with a charge of -2 and m/z of 1540.5 for the reacted fragment indicating a singly adducted strand also with charge -2.

Extracted ion chromatogram of a selected ion as a function of retention time of singly adducted ss-DNA fragment **1** of m/z 1540.5 shows (Figure 8-1A) that there is a possibility of 2 positional isomers for the singly adducted ss-Fragment 1 at retention times 38.67 and 43.75 min. CID of fragment ion 1540.5 for Peak I is as shown in Figure 8-1B and for Peak II in Figure 8-1C.

Differences in m/z of a-b and w ions between the standard ss-DNA fragment **1** and the singly adducted DNA fragment help locate the exact reacted position on a given oligonucleotide.[61-63] Table 8-1 summarizes fragment ions obtained for standard ss-DNA fragment **1**, singly adducted ss-fragment **1** for peaks I and II. Red numbers indicate those ions increased in mass by 302.32 from adducting with BPDE compared to the unreacted fragment.

MS/MS spectrum for peak I of singly adducted ss-fragment **1** (Figure 8-2B) reveals increase in mass of all the ions from a_3-b_3 to a_6-b_6 and w_8 compared with that of unreacted ss DNA standard. This indicates covalent binding of BPDE on the second G base, GG*CGGCATG. This is additionally confirmed by the presence of ion a_2-b_2 with an m/z of 426.2^- and all ions from w_1 to w_7 with m/z the same as that of the standard.

MS/MS spectrum for peak II of singly adducted ss- fragment **1** reflects increases in m/z for all the w ions compared to unreacted standard (Table 8-1). This indicates covalent binding of BPDE to the last G base, GGCGGCATG*, which was supported by all a-b ions having m/z similar to unreacted standard. Similar experiments were performed all the other fragments and reported as shown in Table 8-2.

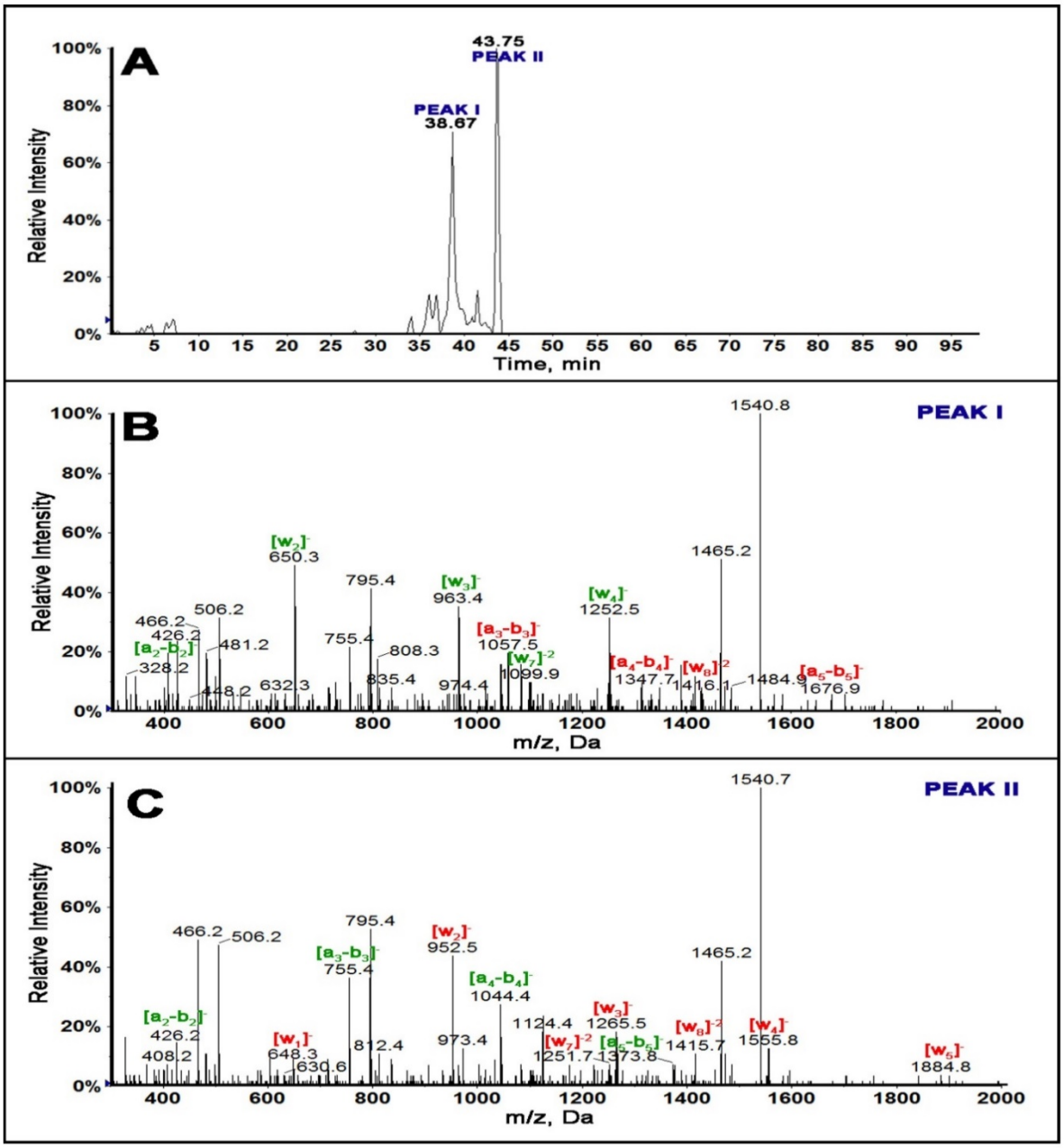

Figure 8-1. LC-MS of ss-DNA fragment **1** (A) Extracted ion chromatogram for fragment m/z 1540.5 representing z = -2 singly adducted fragment 1. (B) MS/MS spectrum of singly adducted BPDE ss- DNA fragment 1, m/z 1540.5 for peak I eluting at 38.67 min and (C) MS/MS of peak II eluting at 43.75 min. (1540.7 or 1540.8 m/z was observed instead of 1540.5 due to isotopic distribution)

Table 8-1. Fragment ions for standard ss-DNA Fragment 1 of m/z 1388.9 and singly adducted BPDE Fragment 1 ion with m/z of 1540.5 from LC-MS/MS.

Fragment Ion	m/z		
	Standard	Peak I	Peak II
a_2-b_2	$[426.2]^-$	$[426.2]^-$	$[426.2]^-$
a_3-b_3	$[755.5]^-$	$[1057.5]^-$	$[755.4]^-$
a_4-b_4	$[1044.7]^-$	$[1347.7]^-$	$[1044.3]^-$
a_5-b_5	$[1373.5]^-$	$[1676.9]^-$	$[1373.8]^-$
w_1	$[346.2]^{-1}$	$[346.2]^-$	$[648.3]^-$
w_2	$[650.3]^-$	$[650.3]^-$	$[952.5]^-$
w_3	$[963.4]^-$	$[963.4]^-$	$[1265.5]^{-2}$
w_4	$[1252.8]^-$	$[1252.5]^-$	$[1555.8]^-$
w_5	$[1582.0]^-$	n/d	$[1884.7]^-$
w_6	n/d	n/d	n/d
w_7	$[1099.7]^{-2}$	$[1099.9]^{-2}$	$[1251.6]^{-2}$
w_8	$[1263.3]^{-2}$	$[1416.1]^{-2}$	$[1415.7]^{-2}$

Table 8-2. Standard single stranded DNA fragments with their corresponding base adducted in comparison with the hot spot database.

Standard ss-DNA	Sequence	LC-MS/MS DATA		Common Hot Spots from Database
		Base adducted	Codon	
Fragment 1	**GGCGGCATG**	**GG*CGGCATG**	**244[b]**	**244[b], 245[a,d]**
		GGCGGCATG*	**246**	**244[b], 245[a,d]**
Fragment 2	**AACCGGAGGC CCATCCTCA**	**AACCGGAGG*C CCATCCTCA**	**249[a,b]**	**248[a,b,c,d,e], 249[a,b,]**
Complementary Strands				
Fragment 3	**GTGAGGATGGGCCTCCGGTTC ATG**		**GTGAG*GATGGGCCTCCGGTTC ATG**	
Fragment 4	**CCGCCCATG**		**CCG*CCCATG**	
			CCGCCCA*TG	
			CCGCCCATG*	

Note: Possible cancers due to BPDE a. Non Small Cell lung cancer, b. Small Cell lung cancer, c. Head and Neck cancer d. Colorectal cancer, e. Skin Cancer

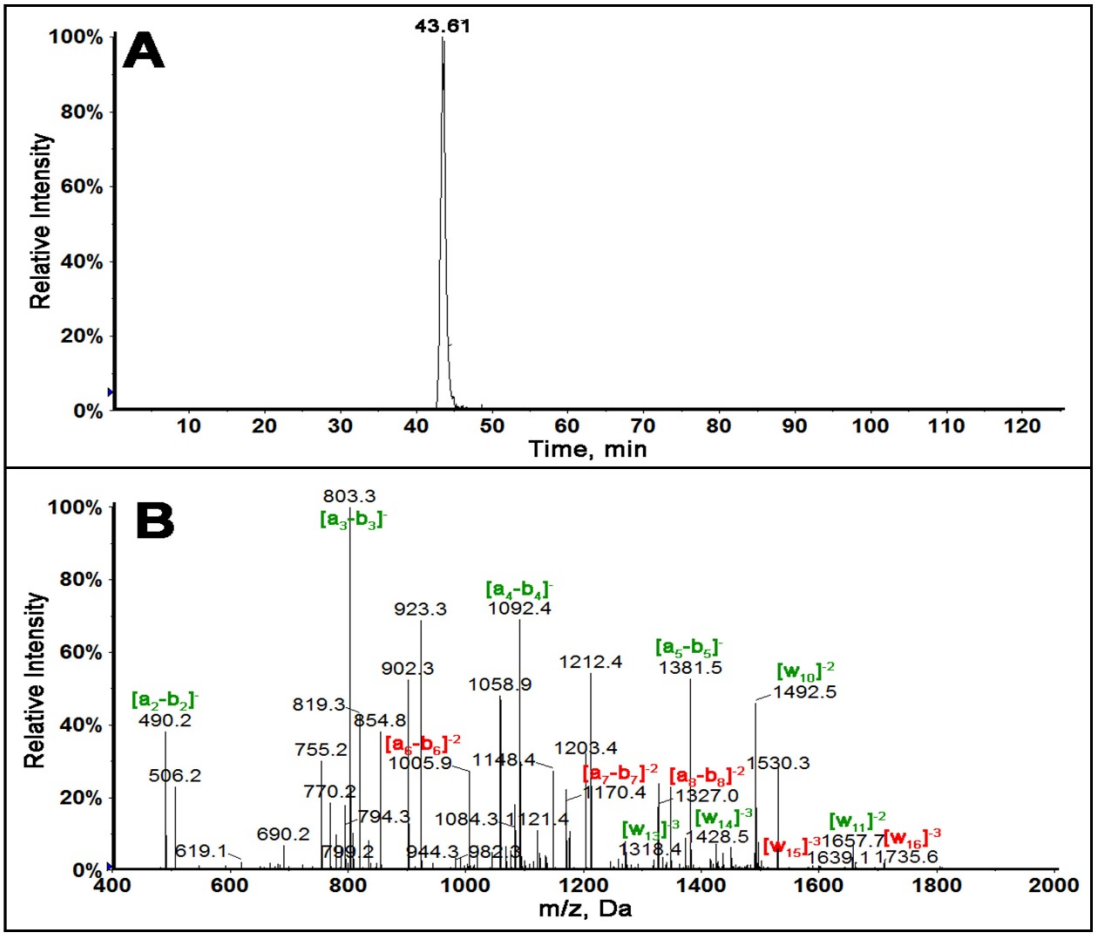

Figure 8-2. LC-MS of ds-32 bp exon 7 fragment: (A) Extracted ion chromatogram of singly adducted fragment **2**, m/z 1530.3, z = -4. (B) MS/MS spectrum of 1530.3 showing a_n-b_n and w_n ions. Ions with m/z similar to standard labeled in green and ions with increased m/z in red.

After establishing and optimizing reproducible methodology on the standard single stranded DNA fragments, the 32 bp ds-p53 exon 7 fragment, which is a combination of fragments **1** and **2** along with the complementary strand, was reacted with BPDE. Four bases, CATG were added to the front of fragment 1 to avoid terminal guanines. The sequence added is consistent with the exon 7 sequence. Excess BPDE was removed using mass cutoff filters, then the aqueous extract was treated with restriction enzyme NIaIII to cut the fragment into smaller fragments suitable for

LC-MS. Subsequently, heating and rapid cooling gave the four single stranded fragments. In order to determine sequence specificity on the entire 32 bp fragment, collision induced dissociation (CID or MS/MS) was performed on all possible single adducted oligonucleotide fragments. Singly adducted fragment **2** is described here as the fragment containing hot spot 248 and 249 active for a number of cancers.[11,14] Singly adducted fragment 2 upon MS ionization produced a ion of m/z 1530.3 with z = -4. The extracted ion chromatogram (XIC) of m/z 1530.3 (Figure 8-2A) gave only one major peak indicating that there is one major adduct on the singly adducted fragment **2** of the reacted 32 bp fragment.

MS/MS spectra for singly adducted fragment **2**, m/z 1530.3, shows all a_n-b_n ions up to a_5-b_5 have m/z similar to that of unreacted standard. An increase in m/z of 302.323 (z = -1) was observed for a_6-b_6, a_7-b_7, a_8-b_8. This suggests that the possible modification is on base 5, (AACCG*GAGGCCCATCCTCA). This was confirmed by increases in m/z for w_{15} and w_{16} ions, while all w ions below w_{14} have m/z similar to that of unreacted standard. Similar experiments were performed on all othet fragments and reported in Table 8-3.

Since the modification is relatively small in the adducted DNA fragments, we assume the adducted and unadducted fragments have only minor changes in electrospray ionization behavior and MS response. Relative abundance of specific adducted nucleobases within codons were estimated by comparing areas of the extracted ion chromatograms of adducted fragments to that of unadducted fragments, and these ratios were further compared with other adducted fragments ratios. Ratios of relative amounts of adduction in the 32 bp fragment for codons 248/244 was 1.5 and codons 248/243 was 1.3 with a relative standard deviation less than 6.5% (n=3). According to p53 handbook database, the mutation frequency ratio of codons 248/243 is 24, 248/244 is 7, 248/249 is 2.7 and 248/245 is 2.1. Increased reactivity of codon 243 compared to p53 mutation frequency ratio may be related to guanine

in codon 243 being the first guanine in our 32 bp fragment which may be more available for reaction due to its position near the end of the strand.

Table 8-3. Fragments of ds-32 bp exon 7 fragment with corresponding base adducted in comparison with the p53 database.

Fragment Name	Sequence	LC-MS/MS DATA		Common Hot Spot Database
		Base Adducted	Codon	
Fragment 1	**CATGGGCGGCATG**	**CATG*GGCGGCATG**	**243**	**244[b], 245[a,d]**
		CATGG*GCGGCATG	**244[b]**	**244[b],245[a,d]**
Fragment 2	**AACCGGAGGCCCATCCTCA**	**AACCG*GAGGCCCATCCTCA**	**248**	**248[a,b,c,d,e], 249[a,b]**
Complementary Strands				
Fragment 3	**TGAGGATGGGCCTCCGGTTCATG**		**TGAGG*ATGGGCCTCCGGTTCATG**	
Fragment 4	**CCGCCCATG**		**CCG*CCCATG**	

Note: Possible cancers due to BPDE a. Non Small Cell lung cancer, b. Small Cell lung cancer, c. Head and Neck cancer d. Colorectal cancer, e. Skin Cancer

Kinetics. Multiple reaction monitoring (MRM) was then used to quantify BPDE adduction at each reactive codon vs. reaction time. Transitions were selected specific to the ss-fragment monitored. For example, transition 1085.4→650.0 for singly adducted MeC fragment 1, and 1009.9→650.0 for unadducted fragment 1. Here 1085.4 and 1009.9 are m/z of precursor ions of single adducted fragment 1 and unadducted fragment 1, respectively, with charge -4. M/z 650.0 represents the product ion of precursor 1085.4 which is also the major transition for the unadducted precursor ion, m/z 1009.9.

The relative amount of BPDE adduction was measured as ratio of peak area for XIC of adducted fragment to total peak area of the corresponding adducted+unadducted fragment.

Relative amounts of BPDE adduction were plotted vs. time for G's in codons 248, 244 and 243 (Figure 8-3a).

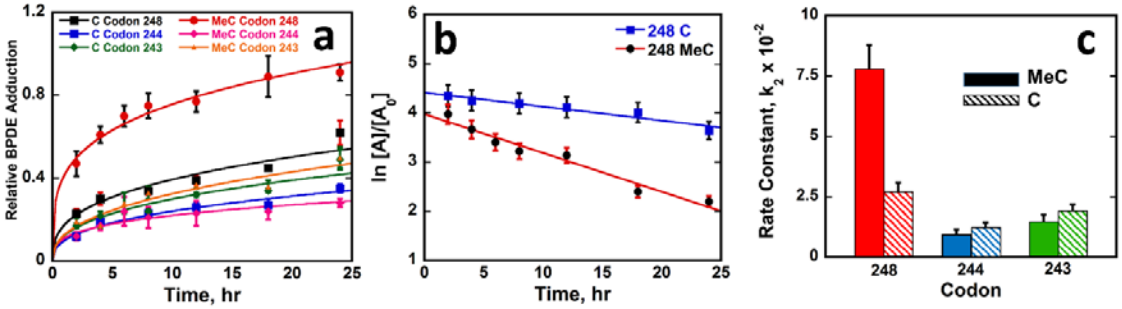

Figure 8-3. Kinetic study of BPDE adduction on MeC and all-C 32 bp p53 exon 7 gene fragments: a) Relative amount of BPDE adducted to guanine within codons 248, 244 and 243. b) Rate plots showing natural log of relative amount of undamaged oligo fragments (*ln [A]/[A$_0$]*) vs time. c) Bar graph showing comparative rate constants k_2 ($s^{-1}M^{-1}$) calculated from the slope of rate plots for BPDE adduction. Error bars represent SD for n=3.

Table 8-4. Rate constants k_1 and k_2 and ratios for different reactive sites.

Rate Constant	**MeC Codon**			**C Codon**		
	248	**244**	**243**	**248**	**244**	**243**
k_1, s^{-1} ($x10^6$)	26±3	3.0±0.7	4.8±1.0	9.0±1.3	4.0±0.7	6.3±0.9
k_2, $s^{-1}M^{-1}$ ($x10^2$)	7.8±1.0	0.9±0.2	1.4±0.3	2.7±0.4	1.2±0.2	1.9±0.3
Rate Constant Ratios						
Me-C/C	**Ratio**	**Me-C/Me-C Codon**		**C-C Codon**		
248	2.9	**248/244** 8.7		**248/244** 2.2		
244	0.8	**248/243** 5.4		**248/243** 1.4		
243	0.8					

Note. Rate constants k_1, for codon 244 and 243 in the methylated fragments are not significantly different according to t-test at 95% confidence interval.

Expressions in eq (1) define k_1 as the pseudo-first order rate constant, and k_2 as the second order rate constant, where C_o is initial amount of unreacted exon 7 fragment and C the amount unreacted at time t. Linear plots that fit eq 1 were obtained (Figure 8-3b), as shown for codon 248 for MeC and all C exon 7 fragments. We obtained k_1 from the slopes, and k_2 from k_1 (eq 1).

$$ln\ C = ln\ C_o - k_1 t\ ;\quad k_2 = k_1/[BPDE] \quad (1)$$

Kinetic results show that k_2 for BPDE adduction on codon 248 CpG is nearly 3-fold larger for the MeC fragment vs. C-only (Figure 8c, Table 8-4). Rate constants for non-CpG adduct at codons 244 and 243, are ~20% smaller for MeC vs C-only, but differences are not statistically significant. The k_2 ratio of the MeC oligonucleotide for codons 248/244 is ~9, close to ratio of mutational frequencies in the p53 gene.[3] For MeC exon 7 (Table 8-4)., codon 248/243 k_2 ratio is 5.3 while the mutation ratio is a bit larger at 24. These results demonstrate the influence of MeC on CpG sites like codon 248 in the p53 gene to greatly increase reaction rates of MeCpG sites. Results show negligible influence of MeC on reactive non-CpG guanines.

8-4. DISCUSSION

The 32 bp p53 exon 7 fragment reacted with BPDE had all reactive bases as Gs, and the most frequently reacted guanine was in codon 248. Guanines within codons 243 and 244 were adducted to a lesser extent. Codon 248 is the major mutation hot spot for most tissue specific cancers such as lung, and head and neck. Thus, there is qualitative correlation of the high reactive frequency of codon 248 in our fragment with its high rate of mutation in many cancers, as well as the observed reactivity of codons 244 and 243. However, the relative mutation frequencies of codons 244 and 243 are lower that the relative reactivities we find in the 32 bp p53 fragment.

Differences in reactivity vs. mutation frequency in tumors at codons 244 and 245 is undoubtedly related to the complexity of living tumors and cell cultures as compared to our *in*

vitro reaction system. In addition to complications from organ-based metabolism, which is absent in our present reactions, differences may be due to DNA being bound to histones and other proteins *in vivo* as well as to in vivo DNA repair. Also, sequences in both 244 and 245 codons are GGC. Codon 243 is close to the end of the fragment, adjacent to an AT sequence, and may be partially unwound exposing the guanine adjacent to it due to fewer hydrogen bonds.[64] Codon 243 may thus be more reactive in the fragment than in the full *p53 gene.* Also, under *in vivo* conditions, a considerable fraction of cytosines are methylated which can mediate codon reactivity.[65,66] 5-Methyl cytosines increase the nucleophilicity of exocyclic amine of adjacent guanine as result of inductive electronic effects.[34] We are currently exploring this issue by additional experiments.

Covalent binding of BPDE preferentially targets guanines in DNA,[67,68] because guanine is the best nucleophile of all the DNA bases. The N7 position of guanine is the most nucleophilic site but the exocyclic amine group, also a good nucleophile, is the most favorable target for polyaromatic hydrocarbon diol epoxides like BPDE. This is because proximity of the N7 group to the hydrophilic sugar chain of the DNA makes it less susceptible to attack of hydrophobic pyrenyl moieties.[69-71]

All exocyclic amines of guanines in single stranded DNA are available for covalent reaction with BPDE. In double stranded DNA the exocyclic amines are involved in hydrogen bonding with the carbonyl oxygen atom of cytosine hence are not freely available for reactions with BPDE. Guanines specifically in the minor groove of duplex DNA can form covalent adducts with BPDE, thereby disrupting the hydrogen bonding between the GC base pair.[72,73]

As per p53 handbook, codon 247 is a hot spot for Melonoma and Skin Squamous Cell Carcinoma, admittedly with a small number of mutations. Although guanine is not in the codon,

the potential of BPDE to react with adenine exists. Since we did not find any adduction on any nucleobase within codon 247 in our study, selectivity of BPDE to guanines was further affirmed.

Our results are consistent with the fact that most damaged codons in tumors and cancer cell cultures involve guanines as the major site of attack by BPDE.[67,74] Guanines were also exclusive targets in the experiments with ss-oligonucleotides. Structural differences of ssDNA and dsDNA may play a role in sequence specific DNA damage. Short single stranded oligonucleotides used in our study have a more flexible structure unprotected with a complementary strand and featuring a free axis of rotation along the phosphodiester backbone.[75,76] Thus, while specificity would be expected to be much lower for ssDNA compared with that of dsDNA we still find that high mutation frequency codons 249 and 244 are highly reactive with BDPE in the short ss-fragments. These results suggest that the relative reactivity of the ds-DNA may be a combination of inherent chemistry of the codon sites and the ds- and higher structure of the DNA.

Double stranded DNAs are relatively inflexible due to GC and AT base pairing and double helical structure resulting in their complicated secondary and tertiary structures.[43] The double helical structure also features major and minor groves in duplex DNA. BPDE specifically attacks the electron donating exocyclic amine in the minor groove containing the nucleophilic GC base pair of DNA. Therefore reactivity of dsDNA will be different to that of ssDNA.[72,73] However in our experiments, we see that the ss-fragments and ds-32 bp fragment both have selective reactivity that includes codons with high frequency of mutation in p53. Thus, selectivity is different in the ss- and ds-fragments, but still exhibited by the single strands.

Very few studies thus far have focused on differential selectivity of specific base sequences.[77] Jernstroem, et. al suggest that guanines adjacent to or flanked by guanines are more reactive[77-79] In contradiction, other studies predict that guanines flanked by pyrimidine bases are

more reactive due to less steric effects as compared to guanines flanked by purine bases.[73,80-82] The reactive site of codon 248 in our 32 bp fragment is a guanine flanked by guanine, while codons 244 and 243 are guanines flanked by purine on one side and pyrimidine on the other side and show intermediate reactivity. Codon adduction sites in ss-DNA oligonucleotides are guanines sandwiched between one purine and one pyrimidine. Hence, our results are in qualitative agreement with the predictions quoted above. However, relating full guanine sequence specificity to adjacent bases is undoubtedly an oversimplification, and in addition to base sequence, specificity most likely involves complex structural and environmental factors *in vivo* including bound histones and proteins.

Structural Analysis. Additional studies were aimed at molecular interpretation of the kinetics. Circular dichroism (CD) spectra of full MeC and C-only versions of the exon 7 fragments (Figure 8-4), suggest different conformations. The MeC exon 7 has an intense negative CD peak at 210 nm and an intense positive peak near 270 nm similar to a pure A-DNA structure,[83] but also a minimum near 245 nm characteristic of B-DNA. For the non-MeC exon 7, the first minimum is shifted to longer wavelength and is weaker, and a maximum at 265 nm is broad, with a shoulder at ~285 nm more characteristic of B DNA[83] (Figure 8-4). We interpret both CD spectra in terms of mixed A-B DNA structures, with MeC's driving structure toward the A.

Molecular Modeling. A and B forms of Me-C and C versions of exon 7 were constructed and molecular modeling was done using Autodock software. Structures were solvated with water and docked with the most reactive isomer (+)anti-BPDE. BPDE conformations at optimal docking sites were in the minor groove close to codon 248 for conformations with the most negative binding free energy. Conformations with distances between reactive exocyclic amine of G in codon 248 and the epoxide carbon of BPDE less 4.5 Å were considered, due to probability of subsequently

forming covalent bonds. Optimal binding of BPDE to guanine in codon 248 (Figure 8-5) gave binding free energies (ΔG_b) for B and A conformations (Table 8-5) which were used to calculate binding constants (K_b) from $K_b = -\Delta G_b/RT$, where R is the ideal gas constant and T in Kelvin. Larger K_b's were found for MeC versions in both A and B form of DNA compared to all-C counterparts. For conformations approximating experimental ones, MeC A-form had 5-fold higher K_b than all-C A-form. Smaller interatomic distances of reactive atoms were found in A-form of DNA (Figure 8-5, Table 8-5) indicating better accessibility for BPDE, with the smallest distance for the MeC A-form. Docking studies were also done with (-) anti BPDE, which gave qualitatively similar results but less dramatic K_b differences. As a control, we modeled BPDE binding to ds-poly(dG-dC).(dG-dC) oligonucleotides with all MeCs and all C, and found 5-fold larger K_b for MeC version similar to experimental measurements.[39] Thus, modeling of MeC exon 7 fragment as an A DNA structure and all-C version closer to B DNA agreed well with a pathway featuring preceding non-covalent binding of BPDE in the minor groove near codon 248 that "sets up" subsequent fast S_N2 covalent coupling.

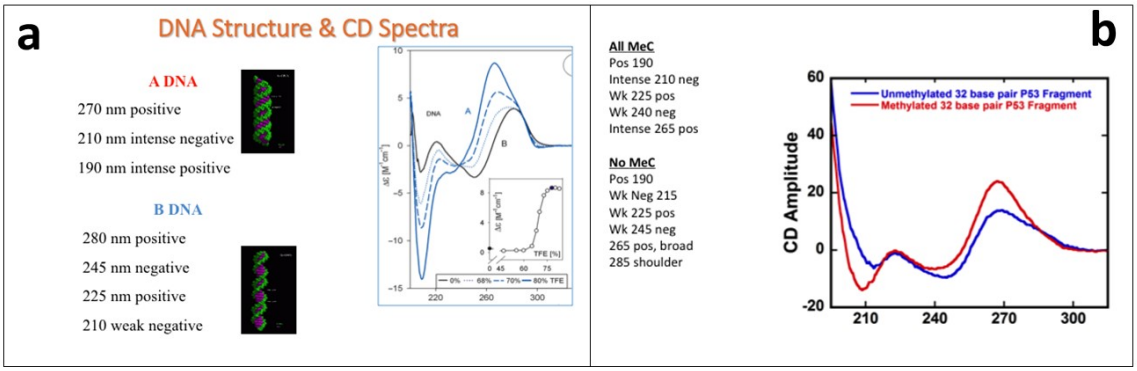

Figure 8-4. a) Circular dichroism showing transition from A to B form of DNA. Reproduced from J. Kypr et. al., *Nucleic Acid Research*, 2009, *37*, 1713-1725. B) Interpretation of CD spectra of the P53 exon fragment in terms of A and B-DNA. Results suggest transition from mixed A- and B-DNA towards more A-DNA content upon methylation of C's.

It's very likely that stronger binding to the A DNA-like structure of the MeC exon 7 is also influenced considerably by hydrophobic interactions that increase for A DNA-like MeC oligonucleotides. An indirect indication of this effect was found in preliminary modeling studies without water, in which similar trends were found in K_b for systems in Figure 8-5, but K_b differences between A MeC and B all-C forms were much smaller. We thus attribute a part of the increases in K_b (Table 8-5) for both the A and B forms of the MeC p53 fragments to the hydrophobic influence on water structure that tends to increase affinity of BPDE for the codon 248 minor groove.

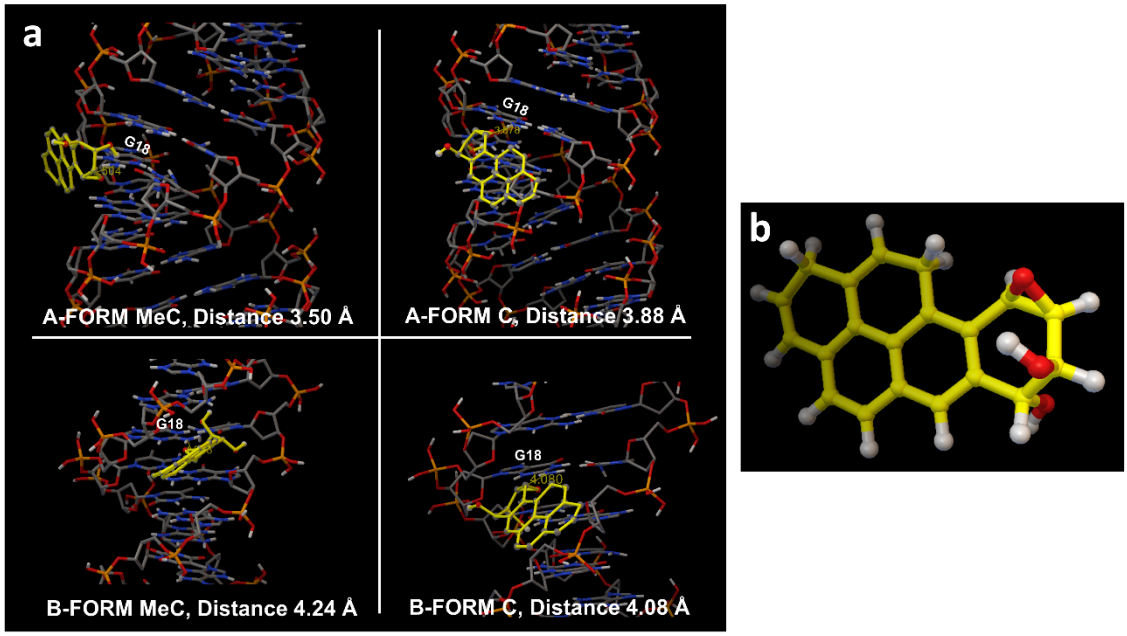

Figure 8-5. a) Models of BPDE docked close to reactive guanine in codon 248 in A and B forms of the 32 bp exon 7 p53 fragment in MeC and C versions. Distance is between exocyclic amine of reactive G and epoxide carbon in Å. (Water is removed for clarity; solvated models with water) b) Model of Benzo[a]pyrene-r-7,t-8-dihydrodiol-t-9,10-epoxide (+) (anti)

Our findings of B-like to A-like structural changes for conversion from the C→MeC exon 7 duplexes are consistent with earlier literature.[84,85] Crystalized oligonucleotides are

predominantly B DNA, but can transition to dehydrated A-forms upon methylation when rich in CG regions, and intermediate structures between A and B have been crystallized.[86,87] The A form has a wider minor groove that provides better accessibility for BPDE.[83] This enables a shorter distance for the reactive exocyclic amine of G to the epoxide carbon of BPDE in A-form than in B form (Table 8-5). Earlier computations showed that epigenetic modifications alter the structure of the DNA making sites of adduction more accessible.[88-91]

Table 8-5. Computed binding free energies, binding constant and distance between exocyclic amine of reactive G in codon 248 and epoxide carbon of BPDE.

DNA	**Binding Energy kcal.mol^{-1}, ΔG**	**Binding Constant, K_b, M^{-1},**	**Distance, Å**
B Form-C	-3.47	3.48×10^2	4.08
B Form-MeC	-4.10	1.00×10^3	4.24
A Form-C	-3.84	6.58×10^2	3.88
A Form-MeC	-4.80	3.32×10^3	3.50

Methods utilized above provide a straightforward approach to directly study kinetics of gene damage reactions. Results suggest that methylcytosines, which predominate in tumor suppressor genes,[19] and influence the kinetics of S_N2 reactions with BPDE mainly at CpG sites of tumor suppressor genes. In the p53 exon 7 fragment studied, codons 248, 244 and 243 were the reactive sites for MeC and all-C versions. Codon 248, the featuring CpG, gave the fastest reaction with the MeC fragment reacting 3-fold faster than the non-MeC version (Table 8-5). CD spectra and computation modeling uncovered a change in conformation from a mixed A-B to a more A-

like duplex structure that drives free-energy for noncovalent binding of BPDE in the codon 248 region more negative for the MeC version, due to better access to the minor groove site and increased hydrophobicity. The resulting larger k_b most likely lowers activation free energy to contribute significantly to the faster kinetics of S_N2 coupling of BPDE to MeCpG in codon 248. The structural change does not significantly influence non-CpG codons 244 and 243 that have similar kinetics for MeC and C versions. The hydrolysis-free methodology used here to measure direct kinetics of damage by metabolites to oligonucleotides longer than 20 bp is applicable to correlate gene damage sites for drug and pollutant metabolites with mutation sites. We speculate that these longer nucleotides are more amenable than shorter fragments to uncover the influence of important structural changes relevant to the reactivity of the entire gene.

8-5. Summary

In summary, we have described methodology to screen chemicals, drugs and metabolites for reactions with oligonucleotides to determine the most frequently adducted nucleobase within codons. Results show that LC-MS/MS and restriction enzymes can be used to prepare carcinogen modified oligonucleotides so as to identify the site of adduction on oligonucleotide fragments longer than 20 base pairs. Our 32 bp fragment reactions represent the first study of a p53 gene fragment representing more than 20 base pairs with multiple mutation hot spots. The highest reaction frequency was at codon 248, consistent with the highest mutation frequency of the p53 gene in many cancers. Also, BPDE reactivity found at codons 243 and 244 is consistent with these codons being mutated in tissue cancers.

Methodology described is directly adaptable to other chemicals and other tumor suppressor gene fragments to investigate kinetics of their DNA damage reactions. Molecular dynamics

modeling can be used as an auxiliary tool to gain a more complete assessment of the chemistry of the associated reaction events. This quantitative methodology can be adapted to multiple chemicals and multiple exons across multiple tumor suppressor genes to expanding knowledge of genotoxicity chemistry pathways in relation to organ specificity of carcinogenesis. Next chapter focuses on development of Magnetic bio-colloid based technology coupled with LC-MS/MS for screening chemicals/prodrugs which require metabolic activation to cause DNA toxicity and co-relation with organ specific cancer.

8-6. References

1. Levine, A. J.; Oren, M. The first 30 years of p53: growing ever more complex. *Nature Reviews Cancer* **2009**, *9*, 749-758.

2. May, P.; May, E. Twenty years of p53 research: structural and functional aspects of the p53 protein. *Oncogene* **1999**, *18*, 7621-7636.

3. http://p53.free.fr/Database/p53_database.html, last accessed 12/06/2016.

4. http://p53.iarc.fr/TP53SomaticMutations.aspx, last accessed 12/06/2016.

5. Soussi, T.; Wiman, K. G. Shaping genetic alterations in human cancer: the p53 mutation paradigm. *Cancer Cell* **2007**, *12*, 303-312.

6. Soussi, T. p53 alterations in human cancer: more questions than answers. *Oncogene* **2007**, *26*, 2145-2156.

7. Cheok, C. F.; Verma, C. S.; Baselga, J.; Lane, D. P. Translating p53 into the clinic. *Nat. Rev. Clin. Oncol.* **2011**, *8*, 25-37.

8. Pfeifer, G. P.; Besaratinia, A. Mutational spectra of human cancer. *Hum. Genet.* **2009**, *125*, 493-506.

9. Ozaki, T.; Nakagawara, A. p53: the attractive tumor suppressor in the cancer research field. *J. Biomed. Biotechnol.* **2011**, 603925, 1-13.

10. Soussi, T. TP53 mutations in human cancer: database reassessment and prospects for the next decade. *Adv. Cancer Res.* **2011**, *110*, 107-139.

11. Leroy, B.; Anderson, M.; Soussi, T. TP53 Mutations in Human Cancer: Database Reassessment and Prospects for the Next Decade. *Hum. Mutat.* **2014**, *35*, 672-688.

12. Olivier, M.; Hussain, S. P.; Caron, d.,Fromentel Claude; Hainaut, P.; Harris, C. C. TP53 mutation spectra and load: a tool for generating hypotheses on the etiology of cancer. *IARC Sci. Publ.* **2004**, 247-270.

13. http://www.binfo.ncku.edu.tw/TAG/GeneFinder.php (Last accessed December 6, 2016)

14. States, J. C.; Ouyang, M.; Helm, C. W. Systems approach to identify environmental exposures contributing to organ-specific carcinogenesis. *Cancer Epidemiol* **2014**, *38*, 321-327.

15. Patel, Y. M.; Park, S. L.; Carmella, S. G.; Paiano, V.; Olvera, N.; Stram, D. O.; Haiman, C. A.; Le Marchand, L.; Hecht, S. S. Metabolites of the Polycyclic Aromatic Hydrocarbon Phenanthrene in the Urine of Cigarette Smokers from Five Ethnic Groups with Differing Risks for Lung Cancer. *PloS one* **2016**, *11*, 1-15.

16. Nelson, D. R. Cytochrome P450: Structure, Mechanism, and Biochemistry, (ed. Paul R. O.) 183-245 (Kluwer Academic/Plenum Publishers, 2005).

17. Wasalathanthri, D. P.; Malla, S.; Bist, I.; Tang, C. K.; Faria, R. C.; Rusling, J. F. High-throughput metabolic genotoxicity screening with a fluidic microwell chip and electrochemiluminescence. *Lab on a Chip***2013**, *13*, 4554-4562.

18. Yang, S. K.; Deutsch, J.; Gelboin, H. V. Benzo (a) pyrene metabolism: activation and detoxification. *Polycyclic Hydrocarbons and Cancer* **2012**, *1*, 205-232.

19. Jabbari, K.; Bernardi, G. Cytosine methylation and CpG, TpG (CpA) and TpA frequencies. *Gene* **2004**, *333*, 143-149.

20. Bird, A. DNA methylation patterns and epigenetic memory. *Genes Dev.* **2002**, *16*, 6-21.

21. Tornaletti, S.; Pfeifer, G. P. Complete and tissue-independent methylation of CpG sites in the p53 gene: implications for mutations in human cancers. *Oncogene* **1995**, *10*, 1493-1499.

22. Denissenko, M. F.; Chen, J. X.; Tang, M. S.; Pfeifer, G. P. Cytosine methylation determines hot spots of DNA damage in the human P53 gene. *Proc. Natl. Acad. Sci. U. S. A.* **1997**, *94*, 3893-3898.

23. Kouidou, S.; Agidou, T.; Kyrkou, A.; Andreou, A.; Katopodi, T.; Georgiou, E.; Krikelis, D.; Dimitriadou, A.; Spanos, P.; Tsilikas, C. Non-CpG cytosine methylation of p53 exon 5 in non-small cell lung carcinoma. *Lung Cancer* **2005**, *50*, 299-307.

24. Xiong, W.; Glick, J.; Lin, Y.; Vouros, P. Separation and Sequencing of Isomeric Oligonucleotide Adducts Using Monolithic Columns by Ion-Pair Reversed-Phase Nano-HPLC Coupled to Ion Trap Mass Spectrometry. *Anal. Chem. (Washington, DC, U. S.)* **2007**, *79*, 5312-5321.

25. Liao, Q.; Shen, C.; Vouros, P. GenoMass - a computer software for automated identification of oligonucleotide DNA adducts from LC-MS analysis of DNA digests. *J. Mass Spectrom.* **2009**, *44*, 549-560.

26. Chowdhury, G.; Guengerich, F. P. Tandem Mass Spectrometry-Based Detection of C4'-Oxidized Abasic Sites at Specific Positions in DNA Fragments. *Chem. Res. Toxicol.* **2009**, *22*, 1310-1319.

27. Chowdhury, G.; Guengerich, F. P. Liquid chromatography-mass spectrometry analysis of DNA polymerase reaction products. *Curr Protoc Nucleic Acid Chem* **2011**, *Chapter 7*, Unit 7.16.1-11.

28. Tretyakova, N.; Villalta, P. W.; Kotapati, S. Mass Spectrometry of Structurally Modified DNA. *Chem. Rev.* **2013**, *113*, 2395-2436.

29. Harsch, A.; Sayer, J. M.; Jerina, D. M.; Vouros, P. HPLC-MS/MS Identification of Positionally Isomeric Benzoc]phenanthrene Diol Epoxide Adducts in Duplex DNA. *Chem. Res. Toxicol.* **2000**, *13*, 1342-1348.

30. Chowdhury, G.; Guengerich, F. P. Direct detection and mapping of sites of base modification in DNA fragments by tandem mass spectrometry. *Angew. Chem. , Int. Ed.* **2008**, *47*, 381-384.

31. Sharma, V. K.; Glick, J.; Liao, Q.; Shen, C.; Vouros, P. GenoMass software: a tool based on electrospray ionization tandem mass spectrometry for characterization and sequencing of oligonucleotide adducts. *J. Mass Spectrom.* **2012**, *47*, 490-501.

32. Satterwhite, J. E.; Pugh, A. M.; Danell, A. S.; Hvastkovs, E. G. Electrochemical Detection of anti-Benzoa]pyrene Diol Epoxide DNA Damage on TP53 Codon 273 Oligomers. *Anal. Chem.* **2011**, *83*, 3327-3335.

33. Sharma, V. K.; Xiong, W.; Glick, J.; Vouros, P. Determination of site selectivity of different carcinogens for preferential mutational hot spots in oligonucleotide fragments by ion-pair reversed-phase nano liquid chromatography tandem mass spectrometry. *Eur. J. Mass Spectrom.* **2014**, *20*, 63-72.

34. Guza, R.; Kotandeniya, D.; Murphy, K.; Dissanayake, T.; Lin, C.; Giambasu, G. M.; Lad, R. R.; Wojciechowski, F.; Amin, S.; Sturla, S. J.; Hudson, R. H.; York, D. M.; Jankowiak, R.; Jones, R.; Tretyakova, N. Y. Influence of C-5 substituted cytosine and related nucleoside analogs on the formation of benzo[a]pyrene diol epoxide-dG adducts at CG base pairs of DNA. *Nucleic Acids Res.* **2011**, *39*, 3988-4006.

35. Wang, H.; Zhang, S.; Hu, Y.; Tang, M. Mutagenicity and sequence specificity of acrolein-DNA adducts. *Chem. Res. Toxicol.* **2009**, *22*, 511-517.

36. Wang, H. T.; Weng, M. W.; Chen, W. C.; Yobin, M.; Pan, J.; Chung, F. L.; Wu, X. R.; Rom, W.; Tang, M. S. Effect of CpG methylation at different sequence context on acrolein- and BPDE-DNA binding and mutagenesis. *Carcinogenesis* **2013**, *34*, 220-227.

37. Satterwhite, J. E.; Trumbo, C. M.; Danell, A. S.; Hvastkovs, E. G. Electrochemical Study on the Effects of Epigenetic Cytosine Methylation on Anti-Benzo [a] pyrene Diol Epoxide Damage at TP53 Oligomers. *Anal. Chem.* **2013**, *85*, 1183-1191.

38. Glick, J.; Xiong, W.; Lin, Y.; Noronha, A. M.; Wilds, C. J.; Vouros, P. The influence of cytosine methylation on the chemoselectivity of benzo [a] pyrene diol epoxide-oligonucleotide adducts determined using nanoLC/MS/MS. *Journal of mass spectrometry* **2009**, *44*, 1241-1248.

39. Geacintov, N. E.; Shahbaz, M.; Ibanez, V.; Moussaoui, K.; Harvey, R. G. Base-sequence dependence of noncovalent complex formation and reactivity of benzo [a] pyrenediol epoxide with polynucleotides. *Biochemistry (N. Y.)* **1988**, *27*, 8380-8387.

40. Deligkaris, C.; Rodriguez, J. H. Non-covalent interactions of the carcinogen ( )-anti-BPDE with exon 1 of the human K-ras proto-oncogene. *Physical Chemistry Chemical Physics* **2014**, *16*, 6199-6210.

41. Bergonzo, C.; Galindo-Murillo, R.; Cheatham, T. E. Molecular modeling of nucleic Acid structure: electrostatics and solvation. *Curr Protoc Nucleic Acid Chem* **2014**, *55*, 7.9.1-7.9.27.

42. Kornyshev, A. A. Physics of DNA: unravelling hidden abilities encoded in the structure of 'the most important molecule'. *Phys. Chem. Chem. Phys.* **2010**, *12*, 12352-12378.

43. Cantor, C. R.; Schimmel, P. R. *Biophysical Chemistry - Part 1 The Conformation of Biological Macromolecules;* Freeman: 1980; pp. 155-201.

44. Chen, Z.; Zhang, G.; Chen, X.; Chen, J.; Liu, J. A label-free method for studying DNA sequence recognition of mitoxantrone based on resonance light-scattering technique. *J. Antibiot.* **2012**, *65*, 517-522.

45. Loechler, E. L. The role of adduct site-specific mutagenesis is understanding how carcinogen - DNA adducts cause mutations: perspective, prospects and problems. *Carcinogenesis* **1996**, *17*, 895-902.

46. Neilson, A. N.; Editor. *The Handbook of Environmental Chemistry, Volume 3: Anthropogenic Compounds, Part I: PAHs and Related Compounds: Chemistry;* Springer: 1997; pp. 41-45.

47. Gelboin, H. V. Benzoa]pyrene metabolism, activation, and carcinogenesis: role and regulation of mixed-function oxidases and related enzymes. *Physiol. Rev.* **1980**, *60*, 1107-1166.

48. Harvey, G. R. Metabolic activation, DNA binding, and mechanisms of carcinogenesis. *Polycyclic Aromatic Hydrocarbons: Chemistry and Carcinogenicity*, Cambridge University Press: New York, 1991, pp. 50-78.

49. Brahim, B.; Alves, S.; Cole, R. B.; Tabet, J. Charge enhancement of single-stranded dna in negative electrospray ionization using the supercharging reagent meta-nitrobenzyl alcohol. *J. Am. Soc. Mass Spectrom.* **2013**, *24*, 1988-1996.

50. http://structure.usc.edu/make-na/server.html last accessed 12/06/2016

51. Schrodinger, L., maestro, New York, NY, (2006).

52. http://www.rbvi.ucsf.edu/chimera/ last accessed 12/06/16

53. Pettersen, E. F.; Goddard, T. D.; Huang, C. C.; Couch, G. S.; Greenblatt, D. M.; Meng, E. C.; Ferrin, T. E. UCSF Chimera—a visualization system for exploratory research and analysis. *Journal of computational chemistry* **2004**, *25*, 1605-1612.

54. Morris, G. M. *et al*. AutoDock4 and AutoDockTools4: Automated docking with selective receptor flexibility. *Journal of computational chemistry* **30**, 2785-2791 (2009).

55. Jung, V.; Pestka, S. B.; Pestka, S. Efficient cloning of PCR generated DNA containing terminal restriction endonuclease recognition sites. *Nucleic Acids Res.* **1990**, *18*, 6156.

56. Murray, K. K. DNA sequencing by mass spectrometry. *Journal of mass spectrometry* **1996**, *31*, 1203-1215.

57. Little, D. P.; Chorush, R. A.; Speir, J. P.; Senko, M. W.; Kelleher, N. L.; McLafferty, F. W. Rapid sequencing of oligonucleotides by high-resolution mass spectrometry. *J. Am. Chem. Soc.* **1994**, *116*, 4893-4897.

58. Potier, N.; Van Dorsselaer, A.; Cordier, Y.; Roch, O.; Bischoff, R. Negative electrospray ionization mass spectrometry of synthetic and chemically modified oligonucleotides. *Nucleic Acids Res.* **1994**, *22*, 3895-3903.

59. J. B. Fenn, M. Mann, C. K. Meng, S. F. Wong and C. M. Whitehouse, *Science,* 1989, **246**, 64-71.

60. http://mods.rna.albany.edu/masspec/Mongo-Oligo (last accessed December 6, 2016).

61. McLuckey, S. A.; Van Berker, G. J.; Glish, G. L. Tandem mass spectrometry of small, multiply charged oligonucleotides. *J. Am. Soc. Mass Spectrom.* **1992**, *3*, 60-70.

62. McLuckey, S. A.; Habibi-Goudarzi, S. Ion trap tandem mass spectrometry applied to small multiply charged oligonucleotides with a modified base. *J. Am. Soc. Mass Spectrom.* **1994**, *5*, 740-747.

63. Rozenski, J.; McCloskey, J. A. SOS: a simple interactive program for ab initio oligonucleotide sequencing by mass spectrometry. *J. Am. Soc. Mass Spectrom.* **2002**, *13*, 200-203.

64. Calladine, C.; Drew, H.; Luisi, B.; Travers, A. Twisting and Curving. In" Understanding DNA: The molecule and how it works", 3rd ed.; Elsevier Ltd, 2004; pp. 70-72.

65. Denissenko, M. F.; Chen, J. X.; Tang, M. S.; Pfeifer, G. P. Cytosine methylation determines hot spots of DNA damage in the human P53 gene. *Proc. Natl. Acad. Sci. U. S. A.* **1997**, *94*, 3893-3898.

66. Varley, K. E.; Gertz, J.; Bowling, K. M.; Parker, S. L.; Reddy, T. E.; Pauli-Behn, F.; Cross, M. K.; Williams, B. A.; Stamatoyannopoulos, J. A.; Crawford, G. E.; Absher, D. M.; Wold, B. J.; Myers, R. M. Dynamic DNA methylation across diverse human cell lines and tissues. *Genome Res.* **2013**, *23*, 555-567.

67. Hermanson, G. *Nucleic acid and oligonucleotide conjugation and modification. Bioconjugate Techniques; 3rd* ed.; Audet. J., Preap, M., Eds.; Academic Press, 2013, 959-987.

68. Gates, K. S. An overview of chemical processes that damage cellular DNA: spontaneous hydrolysis, alkylation, and reactions with radicals. *Chem. Res. Toxicol.* **2009**, *22*, 1747-1760.

69. Beland, A. F., Poirier, M. C. *Methods to Assess DNA Damage and Repair: lnterspecies Comparisons*; Tardiff, R. G., Lohman, P. H., Wogan, G. N., Eds.; SCOPE, John Wiley & Sons: New York, 1994; *pp.* 29-55.

70. Baird, W. M.; Hooven, L. A.; Mahadevan, B. Carcinogenic polycyclic aromatic hydrocarbon-DNA adducts and mechanism of action. *Environ. Mol. Mutagen.* **2005**, *45*, 106-114.

71. Lenglet, G.; David-Cordonnier, M. H. DNA-Destabilizing Agents as an Alternative Approach for Targeting DNA: Mechanisms of Action and Cellular Consequences. *J. Nucleic Acids* **2010**, *290935*, 1-17.

72. Geacintov, N. E.; Cosman, M.; Hingerty, B. E.; Amin, S.; Broyde, S.; Patel, D. J. NMR solution structures of stereoisomeric covalent polycyclic aromatic carcinogen-DNA adducts: principles, patterns, and diversity. *Chem. Res. Toxicol.* **1997**, *10*, 111-146.

73. Penning, M., Poly Aromatic Hydrocarbons: Multiple Metabolic Pathways and the DNA Lesions formed. *The Chemical Biology of DNA Damage;* Geacintov, N. E., Broyde, S., Eds.; Wiley-VCH Verlag GmbH & Co. KGaA, 2010; pp 131-155.

74. Pan, S.; Li, D.; Zhao, L.; Schenkman, J. B.; Rusling, J. F. Genotoxicity-Related Chemistry of Human Metabolites of Benzo [ghi] perylene (B [ghi] P) Investigated using Electro-Optical Arrays and DNA/Microsome Biocolloid Reactors with LC-MS/MS. *Chem. Res. Toxicol.* **2013**, *26*, 1229-1239.

75. Levitt, M. In *In Folding of nucleic acids;* Assoc. Sci. Publ: 1972; pp 147-71.

76. Lodish, H., Berk, A., Matsudaira, P., Kaiser, A. C., Krieger, M. Structure of Nucleic Acids. *Molecular Cell Biology*; 5th ed.; W. H. Freeman: New York, 2003; pp 102-107.

77. Jernström, B.; Gräslund, A. Covalent binding of benzo [a] pyrene 7, 8-dihydrodiol 9, 10-epoxides to DNA: molecular structures, induced mutations and biological consequences. *Biophys. Chem.* **1994**, *49*, 185-199.

78. Said, B.; Shank, R. C. Nearest neighbor effects on carcinogen binding to guanine runs in DNA. *Nucleic Acids Res.* **1991**, *19*, 1311-1316.

79. Rodriguez, F. A.; Cai, Y.; Lin, C.; Tang, Y.; Kolbanovskiy, A.; Amin, S.; Patel, D. J.; Broyde, S.; Geacintov, N. E. Exocyclic amino groups of flanking guanines govern sequence-dependent adduct conformations and local structural distortions for minor groove-aligned benzo[a]pyrenyl-guanine lesions in a GG mutation hotspot context. *Nucleic Acids Res.* **2007**, *35*, 1555-1568.

80. Musafija-Jeknic, T.; Luch, A.; Seidel, A.; Johns, C.; Pereira, C.; Baird, W. M. EFFECT OfFIF NUCLEOTIDE SEQUENCE ON THE BINDING OF (–)–ANTI–DIBENZO–[a, l] PYRENE–11, 12–DIOL 13, 14–EPOXIDE TO SHORT OLIGODEOXYRIBONUCLEOTIDES. *Polycyclic Aromatic Compounds* **2005**, *25*, 103-111.

81. Schwartz, J. J.; Lau, H. H.; Baird, W. M. Base sequence selectivity in the binding of 7 (R), 8 (S)-dihydroxy-9 (S), 10 (R)-epoxy-7, 8, 9, 10-tetrahydrobenzo [a] pyrene to oligodeoxyribonucleotide duplexes. *Chem. Res. Toxicol.* **1994**, *7*, 29-40.

82. Margulis, L. A.; Ibanez, V.; Geacintov, N. E. Base-sequence dependence of covalent binding of benzo [a] pyrenediol epoxide to guanine in oligodeoxyribonucleotides. *Chem. Res. Toxicol.* **1993**, *6*, 59-63.

83. Kypr, J.; Kejnovska, I.; Renciuk, D.; Vorlickova, M. Circular dichroism and conformational polymorphism of DNA. *Nucleic Acids Res.* **2009**, *37*, 1713-1725.

84. Vargason, J. M.; Henderson, K.; Ho, P. S. A crystallographic map of the transition from B-DNA to A-DNA. *Proc. Natl. Acad. Sci. U. S. A.* **2001**, *98*, 7265-7270.

85. Banyay, M.; Gräslund, A. Structural effects of cytosine methylation on DNA sugar pucker studied by FTIR. *J. Mol. Biol.* **2002**, *324*, 667-676.

86. Hunter, C. A. Quantifying intermolecular interactions: guidelines for the molecular recognition toolbox. *Angewandte Chemie International Edition* **2004**, *43*, 5310-5324.

87. Ng, H. L.; Kopka, M. L.; Dickerson, R. E. The structure of a stable intermediate in the A B DNA helix transition. *Proc. Natl. Acad. Sci. U. S. A.* **2000**, *97*, 2035-2039.

88. Carvalho, A. T.; Gouveia, L.; Kanna, C. R.; Wärmländer, S. K.; Platts, J. A.; Kamerlin, S. C. L. Understanding the structural and dynamic consequences of DNA epigenetic modifications:

Computational insights into cytosine methylation and hydroxymethylation. *Epigenetics* **2014**, *9*, 1604-1612.

89. Song, Q.; Qiu, Z.; Wang, H.; Xia, Y.; Shen, J.; Zhang, Y. The effect of methylation on the hydrogen-bonding and stacking interaction of nucleic acid bases. *Structural Chemistry* **2013**, *24*, 55-65.

90. Morris, G. M.; Huey, R.; Lindstrom, W.; Sanner, M. F.; Belew, R. K.; Goodsell, D. S.; Olson, A. J. AutoDock4 and AutoDockTools4: Automated docking with selective receptor flexibility. *Journal of computational chemistry* **2009**, *30*, 2785-2791.

91. Kumalo, H. M.; Bhakat, S.; Soliman, M. E. Theory and applications of covalent docking in drug discovery: merits and pitfalls. *Molecules* **2015**, *20*, 1984-2000.